

Electron Spectroscopic Study of Electronic and Morphological Modifications of the WSe_2 Surface induced by Rb Adsorption

Dissertation
zur Erlangung des Doktorgrades
der Mathematisch-Naturwissenschaftlichen Fakultät
der Christian-Albrechts-Universität
zu Kiel

vorgelegt von

Jens Buck

Kiel, 2010

Referent/-in: Prof. Dr. Lutz Kipp

Koreferent/-in: Prof. Dr. Rainer Adlung

Tag der mündlichen Prüfung: 20.7.2010

Zum Druck genehmigt: 20.7.2010

gez. Prof. Dr. Lutz Kipp, Dekan

Zusammenfassung

Inhalt der vorliegenden Arbeit sind Untersuchungen der rubidiumbedeckten Oberfläche des halbleitenden Übergangsmetalldichalkogenids Wolframdiselenid (WSe_2) durch Photoelektronenspektroskopie (PES) und Photoemissionselektronenmikroskopie (PEEM). Vielfältige, Rb-induzierte Effekte mit Auswirkungen auf elektronische, strukturelle und mechanische Eigenschaften sind von diesem System bekannt.

Diese Arbeit ist der Untersuchung des Oberflächenpotentials als Folge des Ladungstransfers bei der Adsorption von Rb gewidmet. Wie gezeigt werden wird, können durch ein theoretisches Modell unterstützte Messungen des Potentials im thermischen Gleichgewicht ('Bandverbiegung') und im lichtinduzierten, stationären Nichtgleichgewicht ('surface photovoltage'(SPV)-Effekt) in Abhängigkeit von der Lichtintensität zur Bestimmung einer Reihe von Materialkonstanten, insbesondere des unbesetzten Oberflächenzustands, herangezogen werden. Die Wirksamkeit spezieller Maßnahmen zur Integration einer Sekundärlichtquelle in einen konventionellen PES-Aufbau wird anhand von Simulationsrechnungen und Kalibrierungsmessungen belegt. Umfassende Anpassungen eines bestehenden Modells des SPV-Effekts an das untersuchte System werden diskutiert. Anhand von experimentellen Daten wird die Gültigkeit des Modells demonstriert.

Das selbstorganisierte Wachstum von Rubidiumdomänen bei Raumtemperatur konnte mit Hilfe von orts aufgelöster XPS-Spektroskopie am PEEM-Experiment an der Beamline UE49/PGMa an der Synchrotronstrahlungsquelle BESSY II beobachtet werden. Die hier vorgestellten Daten lassen auf die Existenz von Rb-Oberflächengittern schließen. Neben den beobachteten, relativ großen Domänen auf der Mikrometerskala wurden ausgedehnte Netzwerke linearer Nanostrukturen spektroskopisch vermessen. Ein Ansatz zur chemischen Charakterisierung dieser Strukturen mittels Röntgenabsorptionsspektroskopie wird hier präsentiert. Ausgehend von der Annahme, dass die beobachteten Strukturen Spannungsrisse der Oberfläche repräsentieren, wurde eine statistische Analyse geometrischer Eigenschaften durchgeführt und mit den Voraussagen eines zu diesem Zweck entwickelten, stark vereinfachten Modells der Rissverteilung verglichen. Eine erste Übereinstimmung der daraus abgeleiteten Aussagen mit den experimentellen Daten gibt Hinweise auf die Gültigkeit der hierfür gemachten Annahmen.

Besondere Aufmerksamkeit wurde technischen Aspekten der Datenverarbeitung von PEEM-Daten gewidmet. Einige neue Ansätze wurden entwickelt, um den Einfluss wohlbekannter Störungen in den Daten zu quantifizieren und zu entfernen. Wie anhand zahlreicher Beispiele unter realistischen Bedingungen gezeigt wird, gelingt dies mit einer derartigen Effizienz, dass die Vergleichbarkeit aller parallel gemessenen Spektren im Detektorbild sichergestellt ist. Obwohl die Information eines einzelnen Datenkanals

fürgewöhnlich eine relativ schlechte Qualität aufweist, ermöglicht die große Zahl parallel gemessener Spektren neue Ansätze zur Klassifizierung der erworbenen Daten. Hier wird ein Konzept aus dem Gebiet des 'Data Mining' auf spektroskopische Daten übertragen und unter anderem zur Strukturerkennung anhand von spektraler Information eingesetzt.

Abstract

The rubidium-covered surface of the semiconducting transition metal dichalcogenide tungsten diselenide (WSe_2) is examined using photoelectron spectroscopy (PES) and photoemission electron microscopy (PEEM). Adsorbed Rb is known to induce a variety of effects in this system concerning electronic, structural, and mechanical properties.

In this work, the surface potential created by charge transfer upon Rb deposition is examined in thermal equilibrium (band bending) and stationary non-equilibrium (surface photovoltage (SPV) effect), which is induced by the absorption of light. It will be shown that combined measurements and numerical simulations of the SPV effect as a function of the photon flux can be exploited for the estimation of many material parameters of the system, especially of the unoccupied adsorbate state. Issues of extending a conventional photoelectron spectrometer setup by a secondary light source will be discussed in the context of simulations and calibration measurements. The customization of an existing theoretical model of the SPV effect for the $WSe_2 : Rb$ system is introduced and a comprehensive validation of the obtained predictions will be given in the context of experimental data.

In addition, the self-organized formation of Rb domains at room temperature was examined by application of spatially resolved XPS spectroscopy using the PEEM setup at the end station of beamline UE49/PGMa at the BESSY II synchrotron facility. From the obtained results, the arrangement of Rb in surface lattices can be concluded. Furthermore, an X-Ray absorption study of self-organized nanostructure networks, aiming at the chemical characterization, is presented. Based on the interpretation of the examined structures as tension-induced cracks, a statistical approach to analyzing large-scale features was pursued. First accordance with the predictions made by a primitive, mechanical model of crack creation developed here gives gives some evidence for the validity of the proposed structure creation mechanism.

A detailed analysis of technical aspects of processing spatially resolved photoemission data was carried out during this work. Several novel methods were developed as compensation for well-known technical limitations of the experimental setup. As will be shown, specific perturbations of PEEM data can be eliminated efficiently hereby, so comparability of all data channels in a detector image is granted. Extensive tests with actual experimental data prove the great applicability of the approaches made here. Though usually having low individual quality, the large number of data channels allows for novel approaches to the classification of spectroscopic data. A concept originating from the field of data mining was ported to work with photoemission spectra and is applied here as an aid to the recognition of spatial structures from spectral features.

Contents

Zusammenfassung	i
Abstract	iii
1. Surface photovoltage effect	5
1. Introduction	7
2. Tungsten Diselenide (WSe_2)	10
3. Theoretical Aspects	16
3.1. Theory of Photoemission	16
3.2. Theory of the surface photovoltage effect	20
4. Experimental setup	40
4.1. Basics of the experimental setup	40
4.2. PHOIBOS analyzer and detection system	44
4.3. The experimental station for ARPES experiments	48
4.4. Extensions to the setup	53
5. Design of a beam guide for auxiliary light sources	60
5.1. Introduction	60
5.2. Constructional detail	61
5.3. Mechanical stability	63
5.4. Electrostatic compatibility	65
5.5. Layout of the optical components	67
5.6. Calibration measurements	69
5.7. Summary	72
6. Results	73

II. Spatially resolved photoemission spectroscopy	85
7. Introduction	86
8. The (S)PEEM experimental station at beamline UE49/PGMa at BESSY II	88
8.1. Beamline	88
8.2. Photoemission Electron Microscopy (PEEM)	91
8.3. Environment	94
9. Raw Data Processing	100
9.1. Removal of hot pixels	100
9.2. MCP normalization	101
9.3. Beam profile normalization	102
9.4. Calibration of the lateral variation of the photon energy	105
9.5. Drift correction	108
10. Data classification scheme for PEEM data	114
10.1. Separating Hyperplane	115
10.2. Data Reduction	117
10.3. Data Clustering	120
11. PEEM spectroscopy of WSe_2 : Rb	125
11.1. Experiment	125
11.2. Results: The clean surface of WSe_2	128
11.3. Discussion: Clean surface	133
11.4. The Rb covered surface of WSe_2	134
11.5. Discussion: Rb covered surface	142
11.6. Laterally confined adsorption of Rb	145
12. Absorption spectra of self-organized nanostructures	148
12.1. Data Processing	151
12.2. Results	152
12.3. Discussion	158

III. Analysis of nanostructure networks	161
13. Introduction and experiment	163
14. Data processing techniques	165
14.1. Composing survey images	165
14.2. Contrast-enhancing image filter	168
14.3. Skeletonization of monochrome bitmaps	171
14.4. Vectorization of bitmapped data	174
15. Results	177
16. Simple theoretical model of crack creation	183
16.1. Introduction	183
16.2. Definitions	185
16.3. General solutions of the system	186
16.4. Results	187
16.5. Limiting cases	189
16.6. Match with experimental data	190
17. Discussion	194
Summary and Outlook	198

Appendix	204
A. Optical characterization of the SPECS UVS300 He discharge lamp	205
B. Some remarks concerning the SPV simulation code	208
C. Calibration of the light source for the SPV experiment	213
D. Pulsed MCP operation for the PHOIBOS analyzer	217
E. High power laser light supply	221
F. Joypad control for ASPHERE	226
G. ASBridge: Synchronous operation of ASPHERE and SPEC SLAB	231
H. Compact laser alignment system for PHOIBOS	235
I. Shape preserving smoothing window for noisy data	239
J. Automated operation of the FUG power supply	243
Back Matter	250
List of Publications	251
Bibliography	259
Experimental data used in this work	259
Acknowledgment	279

Preface

Functionalized surfaces and interfaces of solids constitute a major field in materials science. Their specific behavior is of crucial interest for the deployment of a material in areas related to optics or chemistry, as they are, due to their exposed location, especially important for the interaction with the environment. A solid understanding of physical processes at surfaces is essential for modern applications. Surface properties of materials, in particular of crystals, commonly show large deviations from the bulk at the atomic scale, which is a consequence of the associated discontinuity. Most prominently, the existence of electronic surface states or structural reconstructions are induced hereby. Moreover, the presence of intentionally deposited foreign atoms can lead to complex reorganization processes with various physical implications. New effects emerge in substrate-adsorbate systems: The interaction with the substrate can lead to a complex self-organized arrangement of the adsorbate, and adsorbate-induced morphological changes of the substrate are known. Effects observed with semiconductor substrates are of specific interest, as surface modifications can lead to considerable effects on the electronic configuration here and, hence, of macroscopic electrical parameters.

This work is dedicated to a study of the Rb-covered surface of the layered semiconductor tungsten diselenide (WSe_2) using photoemission spectroscopy (PES) and photoemission electron microscopy (PEEM). The objective is to gain a deeper insight into aspects of charge transport near the modified surface and the self-organized creation of structures by measurements of the electronic structure. Electron spectroscopic techniques such as PES and PEEM are especially well-suited for this task. Because of their capabilities to probe the binding energy and the dispersion of electronic states along high-symmetry directions in the surface and the bulk of crystalline specimen, they are well-established tools for numerous applications in surface science. Photoemission data potentially allow for the quantification of the chemical composition of a sample and give a microscopic insight into electronic properties that constitute a broad spectrum of macroscopic material parameters. In case of a semiconductor, PES can be used to provide information on electric potentials, i.e., barrier heights or band bending effects, especially in the vicinity of interfaces. These effects can be quantified by the associated energetic shift of photoelectron spectra.

The basically two-dimensional structure of layered crystals from the class of transition metal dichalcogenides, such as WSe_2 , results in extremely low perturbations near the surface, so it is usually considered representative for the bulk. A low defect density is found at cleaved surfaces of WSe_2 . Defects at surfaces and adatoms introduce additional, localized electronic states to the system. The transfer of electric charge between those

states and the bulk induces a surface potential, which can be tuned in magnitude by the adsorbate concentration [1]. Adsorbed alkali metals and in particular rubidium are known to donate electrons to the WSe_2 substrate. Large induced surface potentials, nearly spanning the complete bandgap, have been observed for p-type WSe_2 , so the bulk doping is virtually turned into n-type at the surface in this case.

The effect of absorbed light on the surface potential, the so-called surface photovoltage (SPV) effect, has been explored since the 1980s. Demuth et al. [2] demonstrated a photovoltage of ≈ 0.5 V for the cleaved $Si(111)$ surface at a temperature of 20 K, which was revealed in a photoelectron spectrum using UV light with a photon energy of 21.22 eV. Some years later, similar observations were made with the clean [3] surfaces of $III-V$ compound semiconductors as well as with Schottky contacts at metal covered specimen [4]. Especially Alonso et al. [5] examined the silver-covered (110)-surface of gallium phosphide and found a surface photovoltage of ≈ 1 V. Measurements of the photovoltage as a function of photon flux were carried out by Aldao [4], for instance. Some attempts of a theoretical explanation of the processes at the surface were based on a transfer of the concepts of charge transport in a Schottky contact [6]. This interpretation could partially explain the observations, but neglected the effect of charge carrier recombination. Those were treated by alternative approaches [7], but showed up to be valid only for small photon flux. Noticeable work on experiments and theory of the SPV effect has been performed by Trares-Wrobel [8] and Adelung [9]. A theoretical model that holds for arbitrary light intensity was developed. Good agreement with experimental data originating from the (110)-surface of gallium arsenide was found for the results of a related numerical simulation. The possibility to determine the density and energy level of the surface state by comparative simulations was demonstrated [10].

In this work, a comprehensive discussion of the adaptation of this model to the actual configuration of the $WSe_2:Rb$ system will be given. It will be shown that, besides the mentioned parameters, much more information on the surface can be gained from measurements of the SPV effect. The long-term objective of this project is to carry out spatially resolved measurements of the SPV effect using a photoelectron spectrometer in order to obtain local information from the vicinity of defects and interfaces. Here, the feasibility of this approach, particularly of the theoretical model, is demonstrated by a combined experimental and theoretical study of the $WSe_2:Rb$ system.

Lateral accumulations of the adsorbate are common structural features observed at surfaces. Even when deposited homogeneously, adsorbates tend to form self-organized entities such as islands. Various growth modes are known in the literature for arbitrary adsorbate-substrate systems. Although Rb on WSe_2 is generally expected to have a high room temperature-mobility, the spontaneous formation of structures cannot be excluded a priori. A dedicated PEEM study of the $WSe_2:Rb$ system with the intention to characterize structure formation processes will be presented here. Earlier work applying spatially resolved spectroscopies to this system has not been reported yet.

Complex self-organized morphological modifications of the substrate have been reported for the $WSe_2:Rb$ system. Adelung [11],[12] revealed the creation of nanostruc-

ture networks upon Rb deposition in a scanning tunneling microscopy (STM) study. The microscopic processes that constitute such structures have been discussed extensively, and a definite explanation has not been given yet. Some evidence was revealed that the network is established by cracks which might be filled up with the adsorbate at higher concentration. In this work, the spatial resolution provided by the PEEM technique is applied for dedicated measurements of the electronic structure of the networks. Using a synchrotron light source, spatially resolved XPS data can be acquired, which allows for a characterization of the chemical composition of the networks. The hypothetical stress-induced network growth mechanism is expected to have accentuated implications on the observed features. In this context, large-scale surveys of the network are analyzed statistically. A theoretical approach to interpreting the experimental data will be discussed.

This work is segmented as follows: Part I covers measurements and numerical simulations of the SPV effect. An overview of the research with the WSe_2 substrate and a compilation of crucial properties that are relevant in the scope of this work is given. The fundamentals of SPV measurements in photoemission spectroscopy are introduced in detail. These include an introduction to the theoretical model based on earlier developments [8]. Since the existence of an inversion layer at the surface of the $WSe_2:Rb$ model system requires a strongly modified version, a detailed discussion of the adaptation of the model for high adsorbate concentration and large band bending follows. The photoelectron spectrometer operated in the workgroup in Kiel was used for the experiments. An introduction to the experimental station is given with a focus on new features that have been developed during this work. The design of the essential part, a beam guide supplying in-situ illumination of a sample in the vacuum chamber is documented in a dedicated chapter. A comprehensive analysis of the measured SPV effect is given with respect to the results of numerical simulations under variable photon flux and adsorbate concentration.

In part II, the experiments concerning self-organized growth of surface structures upon Rb deposition are presented. The discussed data were acquired during several beam-times at the experimental end station of beamline UE49/PGMa at the synchrotron radiation facility BESSY II, Berlin. The setup including a photoemission electron microscope (PEEM) deployed there is introduced in detail. Extensive interpretations of the presented experimental data obtained for the $WSe_2:Rb$ system are given. Methodical approaches developed for the treatment of PEEM data are introduced and discussed.

Widespread networks of nanostructures as already reported from earlier experiments [11] can also be imaged in a PEEM experiment. Part III is dedicated to an analysis of large-scale statistical features of the network. A set of methods that are designed for this task is introduced. An attempt is made to support the interpretation of the structures as tension-induced cracks by means of a simple theoretical model. Both surface cracks and the suspected subsequent accumulation of adsorbates is expected to have a large impact on the local SPV effect, so a basic understanding of these features is highly desirable for the interpretation of upcoming SPV measurements.

Part I.

Surface photovoltage effect

1. Introduction

Since the invention of the transistor in the 1940s [13], the application of semiconductors has led to a revolution in electrical engineering. Nowadays, semiconductor components are essential parts of electronic devices. In parallel to this remarkable evolution, the physical understanding of microscopic processes in this class of materials has been developed, so semiconductor parts can be designed from scratch today. A major part of the fundamental research was addressed to the dynamics of charge transport, based on the theory of the electronic band structure. Much attention was paid to interfaces in semiconducting heterostructures, as it showed up that many technically relevant effects are induced by charge carriers crossing these interfaces. An important field of applications is optoelectronics, which exploits specific effects of light interacting with semiconductors. Optoelectronic devices are used for the generation of electrical power (solar cells), emission of light (LEDs, semiconductor lasers), or light detection (photodiodes, CCD chips). As electromagnetic radiation usually has a finite penetration depth in matter, the surface of semiconducting substrates plays an important role in this field.

Semiconductor surfaces often show a deviation from the electrical properties with respect to the bulk, which is basically caused by the discontinuity of the crystal structure. A special treatment of the surface is required here, explicitly taking the related inhomogeneities into account. In this context, the surface can be regarded as a special case of an interface. A common feature observed in such systems is a significant deviation of the charge carrier densities from its bulk values as a result of the presence of additional electronic states. In this case, differences of the electric potential with respect to the bulk and an associated electric field are observed. Stationary illumination of the surface at considerable flux leads to a significant perturbation of this configuration as a consequence of the creation of electron-hole pairs by light absorption. In this case, a strong reduction of the surface potential can be observed, which is caused by a separation of mobile charges in the electric field. This effect is known as surface photovoltage (SPV) effect.

The intention of this work is to give a quantitative analysis of this effect by means of measurements and a numerical model (chapter 3.2). The model has been formulated in earlier work [8] and was refined here. It is based on the well-known semiclassical equations for all relevant processes of charge carrier dynamics, i.e., the generation and recombination of electron-hole-pairs, and transport by drift and diffusion.

Measurements of the SPV effect were carried out using valence band photoelectron spectroscopy (PES). To this end, the experimental setup (chapter 4) was extended by an external light source (chapter 5) for controlled illumination of a specimen. Special

attention was paid to creating a small light spot on the surface with the intention to provide an option for spatially resolved studies by scanning a sample. Similar techniques for the inspection of functional semiconductor surfaces are well-known from the literature [14]. Common methods are the laser beam induced current (LBIC, [15],[16],[17]) and the electron beam induced current (EBIC,[18], [19], [20]) technique. Both methods use a scanning beam of light (LBIC) or electrons (EBIC) in order to provide spatially resolved information of charge carrier dynamics. The approach pursued here is explicitly meant to involve the PES setup and thus to allow for combined measurements of the electronic structure and charge carrier dynamics. Equivalent approaches have not been reported in the literature.

The numerical model is to be validated by a comparative study involving experimental data acquired in this work. For the simulations of the SPV effect, precise knowledge of crucial material parameters is required. Tuning the simulation results with the intention to reproduce the experimental data is therefore expected to provide a quantification of these parameters, which would not be accessible by exclusive application of PES.

Tungsten diselenide (WSe_2) was chosen as model system for this work (chapter 2). Caused by its special crystal structure, no surface potential is observed here. Instead, it can be tuned continuously by the controlled adsorption of Rb. This option makes WSe_2 especially interesting, as it allows for validation of the model for a broad range of configurations. Besides this, WSe_2 is a promising candidate for many proposed applications, which highly encourages fundamental research with this material.

The SPV effect is well known as a side effect in spectroscopies. Combined measurements of the occupied (valence band) and the unoccupied (conduction band) band structure (CARPIP, [21]) are biased by stationary modifications of the surface potential [22], so measurements of the band gap can include a systematic offset. As the surface potential is a function of incident light intensity, PES applied to a semiconductor surface using high-brilliance excitation sources potentially results in blurred spectra caused by inhomogeneous illumination due to the finite spot size.

While the SPV effect occurred as a perturbation during these experiments, it is generated intentionally here. It will be shown that a systematic study backed with a solid theoretical model can be exploited to gain crucial parameters of the charge transport near semiconductor surfaces with a considerable surface potential. Earlier simulations [8] predicted an unexpected, non-linear surface photovoltage effect with extreme sensitivity to the photon flux at a distinct excitation level. An improved model of this effect, and surface photovoltage in general, offers a variety of potential applications in the field of sensor design, for instance.

This part of the work is organized as follows: Some fundamental properties of tungsten diselenide are summarized in chapter 2. Theoretical foundations used in this work are introduced briefly in chapter 3, before the numerical model is presented in detail. Based on the work of Nils Trares-Wrobel [8], wide modifications of the model will be discussed, which are attributed to the specific configuration prepared in this work.

In chapter 4, detailed documentation of the experimental station operated in the

workgroup is presented. Numerous new features have been implemented prior to the experiments and are discussed there. Additional technical reference is given in the appendix. Chapter 5 is focussed on the integration of a versatile additional light source into the PES setup. Besides constructional details, the results of simulations and calibration measurements are shown there.

A comprehensive study including all results derived in this part were summarized in a publication (in preparation). It is reproduced as chapter 6 in its current state here.

2. Tungsten Diselenide (WSe_2)

Tungsten Diselenide (WSe_2) belongs to the class of transition metal dichalcogenides (TMDC). TMDCs are composed of at least one atomic species out of Ti , Zr , Hf , V , Nb , Ta , Mo , W and (at least) one out of S , Se , Te . In general, the stoichiometry of such compounds is TX_2 , where T is the transition metal and X is the chalcogen. All TMDCs condensate in a layered, basically two-dimensional structure that is constituted by a central layer of transition metal atoms surrounded at the top and bottom by a layer of chalcogens. Chemical bonds are all saturated within one triple-layer. The bulk crystal is made up by stacking these layers, where different polytypes with different stacking order and periodicity are known. Because of the in-plane saturation of all valence electrons in a layer, the layers are coupled just by relatively small van der Waals-forces. Thus, TMDC surfaces parallel to the planes can easily be prepared by cleaving. The resulting surfaces are found to be highly chemical inert.

Much attention was paid to this class of crystals in the past decades. The paper by Wilson and Yoffe [23] gives an overview. Among the TMDCs, metals, half-metals, semiconductors and insulators can be found. Some TMDC are subject to recent work on strongly correlated electrons in a low-dimensional system and especially superconductivity [24],[25].

The crystal structure usually induces extreme anisotropy of physical properties such as electron mobility [26] or heat conductivity [27],[28], so they were used as model systems for experimental studies of low-dimensional systems in many cases. Surfaces that are basically inert are interesting to electrochemical applications, where elaborate passivation techniques would be required otherwise [29],[30]. Highly hydrophobic surfaces could be created by deposition of the precursors of WSe_2 on a glass substrate [31]. Charge density waves with a complex phase transition behavior could be observed (see [32] and references therein) and, for some cases, even structural transformations of the crystal structure are well known [33],[34]. This large variety of physical properties makes the members of this crystal class interesting for basic research and much-proposed candidates for special applications.

Besides the mentioned topics, particularly WSe_2 was considered for various applications in a wide range of fields. An overview of the literature is given here. Numerous references concerning material parameters that are relevant for the simulations of the SPV effect were accumulated. A compilation of parameter values originating from literature is shown in the table in figure 2.3 at the end of this chapter. The actual crystal structure of $2H - WSe_2$ is shown in figure 2.1. As for all TMDCs, the unit cell shows

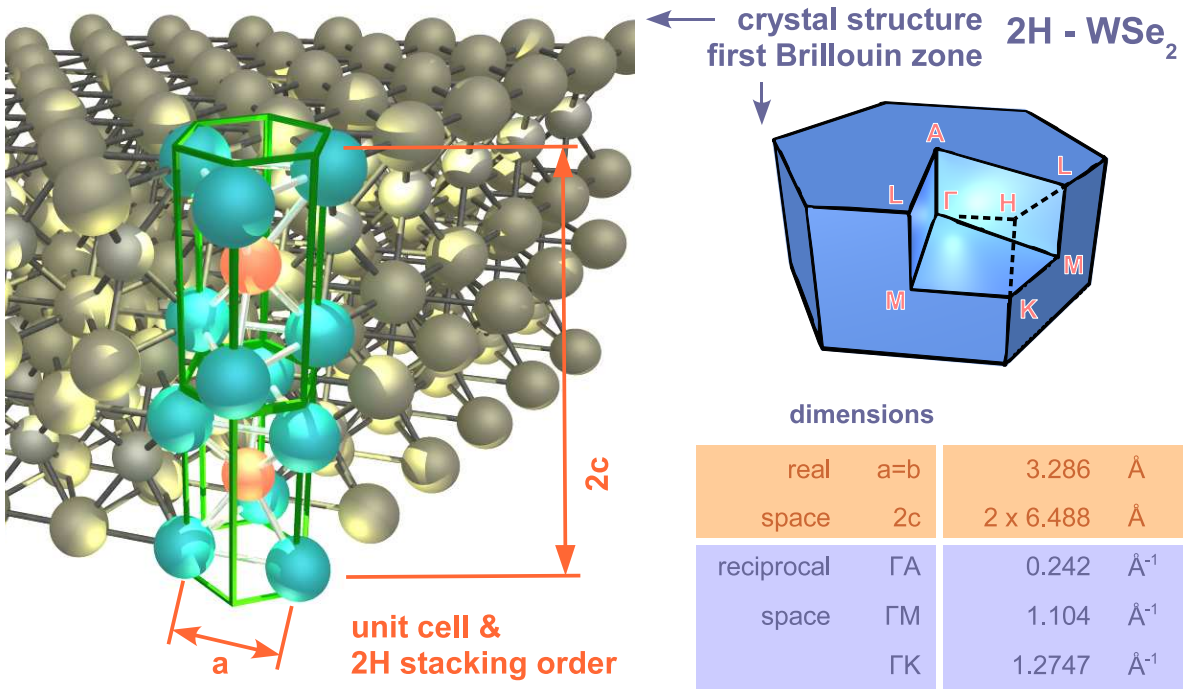


Figure 2.1.: **Left** : Crystal structure of $2H - WSe_2$. The stacking order in c -direction of this polytype has a periodicity of 2. The covalent bonds inside a crystal layer are depicted by bars. The hexagonal units cell and included atoms are highlighted. **Upper left** : First Brillouin zone of WSe_2 . Points of high symmetry are indicated and labeled with their common names as used in electron spectroscopy. **Lower left** : Compilation of relevant parameters of the units cell of WSe_2 as stated in [35].

hexagonal symmetry in the ab -plane. Especially the $2H$ polytype consists of two trigonal prismatic unit cells, rotated against each other by 180° and stacked up along the crystallographic c -direction. This is known to be most common structure for WSe_2 , but different unit cell configurations and stacking orders are known for TMDCs in general.

The transformation of the unit cell into reciprocal space (or k -space) gives the first Brillouin zone, which is also shown in figure 2.1. It is usually used to depict the electron dispersion relation $E(\vec{k})$, which has the same symmetry as the Brillouin zone. Typical points of high symmetry and their common notation for this crystal structure are shown in the figure.

Features of the electronic band structure of tungsten diselenide that are relevant in the scope of this work are summarized here. Comprehensive reference data can be found in [36] and [37]. WSe_2 has an indirect band gap of 1.2 eV . While the valence band maximum is found at the Γ -point, the conduction band minimum is located at

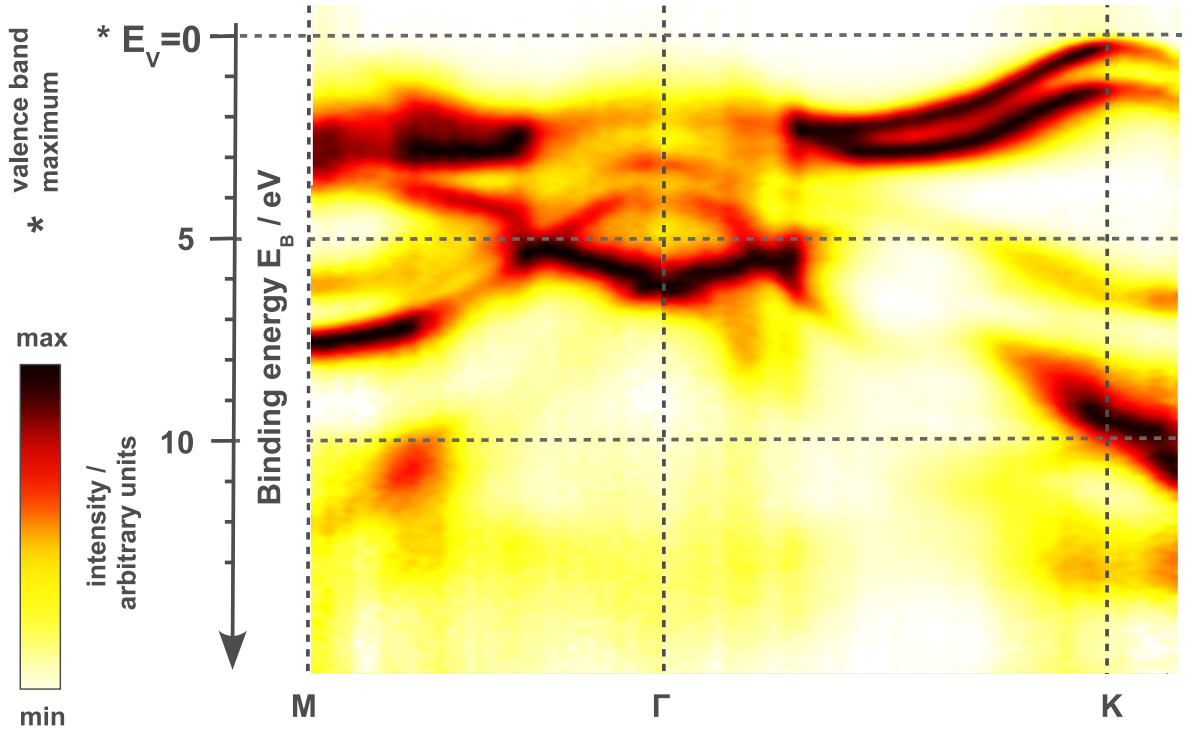


Figure 2.2.: Occupied band structure of WSe_2 along high symmetric directions of the first Brillouin zone. Dark areas depict high density of states, from which the energy bands can be identified. The dispersion $E(\vec{k})$ of the band structure near the valence band maximum E_V is shown here. The data was acquired with angular resolved photoelectron spectroscopy (*ARPES*, introduced in chapter 3.1) using the PHOIBOS experimental setup and a photon energy of $h\nu = 21.22$ eV (Details are presented in chapter 4).

$\approx 0.55 \cdot \overline{\Gamma K}$ (see data in figure 2.2). Along the direction $\overline{\Gamma A}$, almost no dispersion of the energy bands is found. This is typical for transition metal dichalcogenides and manifests the reduced dimensionality in the electronic structure. From the dispersion relation at the valence band maximum and the conduction band minimum, the effective mass of holes and electrons can be derived. For a precise discussion of this relationship, see chapter 3.2.1. The observed anisotropy of the dispersion relation leads thus to the expectation of strong anisotropy of the material constants for charge transport, i.e., the mobilities of electrons and holes.

In the following, an overview of the literature on WSe_2 is given without claiming the completeness of the covered subjects. Many of the references cited here are directly relevant for the numerical model of the surface photovoltage effect, which will be introduced in chapter 3.2.

WSe_2 is usually grown using the chemical vapor transport (CVT) technique [40]. The

precursors, elemental Tungsten and Selenium, and a transport gas at low partial pressure are therefore encapsulated in an evacuated ampoule. The two ends of the ampoule are kept at high, but slightly different temperature in a furnace for some days up to some weeks. Typical parameters are temperatures of $930\text{ }^{\circ}\text{C}$ and $850\text{ }^{\circ}\text{C}$ for a period of 25 days. At the hotter end, where the precursors are located, the transport gas will react with the precursor to give a volatile derivative that is decomposed after diffusing towards the cold end, where the compound crystal grows. The iodine acts as a catalyst here. Some of the transport agent will always be embedded, resulting in a doped crystal. Especially for semiconductors, the presence of foreign atoms cannot be ignored, as a considerable shift of the Fermi level with respect to band edges results even for a small concentration. Different halogens were applied as transport agents by several groups. As reported in the literature, the application of iodine results a p-doped crystal [36],[41]. Alternatively, Rhenium or Bromine can be used to achieve n-doping [26],[42].

The mobility μ of charge carriers is a fundamental material constant for electronic applications. Hence, several studies have been carried out in the past to determine this parameter for electrons and holes in WSe_2 with various dopant concentrations. Remarkable results have been reported by Podzorov [43] for the mobility inside the crystallographic ab -plane, finding values up to $\mu_h = 500\text{ cm}^2/\text{Vs}$ for holes. An extremely high anisotropy of this value is stated by [26], giving ratios in the range $40 \leq \mu_{e,\parallel}/\mu_{e,\perp} \leq 1205$ for the mobilities parallel ($\mu_{e,\parallel}$) to the ab -plane and perpendicular ($\mu_{e,\perp}$). The large interval holds for a variety of different doping-induced carrier concentrations between $7.3 \cdot 10^{15}\text{ cm}^{-3}$ and $1.02 \cdot 10^{17}\text{ cm}^{-3}$, where increasing dopant concentration results in a smaller anisotropy.

The relative dielectric constant \mathcal{E} of a material affects the formation of space charge layers near potential gradients. In addition, carrier drift transport is characterized by its value. Thus, it is a parameter to the numerical model discussed in chapter 3.2. Davey and Evans [42] report an in-plane(ab) value of $\mathcal{E} = 16$, derived from optical measurements. To our knowledge, publications on direct measurements for the c -direction do not exist. Common WSe_2 crystals grow as thin platelets with their ab -plane oriented parallel to the macroscopic faces. For only a few cases, the thickness of the crystals exceeds $100\text{ }\mu\text{m}$, a typical value is about $30\text{ }\mu\text{m}$. For such thin specimen, the dielectric constant cannot be determined in this direction with common techniques. The strongly anisotropic crystal structure leads to the expectation of anisotropic dielectricity, so it can be expected that the value in the c -direction differs from that in the ab -plane.

Frindt [39],[44] published data on the optical absorption of WSe_2 in the $UV - VIS$ range, revealing onset of optical absorption at a photon energy of 1.45 eV , a value slightly larger than the indirect bandgap. An absolute absorption coefficient of $3.9 \cdot 10^7\text{ m}^{-1}$ is reported for a wavelength of the green laser pointer (532 nm) that is used for the experiments in Part I. His data is used as reference throughout this work.

The thermal conductivity of WSe_2 has been subject for studies [27],[28]. It turned out that the thermal conductivity in the crystal c -direction shows a large anomaly and is even much smaller than thermal conductivity of most solid disordered systems, which

2. Tungsten Diselenide (WSe_2)

is not expected at all for a crystal.

Many TMDCs show complex phase transitions and structural transformations, but few experiments were reported for WSe_2 . To mention one WSe_2 -related work in this field, high-pressure studies were carried out by Vaidya et al. [34] while monitoring the electrical resistivity, but effects indicating a phase transformation were revealed.

The transition metals and the chalcogens all show similar chemical behavior, so that the same similarity among their compounds, the TMDCs, can be expected. This subject was explored by growing crystals with mixtures of either the metal ($W_xMo_{1-x}Se_2$, [45]) or the chalcogen (WSe_xS_{2-x} , [46]). It turned out that all observed physical properties in the study varied continuously as a function of x , indicating that no substantial changes in the electronic structure occur at the transition $MoSe_2 \rightarrow WSe_2 \rightarrow WS_2$, which is especially interesting for bandgap engineering.

Motivated by the special properties of WSe_2 , several applications of this material have been proposed in the past.

The low coupling between the layers of TMDCs eases lateral shearing and provides low adhesion, so the whole class has been considered as solid state lubricant for specialized applications. Such lubricants might prove their superiority under extreme conditions, i.e., at high temperature or in high-mechanical-load applications. The chemical inertia of TMDC surfaces makes them well-suited in a chemically reactive environment. WS_2 , which is closely related to WSe_2 , has been considered as a substitute for common lubricants [47],[48]. In a recent work, Yang et al. [49] studied the properties of conventional HV1500 oil with additive WSe_2 nanorods and found considerable improvement of the overall performance.

Despite their crystal structure, thin layers of tungsten diselenide are remarkably flexible. Combined with the excellent electronic properties of WSe_2 single crystals and its capability to be tuned by dopants, it has often been proposed as substrate for flexible electronics. Podzorov et al. [43] reported the properties of a WSe_2 -based *FET* device and found excellent in-plane carrier mobilities.

In another interesting field, tungsten diselenide is used as electrode material for photoelectrochemical solar cells (*PEC*) [50],[51]. *PEC* consist of a semiconducting photoanode and a metal cathode, immersed in an electrolyte. When irradiated with electromagnetic radiation, namely visible light, water is split up into gaseous hydrogen and oxygen by electrolysis. Prasad [52] reported a conversion efficiency of 17.1% for this material, which was the highest value ever achieved when published in 1988.

A brief, subjective overview of some interesting topics in research with WSe_2 was given in this chapter. Numerous properties of WSe_2 have been studied, explicitly aiming at technical applications. A large variety of physical effects was observed with WSe_2 , as with TMDCs in general, so it is still subject to fundamental research. From a large number of publications in this field, reference data of crucial material parameters is obtained, which is used as starting point for further investigations in this work. Though well-understood in essential properties, many amazing effects observed with this complex material are still to be studied.

Quantity	Symbol	Value	Unit	Ref.	Note
Band gap	E_G	1.2	eV	[36]	¹
Effective density of states in valence band	N_V	10^{19}	cm^{-3}	[10]	
Effective density of states in conduction band	N_C	10^{19}	cm^{-3}	[10]	
Acceptor energy level	E_A	0.03	eV	[10]	
Hole mobility	$\mu_{h,\parallel}$	236	$\text{cm}^2 (\text{V s})^{-1}$	[38]	²
Electron mobility	$\mu_{e,\parallel}$	105	$\text{cm}^2 (\text{V s})^{-1}$	[38]	²
Anisotropy of carrier mobility	$\mu_{\parallel}/\mu_{\perp}$	40 ... 1205		[26]	³
Relative dielectric constant	ϵ_s	16		[38]	²
Optical absorption coefficient	α	$3.9 \cdot 10^7$	m^{-1}	[39]	⁴

¹Indirect band gap

²In crystallographic *ab*-plane

³Depending on doping concentration

⁴Found for $\lambda = 532 \text{ nm}$

Figure 2.3.: Compilation of relevant reference data found for tungsten diselenide (WSe_2) in the literature. The stated values originate from the mentioned references.

3. Theoretical Aspects

The experimental techniques applied in this work, i.e., photoelectron spectroscopy (PES) and photoemission electron spectroscopy (PEEM), are based on the photoelectric effect. During the past decades, a strong theoretical background of this effect was developed, and sophisticated quantum mechanical approaches are known in the literature today. These theoretical models have been reproduced in many theses with more or less detail ([53], [35], [8], [54],[55], and [12], to mention just a few), and various textbooks are dedicated to this subject, such as [56]. Theoretical considerations of the photoemission process will be outlined briefly in section 3.1. Some technical issues as exploited in modern electron spectroscopies will be discussed. Chapter 4 is dedicated to developments of instrumentation in this field.

The major part of this chapter covers a theoretical model of the surface photovoltage (SPV) effect, which is observed at semiconductor surfaces. First, a summary of the pioneering work of Trares-Wrobel [8] is given. Based on his derivations, the necessity of crucial modifications of the model for the system examined in this work, $WSe-2 : Rb$, is discussed. In contrast to earlier work, rather large surface potentials were prepared here, and a large magnitude of the SPV effect was observed. The extreme configuration of the associated space charge layer near the surface requires the novel approach presented here: While the exclusive treatment of charge carriers of only one type was justified well in the earlier model, both types, i.e. electrons and holes, must be accounted for in this work. A detailed discussion of the modifications is given in section 3.2. The results derived there were used for a numerical simulation of the SPV effect. Technical considerations of the implementation are given in appendix B. As will be shown in chapter 6, the model is in good agreement with experimental data. As an extension of a PES setup, combined experimental and theoretical studies of the SPV effect allow for the estimation of a variety of material parameters of semiconductor surfaces.

3.1. Theory of Photoemission

3.1.1. The Photoelectrical Effect

When a crystal surface is irradiated with ultraviolet light, bound electrons are enabled to leave the crystal with characteristic kinetic energy E_{kin} which is found to scale with the photon energy $h\nu$ of the incident light, but not with intensity. This observation was first made by Hertz and Hallwachs in 1887 [57] and is known as photoelectric effect

today. In his work that was awarded the Nobel prize in 1921, Einstein [58] explained this phenomenon with the assumption that the energy of an absorbed photon gets entirely transferred to one electron. Given the binding energy of an electron and obeying conservation of energy, the kinetic energy of the free photo-electron can be found. The transition in figure 3.1 gives the following equation:

$$E_{kin} = h\nu - E_B - \Phi. \quad (3.1)$$

Here, the work function Φ of the crystal is introduced. The binding energy E_B of a photoelectron in its initial state, i.e., prior to photoemission, can be determined by measuring the kinetic energy E_{kin} and claiming energy conservation, which results the above equation. Here, the binding energy E_B of an electron is given in relation to the Fermi level E_F .

At given photon energy, photoelectrons with a distinct distribution of kinetic energy will be emitted from the crystal surface. This distribution is mainly governed by the energy distribution of bound electrons in the crystal. Therefore, the energetic structure of the electrons in a solid can be probed by analyzing the distribution of photoelectrons. Experimental techniques exploiting the photoelectric effect are summarized under the term 'photoelectron spectroscopy' (*PES*) today. Over the past decades, this approach has found a vast range of applications.

3.1.2. Photoelectron Spectroscopy (PES)

The quantum mechanical wave function of an electron bound in a crystal is described by Bloch functions, introducing the crystal periodicity to the electron density of states. An electron occupying a state in the crystal can be assigned a momentum eigenvector \vec{k} . The energy dispersion $E(\vec{k})$ is found to be periodic with the crystallographic primitive unit cell transformed into inverse space, or k -space. The k -space equivalent of the crystal unit cell is called Brillouin zone.

The photo-induced emission of an electron can be modeled as a three-step process:

- Absorption of a photon
- Transport of the photoelectron to the surface
- Escape of the electron into vacuum

The first step is usually modeled by a perturbation of the stationary system. For the most simple case, the dipole approximation holds for the transition Hamiltonian [59]. When a quantitative analysis of photoelectron yield is demanded, the photon-energy dependent absorption cross sections have to be considered. For pure elements, this data is tabulated [60] and can also be applied to compound materials in many cases. For a complete description of the derivations done here, refer to the excellent book of Hüfner [56].

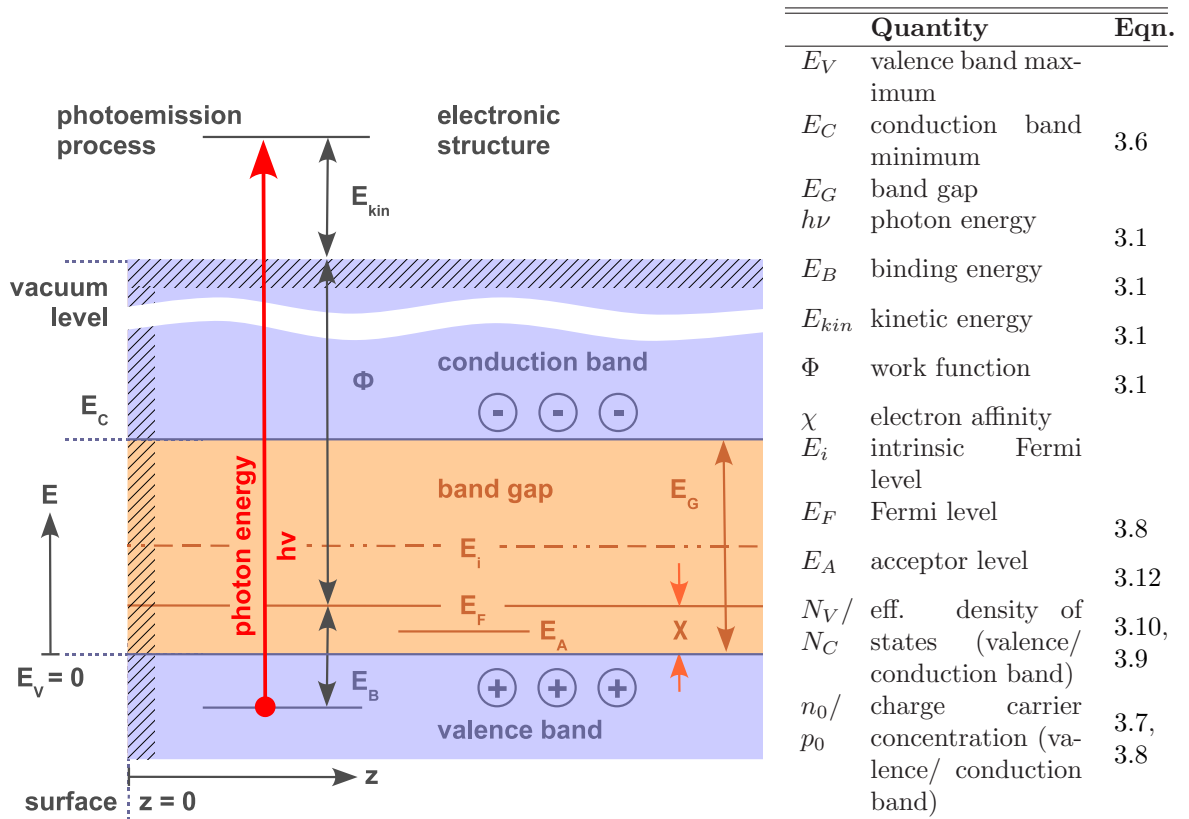


Figure 3.1.: Qualitative energy diagram for the photoemission process. The absorption of a photon with energy $h\nu$ leads to the emission of an electron with distinct kinetic energy (transition marked with red arrow). The shown configuration depicts a semiconductor. The center region is the band gap with a negligible density of electronic states. Commonly used quantities are depicted.

The radiation used to create photoelectrons penetrates the crystal into a mean depth before it is absorbed. In average, a photoelectron has to be transported this distance towards the surface before it is emitted. During transport, it suffers inelastic scattering with a mean free path defined by its kinetic energy. For the relevant photon energy and kinetic energy range, the mean free path for the scattering process shows up to rigidly limit the distance from the surface of which unscattered electrons can be found in emission. In general, this makes photoemission techniques extremely sensitive to the surfaces of solids. A general relationship has been found experimentally for the mean free path of excited electrons and was tabulated for a wide energy range [61]. Its global minimum is found near $E_{kin} = 30 eV$. The mean escape depth of an electron amounts to just a few Angstroms (\AA) here.

Taking the angular distribution of photoelectrons into account, information on the momentum distribution of electronic states in the Brillouin zone can be gained. Therefore,

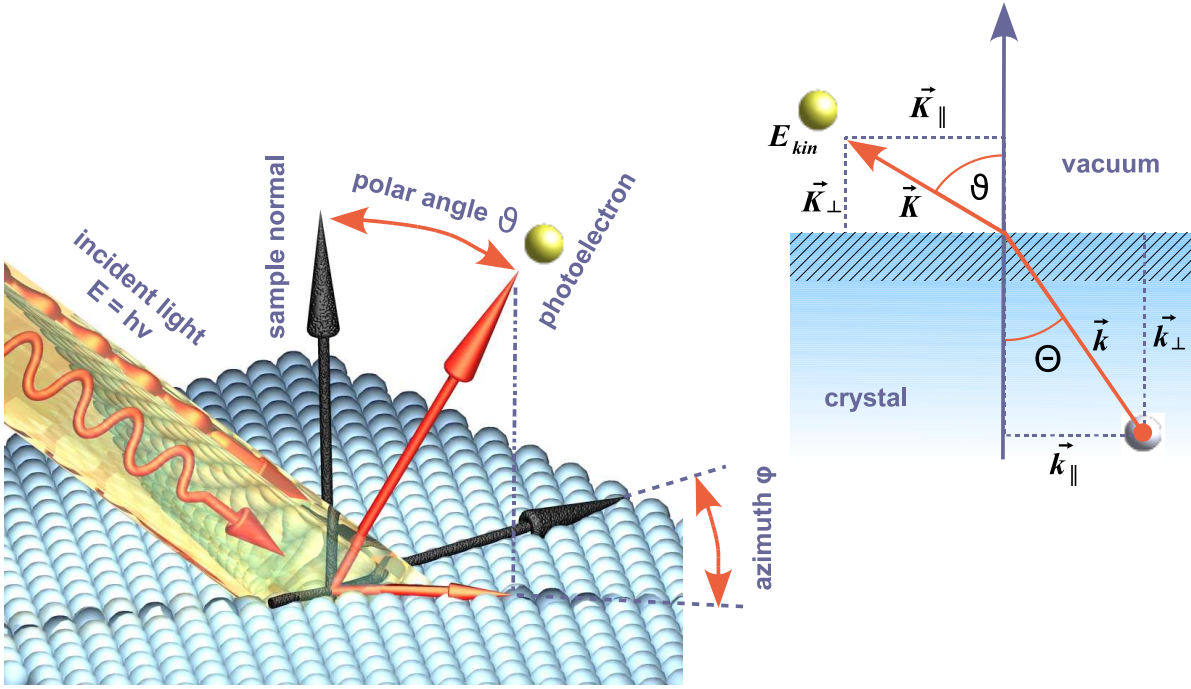


Figure 3.2.: Common quantities in angular resolved photoemission spectroscopy (ARPES) as used in the text. The components of the momentum vector of the initial state can be reconstructed when the emission angles (ϑ, φ) of a photoelectron with respect to the normal of the sample surface and its kinetic energy E_{kin} are known. These quantities can be measured using a photoelectron spectrometer as introduced in chapter 4.1

the photoemission process has to be modeled with regard to momentum conservation. Let \vec{k}_i and \vec{k}_f be the momentum of the initial and final state of the electron, i.e. of the bound electron and the free photoelectron, respectively. Then, $\vec{k}_f = \vec{k}_i + \vec{G}$ must hold for the photoemission process. Here, the introduction of a reciprocal lattice vector \vec{G} is a consequence from the periodicity stated above. The momentum of the absorbed photon can be neglected for the following discussion.

To derive the relation between angular distribution of the photoelectrons and crystal momentum in the initial state, a separation of momentum vector parallel \vec{k}_{\parallel} and a scalar component perpendicular k_{\perp} to the crystal surface is necessary.

Consider a photoelectron with kinetic energy E_{kin} that is emitted at a polar angle ϑ and an azimuthal angle φ from the sample (figure 3.2). Then, the momentum can be

written as

$$K_{\perp} = \sqrt{\frac{2m_e}{\hbar^2} E_{kin}} \cdot \cos \vartheta \quad (3.2)$$

$$\vec{K}_{\parallel} = \vec{k}_{\parallel} = \sqrt{\frac{2m_e}{\hbar^2} E_{kin}} \cdot \sin \vartheta \begin{pmatrix} \cos \varphi \\ \sin \varphi \end{pmatrix} \quad (3.3)$$

When the electron escapes into vacuum, the momentum parallel to the surface is conserved: $\vec{K}_{\parallel} = \vec{k}_{\parallel}$. For the determination of the perpendicular component of the crystal momentum, a constant offset V_0 has to be introduced, which is a phenomenological parameter and must hence be estimated. Therefore, the normal components reads:

$$k_{\perp} = \sqrt{\frac{2m_e}{\hbar^2} (E_{kin} \cos^2 \vartheta + V_0)}. \quad (3.4)$$

Using these relations, the origin of a photoelectron in momentum space can be determined completely. Measurements of the photoelectron yield $I(h\nu, E_{kin}, \vartheta, \varphi)$ with incident light of a given photon energy and well-defined flux results a measure for the density of electronic states in the crystal. Therefore, angular resolved photoemission spectroscopy allows for a complete determination of the dispersion $E(\vec{k})$ of bands in the electronic structure of a specimen.

3.2. Theory of the surface photovoltage effect

This section covers the theoretical model of the surface photovoltage effect. It is based on well-known, general equations for the treatment of semiconductors. The theoretical background summarized here has been implemented as numerical simulation code [8], which was reviewed and modified to reflect the actual system treated in this work. Some annotations concerning the implementation of the code can be found in appendix B. The model is derived from generally accepted equations of semiconductor physics, so it should be referred to standard textbooks for derivations. Some specialized formula have been developed in ref. [8], so detailed information can be found there.

Experiments with WSe_2 will be discussed throughout this work, which has a known p-type doping as a result of the growth conditions (see chapter 2 and references given there). The cleaved surface of WSe_2 shows no significant concentration of electronic states, so its density can be tuned by intentional adsorption of alkali metals, for instance. The Rb adsorbed during the experiments had shown donor-like behavior. The theoretical model will be introduced in the context of this configuration, but could easily be modified to work with arbitrary n-type semiconductors and arbitrary surface states.

The model can be divided into two major parts: The first one to be introduced (section 3.2.3) deals with semiconductor thermodynamics and will give the equations that are required to find bulk and surface charge concentrations. All derivations given here are

based on generally accepted semi-classical semiconductor physics, as found in [62],[63], for instance. Based on this, an implicit solution for the resulting surface potential ('band bending') is derived from Poisson's equation. Similar models can be found in [64]. The model is extended to stationary non-equilibrium then. These efforts result in a generalized description of space charge, the so-called space charge function.

In the second part (section 3.2.5 and the following), dynamics of charge carriers at given non-equilibrium found before will be discussed. The loss of mobile charge carriers by recombination and transport has to be compensated by the generation of electron-hole pairs, i.e. absorption of light, as was realized in the experiments discussed in chapter 6. While the space charge function is used to find the band bending at given non-equilibrium conditions, the solution of the transport equation is required to find the photon absorption rate that is required to upkeep the given stationary state. Finally, the equations have to be adapted to the actual conditions found at the $WSe_2 : Rb$ surface, which will be presented in section 3.2.7.

3.2.1. Semiconductor basics

The existence of an energy interval with zero (or negligible small) density of electronic states around the Fermi level, the so-called band gap, is crucial for a semiconductor. Electrons with a ground state in the highest occupied energy band, the valence band, can be transferred into the lowest unoccupied energy band, the conduction band, by thermal excitation, for instance, leaving behind a positively charged unoccupied state, referred to as hole. Here, speaking about an electron in a semiconductor implicitly states that it is in an excited state in the conduction band. In this excited state, the electron and hole can be considered independent quasi-particles, that are mobile with an individual mobility and opposite sign of electric charge. Figure 3.1 gives an overview of commonly used quantities in semiconductor physics.

In a semiconductor, transport of electric charge and particles is made up by electrons in the conduction band and holes in the valence band exclusively. Due to the fact that charge carriers tend to relax to minimum energy, electrons are basically concentrated at the global energy minimum of the conduction band E_C and holes are found at the valence band maximum E_V , which are usually referred to as band edges.

Both types of charge carriers can be assigned an effective mass m^* that is derived from the dispersion relation $E(\vec{k})$ at the edges of the associated energy band:

$$m^* = \hbar^2 \cdot \left[\frac{\partial^2 E}{\partial k^2} \right]^{-1}, \quad (3.5)$$

$$\text{assuming that } E = \frac{\hbar^2}{2m^*} |\vec{k}|^2.$$

Here, the approximation of a quasi-free particle is made, which implicates the parabolic dispersion relation. In an anisotropic crystal, the band dispersion will not only depend

on $|\vec{k}|$, but also on the orientation of the wave vector \vec{k} . For this case, the effective mass becomes a tensor with m_x^*, m_y^*, m_z^* on the main diagonal (in principal axis representation). When the approximate parabolic dispersion relation is used to compute the effective density of states in the energy bands, the elements of the effective mass tensor can be reduced to give a single, isotropic effective mass.

$$m^* = (m_x^* \cdot m_y^* \cdot m_z^*)^{\frac{1}{3}}$$

For the density of states in the conduction band of a semiconductor

$$D_C(E) = 2\pi M_C \left(\frac{2m^*}{h^2} \right) \cdot \sqrt{E - E_C} \quad (3.6)$$

can be found, when parabolic dispersion ($E \propto k^2$) is assumed. An analog expression can be derived for the valence band. The cumulative charge concentration in such a band is given by the product of density and occupancy obeying Fermi statistics. The resulting integral cannot be solved analytically and is performed numerically by the space charge simulation code [8]. The electron density n_0 and hole density p_0 as used in the following are:

$$n_0(z) = \frac{2}{\sqrt{\pi}} N_C F_{\frac{1}{2}} \left(\frac{E_F - E_C}{k_B T} \right) \quad (3.7)$$

$$p_0(z) = \frac{2}{\sqrt{\pi}} N_V F_{\frac{1}{2}} \left(\frac{E_V - E_F}{k_B T} \right) \quad (3.8)$$

with

$$N_C = 2 \left(\frac{2\pi m_e^* k_B T}{h^2} \right)^{\frac{3}{2}} M_C \quad (3.9)$$

$$N_V = 2 \left(\frac{2\pi m_h^* k_B T}{h^2} \right)^{\frac{3}{2}} M_V \quad (3.10)$$

N_C and N_V are called 'effective density of states' of the conduction band and the valence band, respectively. In general, electrons and holes have different effective masses m_e and m_h . $F_j(\eta)$ denotes the Fermi integral of order j

$$F_j(\eta) = \int_0^\infty \frac{x^j}{1 + \exp(x - \eta)} dx \quad (3.11)$$

No analytical expression of the Fermi integrals are known, but there exists a collection of analytical expansions for certain orders $j = -1/2, 1/2, 3/2$ and different ranges of the argument η ([65], [66]) in the literature.

The charge carrier concentration in a semiconductor can be influenced drastically by the existence of extrinsic states inside the band gap, usually energy levels of dopants. In this work, only acceptor states will be introduced to the model, as only p-doped crystals will be treated. Consider an unoccupied energy level E_A with bulk concentration N_A just a few meV above the valence band maximum. Because of the small energy difference to the valence band, electrons are very likely to be excited into this state, again leaving behind a hole. The electron is usually regarded as being 'trapped', i.e. not mobile in that state, but the hole created here fully contributes to the concentration of mobile charges. Thus, dopants introduce huge modifications of the charge concentration, even though their concentration is usually held clearly below 1 % in the crystal. For a non-degenerate energy level, the density of ionized acceptors can be found by

$$N_{A0}^- = \frac{N_A}{1 + \exp((E_A - E_F)/k_B T)} \quad (3.12)$$

An analog expression holds for the concentration of ionized donors.

The donor concentration N_D could be introduced to the equations in an identical manner in order to handle n-type doping. Summarizing the contribution from the energy bands and the acceptor level, the total charge in the bulk crystal amounts to

$$\rho_0 = -e_0 (n_0 - p_0 + N_{A0}^-) \quad (3.13)$$

The Fermi level is included implicitly in this equation. For a given semiconductor configuration, it can be computed by claiming charge neutrality for the bulk crystal ($\rho_0 = 0$) and solving the equation numerically.

3.2.2. Model of the surface state

The presence of additional electronic states near the surface can significantly influence the bulk equilibrium derived above. In general, such states could originate from dangling bonds that exist wherever the perfect symmetry of the crystal lattice is broken. As is well-known from the literature, for the special structure of transition metal dichalcogenides, these states do not exist at surfaces parallel to the ab -plane (see chapter 2). Another reason for the existence of surface states is the coverage of adsorbates, as intended in the experiments presented in this work. Here, Rb is adsorbed on the cleaved surface in a controlled manner such that a defined coverage with a homogeneous density N_T is achieved.

In analogy to foreign atoms in the bulk, surface atoms can either be acceptors or donors. Depending on the energy level E_T , an electron can be transferred to the surface from an occupied atomic state if $E_T > E_F$, or an unoccupied atomic state can absorb an electron from the conduction band if $E_T < E_F$. For Rb atoms, the first possibility is realized. Therefore, the adsorbed Rb atoms can either have a positive charge of $+e_0$ or be neutral. This surface charge density strongly biases the charge neutrality condition

in equation 3.13. For a quantitative analysis, the energetic structure of the surface state has to be defined. For simplicity, a Gaussian density of states with mean energy E_T and variance σ_T is assumed to model the density of states. N_T denotes the areal density of states. If at most one electron per atom is transferred and no degeneracy has to be considered, N_T equals the density of adsorbate atoms.

$$D_T(E) = \frac{N_T}{\sigma_T\sqrt{2\pi}} \exp\left(-\frac{(E - E_T)^2}{2\sigma_T^2}\right) \quad (3.14)$$

Again, Fermi statistics rules the occupancy of these states, so the surface charge density can be expressed as follows:

$$Q_{T0} = e_0 \int_{-\infty}^{\infty} D_T(E) \left(1 - \frac{1}{1 + \exp\left(\frac{E - E_F}{k_B T}\right)}\right) dE \quad (3.15)$$

All quantities introduced here can be depicted in an energy diagram of the semiconductor surface. The resulting configuration as a consequence from adsorbing donor-type adatoms is shown in figure 3.3.

3.2.3. The space charge layer

The presence of positively charged adatoms leads to the accumulation of conduction band electrons near the surface, so locally constrained non-zero charge density results. The total space charge Q_{SC} can be found from eqn. 3.13: $Q_{SC} = \int_0^{\infty} \rho_0(z) dz$.

To find the electric potential of this charge configuration, Poisson's equation has to be solved. For the bulk ($z \rightarrow \infty$), a constant potential can be assumed. Inserting the expression for Q_{SC} and implementing this boundary condition, the Poisson's equation can be simplified and reads:

$$L_D \left(\frac{du_0(z)}{dz}\right) = F(u_0(z), u_b) \quad (3.16)$$

$$\Rightarrow Q_{SC,0} = 2e_0 n_i L_D F(u_{s0}, u_b) \quad (3.17)$$

The abbreviations are

$$u_{s0} = \frac{E_F - E_{is0}}{k_B T} \quad ; \quad u_b = \frac{E_F - E_{ib}}{k_B T}$$

$$n_i = \frac{2}{\sqrt{\pi}} N_V F_{\frac{1}{2}}(\omega_{V,i}) \quad ; \quad \text{Intrinsic charge carrier concentration} \quad (3.18)$$

$$\omega_{\vartheta, \varphi} = \frac{E_{\vartheta} - E_{\varphi}}{k_B T} \quad ; \quad \text{for arbitrary symbols } \varphi, \vartheta$$

$$L_D = \sqrt{\frac{\epsilon_s k_B T}{2e_0^2 n_i}} \quad ; \quad \text{Debye length} \quad (3.19)$$

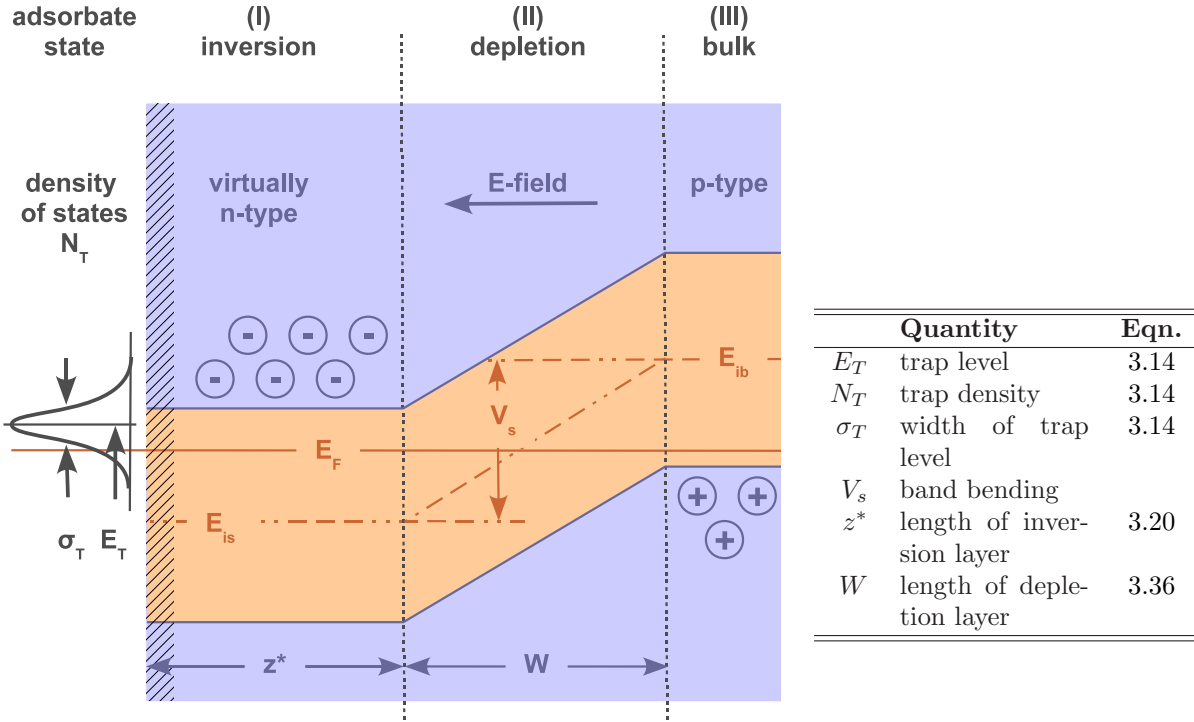


Figure 3.3.: Band diagram of the space charge layer on a p-type substrate. The positive charge of adsorbed donors (here: Rb atoms) is screened by electrons in the substrate. At high adsorbate concentration, an inversion layer constitutes at the surface, so it appears virtually n-type. The interface between regions with majority charge carriers of opposite charge includes a depletion region. The simulation of charge carrier dynamics is carried out separately in three separate regions [(I)-(III)], which are assumed to be homogeneous. Consistency of the solutions is granted by choosing appropriate boundary conditions (see text).

F is called 'space charge function' [67] and is proportional to the total charge density modification in the crystal when the reduced Fermi level u_0 at the surface is shifted towards its bulk equilibrium analogue u_b . For thermal equilibrium, which is treated here, the Fermi level remains constant over the complete system. Thus, the relative shift of the Fermi level has to be interpreted as shift of the band structure of the crystal in the opposite direction, caused by the electric surface potential.

Poisson's equation has not been solved explicitly here, and to find its complete solution, i.e., for all z , is not required. Sufficient information is gained by finding a solution that satisfies the demand for overall charge neutrality in the complete surface region by claiming $Q_{SC} + Q_T = 0$. Inserting equations 3.17 and 3.15, u_0 can be determined numerically to comply with the boundary condition. From the solution, the band bending

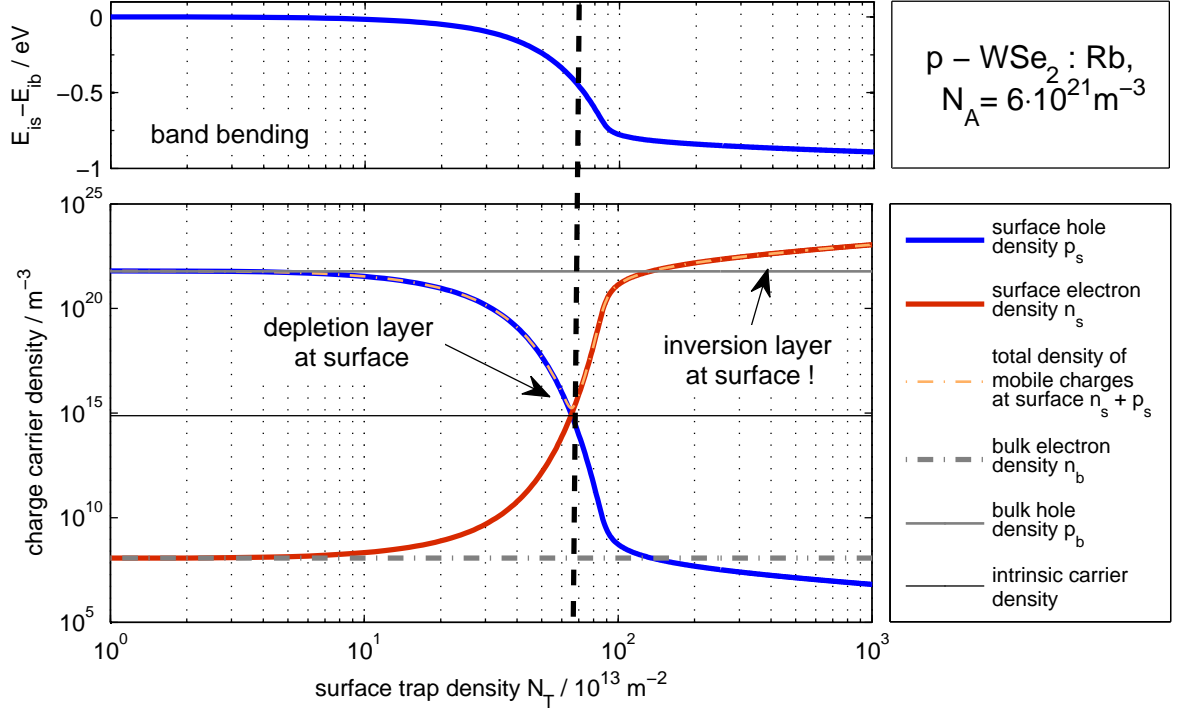


Figure 3.4.: Simulated equilibrium surface charge carrier concentration as function of adsorbate concentration for p-type $WSe_2 : Rb$ with a bulk acceptor density $N_A = 6 \cdot 10^{21} m^{-3}$. With increasing adsorbate concentration, depletion is reached in a narrow range of the trap level density. At even higher Rb coverage, the surface becomes virtually n-type. These conditions have been prepared during this work.

$V_s = k_B T(u_b - u_0) = E_{ib} - E_{is}$ is found. Once the band bending at the surface is known, equation 3.16 can be resolved for z

$$z^* = L_D \int_{u_s}^{u_b} \frac{1}{F(u, u_b)} du \quad (3.20)$$

The solution z^* is the length of the space charge layer. It will be used later when modeling charge transport. Some technical remarks concerning the numerical determination of z^* are discussed in appendix B.

The derivations given up to now allow for simulations of the surface potential as a function of adsorbate coverage. An exemplary case is shown in figure 3.4. The Rb-covered surface of WSe_2 was taken as model system here. Actual material parameters originate from the literature given in chapter 2 or could be determined during this work. An extensive discussion of the simulations is given in chapter 6. The equilibrium concentrations of holes and electrons shown in the figure clearly indicate the formation

of an inversion layer at sufficient adsorbate density, so the majority of charge carriers near the surface is represented by electrons. This finding is essential for the treatment of charge transport near the surface.

3.2.4. The space charge layer in non-equilibrium

The surface photovoltage (SPV) effect is observed when the charge arrangement derived before is perturbed by the generation of mobile charge carriers near the surface. During the experiment, electron-hole-pairs are created when laser light with photon energy exceeding the bandgap is absorbed at a constant rate. Therefore, the model of space charge layers developed above needs to be extended for stationary non-equilibrium. A common approach to introduce non-equilibrium is to split up the system into interacting subsystems that are assumed to be in individual thermal equilibria. Then, the complete system is denoted to be in quasi-equilibrium and individual quasi-Fermi levels have to be introduced for each subsystem.

For the system discussed here, a separate treatment of holes and conduction band electrons is justified, as the carrier recombination lifetime τ shows up to be in a typical range of μs , whereas the decay constant for a 'hot' electron relaxing to the conduction band minimum usually occurs within ps or less. The same holds for holes. The subsystems of charge carriers of one type can thus be considered to be in individual thermal equilibrium. A surface state is segregated in the same way, so it can be treated as a third subsystem.

In a modified version of the surface band diagram in figure 3.3, the stationary non-equilibrium state can be visualized including the symbols to be introduced therefor (see figure 3.5). The extension for non-equilibrium is performed by replacing the Fermi level E_F by the quasi-Fermi levels for electrons E_{Fn} and holes E_{Fp} in the space charge function in equation 3.17. For details, refer to the work of Trares-Wrobel [8]. The modified version of the space charge function is stated there in equation 2.32. By introducing quasi-Fermi levels, it gains two additional arguments such that $F = F(u_s, u_b, \delta u_n, \delta u_p)$ with $\delta u_n = (E_{Fn} - E_F)/k_B T$ and $\delta u_p = (E_{Fp} - E_F)/k_B T$. To find an adequate representation of a non-equilibrium state, E_{Fn} has to be determined as function of a given E_{Fp} (or vice versa) with respect to bulk space neutrality. Once again, this task can only be performed numerically and is implemented in the space charge simulation code.

3.2.5. Recombination of carriers

Now that the stationary states are modeled thermodynamically, a connection to their origin, the carrier generation rate G_0 , needs to be established. Thus, temporal dynamics of charge carriers will be discussed here and in the subsequent sections. The interaction between virtually separate pools of particles (electrons, holes and charge in the adsorbate state) is given by recombination of carriers. The charge concentration, Fermi level etc. found for equilibrium can be thought of making up the stage for the carrier concentration

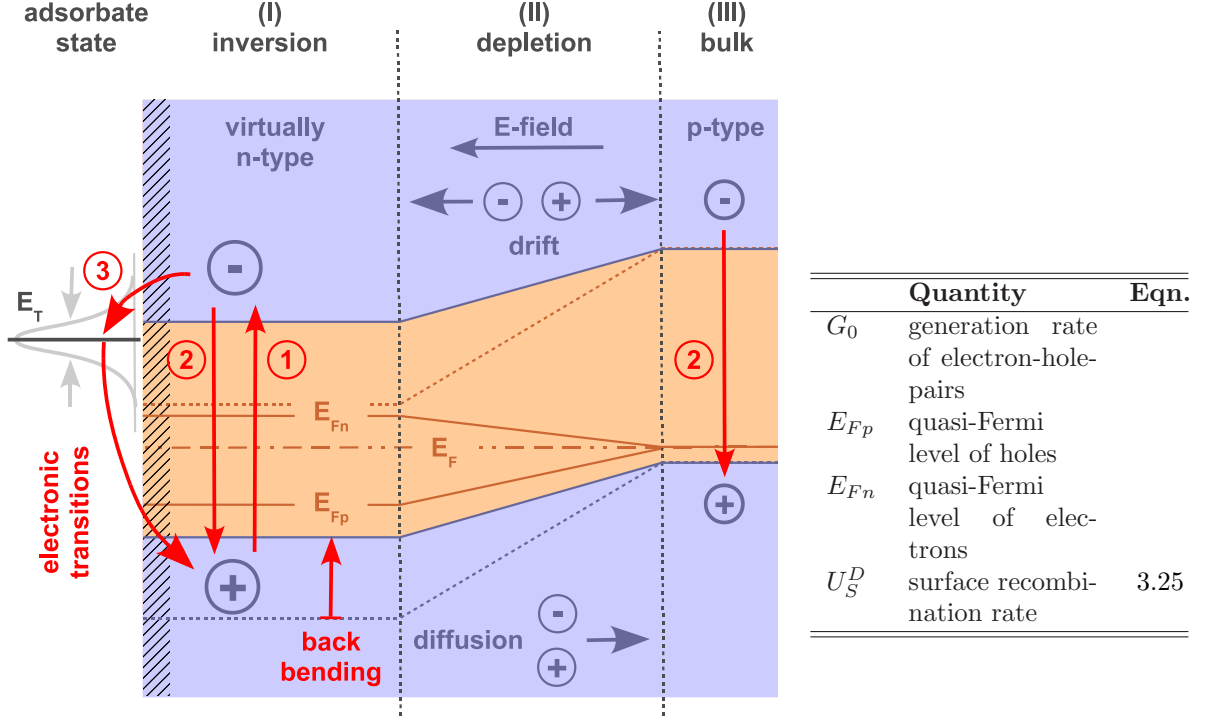


Figure 3.5.: Schematic of the dynamic processes involved in the model. The rate of generation (1) by light absorption and recombination (2) of electron-hole-pairs depends on the actual carrier concentrations. In region (I), an alternative recombination channel (3) including the surface state significantly contributes to the total recombination. Drift transport is limited to the depletion region (2) in this setup. Due to the low equilibrium charge carrier concentration in (2), a very low recombination rate results.

found in excess here. That is, not the absolute density of charge carriers will be treated, but the deviation from thermal equilibrium, i.e. $\Delta n = n - n_b$ and $\Delta p = p - p_b$. The nomenclature implies that the crystal is in equilibrium for $z \rightarrow \infty$. The subscript 'b' is used here to denote bulk and equilibrium concentration, which is equivalent if not stated explicitly.

In a transition of an electron from the conduction band to the valence band, an electron-hole pair is annihilated, dissipating the excess energy. The according band-to-band recombination rate U_b is given by [8]

$$U_b(z) = n(z) \cdot p(z) \cdot r_{CV} \left\{ 1 - \exp \left(\frac{E_{Fp} - E_{Fn}}{k_B T} \right) \right\}, \quad (3.21)$$

which can be simplified for the case of a non-degenerate semiconductor, i.e., $E_V \leq E_F \leq$

E_C to give

$$U_b(z) = r_{CV} \cdot \{n(z) \cdot p(z) - n_0(z) \cdot p_0(z)\} \quad (3.22)$$

Here, the transition probability r_{CV} ($[r_{CV}] = cm^{-3} \cdot s^{-1}$) of an electron per unit volume and time is introduced. Assuming that the deviation from equilibrium is small ($\Delta p \ll p$, $\Delta n \ll n$) and charge neutrality is retained ($\Delta p = \Delta n$), the equation can be simplified to

$$U_b(z) = \frac{\Delta p(z)}{\tau} \quad (3.23)$$

$$\text{with } \tau = [(n_b + p_b) \cdot r_{CV}]^{-1} \quad (3.24)$$

with the average carrier lifetime in the bulk τ . The approximation made here is crucial for setting up the carrier transport equation in section 3.2.6, because it offers a way to separate the equations for electrons and holes and renders both of them linear.

At the surface, an alternative recombination path involving the surface state is possible. An equation for the recombination rate including an extrinsic state had first been derived for the bulk by Shockley and Read [68], [69]. Later work showed that the results can easily be transferred to surface states [70],[71]. In this case, the surface recombination rate for a donor state U_s^D reads

$$U(E) = D_T(E) \cdot r_{CT} r_{TV} \frac{p_s \cdot n_s - p_1 \cdot n_1}{r_{CT}(n_s + n_1) + r_{TV}(p_s + p_1)}, \quad (3.25)$$

with

$$\begin{aligned} n_1(E) &= n_s \cdot \exp\left(\frac{E - E_{Fn}}{k_B T}\right) \\ p_1(E) &= n_s \cdot \exp\left(\frac{E_{Fp} - E}{k_B T}\right) \\ \Rightarrow p_1 \cdot n_1 &= \dots = n_i^2 \end{aligned}$$

where p_s and n_s are the particle densities in the valence band and the conduction band, respectively. Trares-Wrobel generalized the equation for a state of finite width by introducing the surface density of states (Here: eqn. 3.14) and integrating over binding energy

$$U_s = \int_{-\infty}^{+\infty} U(E) dE \quad (3.26)$$

The complete derivation of equation 3.25 can be found in reference [8], chapter 2.4 and the article by Shockley and Read [68].

3.2.6. Carrier transport equation

Because of the finite penetration depth of light, the generation of mobile charges and thus the non-equilibrium is restricted to an interval near the crystal surface. Electrons and holes are not constrained to this region and are transported mainly by two processes: Drift and diffusion. Drift motion is observed for charged particles in an electric field. Charge carriers accelerated by the field suffer various scattering processes so that a stationary average 'drift velocity' results. Drift motion is parametrized by the mobility μ ($[\mu] = m^2/(V \cdot s)$) of a particle. For the drift velocity \vec{v} in a given electric field $\vec{\mathcal{E}}$, $\vec{v} = \mu \cdot \vec{\mathcal{E}}$ holds.

The second transport mechanism is diffusion, driven by a gradient of charge carrier concentration $\nabla \cdot \Delta n$. The relation between particle flux density and a given gradient is $\vec{j} = \nabla \cdot \Delta n \cdot D$ with the diffusion coefficient D ($[D] = m^2 \cdot s^{-1}$). D can be expressed in terms of the particle mobility by the Einstein-Smoluchowski-relation $D = k_B T / e \cdot \mu$.

Now, the one-dimensional transport equation for minority carriers can be posed, including the mentioned transport mechanisms and the recombination model from the preceding section. The stationary state to be found is driven by light being absorbed at a rate $G(z)$ that depends on the distance z from the crystal surface:

$$G(z) = G_0 \cdot \exp(-\alpha z) \quad (3.27)$$

α is the absorption coefficient of the bulk material at given wavelength. In this formulation, G_0/α equals the total absorbed photon flux, ($[G_0] = cm^{-3} \cdot s^{-1}$). In the following, the generation of one electron-hole pair per absorbed photon is assumed, so the absorption rate in eqn. 3.27 is equal to the generation rate of electron-hole-pairs. Starting with the continuity equation and the claim for stationarity

$$\frac{\partial}{\partial t} \Delta n = \nabla \cdot \vec{j} - U_b + G \stackrel{!}{=} 0 \quad (3.28)$$

and inserting the above terms for transport and recombination, we find the equations for excess minority electrons Δn or holes Δp . Which one is to be applied depends on the actual equilibrium charge carrier concentration.

$$D \cdot \frac{\partial^2 \Delta p}{\partial z^2} + \mu \mathcal{E} \cdot \frac{\partial \Delta p}{\partial z} - \frac{1}{\tau} \Delta p = -G_0 \cdot e^{-\alpha z} \quad (3.29)$$

$$D \cdot \frac{\partial^2 \Delta n}{\partial z^2} - \mu \mathcal{E} \cdot \frac{\partial \Delta n}{\partial z} - \frac{1}{\tau} \Delta n = -G_0 \cdot e^{-\alpha z} \quad (3.30)$$

As discussed above, the equation requires constant 'background' charge densities p and n . The application to the realistic configuration of the space charge layer will be discussed in the following section. Up to now, surface recombination is not included in the equation. This effect naturally only affects the surface. Thus, the treatment of the surface state is implemented below when discussing boundary conditions the solution has to meet.

In the above equations, the dynamic constants μ and D are not identical in general, as they refer to holes (eqn. 3.29) and electrons (eqn. 3.30), respectively.

Equations 3.29 and 3.30 are ordinary inhomogeneous partial differential equations which can easily be solved using an ansatz made up by a combination of exponential functions. A particulate solution of the inhomogeneous solution is given by

$$\Delta p_{inh.} = A^+ \cdot e^{-\alpha z} ; \Delta n_{inh.} = A^- \cdot e^{-\alpha z} \quad (3.31)$$

where the coefficient A^+ is determined by the boundary conditions. Inserting equation 3.31 into the differential equation 3.29, A^+/A^- can be expressed in terms of the system parameters and the yet unknown carrier generation rate G_0 .

$$A^+ = -\frac{G_0}{D\alpha^2 - \alpha\mu\mathcal{E} - 1/\tau} \quad ; \text{ for holes} \quad (3.32)$$

$$A^- = -\frac{G_0}{D\alpha^2 + \alpha\mu\mathcal{E} - 1/\tau} \quad ; \text{ for electrons} \quad (3.33)$$

The general solution of the system is given by a linear combination of particulate solution and general solution of the homogeneous equation. As the equation is of second order, the homogeneous solution consists of two independent solutions. The complete solution for holes reads:

$$\Delta p = B^{+/-} \cdot e^{\lambda_1^{+/-} z} + C^{+/-} \cdot e^{\lambda_2^{+/-} z} + A^{+/-} \cdot e^{-\alpha z}$$

$$\text{where} \quad (3.34)$$

$$\lambda_1^+ = -a \cdot (1 + b) \quad ; \quad \lambda_2^+ = -a \cdot (1 - b)$$

$$a = \frac{\mu\mathcal{E}}{2D} \quad ; \quad b = \sqrt{1 + \frac{\epsilon}{a^2}}$$

$$\epsilon = \frac{1}{D\tau}$$

$$\Rightarrow \lambda_1^+ > 0 \quad ; \lambda_2^+ < 0 \quad ; |\lambda_1^+| \gg |\lambda_2^+|$$

An analog expression can be formulated for electrons. The signs of λ_1^+ and λ_2^+ hold for a negative electric field \mathcal{E} , as is the case for $WSe_2 : Rb$. In conjunction with the coefficient of the inhomogeneous solution A^+ , B^+ , and C^+ must also be found by an appropriate choice of boundary conditions.

3.2.7. Solving the transport equation in the current setup

The formation of the space charge layer leads to surface charge carrier concentration (p_s, n_s) that easily deviate from the bulk values (p_b, n_b) by some orders of magnitude.

Results of the numerical space charge simulation (fig. 3.4) using realistic parameters of p-type WSe_2 show the existence of an inversion layer at the surface, i.e. the electron density exceeding the hole density by far. The surface can thus be considered virtually n-type here. For high adsorbate coverage, the simulation predicts that the surface electron density will even exceed the bulk hole concentration ($n_s > p_b$). When comparing the simulated band bending (upper panel in fig. 3.4) with that prepared experimentally (chapter 6), the existence of an inversion layer is expected for most of the experimental data.

The junction between two regions with majority charges of different sign is not abrupt, but rather accompanied by the formation of a depletion layer. Electrons and holes near the transition are likely to recombine, resulting in a drastically lowered charge concentration on both sides near the junction. For reference, see beginner's textbooks on semiconductor physics such as Sze [63].

To find an exact solution of carrier dynamics for this charge configuration, a sophisticated treatment of the depth-dependent charge distribution would be necessary. Here, a simplified approach will be made to solve the transport equations 3.29 and 3.30 for excess carriers by separating the surface into distinct depth intervals and finding individual solutions. Homogeneous charge densities will be assumed within each interval, as is required for the transport equations to hold.

Figure 3.3 gives an impression of the segmentation made here. Perpendicular to the surface, the space charge layer is modeled in a sequence of three regions. Using this scheme, some individual simplifications can be made before solutions of the transport equations (3.29, 3.30) for each region are derived.

The top layer(I) is the inversion layer mentioned above. It ranges from the crystal surface to the end of the space charge layer ($0 \leq z \leq \beta \cdot z^*$), determined using equation 3.20. Within this region, the carrier concentration and electrostatic potential are extrapolated constantly from the surface values found from the simulation. The coefficient $\beta > 0$ is introduced here to compensate errors introduced by this approximation and is used as a free parameter when simulation results are fitted to experimental data (chapter 6). Basically constant values $\beta \approx 1$ are found for common cases there, so the proceeding is justified. In the inversion layer, the majority of mobile charges is made up by electrons, so eqn. 3.29 for excess holes is applicable here.

The constant electric potential yields zero electric field and thus zero drift current. Therefore, the parameters of the solution $\Delta p_s(z)$ in eqn. 3.34 simplify to

$$\lambda_{s1} = +\frac{1}{\sqrt{D_s \tau_s}} \quad ; \quad \lambda_{s2} = -\frac{1}{\sqrt{D_s \tau_s}}$$

$$A_s = -\frac{G_0}{D\alpha^2 - \frac{1}{\tau}} \quad (3.35)$$

These values inserted into equation 3.34 make up the excess hole concentration $\Delta p_s(z)$ for the inversion layer (I).

Region (II) basically represents the depletion layer. It ranges from $\beta \cdot z^* < z < \beta \cdot z^* + W$, where W is the width of the depletion region found for an arbitrary p-n-junction [63]

$$W = \sqrt{\frac{2\epsilon_s}{e_0} \cdot \frac{p_b + n_s}{p_b \cdot n_s} \cdot V_s} \quad (3.36)$$

As with the built-in potential of a p-n-junction, the electric potential falls off linearly within this region, so a constant electric field $\mathcal{E} = V_s/W$ results. It is directed such that majority carriers cannot pass the depletion layer, but minority carriers can. In the depletion layer, only a small amount of mobile charges is present. Here, the intrinsic concentration for electrons and holes is assumed:

$$n_i = p_i = \sqrt{N_C \cdot N_V} \cdot e^{\frac{-E_G}{2k_B T}} \quad (3.37)$$

This formula is an approximation to the precise expression. The band-to-band recombination rate r_{CV} becomes extremely small here, though different from zero. Unfortunately, the role of minority and majority carriers is not defined here, as $p_i = n_i$ holds, so the deviation from equilibrium concentration has to be taken into account for both carrier species. According to equation 3.35, the parameters to the solution of eqn. 3.34 for holes read:

$$\begin{aligned} \lambda_{d1}^+ &= a(1+b) \\ \lambda_{d2}^+ &= a(1-b) \\ A_d^+ &= -\frac{G_0}{D\alpha^2 - \alpha\mu\mathcal{E} - \frac{1}{\tau}} \end{aligned} \quad (3.38)$$

and for electrons

$$\begin{aligned} \lambda_{d1}^- &= -a(1+b) \\ \lambda_{d2}^- &= -a(1-b) \\ A_d^- &= -\frac{G_0}{D\alpha^2 + \alpha\mu\mathcal{E} - \frac{1}{\tau}} \end{aligned} \quad (3.39)$$

The layered arrangement is terminated by the bulk (III) for $z > \beta \cdot z^* + W$, which represents the part of the crystal that is undisturbed by the surface charge. For the penetration depth of the light, $1/\alpha \ll \beta \cdot z^* + W$ holds, i.e. the generation rate of mobile charges can be neglected in the bulk. The electric potential is assumed to be constant here, so in analogy to (I), no drift transport is included. The parameters for the distribution of excess electrons in the bulk hence reads

$$\begin{aligned} \lambda_{b1} &= -a(1+b) \\ \lambda_{b2} &= -a(1-b) \\ A_b &= -\frac{G_0}{D\alpha^2 - \frac{1}{\tau}} \end{aligned} \quad (3.40)$$

Now that all expressions are derived for the three zones, a globally consistent solution must be found by introducing appropriate boundary conditions, so a detailed discussion follows. Up to now, the model discussed here is identical to that developed in reference [8], but the segmentation into zones (I) to (III) done here requires a new strategy to find a solution. No more simplifications will be made, so we have a total of four solutions for excess carrier concentration in regions (I) to (III) (Note that in the depletion layer (II), both electrons and holes must be treated!). This gives 12 coefficients to be determined from boundary conditions plus the unknown carrier generation rate G_0 . In the following, all coefficients of the solution in a specific region have a subscript (one out of {s,d,b} for 'surface', 'depletion' and 'bulk'). The majority of the conditions is based on particle flux and current density. The combined particle flux driven by drift and diffusion is found from the general expression for particle concentrations Δn and Δp :

$$\mathcal{F}_n = -\mu\mathcal{E}\Delta n - D\frac{\partial\Delta n}{\partial z} \quad (3.41)$$

$$\mathcal{F}_p = \mu\mathcal{E}\Delta p - D\frac{\partial\Delta p}{\partial z} \quad (3.42)$$

The different sign here is a consequence of the opposite drift velocity due to opposite sign of the charges. For the current density,

$$\begin{aligned} j_n &= -e_0 \cdot \mathcal{F}_n \\ j_p &= e_0 \cdot \mathcal{F}_p \end{aligned}$$

is found.

Due to the fact that none of the mobile charges can leave the crystal, i.e. the photoemission current is neglected here, the total particle flux towards the surface must equal the surface recombination rate U_s^D :

$$\begin{aligned} -\mathcal{F}_p &\stackrel{!}{=} U_s^D \\ \Rightarrow \lambda_{s1}B_s + \lambda_{s2}C_s - \alpha A_s &= \frac{U_s^D}{D} \end{aligned} \quad (3.43)$$

The expression below results when the solution for excess holes in (I) is inserted. Here, recombination involving the surface state is introduced to the system, so the model is completed by this boundary condition.

The surface charge concentration ΔP_s is determined from the simulation. The general solution 3.34 has to meet this criterion:

$$\begin{aligned} \Delta p_s(z=0) &\stackrel{!}{=} \Delta P_s \\ \Rightarrow B_s + C_s + A_s &= \Delta P_s \end{aligned} \quad (3.44)$$

The next condition can be seen to be rather trivial and implements the crucial assumption that the bulk crystal far from the surface is not affected by adsorbates or

light absorption. For the excess carriers, this simply means that the concentration must vanish for $z \rightarrow \infty$:

$$\begin{aligned}\Delta n(z \rightarrow \infty) &\stackrel{!}{=} 0 \\ \Rightarrow B_b &= 0\end{aligned}\tag{3.45}$$

Some more conditions are found from the inhomogeneity of the region specific solutions in equations 3.35, 3.38, 3.39, and 3.40. $A_b = 0$ can be claimed here, as the light penetration depth is much smaller than the combined width of layers (I) and (II) here.

While the equations stated up to now apply to only one of the solutions, some more equations relate the solutions to each other at the boundaries of the zones.

First of all, continuity is required for Δp at the border between (I) and (II), i.e. at $z = z_{sd}$. The same holds for electrons at the border between depletion layer (II) and bulk (III) at $z = z_{db}$:

$$\begin{aligned}\Delta p_s(z = z_{sd}) &\stackrel{!}{=} \Delta p_d(z = z_{sd}) \\ \Rightarrow B_s + C_s + A_s - B_d^+ - C_d^+ - A_d^+ &= 0\end{aligned}\tag{3.46}$$

$$\begin{aligned}\Delta n_d(z = z_{db}) &\stackrel{!}{=} \Delta n_b(z = z_{db}) \\ \Rightarrow B_d^- + C_d^- + A_d^- - C_b &= 0\end{aligned}\tag{3.47}$$

Physically speaking, this claims finite particle flux created by drift and diffusion, which are proportional to the first and the second derivative of the carrier concentration, respectively. Equation 3.47 has already been reduced using the boundary conditions 3.45 and the approximation of small light penetration depth.

As there are no particle generation or destruction mechanisms except for generation and recombination, the total number of particles must be constant in a stationary state. The following equation assures particle conservation for the region borders by claiming conservation of particle flux across the border

$$\mathcal{F}_{p,s}(z = z_{sd}) \stackrel{!}{=} \mathcal{F}_{p,d}(z = z_{sd})\tag{3.48}$$

$$\mathcal{F}_{n,d}(z = z_{db}) \stackrel{!}{=} \mathcal{F}_{n,b}(z = z_{db})\tag{3.49}$$

Once again, the equations apply to excess holes at the border between (I) and (II) and to excess electrons at the border separating (II) and (III). The extra subscripts 's', 'd', and 'b' of the flux \mathcal{F} indicate the region from which the solution has to be inserted into the flux equation 3.48 and 3.49. Inserting the general solutions into the boundary conditions gives lengthy expressions. For better readability, they have been moved to the end of this chapter (see eqns. 3.54 and 3.55).

In zones (I) and (III) only dynamics of the minority carriers is taken into account. The majority carrier concentration is assumed to follow small perturbations of minority

charges easily because of its huge majority. For instance, every excess electron in (III) can be seen to be traced by a hole, so no charge accumulation and, in equivalence, no total charge transport occurs. Treating electrons and holes in the depletion layer separately opens up the possibility of a non-vanishing current density. The system is designed to be free of current sources and drains and especially no current except for the (neglected) photocurrent can cross the surface. Therefore, the stationary state sought after here requires the current density to vanish locally. For the depletion layer (II), this is granted by the demand that the current density must vanish at the borders to regions (I) and (III). The particle flux across the boundary is already equalized by equations 3.48 and 3.49, such that here, only the particle flux of electrons and holes inside the depletion layer (Δn_d and Δp_d) need to be balanced. Writing down for $z = z_{sd}$ and $z = z_{db}$ gives

$$-\mathcal{F}_{n,d}(z = z_{sd}) + \mathcal{F}_{p,d}(z = z_{sd}) \stackrel{!}{=} 0 \quad (3.50)$$

$$-\mathcal{F}_{n,d}(z = z_{db}) + \mathcal{F}_{p,d}(z = z_{db}) \stackrel{!}{=} 0 \quad (3.51)$$

The expression derived from this boundary condition when the actual solution is inserted can be found at the end of this chapter (eqn. 3.55).

All equations required to find a unique solution of the system are formulated hereby. Fortunately, all of them are found to be linear combinations of the unknown coefficients $A_x, B_x, C_x, ; x \in \{s, d, b\}$ such that all equations can be compiled as inhomogeneous system of linear equations and can be solved using standard techniques like matrix inversion. A non-zero determinant of the coefficient matrix is essential here, indicating that all boundary conditions are linearly independent. A deeper analysis of the determinant would be desirable, as single boundary conditions might already be included implicitly by others. As a profound mathematical discussion cannot be given here, practitioners should be aware of possible ill-conditioned cases that might occur. Nevertheless, practice shows no difficulties in solving the system and physics requires all of the stated equations to be included, so the system can be considered complete.

3.2.8. Approximate solutions of the model

Having developed a model and a complete strategy to find a solution, some special issues need to be discussed now. Though simple in detail, no straightforward and intuitive, comprehensive discussion of the complete system can be given. Significant simplification of the system of equations is found under special circumstances. In order to provide a better understanding of the complete system, some limiting cases will be discussed now.

Another point makes the formulation of approximations to the system even more crucial. When studying realistic configurations of the system, the resolvability might be restricted by floating point precision. Whereas 16 digits of numerical precision (64 Bit floating point arithmetic, 'double precision') might appear outstandingly high, the user finds himself confined to a small range of parameters, as many values appear in

the argument of exponentials here. As, basically, a linear system of equations is to be solved here, errors due to computational precision might not only degrade the results, but also make the equations impossible to resolve. Thus, analytical expressions are required for the cases where finding a solution is denied by computational precision. Some approaches for special cases will be discussed now.

In general, the linear system derived above cannot be split up into independent sub-systems, so an analytical expression for the generation rate G_0 is expected to be lengthy and non-illustrative. The coupling between the equations is annulled for some limiting cases: Two of them concern the band-to-band recombination rate, parameterized by the transition probability r_{CV} . When the recombination is considered the dominating process in the system, i.e., r_{CV} is large, it can be simplified as follows: $\tau_x \approx 0$ results for the recombination lifetime in all regions. As a consequence, a small value of the Debye length $L_D = \sqrt{D\tau}$ is obtained. If the average carrier lifetime is small, recombination is the major process in the system. In this case, the parameters λ in the depletion layer are affected as follows:

$$\begin{aligned} b &\approx \frac{1}{L_D a} \\ \lambda_{d1}^+ &\approx -\frac{1}{L_D} \quad ; \quad \lambda_{d2}^+ \approx -\lambda_{d1}^+ \\ \lambda_{d1}^- &\approx +\frac{1}{L_D} \quad ; \quad \lambda_{d2}^- \approx -\lambda_{d1}^- \end{aligned}$$

Specific attention has to be paid to equations 3.35 and 3.43: C_b is dropped out of the system as its prefactor vanishes. At the same time, the prefactor of B_s approaches infinity, requiring B_s to tend towards zero. In addition, the rest of equations 3.46 and 3.48 becomes nearly equivalent. Thus, both equations must be replaced by

$$\begin{aligned} B_s &= 0 \\ C_b &= 0 \end{aligned}$$

With these modifications, the system can be solved as before.

Switching to the opposite extreme $r_{CV} \rightarrow 0$, i.e., very low band-to-band recombination, a very simple expression for G_0 is found. Throughout the system, $r_{CV} \rightarrow 0$ yields $\tau_x \rightarrow \infty$. Inserting τ_x into the abbreviations ϵ and b in equations 3.35, 3.38, and 3.39, the effect on the coefficients λ is derived:

$$\begin{aligned} \lambda_{s1,2} &\rightarrow 0 \quad ; \quad \lambda_{b1,2} \rightarrow 0 \\ \lambda_{d1}^+ &\rightarrow -2 \cdot a \quad ; \quad \lambda_{d2}^+ \rightarrow 0 \\ \lambda_{d1}^- &\rightarrow +2 \cdot a \quad ; \quad \lambda_{d2}^- \rightarrow 0 \end{aligned}$$

This partially cancels the coupling between the equations, so G_0 can be found explicitly

from the simplified versions of equations 3.35 and 3.43

$$\begin{aligned} A_s + \frac{1}{D\alpha^2} \cdot G_0 &= 0 \\ -\alpha \cdot A_s &= \frac{U_s^D}{D} \end{aligned}$$

Here, A_s can be eliminated and G_0 simply reads

$$G_0 = \alpha U_s^D, \quad (3.52)$$

i.e., the recombination rate becomes independent of the actual configuration of the space charge layer.

The next case to be discussed here is especially interest for the numerical solution of the system at high excitation levels, i.e., at large SPV effect. Starting from the well-known layered space charge configuration with surface inversion in thermal equilibrium, large band back bending can lead to a situation in which the surface layer (I) shows pronounced depletion of carriers. Following equation 3.36, a strongly enlarged depletion layer thickness W results. For this case, the bulk solution must completely vanish from the system. The boundary conditions at $z = z_{db}$ are modified to claim thermal equilibrium ($\Delta n_d \rightarrow 0$). The system can thus be solved in this situation by replacing equations 3.47 and 3.49 by

$$\begin{aligned} C_b &= 0 \\ B_d^- &= 0 \end{aligned}$$

A connection to the result derived earlier for the one-region-model [8] is established by the limiting case $z_{sd} \rightarrow \infty$. Then, regions (II) and (III) completely vanish from the system, and the remaining boundary conditions must comply with the solution for surface excess minority carriers (here : Δp_s). In this case, the solution derived in previous work (appendix E in [8]) is reproduced. The only difference is that the inversion is still present so that holes should be handled here in consequence, whereas the one-region approach would deal with electrons. Here, drift transport also vanishes from the system, as a reasonable effect is found for the depletion layer exclusively. Then, the equation stated in appendix E of [8] simplifies to

$$G_0 = (L_D\alpha - 1) \cdot \left(\frac{U_s^D}{L_D} - \frac{\Delta P_s}{\tau} \right) \quad (3.53)$$

when $\lambda_{s,2} = -1/\sqrt{D\tau_s} = -1/L_D$ is inserted and the equation gets simplified.

This chapter dealt with the development of a simplified model of the surface space charge layer in inversion, taking into account carrier transport by drift and diffusion as well as recombination in the bulk or, involving the adsorbate state, at the surface. A strategy to solving the system was discussed, and some special cases were treated in order

to extend the system to the full range covered by the experiments done during this work. Data found by a numerical simulation of the model will be matched to experimental data in the following chapters, demonstrating the validity of the theoretical aspects discussed here. The following section shows the complete expressions obtained for the boundary conditions dealing particle flux(3.49) and current density(3.51) and may be skipped at first reading.

3.2.9. Complete formulations of the boundary conditions

Starting from boundary condition 3.49 and using the expression for the particle flux in equation 3.42, the solution of the differential equation 3.34 can be inserted. This results in a linear relation between the unknown coefficients and is part of the system of linear equations that is solved to find a solution of the model. Sorting for the coefficients in the specific solutions, the boundary condition for excess holes at the border between inversion (I) and depletion region (II) reads:

$$\begin{aligned}
 & B_s \cdot (\quad + \lambda_{s1} D) \cdot e^{\lambda_{s1} z_{sd}} \dots \\
 & + C_s \cdot (\quad + \lambda_{s1} D) \cdot e^{\lambda_{s2} z_{sd}} \dots \\
 & + A_s \cdot (\quad - \alpha D) \cdot e^{-\alpha z_{sd}} \dots \\
 & + B_d^+ \cdot (-\mu \mathcal{E} - \lambda_{d1}^+ D) \cdot e^{\lambda_{d1}^+ z_{sd}} \dots \\
 & + C_d^+ \cdot (-\mu \mathcal{E} - \lambda_{d2}^+ D) \cdot e^{\lambda_{d2}^+ z_{sd}} \dots \\
 & + A_d^+ \cdot (-\mu \mathcal{E} + \alpha D) \cdot e^{-\alpha z_{sd}} \dots \\
 & = 0
 \end{aligned} \tag{3.54}$$

An equivalent expression is found for the flux conservation of excess electrons at the border between (II) and (III).

The boundary conditions claiming vanishing current density (equation 3.48) are equivalent except for the argument z of the exponentials. Hence, a representation for electrons at the border $z = z_{db}$ can easily be found by replacing z_{sd} by z_{db} in the equation below.

$$\begin{aligned}
 & B_d^+ \cdot (-\mu_p \mathcal{E} - \lambda_{d1}^+ D_p) \cdot e^{\lambda_{d1}^+ z_{sd}} \dots \\
 & + C_d^+ \cdot (-\mu_p \mathcal{E} - \lambda_{d2}^+ D_p) \cdot e^{\lambda_{d2}^+ z_{sd}} \dots \\
 & + A_d^+ \cdot (-\mu_p \mathcal{E} + \alpha D_p) \cdot e^{-\alpha z_{sd}} \dots \\
 & + B_d^- \cdot (-\mu_n \mathcal{E} + \lambda_{d1}^+ D_n) \cdot e^{\lambda_{d1}^- z_{sd}} \dots \\
 & + C_d^- \cdot (-\mu_n \mathcal{E} + \lambda_{d2}^+ D_n) \cdot e^{\lambda_{d2}^- z_{sd}} \dots \\
 & + A_d^- \cdot (-\mu_n \mathcal{E} - \alpha D_n) \cdot e^{-\alpha z_{sd}} \dots \\
 & = 0
 \end{aligned} \tag{3.55}$$

This is the only type of boundary condition that is mixing dynamic constants of electrons and holes. The subscript 'p' was introduced here for parameters of holes and 'n' for electrons.

4. Experimental setup

In this chapter, the actual implementation of the experimental setup for angular resolved photoemission spectroscopy (ARPES) as designed in the workgroup will be outlined. It is specified to work with modern soft X-ray sources as supplied by synchrotron facilities such as HASYLAB at DESY, Hamburg. For laboratory applications, an optional XUV-emitting plasma discharge lamp is available. All parts of the photoelectron detection system and the XUV source are supplied by SPECS, a commercial manufacturer of ARPES equipment.

The setup is still in a constant evolutionary process. The features reported here represent a snapshot of the state during the experiments reported in this work. Before going into detail, some principles of an ARPES experiment will be outlined. Basics of the energy-resolved detection of photoelectrons are introduced in section 4.1. In section 4.2, the specifications of the main components, i.e. the electron analyzer and the XUV source, are summarized. Measurements under well-defined conditions are ensured by a variety of additional components of the experimental chamber such as the ultrahigh-vacuum system or the sample manipulator. An overview of the general layout is given in section 4.3. Numerous upgrades of the original setup allow for advanced modes of spectrometer operation, more comfortable handling of the system, and a higher degree of automation during the acquisition of data. Several features that have been designed and implemented in the course of this work are discussed in section 4.4.

4.1. Basics of the experimental setup

The capability of detecting photoelectrons with sensitivity to their kinetic energy is crucial to call ARPES a spectroscopic technique. In practice, this means selecting photoelectrons within a small energy interval from the total energetic distribution that is emitted simultaneously. Furthermore, the emission angle relative to the surface normal must be determined with low tolerance. These requests are equivalent to finding the complete momentum vector of photoelectrons. As was already described in chapter 3.1, this information can be used to obtain information of the quantum mechanical state that an electron occupied before emission. The emission rate of electrons with given momentum is measured to give the photoemission intensity, which depends on the density of states in the sample. Thus, a generic photoelectron detection system consists mainly of two parts: the electron analyzer and an electron detector.

The cross section of a typical hemispherical electron analyzer is shown in figure 4.1. It

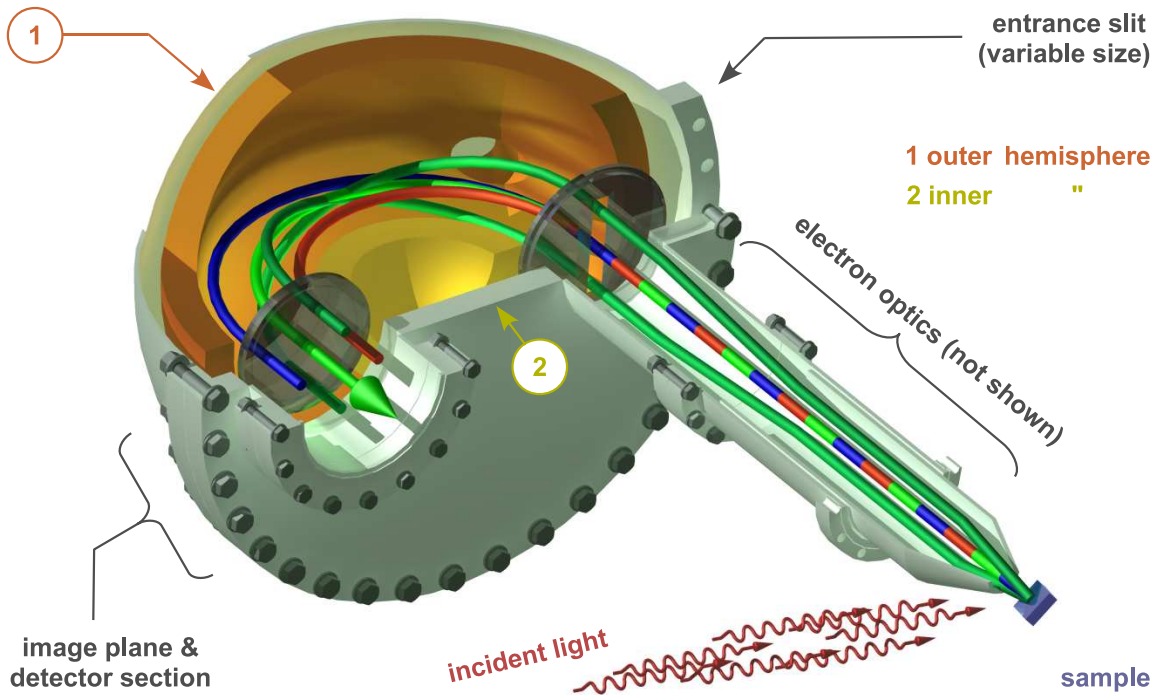


Figure 4.1.: Principle sketch of electron trajectories in the analyzer. Energy dispersion is achieved by means of the hemispherical setup (light green, red, and blue trajectory). Electrons emerging at different angles from the sample enter the analyzer at different height and are imaged at a 1:-1 ratio in the detector plane (green trajectories)

basically consists of two hemispherical capacitor plates with radii R_1, R_2 whose centers are matched. When different voltages are applied to the plates, a radial electric field results in the gap between the plates. For this setup, the trajectory of a charged particle can be computed in analogy to the two-body problem with one body fixed at the center of the hemispheres, so electrons follow Keplerian ellipses defined by their kinetic energy and the electric field in the analyzer. Starting at the center radius between the two plates $R = (R_1 + R_2)/2$ in the entrance plane and directed tangentially, an electron will reach the exit plane of the analyzer at an energy-dependent radius. If the entrance and exit radius are delimited by apertures, only electrons with distinct kinetic energy can enter the detector mounted in the exit plane. This energy is tuned by the potential difference between the analyzer plates. The emission angle from the surface that is to be detected is usually defined by the relative geometric orientation of the analyzer entrance aperture and the sample normal. In earlier experimental setups, the emission angle was selected by rotating the analyzer around the sample, while modern spectrometer designs allow for parallel detection of emission angles to some extent.

4. Experimental setup

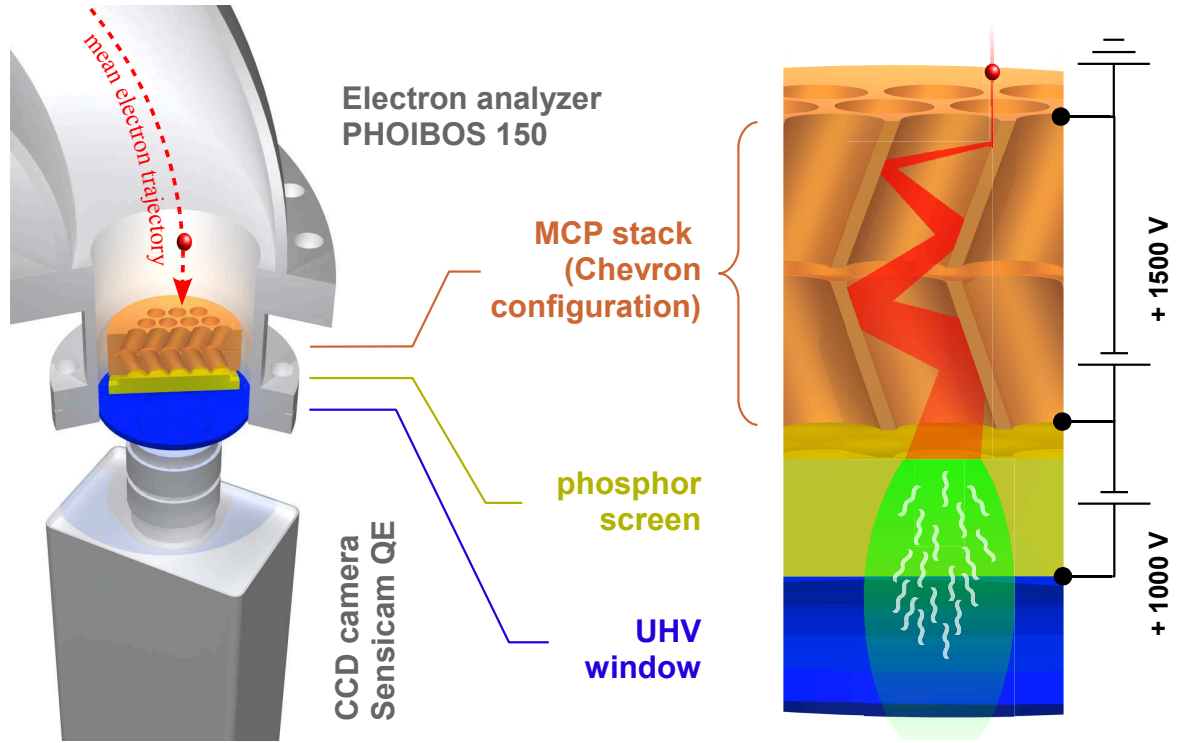


Figure 4.2.: Schematic of a two-dimensional electron detector with multi-channel plates (MCP) and fluorescent screen. The analyzer provides angular and energy dispersion of electron trajectories, so a signal can be assigned kinetic energy and emission angle from its position in the two-dimensional detector plane. Incident electrons are accelerated by high-voltage and emit secondary electrons upon impact at the channel walls of the MCPs, giving an amplified electron signal that is converted to visible light by means of the fluorescent screen.

For a hemispherical analyzer, the theoretical energy resolution at given kinetic energy can be defined as follows: The kinetic energy required for a circular orbit with radius R is called the pass energy E_p . Consider electrons passing the analyzer, which are constrained by slit apertures with a width S located in the entrance and the exit plane. The energy resolution ΔE denotes the kinetic energy interval of electrons that are transmitted when the analyzer accepts electron trajectories at a maximum angle of $\pm\alpha$ towards the normal to the entrance plane.

$$\Delta E = E_p \cdot \left(\frac{S}{2 \cdot R} + \frac{\alpha^2}{4} \right) \quad (4.1)$$

Electrons within this energy interval reach the exit plane at radius R . In the general case of two different aperture sizes S_1 and S_2 , $S = (S_1 + S_2)/2$ holds. When using a two-dimensional image detector, no exit slit exists in the setup. Instead, its width is

defined by the bin size in the image plane.

In addition to parallel detection of emission angles, modern analyzers allow for the detection of more than one kinetic energy in parallel. For a known analyzer dispersion relation $r(E_p + E)$, i.e., exit radius of the electron trajectory for given kinetic energy, a simultaneous detection of several kinetic energies becomes possible as the exit aperture is replaced by a spatially resolving detector. The red, light green, and blue electron trajectories drawn in figure 4.1 give an impression of the energy dispersion. Electrons following the light green trajectory have pass energy, while the energies associated with the blue and red trajectories are slightly larger or smaller, respectively.

The pass energy setting determines the performance of the electron analyzer concerning energy resolution (eqn. 4.1), energy dispersion, and transmission, i.e., detected signal over photoelectron flux. When recording a photoelectron spectrum $I(E_{kin})$, i.e., the flux of photoelectrons as a function of kinetic energy at constant photon energy, it is desirable to keep these parameters constant.

Thus, an electrostatic lens system upstream the analyzer entrance plane is used to accelerate or decelerate incoming electrons to the pass energy. It also serves to image the sample surface to the entrance slit and therefore defines a maximum area and angle from which electrons are accepted.

Up to now, the analyzer has only been discussed in terms of a two-dimensional cross section. In a realistic analyzer setup, also trajectories in planes tilted towards the central cross section are transmitted through the analyzer (dark green trajectories in figure 4.1) if allowed by the aperture design. The associated electrons emitted at an angle against the mean accepted emission angle reach the detector plane at a position deviating perpendicularly to the energy dispersive direction. Applying a two-dimensional detector, the combined detection of an interval of the kinetic energy and emission angle becomes possible.

While the preceding paragraphs dealt with the optical properties of the electron analyzer, the general concept of the electron detection system used here is presented now. The schematic cross section of a detector arrangement is shown in figure 4.2. The basic task is to detect the occurrence of a very small amount of charge being transmitted through the detector per unit time. The integral emission current is found in the range of 1 nA typically, distributed in the half-space over the sample surface and the total energy spectrum. As a common electron analyzer might accept $\approx 0.1\%$ of half-space and a much smaller fraction of the total spectral range, it quickly comes to detecting single electrons. High amplification of such small signals is required in order to detect the signals using electronic or optoelectronic hardware.

A channeltron provides the capability of multiplying a single incident electron to a macroscopic pulse of 10^5 to 10^6 electrons. This is achieved by accelerating the electron by high voltage inside an insulating, twisted tube. Secondary electrons are emitted by accelerated electrons hitting the tube walls, initiating a cascade of acceleration and secondary electron emission. At the end of the tube, the particle avalanche can be read out as voltage pulse. Downstream electronic hardware provides further amplification.

The photoemission intensity is represented by the rate of detected pulses then.

For spatially resolved electron amplification, multi-channel-plates (MCP) are used. Based on the same secondary electron emission principle, an MCP consists of a thin (typical: $500\mu m$) insulating disk with a close-packed grid of tiny holes, the channels. A typical hole diameter is $10\mu m$ at a center-to-center spacing of $12.5\mu m$ giving an areal coverage of $\approx 60\%$ when arranged hexagonally. High voltage is applied between the front and the back, making each channel a miniaturized version of a channeltron. For an improved electron impact rate, the channels are tilted towards the face normals by an angle of 12° , for instance. The amplification can be increased by stacking up two ('Chevron' configuration) or more ('Z-stack') MCPs. However, the expected power law for the total amplification of multiple MCPs cannot be achieved in practice because of channel mismatching and saturation effects.

An amplified electron pulse is confined within a channel, so spatially resolved amplification is gained. In advance, the pulses are accelerated towards a fluorescent screen which converts the electrons into visible light. The resulting image is recorded by a low-noise CCD camera. Dedicated software is used for a virtual segmentation of the detector area into energy and angular channels such that real multi-channel detection is possible.

For a segmented CCD-Detector, the area covered by a single virtual channel can be considered as the exit slit, so its size can be inserted into equation 4.1 when calculating the energy resolution of this setup.

Ultra-high vacuum (UHV) conditions are required for experiments involving the detection technique discussed here. For the analyzer, vacuum is obligatory to grant a large mean free path of the electrons as ballistic transport is required. If the components of the detector unit would not be operated in vacuum, the applied high voltage would lead to electrical breakdowns resulting in the destruction of the detector. The MCPs and the screen are thus kept inside the vacuum system and the screen image is acquired from outside the vacuum chamber through a window.

4.2. PHOIBOS analyzer and detection system

While the preceding section dealt with general detection techniques for photoelectron spectroscopy, the actual implementation of the experimental setup will be discussed here. The detection components and the radiation source are supplied by SPECS, a commercial manufacturer of surface science equipment.

The electron analyzer model is a PHOIBOS 150, with a hemispherical layout as described in the previous section. Its inner and outer hemisphere has radii of $S_1 = 112.5\text{ mm}$ and $S_2 = 187.5\text{ mm}$, giving a mean radius $S = 150\text{ mm}$. The electron lens system is designed for a working distance of 40 mm and is enveloped by a cone with 44° opening angle, so only a small fraction of the half-space above the sample surface is occupied, leaving much space for the excitation light source and auxiliary components

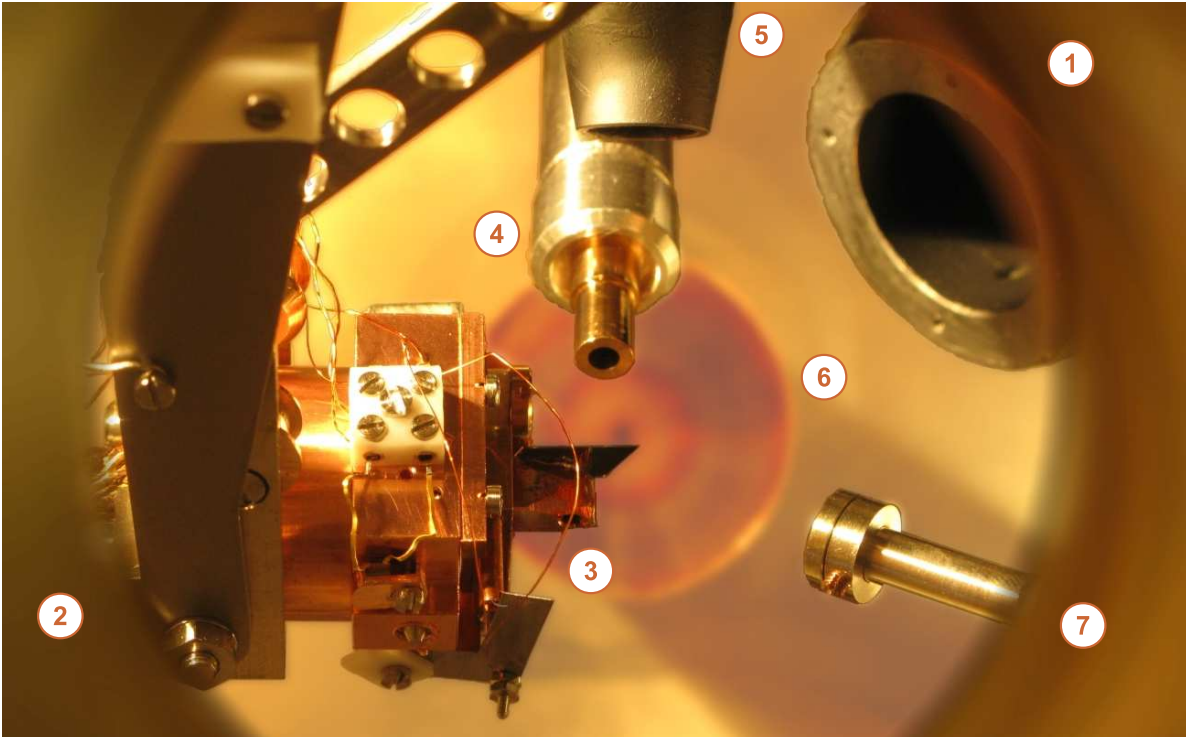


Figure 4.3.: Interior view of the main chamber of the ARPES setup including the PHOIBOS 150 electron analyzer. The photograph illustrates the state of the experiment during the measurements carried out in spring 2009. The sample holder does not carry an actual sample, whose surface normal would point to the right in the image. The numbered components are (1) Opening of electron analyzer, (2) Manipulator head, (3) Sample holder, (4) Focussing capillary of the XUV source, (5) Tip of the beam guide (chapter 5), (6) Evaporator for organic molecules (background, Ref. [72]), (7) Tip of optical fiber (Ref. [72]).

for various techniques as can be seen in figure 4.3.

Different modes of operation are possible for the electron imaging system, giving the non-energy dispersive analyzer direction either angular or spatial dispersion. Additional modes achieve optimal transmission for given areas of photoelectrons emerging. Besides well-defined retardation of electrons, the optics' purpose is to image the sample surface to the entrance slit of the hemispherical capacitor. The entrance slit can be chosen from a set of fixed slit apertures with width ranging between 0.2 mm and 7 mm . In angular dispersive lens modes, the acceptance angle of the analyzer can be tuned continuously using an iris aperture located in the plane of an intermediate image in the lens system. The electron analyzer is designed for UPS and XPS measurements, covering a wide range of kinetic energy of the particles between $\approx 10 \text{ eV}$ and up to the low keV range.

4. Experimental setup

This requires precise adjustment of lens and analyzer voltages over a vast range. To ensure this, the analyzer voltage supply is equipped with specialized digital-to-analog converters for voltages between 0 V and a maximum of 40, 400, 1500, and 3500 V.

Amplification of photoelectrons in the detection unit is performed by two MCPs in a Chevron configuration. They are provided by the tectra GmbH (Serial number DB8056002-33). The high quality level 'imaging grade' is required for spectroscopic applications, and especially the low lateral variance of the gain factor is crucial. Tectra states a gain factor of $\approx 1.9 \cdot 10^4$ at the maximum operation voltage of 1000 V. An outer diameter of 50 mm of the substrate and a minimum active diameter of 40 mm are specified for the MCPs. All other specifications roughly match the values given in the previous section.

The conversion of charge pulses to light pulses is realized by a luminescent screen. It basically consists of a glass substrate and an active phosphor layer of about 100 μm thickness. Different compositions of the active substance are known for special applications, differing in typical properties such as light emission and temporal behavior. The specimen used here was manufactured by Proxitronic and follows the P43-phosphor specification, for which light emission in the spectral range $\lambda = 360 \text{ nm}$ to $\lambda = 680 \text{ nm}$ is found. The maximum is reported at $\lambda = 545 \text{ nm}$, giving the overall emission a green color. Another important characteristic of a phosphor screen is its decay time, i.e., the time constant of light emission falling off after impact of a charge pulse. For a P43 screen, a decay time of 1 ms from 90% to 10% intensity is reported. Considerably faster coatings can be found, but a trade-off between speed, emitted spectrum and quantum efficiency has to be found. Basically, the major emission of the screen should be adapted as good as possible to the spectral sensitivity of the CCD detector.

The 'Sensicam qe' manufactured by PCO serves as detector for the luminescent light. It is based on a 2/3" monochrome CCD detector with 1376×1040 pixels. For noise reduction, the detector is automatically cooled down to a constant operating temperature of -12°C . Intensity information is acquired at 12-Bit precision with $< 1\%$ non-linearity and excellent dark noise level. The maximum of the spectral sensitivity is located at $\lambda = 520 \text{ nm}$, so a fairly good match with the maximum of spectral emissivity of the phosphor screen is given. The maximum quantum efficiency amounts to $\approx 60\%$ at this wavelength. The camera can be operated with variable frame rate and exposure times up to infinity, making it best-suited even for low intensity measurements. All data cited here originate from the data sheet appended to the camera manual [73].

A typical signal obtained from the detector system introduced here is shown in figure 4.4. It demonstrates parallel detection of photoelectrons emitted in an interval of kinetic energy and at angles of $\pm 13^{\text{circ}}$ against the sample normal of a WSe_2 -sample. The excitation source used here is described below.

The experiment was designed for and has successfully been operated at different soft X-Ray sources like beamline BW3 at HASYLAB or beamline PG2 at FLASH, both located at DESY, Hamburg. For laboratory applications, the plasma discharge lamp SPECS UVS300 is available. In the lamp, ultraviolet radiation is produced by a plasma

discharge that is established when electrons emerging from thermionic emission at the cathode are accelerated towards the anode by an electric field in a rare gas atmosphere. The manufacturer recommends the lamp for operation with Helium, Neon, Argon, or molecular hydrogen (H_2).

During this work, Helium was chosen as process gas, giving high-flux, nearly monochromatic emission from the $He I_\alpha$ line at a photon energy of $h\nu = 21.22 eV$. Typical operational parameters were a He partial pressure of $\approx 4 \cdot 10^{-5} mbar$ and a cathode heating current of 1.5 A. Under these conditions, SPECS states a photon flux in the range of $10^{15} (s \cdot sr)^{-1}$. Light emitted by the $He I_\alpha$ transition is best-suited for photoemission experiments as it has a very small natural line width of just a few meV for the operating parameters used here. For a pure $He I_\alpha$ -spectrum, the contribution of the spectral width of the UV radiation to the total energy resolution of the photoemission setup can be ignored here.

In practice, a small emission from the $He I_\beta$ satellite and from atomic transitions of non-Helium atoms in the discharge section of the lamp are observed. These undesired spectral components cannot be ignored in general. When the lamp is driven with Helium partial pressure considerably below $3.5 \cdot 10^{-5} mbar$, an enhanced emission of $He II$ -line with photon energy $h\nu = 40.8 eV$ results, which can also be exploited for photoemission measurements, as a noteworthy fraction of the $He I$ photon flux can be achieved.

As an optional extension, the UV source is completed by the plane-grating monochromator SPECS TMM 302. It is designed for high transmission of the photon energy range between 41.2 eV (30 nm) and 5.1eV (240 nm). Because of the quite low energy resolution of $E/\Delta E \approx 70$, it should rather be seen as kind of energy filter than as a full-featured monochromator. At least, experience gives the strong suspicion that the real resolution is even worse than the value suggested by SPECS. The monochromator will not contribute to generating a narrow excitation line, as it already consists of rather discrete spectral components. Anyway, as it comes to the suppression of undesired spectral components, it performs satisfactorily. When working with the $He II$ line, this capability is crucial to suppress the $He I$ -line, which dominates the emission spectrum under all circumstances.

Here, a substantial drawback of the monochromator design could be revealed: Referring to the documentation, the monochromator can be adjusted for transmission of the second to the fourth diffraction order of $He I_\alpha$ radiation. First of all, this contradicts the claim for optimal transmission, as the intensity of higher diffraction orders decays with the order. Second, even higher diffraction orders are required for $He II$ -radiation to be transmitted in such a setup. When trying to adjust the monochromator for maximum transmission of $He II$ at minimum transmission of $He I$, it is found that the monochromator is not capable of separating $He II$ orders $m = 4, 6, 8, \dots$ from $He I$ orders $n = 2, 3, 4, \dots$ as these are found relatively close to each other. An acceptable separation could also not be achieved for the remaining odd diffraction orders m , which presumably show sufficient coincidence with transmission of higher diffraction orders of $He I_\beta$ radiation with photon energy $h\nu \approx 23 eV$. Because of the fundamental difficulties

faced here, the experiments were carried out with exclusive usage of $He I_\alpha$ at the second diffraction order of the monochromator.

The monochromatized UV radiation is guided into the main chamber through a capillary. Its small cross section gives a good insulation of the vacuum in the main chamber to He escaping from the discharge section of the lamp. Whereas the pressure in the monochromator is typically in the 10^{-7} mbar regime during lamp operation, the pressure in the main chamber clearly remains below $1 \cdot 10^{-9}$ mbar. The capillary inner surface has an ellipsoidal shape and reflective coating. The aim of this measure is to provide a small focus at the sample position, i.e. in the working distance of 10 mm from the end of the capillary. For the needs in the actual setup, an extra-ordinary monochromator-to-sample distance of 594 mm was specified, so an elongated layout of the capillary needed to be installed here. The theoretical focus diameter of 50 μm (which was revised later to 500 μm by the manufacturer) was to be verified experimentally. Experiments done with this intention are discussed in appendix A. In summary, no focussing could be demonstrated at all, and the beam diameter amounts to constant 1.7 ± 0.2 mm, independent from the distance from the capillary.

Figure 4.3 shows the general arrangement of all components described above in the main vacuum chamber of the experiment. The manipulator cryostat is mounted vertically with the sample holder located at the center of the chamber. The analyzer is mounted horizontally such that the center trajectory of transmitted electrons is found in the experiment's horizontal plane. Therefore, energy dispersion is found in the horizontal direction in the exit plane of the analyzer, whereas the angular dispersive direction is vertical. Defined by the layout of the main chamber, the analyzer points at the geometrical center of the chamber so that a sample located there is located exactly at working distance of the analyzer. The angle of incidence of the UV radiation amounts to 45° towards the analyzer mount as can be seen from the end of the focusing capillary. The He lamp setup including the monochromator is mounted to an individually movable chassis such that the beam can be directed precisely to match the analyzer focus. Positioned above the end of the capillary at an elevation angle of 45° , the end of the beam guide for the auxiliary light source is found, giving a total angle of 60° towards the axis of the analyzer flange. At the current stage of expansion, some more components used for the in situ preparation of molecular thin films [72] can be seen in the figure, which will not be discussed here.

4.3. The experimental station for ARPES experiments

The preceding sections discussed basic experimental hardware for photoemission spectroscopy as it is applied in the setup. Here, some more features of the experiment will be introduced.

Precise positioning of the sample is required for successful operation of a photoemission experiment. The main task is proper alignment of the sample surface in the center

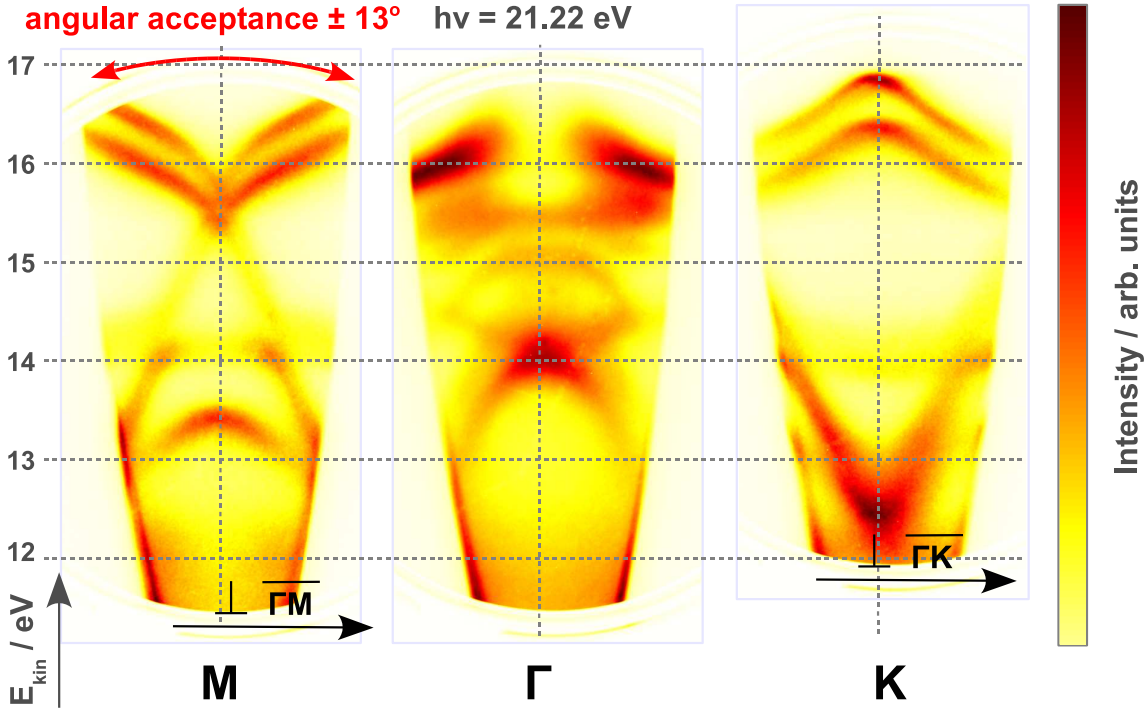


Figure 4.4.: Raw data image as acquired with the PHOIBOS 150 system using the *UVS300* He lamp with monochromator. The signal originates from a *WSe₂* sample at different mean emission angles (center: normal emission), representing high-symmetric points of the Brillouin zone (see chapter 2). Settings: $h\nu = 21.22 \text{ eV}$, $E_{\text{pass}} = 40 \text{ eV}$, Analyzer Slit No. 2 (width 0.5 mm , length 20 mm), Wide Angle Mode (WAM, accepted angles $\pm 13^\circ$) [74].

of the UHV chamber to grant best photoelectron transmission in the analyzer and to exclusively illuminate the sample surface with UV light in order to suppress undesired emission from surrounding parts as, for instance, the sample holder. For this purpose, the sample holder is mounted to a VG manipulator cryostat that is capable of positioning the sample inside the chamber with full six degrees of freedom, i.e., three-axis translation combined with rotation about the sample surface normal and the experiment's up axis as well as a tilt about a horizontal axis. The manipulator head is designed to have good thermal contact to the built-in cryostat that is specified for operation with liquid nitrogen for sample cooling down to $90 - 100 \text{ K}$. The minimum achievable temperature with liquid nitrogen cooling of 77 K is easily achieved for the cooling head, but cannot be conducted to the sample holder as this is contacted by some centimeters of copper cord to the sample holder. Lower temperatures can be achieved optionally by driving the cryostat with liquid He. Temperature monitoring is performed by two resistive probes (PT100 resistors), located at the cooling head and at the sample holder. Both are

4. Experimental setup

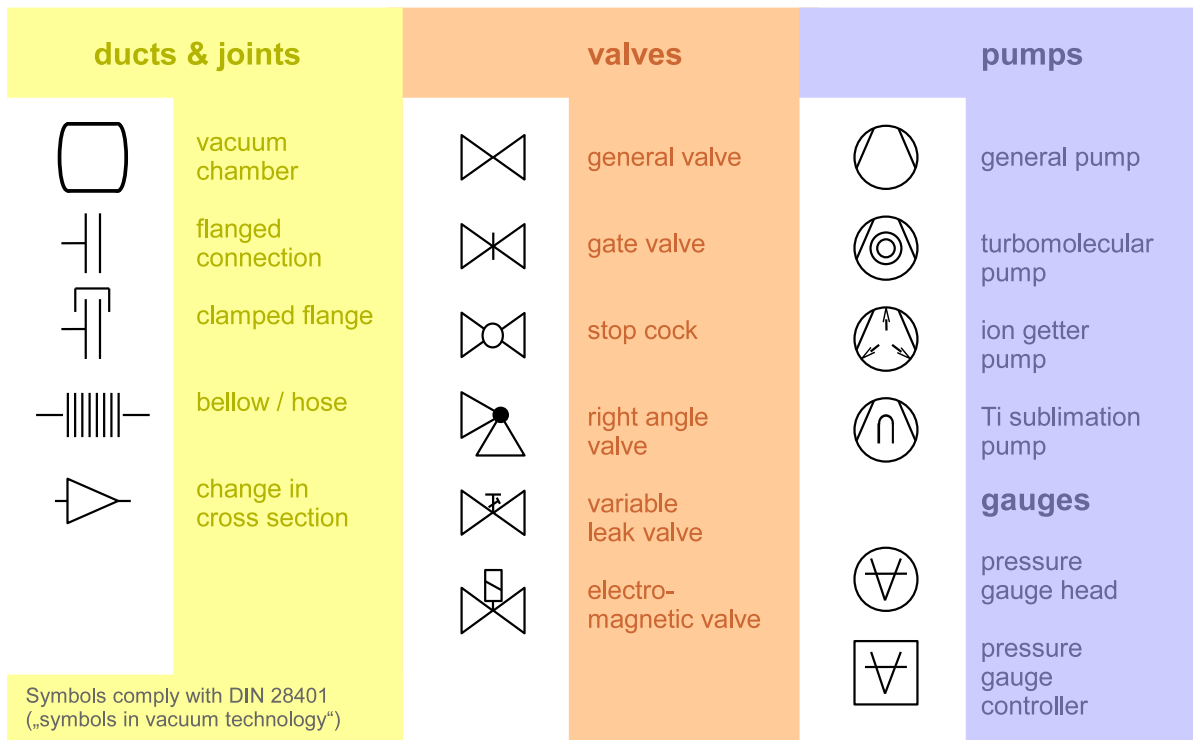


Figure 4.5.: Standard symbols used in vacuum technology (excerpt) as defined in *DIN28401* (Ref. [75]).

read out simultaneous by a *Scientific Instruments Model 9700* temperature controller. The device is also capable of controlling the integrated counter-heating of the cryostat, achieving stable temperature setpoints up to 350 K.

The manipulator is equipped with an insulated conduct that can be contacted by specialized sample holders. Usually, the photoemission current emerging from the sample is probed with this line in order to provide flux monitoring of the excitation source. In this work, it was also used in alternative applications where an electrical conduct is required, such as in situ beam characterization applying a photodiode (chapter 5.6 and appendix A).

Photoemission spectroscopy is a surface-sensitive technique that must be carried out in ultra-high vacuum. One reason has already been stated when discussing the analyzer hardware: The components of the detector can only be operated in vacuum. Furthermore, ballistic flight of the photoelectrons with long mean free path is crucial for the analyzer to work. The main reason concerns the samples. Unbiased information on the sample surface can only be gained as long as no significant contamination by adsorbed residual gas atoms is found on the surface. It is well-known that a pressure as low as the 10^{-10} mbar regime is prerequisites in order to retain clean surfaces for typically some hours to some days of measurements. As a consequence, the complete system, starting

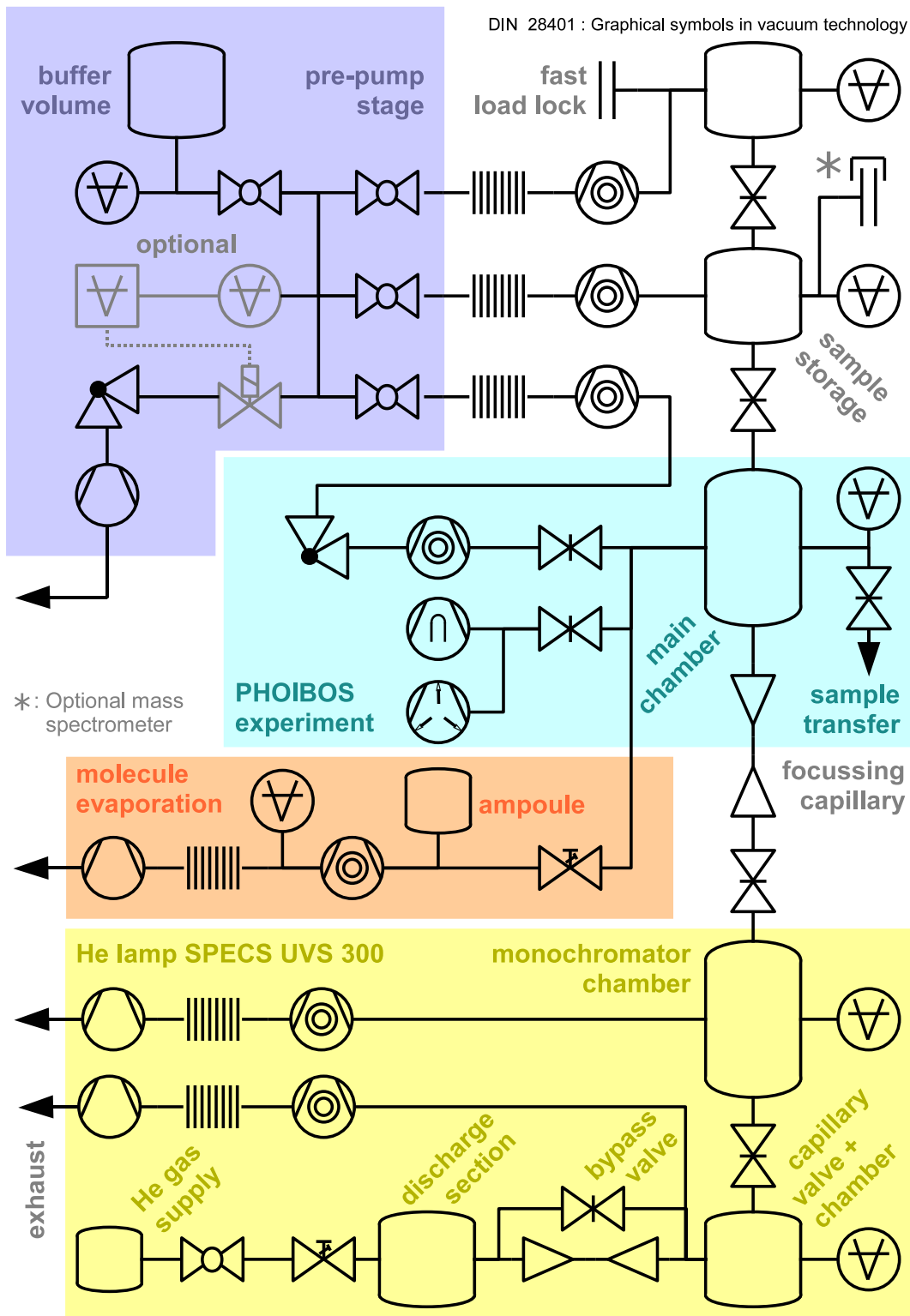


Figure 4.6.: Chart of the vacuum system for the PHOIBOS experiment.

4. Experimental setup

with the sample cleaving stage, must be kept under constant ultra-high vacuum.

Figure 4.6 shows a schematic of the vacuum environment, including all components of the experimental setup. All included symbols comply with *DIN 28401*, 'Symbols in vacuum technology'. An excerpt of that standard is shown in figure 4.5. The shaded box in the center of the figure contains the components that are mounted directly to the main chamber. Vacuum is kept up by three complementary types of pumps: A turbomolecular pump is used to pump down the chamber before and during bake-out. For operational safety, the upstream valve is closed during operation and pumping is performed by an ion getter pump and a titanium sublimation pump with cooling option. Using this setup, a base pressure between $3 \cdot 10^{-10}$ mbar and $5 \cdot 10^{-10}$ mbar is achieved. The molecular evaporation section (shaded red) used in [72] is implemented as a separate subsystem that can be operated independently from of the main chamber.

The yellow shaded section depicts the separate vacuum system of the UV source and monochromator as designed by SPECS. Gas supply ducts have been incorporated. The diagram depicts the lamp and its attached components as can be derived from the user's manual, though no precise layout is given there.

Some extra chambers are required for transferring samples into the system and preparation. Here, a fast load lock chamber with small volume is used to transfer up to three samples at once into the experiment without the need of bake-out. A sample storage chamber also serves as a buffer between the main chamber and the relative high pressure found in the load lock. When avoiding frequent sample transfer, the base pressure in the storage section is as good as in the main chamber, so samples can be cleaved or stored here. This allows for working with different samples sequentially, which is especially advantageous in a multi-user environment.

Prevacuum is provided to the experiment by a dedicated roughing pump stage (shaded blue in the figure), that is designed to work with several turbomolecular pumps. All connections between roughing pump and recipients can be interrupted by stop cocks separately, so venting a single section of the setup does not affect the rest. This is exploited when using the fast load lock stage. The vacuum system was designed that way in order to minimize the total number of roughing pumps in the lab, such that mechanical vibrations are reduced to a minimum level. This is especially important for the application of sensitive optical arrangements like the optical bench setup described in section 5.5. Integrating the roughing pumps of the UV source into the roughing pump stage design is not feasible with the current layout. Experience shows that these pumps have a large Helium gas ballast during operation of the Helium lamp, as the discharge section is flooded with a Helium partial pressure of up to $1 \cdot 10^{-4}$ mbar then. When integrated into the pumping stage, the Helium could reach the experimental chambers via the prevacuum ducts, degrading the total gas pressure there.

The photoemission experiment is integrated in the lab environment of the workgroup by a connection to the central sample transport pipe. This gives full access to all supplementary experimental techniques that are driven in the lab, among them LEED, STM, and inverse photoemission (IPES) as well as several sample preparation stages.

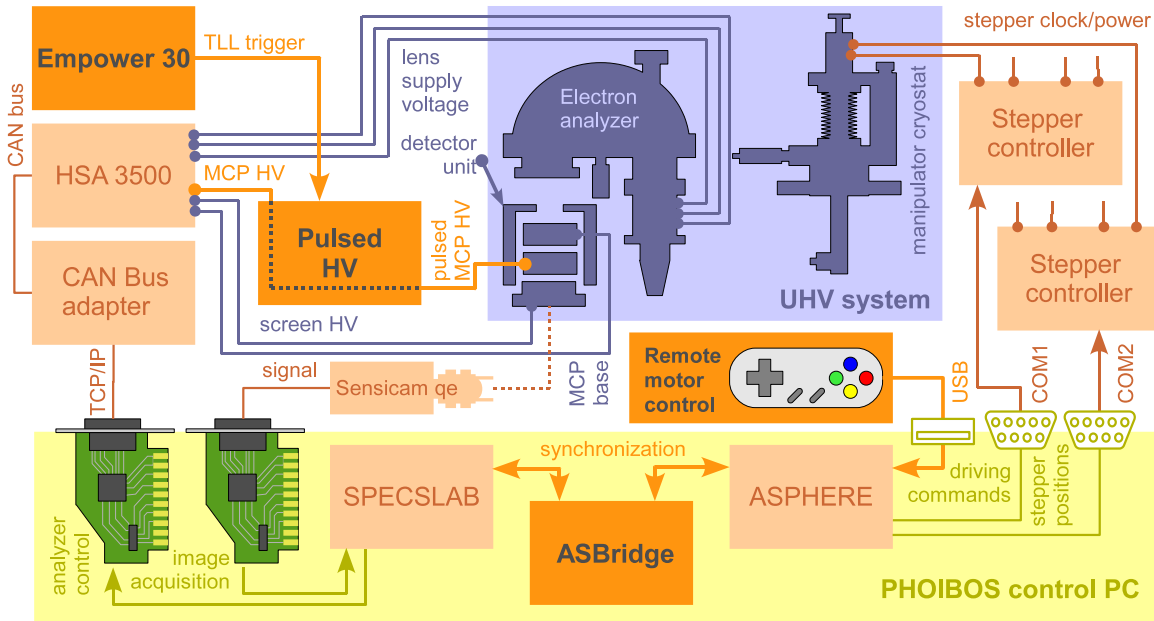


Figure 4.7.: Wiring diagram of all hardware and software components involved in the data acquisition process. Details are presented in the text. New features that have been implemented during this work are highlighted (bright orange boxes).

The closed UHV system connecting all experimental stations through the central transfer pipe allows for combined measurements using a single sample.

4.4. Extensions to the setup

The basic components of the photoemission setup have been discussed above. During this work, various expansions were made in order to customize the experiment for the surface photovoltage measurements and to establish some more experimental options. At the same time, the system was upgraded for experiments with molecular thin films [72], so special care had to be taken that none of the new and old components interfere. Most of the new features are directly relevant to this work, some give general support and have been applied in different related photoemission experiments, as presented in [72],[76]. Here, all new features shall only be introduced briefly. For comprehensive documentation, most of the topics are covered in dedicated appendices. To give an impression of all components that are involved in a measuring process, figure 4.7 shows a general wiring diagram of the experiment. Current upgrades are highlighted.

- **Combined scanning and manipulator motion**

In the actual photoemission experiment, the electron analyzer is mounted at a fixed position. For angular resolved studies, full access to the half space above the sample surface is required. This can be achieved by rotating the sample relative to the analyzer using the degrees of freedom provided by the sample manipulator. For k-space mapping, spectra at equidistant angular steps must be taken. In order to automate the measuring process, combined motorized motion of several manipulator axes is crucial. While the rotational axes were equipped with stepper motors by the manufacturer, the translational ones were not, so an upgrade was designed. All motors are controlled by stepper motor drivers developed in the workgroup and are therefore accessible via the automated data acquisition software ASPHERE [53]. Manual operation of these axes is not degraded hereby as the motors actuate the existing micrometer screws. The distance per motor step was calibrated for each manipulator axis and the mechanical performance of the setup was tested excessively during this work. Small backlash was revealed for all axes, but showed up to be within an acceptable range. The calibration results are listed in the table in figure 4.8.

- **Linking SPEC SLAB to ASPHERE**

Photoemission spectra are usually acquired using SPEC SLAB, a specialized integrated analyzer hardware driving and data acquisition tool provided by SPECS. A comfortable solution to scanning the manipulator is given by ASPHERE, which, among other features, allows for scripting motor positions. For combined angular scanning by the motorized manipulator and data recording, synchronized action of both applications has to be granted. For this purpose, a dedicated software module was developed in this work. A detailed description can be found in appendix G.

- **Remote operation of the manipulator**

Manual operation of the manipulator is often complicated by the dimensions of the experimental setup, so that most of the turning knobs and micrometer screws are not easy to access. Once the manipulator is equipped with stepper motors, all degrees of freedom can also be operated remotely. For easy direct access to the manipulator position, a commercial gaming joypad was integrated into the ASPHERE framework such that all motors can be operated from arbitrary locations in the lab. Another software module allows for real-time readout and precise input of motor positions. Both are discussed in detail in appendix F.

- **Rb evaporation**

In this work, Rubidium is deposited on crystal surfaces. For this purpose, a UHV evaporation source had to be implemented and integrated into the experiment. The *Rb* is evaporated from a commercial *SAES Getters Rb* dispenser. The applied Ohmic heating current is dosed to give a defined, reproducible flux. During the actual experiments, constant steps of *Rb* coverage on a surface were achieved by

driving the dispenser with defined current for a fixed time and at a defined distance from the sample surface. The heating current is provided by a standard lab power supply, extended by the option for remote PC controlled operation. The software module developed to run the supply is documented in appendix J.

- **Powerful laser light supply for the ARPES lab**

In cooperation with the workgroup of Prof. Bauer, the experiment is planned to be driven with an ultrafast higher-harmonic-generation laser excitation source ([77],[78]). With this intention, a commercial high-power $Nd : YLF$ laser was purchased to serve as seeding laser. This laser source might also be used as an additional light source for conventional photoemission, opening up various options for sample treatment with high-power laser pulses. As the laser is set up in the neighboring laser laboratory, a long-range beam guide based on a high-power optical fiber needed to be constructed in order to provide laser light to the PHOIBOS setup. Constructional details on this topic are found in appendix E.

- **Triggered MCP operation**

When operating pulsed sources in general, triggered operation of the photoelectron detector is desirable to suppress unwanted inter-pulse noise or to establish kind of rough temporal selectivity of the signal. An approach to supply this new feature to the photoemission experiment is presented in appendix D. Some technical difficulties faced here might be avoided by the implemented design, but a general demonstration of feasibility is still subject to future work.

The upgrades realized here basically enable two measuring modes for angular resolved photoemission. The principle drawings in figure 4.9 show how the k-space is scanned using these modes. The first one is based on a sample alignment providing that the Γ -point of the first Brillouin zone, i.e., emission perpendicular from the sample surface, is projected to the center of the detector. All angular channels detected in parallel are arranged on a radial section through the Brillouin zone and centered around the Γ -point. By rotation about the sample normal, a distinct high-symmetric direction such as $\overline{\Gamma M}$ or $\overline{\Gamma K}$ may be adjusted. Stepwise rotation about the up axis of the manipulator is used in advance to scan a two-dimensional equidistant grid on the hemisphere over the sample surface, gathering a stripe through the Brillouin zone.

In principle, this technique could be used to cover the full polar angle of $\pm 90^\circ$ over the sample in scanning direction, if the sample could be illuminated in all orientations. The 'width' of the stripe is limited by the acceptance angle of the analyzer. Thus, only a constrained area around the Γ -point can be covered in that direction. The angle between emission from the Γ -point and the high-symmetric points M and K and the border of the Brillouin zone (as depicted in figure 4.9) is defined by the photon energy and the lattice constants of the crystal structure. For typical lattice constants found for transition metal dichalcogenides and an excitation source with photon energy of 21.22 eV , it can easily be seen that the maximum acceptance angle of the analyzer of $\pm 13^\circ$ is not sufficient

4. Experimental setup

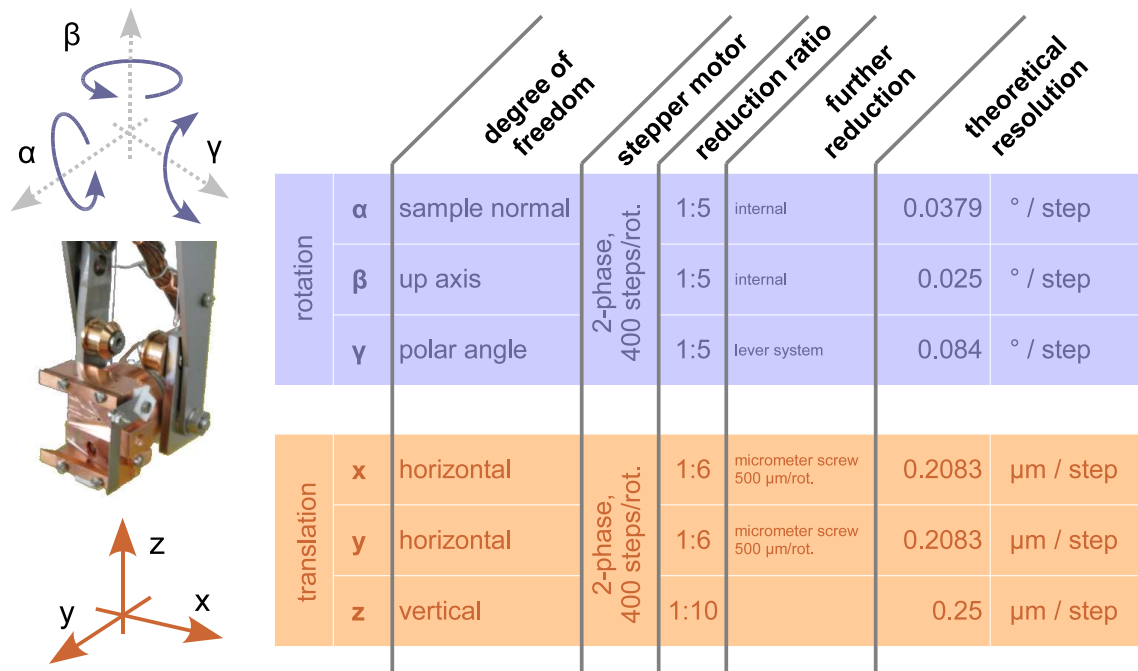


Figure 4.8.: Step size calibration of the stepper motors driving the axes of the manipulator cryostat. All degrees of freedom are illustrated to the left using the vacuum side of the sample manipulator as reference.

to cover the full Brillouin zone in one sweep. Combining scans at different polar angle γ (see fig 4.8) are not feasible with this geometry, because it is constrained to a small range between $\approx -10^\circ$ to $\approx +15^\circ$ relative to the horizontal by specification.

Substantial drawbacks of this mode are caused by the varying angle of incidence of the UV light. Combined effects of finite penetration depth of the light and finite escape depth of the photoelectrons makes spectra taken at different angles of incidence of the light hardly comparable. At finite beam diameter, the total illuminated area on the sample surface varies significantly, so the emission signal does not originate from a constant surface region over one sweep. Combining radial sweeps taken at different angle α (figure 4.8) might be combined to cover the complete Brillouin zone, creating a large overhead of data points near the emission at the Γ -point. The problem is worsened by a constructional fault of the manipulator: The sample surface cannot be aligned in the center of the up-axis rotation, so its position must be kept constant by additional translation when scanning. As ASPHERE allows only for linear tracking, this measure is limited to an approximate correction of the sample position.

Furthermore, the signal-to-background ratio of the photoelectrons is influenced by a change in the experimental geometry. This complicates quantitative analysis of data

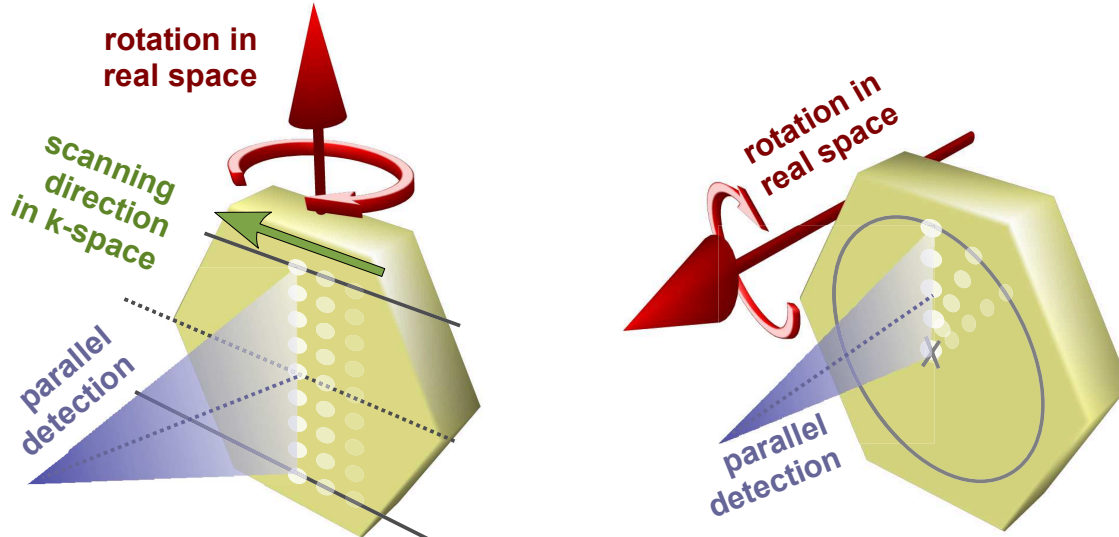


Figure 4.9.: Two-dimensional mapping of angular channels can be achieved using the shown scanning modes. **Left:** As the up axis of the manipulator is rotated between subsequent spectra, a stripe of the k-space gets covered. **Right:** Rotation about the sample normal axis gives access to a circular area around the Γ -point.

acquired using this mode. Nevertheless, as long as the user is aware of these limitations, the mode can be applied successfully. The valence band map depicted in figure 4.10 was acquired using this mode. The surface shown there represents the evolution of the valence band maximum of WSe_2 inside the first Brillouin zone. The raw data consists of two sweeps along the $\overline{\Gamma K}$ and the $\overline{\Gamma M}$ direction, respectively. Where both scans overlap, each of the two data sets was truncated to cover a wedge-shaped area with an opening angle of 15° at the Γ -point. The full Brillouin zone was reconstructed by repeating the wedges periodically, so every of the six equivalent high symmetric points K and M is found in the result. Some more sample data based on the scanning technique introduced before can be found in [76].

Some of the difficulties faced here can be circumvented by using the scan mode depicted right in figure 4.9. In this arrangement, the sample is tilted such that a radial section through the Brillouin zone starting at the Γ -point is detected in parallel. Then, the half-space over the sample surface is scanned by rotation about the normal angle α . Once again, the maximum polar angle detected with this method is limited by the maximum

Tungsten Diselenide (WSe_2)

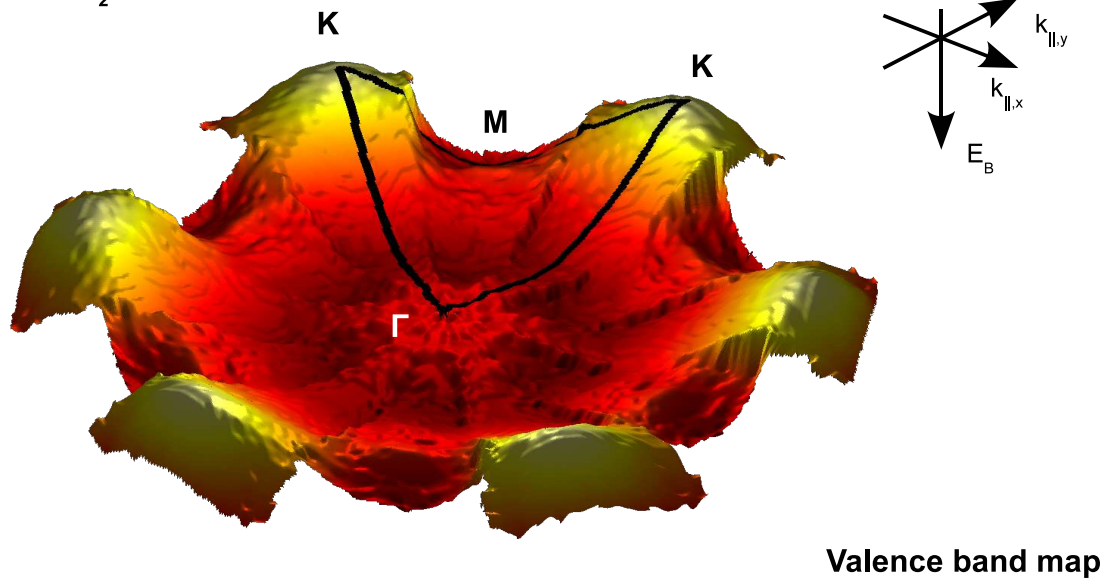


Figure 4.10.: Angular resolved study of the valence band of WSe_2 , recorded with PHOIBOS. The surface depicts the evolution of the valence band inside the first Brillouin zone. Points of high symmetry are highlighted. The data was assembled from two overlapping sweeps in $\overline{\Gamma K}$ - and $\overline{\Gamma M}$ - direction as depicted left in figure 4.9. The sweeps were recorded using a total acceptance angle of $\pm 13^\circ$ ('Wide Angle Mode'), 27 angular channels, scanning step size $\beta = 0.5^\circ$ (see fig. 4.8), $h\nu = 21.22 \text{ eV}$.

acceptance angle of the analyzer. None of the outer high-symmetry points can be probed in parallel with the Γ -point using the actual setup, so this mode shows up to be better suited for higher photon energy, where the Brillouin zone is found to cover a significant smaller solid angle. In general, such a scan could be combined with another taken at higher tilt angle to cover the full Brillouin zone. In practice, this approach is denied by the limited tilt angle γ . Once again, the grid scanned using this scanning mode has an extremely inhomogeneous distribution of points with a high accumulation near normal emission, so a large amount of redundant data is acquired. The advantage of this scanning mode can be seen in the constant angle of incidence of the radiation. As long as the beam is aligned to hit the sample at the center of rotation, emission from a constant surface area is granted, avoiding the elaborate tracking procedure. Unfortunately, the implementation of the rotary feedthrough does not guarantee continuous motion of the surface normal rotation under all circumstances. When applying this mode, a feedback

of the rotation angle is required.

Involving the new features that have been realized during this work, some more interesting applications are possible.

The motorized translation stage of the manipulator allows for various scanning modes. When using a small excitation source as provided by a microfocus beamline or upcoming higher-harmonic-generation laser sources, a primitive imaging of the sample surface can be achieved by scanning the focus of the radiation along the surface. Many applications require precise knowledge of beam dimensions achieved in the vacuum chamber. In combination with a specialized sample holder, calibration of various beam properties was performed in this work. In appendix A, some results obtained from scanning the UV beam are discussed. Characterization of the performance of an optical feedthrough system using this technique is done in the subsequent chapter.

The extensions of the experimental station presented here have been applied with great success during this work, and some more users could already benefit from the additional options. The general design showed up to be extremely versatile with respect to individual requirements, as proven by a variety of experiments carried out at this setup during the past years. At the current state, the full potential of automated ARPES measurements can be exploited, so finally, it can be considered complete and ready to be combined with modern high-end light sources.

5. Design of a beam guide for auxiliary light sources

5.1. Introduction

In the preceding chapter, the current state of the experimental station was presented. Special attention was paid to various upgrades that were realized during this work. Here, the approach to integrating an additional light source into the setup is discussed in detail. Probing the surface photovoltage effect by photoemission spectroscopy in situ requires a highly versatile illumination source. The demands for an appropriate optical setup essentially include options of tuning the photon flux, spot diameter and spot position inside the vacuum chamber over a wide range. Small spot diameters in the low micrometer range as achieved with modern synchrotron beamlines must be reached. A perfect match with the XUV or soft X-ray source for photoemission is prerequisites here, so high mechanical stability must be granted.

The design has to be compatible to the UHV conditions met in the main chamber of the experimental setup, so the choice of available materials is restrained. Special construction principles have to be obeyed, especially with respect to avoiding cavities and granting a sufficient pumping cross section. More constraints arise from the demand for full compatibility to the photoelectron spectrometer. First, the free path between sample surface and analyzer entrance must not be blocked. Second, the space between the sample and the analyzer must remain free of electric and magnetic fields in order to avoid biased electron trajectories.

The specification of a small focus requires a lens with the smallest feasible focal length, so that it can be located as close as possible to the sample surface. Here, the design is affected by further limitations: In a vacuum environment with free electrons, the electrical insulating glass surface of a lens tends to accumulating fixed negative surface charge. As a rule of thumb, the maximum potential of the lens is given by the maximum kinetic energy of photoelectrons, which is limited by the photon energy $h\nu$ of the excitation source. As a first approach, the lens might get coated with a conductive gold film and grounded hereby, which is a common measure for vacuum windows in a charge sensitive environment. A conductive coating would strongly increase reflection losses, so this concept has to be rejected. Sufficient screening of surface charges might also be achieved using metal meshes that are available with a large range of mesh sizes. The rather low open area ratio and a decrease of imaging performance due to scattering and diffraction

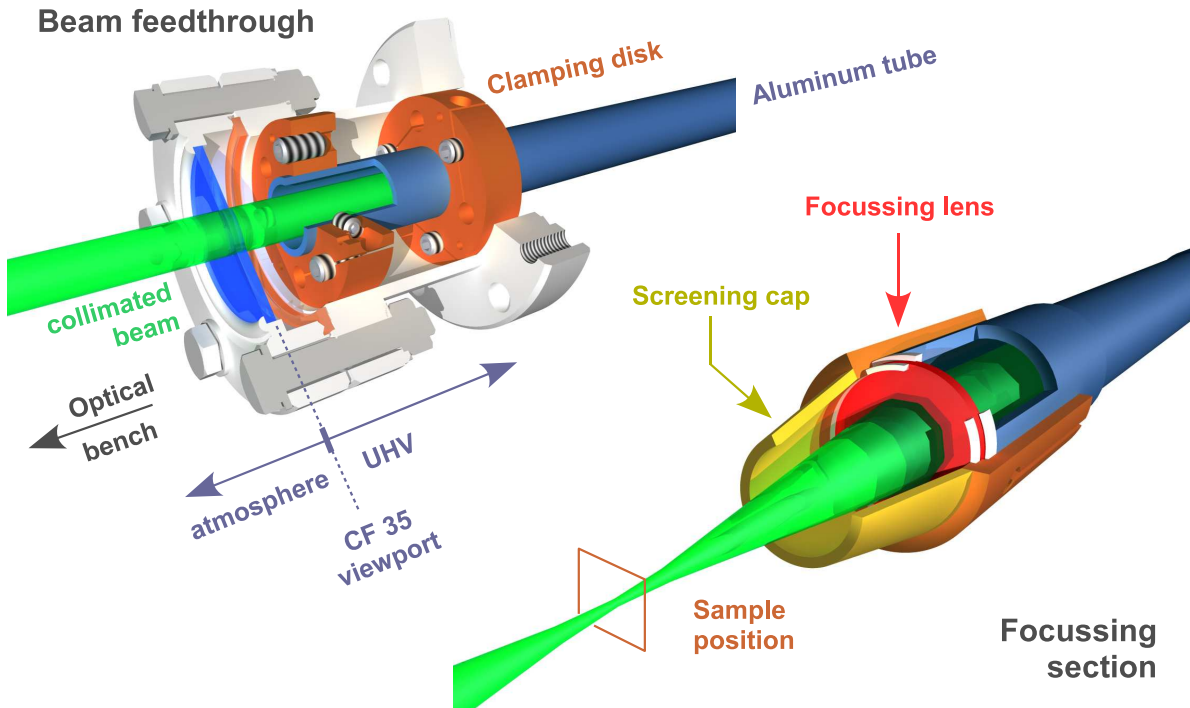


Figure 5.1.: Constructional detail of the beam guide. **Upper left:** vacuum feedthrough of the laser beam and fixation of the aluminum tube. **Lower right:** Assembly at the tip of the tube. Details see text.

would result, so this solution was also discarded. An acceptable approach satisfying the demands for high transmission and good screening will be presented and discussed in section 5.4.

Another competition is found for the mechanical layout of the device, which requires free alignment of the lens and stability at the same time. Only limited space is available inside the vacuum chamber and the lens mount must not interfere with one of the additional components located inside. When setting up the system, much space was consumed by another project integrating in situ molecular thin film deposition in the experiment [72]. Therefore, only a single *CF* 35 flange of the chamber, located approximately 25 *cm* from the chamber's center at an elevation of 45° is occupied by the solution presented here.

5.2. Constructional detail

A satisfactory solution to the task defined above could be realized during this work. Detailed section views of the sensitive parts are shown in figure 5.1. The approach prerequisites a well-collimated light beam that is guided into the vacuum chamber and

then focused onto the sample surface by a plano-convex lens with a focal length of 40 mm. It is made of common borosilicate glass (BK7) and has no anti-reflex coating in order to grant UHV compatibility. The lens-to-sample distance given hereby showed up to be a good tradeoff between good focusing capability and low consumption of space near the sample. The lens is located at the lower end of a radially mounted aluminum tube and the beam is guided through the center of the tube. The outer diameter of the tube amounts to 16 mm at a wall thickness of 1.5 mm. The diameter of the guided beam is thus limited to 13 mm. The specification of a CF 35 mounting flange states a clear inner diameter of the attached pipes of 35 mm, so the pipe can still be translated within a circle of 19 mm diameter along the cross section of the flange. Two PTFE (Teflon) retaining rings constitute an embedding for the lens. The tip assembly is kept in position by a low-tolerance mount that is pressed over the outer tube wall and fixated by radial spreading forces. No screws or pins are required here. The hollow truncated cone at the end of the component was appended later for electrical screening. A detailed discussion follows in section 5.4.

The upper end of the beam guide is depicted in figure 5.1(upper left). It is made of a stub of CF 35 stainless-steel pipe. The window mounted on top acts as vacuum feedthrough for the collimated light beam. Precise centering of the aluminum tube to the inner wall of the steel pipe is achieved by the application of two aluminum clamping disks. The beam guiding tube is fixated by worm screws inside the radial tapped bores. The axial bore holes placed on the tangential slots are equipped with incomplete threads such that screwing results in spreading the slots and bending the outer parts of the clamping disks towards the inner wall of the pipe. All screws applied here are made of full UHV-compatible stainless steel that is known to be hardly magnetic. As the lower end of the beam guide is closed by the lens, the upper end requires a sufficiently large pumping cross section. Special care was taken to avoid virtual leaks in the clamping components. In the end, all vacuum components of the beam guide could be integrated into the system without negative effect on the achieved base pressure. The mechanical stability of the assembly was analyzed in detail using FEM simulation. All results are presented in section 5.3.

The requested option for fine positioning of the light spot inside the vacuum chamber is achieved by a manipulator with three translational axes onto which the combined beam feedthrough and guide section is mounted. It allows for a lateral shift that is only limited by the tube outer diameter, as mentioned above. By its maximum axial translation of ≈ 50 mm, the lens can be completely retracted from the sample holder.

All optical components required for creating and shaping a collimated beam are located outside the vacuum, so easy handling is granted and standard optical systems may be applied here. The actual implementation of the optics will be discussed in section 5.5.

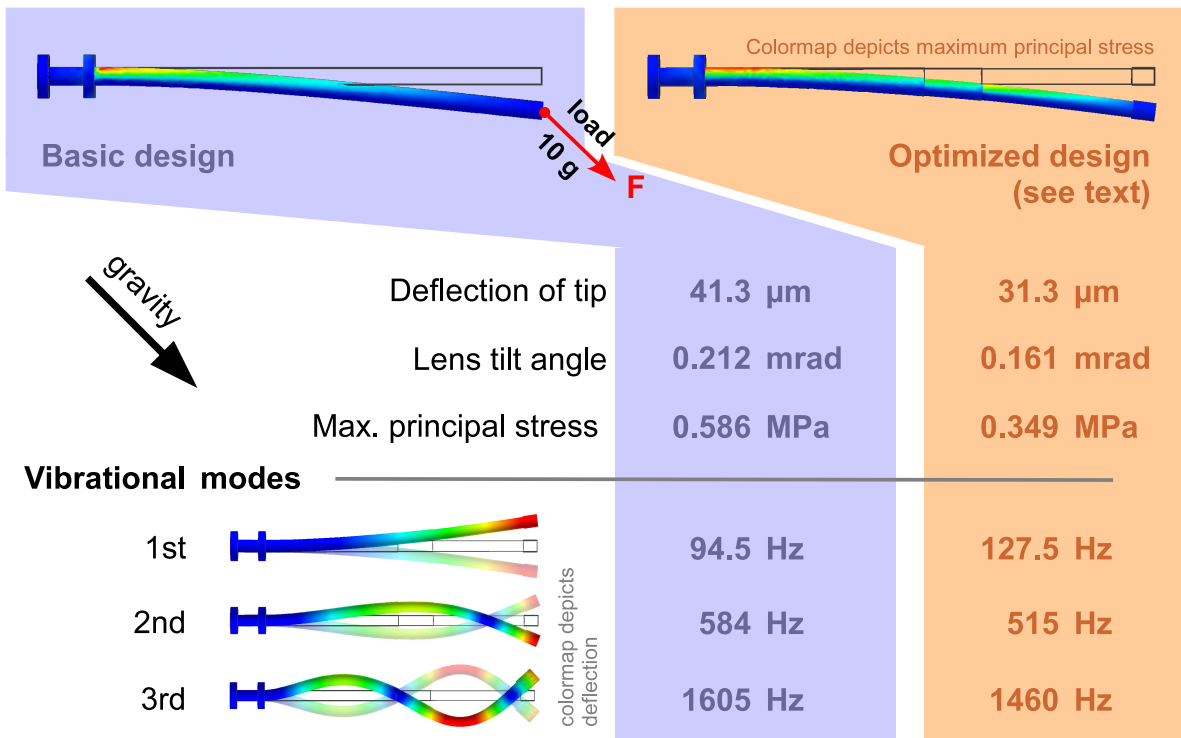


Figure 5.2.: Table of vibrational modes of the beam guide. The optimized design has a reduced wall thickness near the tip. A significant increase of the first vibrational mode results, so resonant excitation by external sources is expected to be less pronounced. A considerable degradation of the optical alignment by static deformation can be excluded for both layouts. The reduction of peak principal stress in the optimized design is expected to reduce long-term plastic deformation of the tube.

5.3. Mechanical stability

The critical part concerning mechanical stability is the aluminum tube used for supporting the focusing lens. Because of the diagonal mounting position, the tube is expected to suffer from self-loaded deformation. This leads to a systematic misalignment of the focusing lens that has to be considered here. A comprehensive stress analysis of the aluminum tube was carried out using the 3D CAD environment *Autodesk Inventor*, which includes a versatile simulation tool for static and dynamic load simulations of a structural part. Static deformation, tension and vibrational modes are determined by using the finite element method (FEM).

The simulations were focused on the most sensitive part, the aluminum tube, in its mounted position. Thus, a solid model integrating the tube and the clamping disks was created in order to provide realistic boundary conditions to the simulation. A

small additional load was applied to the tip of the pipe, simulating the mass of the lens assembly. For the lens mount and the screening cap, masses of 7.25 *g* and 1.57 *g* were determined by the CAD program, and a small contribution by the remaining parts. Altogether, an additional load of 10 *g* is applied here to the tip of the tube. The part was then virtually exposed to gravity, directed as in the realistic mounting position.

The basic design of the beam guide just consists of a tube of the above mentioned dimensions. Its mechanical performance was obtained from simulation and is summarized in the left column of figure 5.2. As could be expected, the static deformation of the tube is found to be acceptable for this purpose. Static deflection is accompanied by a small tilt of the pipe cross section at the tip, so a small angular misalignment of the lens results. Assuming that the deflection can be approximated as a parabolic function of distance from the mount, the tilt angle of the lens is given by the arc tangent of the elevation at the tip:

$$y = \frac{x^2}{\ell^2} \cdot \Delta x,$$

$$\Rightarrow \alpha_{tip} = \arctan 2 \cdot \frac{\Delta x}{\ell}, \quad (5.1)$$

where Δx is the deflection of the tip and ℓ is the distance from the tip to the closest clamping disk, where x equals zero. This expression is explicitly meant to be approximate. When based on a hyperbolic cosine, a prefactor of 1.54 instead of 2 results for the argument of the arc tangent, while a linear dependency gives a factor of 1. The true tilt is expected inside this interval.

The tilt angles in figure 5.2 are obtained when inserting the actual dimensions ($\ell = 390$ *mm*, Δx as stated in the table) into the above equation. Such small angles can easily be tolerated in the setup.

Besides static deformation, the setup was also optimized with respect to its dynamic behavior in the context of an analysis of the vibrational modes of the tube, especially of the low frequency range below 100 *Hz*. This region is of special interest because of the presence of low frequency vibrations in the laboratory environment. These mainly originate from mechanical roughing pumps and also from inevitable human activity near the experiment. Both must be tolerated to some extent. In order to avoid resonance with the beam guide as good as possible, its oscillation frequency should be as high as possible. The analysis of the range between 0 *Hz* and 2000 *Hz* shows that the basic design only has bending modes in this interval. It can be suspected that the first mode found at 94.5 *Hz* is excited by external low-frequency vibrations.

Therefore, the tube design was optimized subject to high-frequency modes. At constant outer dimensions and the given cross section, only the wall thickness can be modified. A considerably higher first vibrational mode is found for the optimized design presented in the right column of figure 5.2. Here, the wall thickness near the free end of the part was reduced to 1 *mm* and 0.5 *mm*, respectively. Near the fixed end, the basic diameter was retained in order to provide maximum stiffness. Due to the optimized

mass distribution along the tube, the maximum deflection is reduced. Mechanical stress is delivered across the full length, reducing the maximum stress that is found near the clamping disk. The color map texture on the parts on top of figure 5.2 indicate the stress distribution by encoding the maximum principal stress, i.e., the maximum principal axis of the stress tensor [79],[80].

Alternative materials were tested to realize the beam guide. Other metals like stainless steel or titanium did not perform much better in the simulations. In addition, a major problem with steel arises from the magnetic remanence

For this work, the optimized tube design was implemented using aluminum. Its simulated performance is found to be sufficient for the application, which is confirmed by calibration measurements carried out with the complete optics system. These experiments are discussed in section 5.6.

5.4. Electrostatic compatibility

As already mentioned, the surface of the glass lens tends to charge by capturing free photoelectrons. The resulting electric field might reach into the space between sample surface and electron analyzer, where it would perturb the trajectories of the free electrons. Charging cannot be suppressed here as the lens must necessarily cover a noteworthy fraction of half-space over the sample and photoelectrons are emitted all over there. In consequence, an efficient concept to suppress long-range electric fields without blocking part of the beam cross section was developed. It simply consists of an extension of the design by a conical aluminum cap that is mounted at the tip of the beam guide (see figure 5.1) and is thus held at ground potential. The charged lens surface causes induced charge of opposite sign in the cap to give a local compensation. Strong reduction of the magnitude of the electric far field with respect to the unscreened arrangement is expected.

This approach was tested by numerical simulations using the *SimION* software by *Scientific Instrument Services*, a software package dedicated to the simulation of electric fields and ion particle trajectories, especially for ion optics. It has been successfully applied to optimization problems concerning design of the electron source for the inverse photoemission technique applied in the workgroup [81]. For a brief summary of the program, see also [82].

For the simulations, a CAD model of the beam guide tip including realistic dimensions was imported into *SimION*. All metal parts, i.e. the tube, fixation parts and the screening cap where set to ground potential, while the lens was assumed to be homogeneously charged to a potential of +10 V. For the following discussion, the sign of charge does not matter, so the fact that the lens would in fact be charged negatively can be neglected here. Two versions of the assembly were tested with these voltage settings: One version without the cap (I) and a second including the cap (II). The resulting potential arrays are shown in figure 5.3. As the complete arrangement is rotational symmetric,

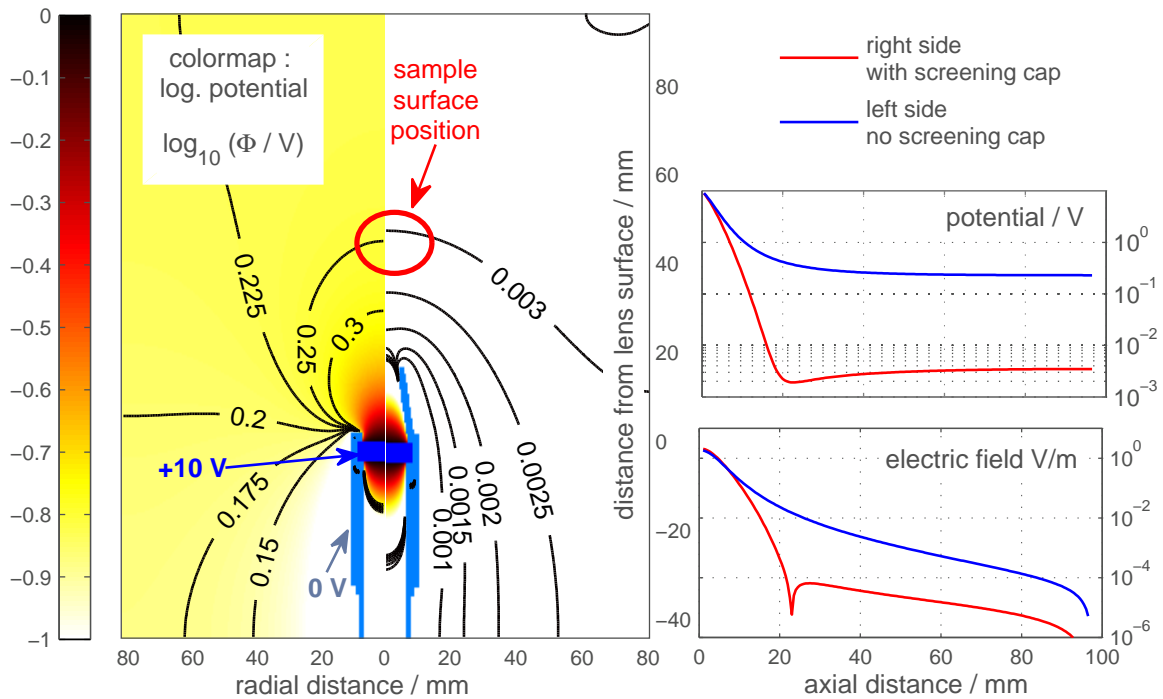


Figure 5.3.: Electrostatic simulation of the tip of the beam guide. The electrostatic far field induced by trapped charges at the lens surface is reduced significantly by the screening cap, so the demand for a field-free space between sample and electron analyzer is satisfied. **Left:** Cross section of the simulated potential distribution with (right half) and without (left half) screening cap. **Right:** Axial electrostatic potential and electric field.

only a radial cross section is shown. The 'electrode' geometry is shown as blue shape. For configuration (I), the suspicion is confirmed that the potential modification by the charged lens cannot be tolerated in photoemission spectroscopy.

This influence is drastically reduced by the screening cap, as can be seen in the right half of the figure. Note that the equipotential lines drawn here belong to much smaller potentials! For a quantitative analysis, the potential along the symmetry axis of the assembly was extracted from the map (inset upper right). The absolute value of the electric field strength was derived from this data by numerical differentiation, giving the inset at the lower right of figure 5.3. At the intended position of the sample surface, 40 mm from the lens surface, an electric field strength of $\approx 3.7 \cdot 10^{-2} \text{ V/m}$ is found, which is a factor of 64 smaller than for the setup without cap. As a result, it can be concluded that, concerning the requirements of spectroscopic resolution, charging of the lens can be tolerated to some extent when the screening cap is used in the system, while integration of the beam guide into the ARPES experiment would just not be feasible

without electrostatic screening.

The opening angle of the conical cap is designed to match the convergence of the focused beam. Even better screening capabilities could hence be achieved when working with a smaller beam diameter, such that the aperture on top of the cap could be laid out with a smaller diameter. It is well known that aluminum surfaces tend to form an insulating oxide layer when exposed to air, so the electrical contact to ground can be degraded. Therefore, all surfaces of the beam guide exposed to free electrons were coated with a conductive graphite film in order to grant low surface resistivity. The coating also showed up to be a good absorber of stray light. In reality, the simulated potential distribution will be influenced by the presence of further metal parts in the chamber such as the vacuum side of the sample manipulator assembly. Thus, the considerations made here should be seen as an approximation to the actual field configuration found for the charged lens.

5.5. Layout of the optical components

While the preceding sections covered the integration of auxiliary optics components into the ARPES experiment, the implementation of a simple optical bench system for beam shaping is presented here. It is basically intended to provide versatile access to a laser pointer source for the SPV experiments, but was later extended to work with various light sources used in alternative projects.

All components are integrated in the *Linos Microbench* system, a high-precision building block-system for collinear optical arrangements. The bench assembly is flanged to the outer side of the beam feedthrough described in section 5.2 and is translated by the optics manipulator used for beam positioning. Figure 5.4 shows the optical setup as realized in this work. For better stability, the complete bench is supported by an aluminum construction profile with $50 \times 50 \text{ mm}^2$ cross section.

For general light sources, the main task of the optical setup is to provide a well-collimated light beam in order to minimize divergence loss in the UHV beam guide. For good focussing performance of the plano-convex lens near the sample surface, a collimated beam is also desirable.

During the SPV experiments presented in chapter 6, a green laser pointer ($\lambda = 532 \text{ nm}$) with 5 mW output power was used. It is held by a specialized mount that allows for rigidly constraining the laser housing in a defined, slightly deflected position in order to align the laser beam to the bench geometry. The laser intensity is attenuated by a pair of polymer polarizer foils that can be rotated independently. The extinction coefficient of such polarizers is limited, but sufficient to cover roughly two orders of magnitude of laser flux. The intensity calibration procedure is summarized in appendix C.

The divergence of the laser beam is reduced by a Kepler-type beam expander, that basically consists of two biconvex lenses with different focal length f_1 (near the source)

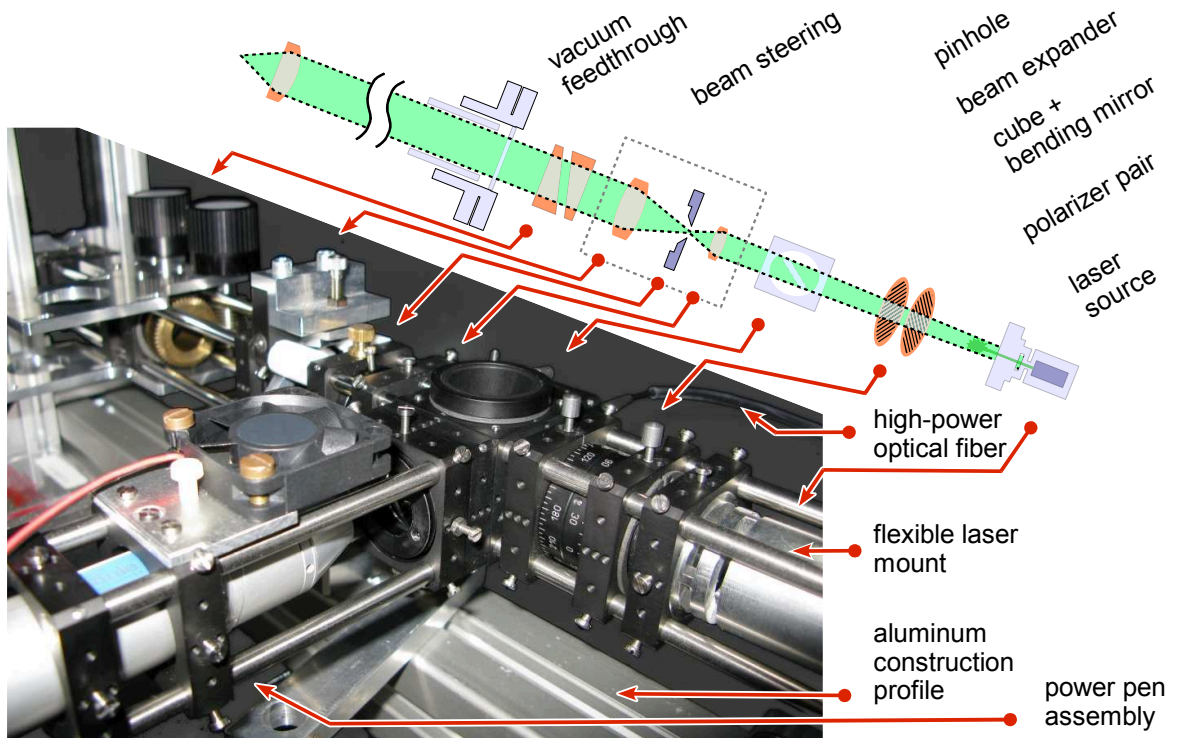


Figure 5.4.: Photograph of the implementation of the beam shaping optics with several light sources mounted to the bench system. Light sources are selected by the optional bending mirror inserted into the cube in the center of the photograph. Attached to the cube: Hönle PowerPen (foreground, [72]), laser pointer assembly (right), and high-power optical fiber (background, appendix E). The bench system is supported by an aluminum construction profile and enclosed in a protective housing.

and f_2 (far from the source) with $f_1 < f_2$. Here, the beam diameter is increased by a factor f_2/f_1 and the divergence is reduced by the same factor, so a broadened, collimated beam results. For fine adjustment of the distance, the remote lens can be moved with micrometer precision via a lever system driven by a micrometer screw. This mechanism can also be used for fine positioning the axial focus position, as a slightly misaligned beam expander will have finite focal length.

An adjustable pinhole is located in the intermediate image plane of the beam expander to allow for a tradeoff between high transmission and even better collimation. For electron microscopy applications, well-defined pinholes in a large range of diameters down to some micrometers are available commercially (*Plano GmbH*, e.g.), so an appropriate choice could be made here. The pinholes are available in a broad range of materials. Among them, versions made of Molybdenum were tested, but showed up to be corroded quickly when operated a high temperature in air. Alternatively, pinholes

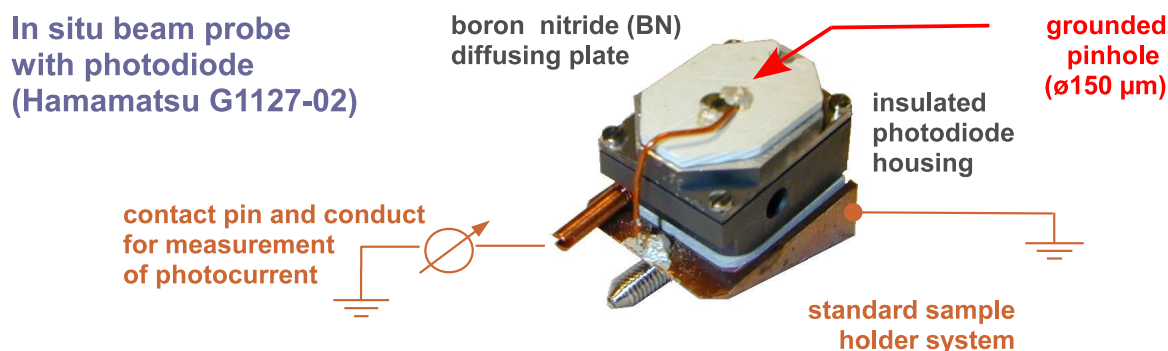


Figure 5.5.: A photodiode enclosed by a housing except for a small, defined aperture was mounted on a standard sample holder. The photocurrent can be measured in situ using the sample current line contacted by the pin.

made of Platinum-Iridium alloy were tested for high-power applications. These showed up to reflect most of the blocked radiation and to be sufficiently inert to stand high heat load in air.

The optics system has been extended to work with several light sources. The PowerPen (Dr. Hönle AG) used for switching conformational switching of molecular adsorbates by UV-light [72] was equipped with a dedicated mount for the Microbench system including a cooling fan to provide high stability continuous operation. The lens configuration is currently subject to optimization for this purpose. The third optional light source is pulsed laser radiation generated by the Empower 30 (Newport Spectra-Physics GmbH). In appendix E, the implementation of a high-power fiber guide system for the laser light from a remote laboratory is presented. The fiber end station is integrated into the optical bench. Several sources may be mounted to the system in parallel to different ports of the cube. A specific radiation source can then be selected by an optional bending mirror inserted into the cube (see fig. 5.4).

For protection of the sensitive optical components and to comply with laser safety issues, the whole assembly is surrounded by a closed housing. The laser system was successfully used in the Diploma thesis of Andrej Lang [76] for controlled, exclusive heating of a sample surface.

5.6. Calibration measurements

After realizing the setup as described in the preceding sections, the optical performance had to be checked under realistic conditions. Here, an approach to determine the focusing capabilities is discussed and an example for the top performance reached so far is given.

In order to probe the focus at the sample position, a standard sample holder was equipped with a housing for a photodiode. A photograph of the solution is shown in

figure 5.5. It is designed to block visible light completely except for a well-defined small aperture at the position where the sample surface would be found otherwise. Here, a pinhole with a diameter of $150\ \mu\text{m}$ (*Plano GmbH*) is applied. By using this design, the experiment can easily be switched between photoemission measurements and calibration without venting the system.

For monitoring the photocurrent, the photodiode is connected between the grounded sample manipulator and the insulated sample current line, which is contacted by a pin mounted to the sample holder. The *Hamamatsu G1127-02* photodiode used in this setting is well-suited for this task. The manufacturer states a spectral sensitivity of $0.17\ \text{A/W}$ for the wavelength of the laser pointer ($\lambda = 532\ \text{nm}$) and an excellent short circuit current linearity over nearly ten decades of light intensity. In its original state, the sensitive surface of the photodetector is enclosed by a sealed protective housing with a glass window. This would introduce a virtual leak to the UHV environment, so it was removed. Therefore, the beam probe is also suitable for detection of the UV light from the He lamp, which would be absorbed by the quartz glass window otherwise. Experimental results of scanning the spot profile of the He lamp are discussed in appendix A. Although a maximum safe storage temperature of $70\ ^\circ\text{C}$ is declared in the datasheet, the photodiode showed no significant degradation after several cycles of mild bake-out at $90\ ^\circ\text{C}$ for up to $36\ \text{h}$.

The wiring diagram of the data acquisition setup is given in appendix A. As required for optimal linearity, the photodiode is short circuited via $100\ \Omega$, and the resulting voltage is measured via an analog Keithley electrometer. Further components serve to convert the analog voltage signal to a frequency of TTL pulses, which are required to record the data using specialized hardware driven by ASPHERE [53]. With this approach, ASPHERE can be driven as if the data originated from a channeltron detector. At first glance, this appears to be a circumstantial solution, but it is justified by the comfortable stepper motor control offered by ASPHERE.

The basic idea is to translate the pinhole across the beam cross section in defined steps using the stepper motors of the sample manipulator. At each position, a signal proportional to the photocurrent is recorded, giving information on the total light intensity reaching the photodiode. As the best focal width of the laser spot is found to be much smaller than the pinhole diameter, edge scans of the beam are acquired when shadowing the beam partially. The result of an edge scan after optimization of the optics and finding the correct working distance is shown in figure 5.6. In order to avoid local saturation of the photodiode, the laser light intensity was reduced as much as possible by the polarizers, so linear response of the detector is expected. The raw data was smoothed by applying a binomial filter (appendix I). From the scanning geometry, a flat top of the intensity curve would be expected. The elevation observed here can be attributed to drift of the unstabilized laser source. When transmitted at the center of the aperture, the two edge features should be distanced exactly by one diameter. Here, a smaller distance is found, indicating that the laser beam was not centered to the pinhole.

An impression of the focal width can be extracted from the rising and falling flank,

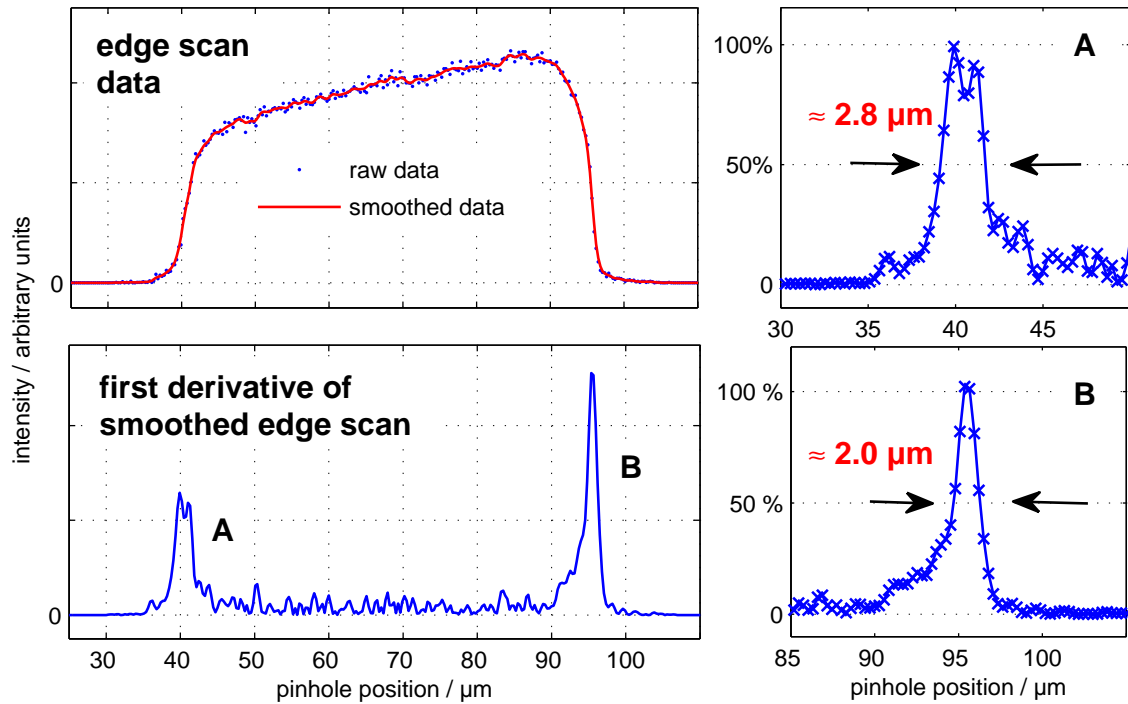


Figure 5.6.: Scan of the laser focus at the sample position acquired using the beam probe (figure 5.5) mounted to the sample manipulator. The diameter of the pinhole is much larger of the focus, so edge scans of the focus result when the edges of the pinhole cross the beam. The full width at half maximum of the focus amounts to $< 3 \mu m$.

i.e. that parts of the scan where the pinhole border crossed the laser focus. As the raw data is cumulative intensity over the total pinhole area, information on the focal profile is found from the first derivative of the signal. Its absolute value is depicted in the lower panel of figure 5.6. From the data, a focal width in the range between $2 \mu m$ and $3 \mu m$ is found. This result holds for a carefully adjusted optical bench with a pinhole of $30 \mu m$ diameter located in the intermediate image plane of the beam expander. Using larger apertures would significantly degrade the performance.

The small focus achieved here can also be used for precise determination of vibrational modes that cause a displacement between the optical bench and the sample manipulator. With this intention, the scanning aperture is positioned to shadow exactly half of the laser beam, so vibrations in scanning direction cause fluctuations of the photocurrent, which is recorded using an oscilloscope. Even small amplitudes below $1 \mu m$ can be detected with this method. The procedure was done for different scanning directions to test the effect of pump operation or human activity on the setup. The results can be summarized as follows. Basically two vibrational modes are found for the system.

One at a frequency of ≥ 100 Hz, which is around the expected eigenfrequency of the beam guide (see section 5.3) and a second one below 10 Hz. The small frequency is suspected to be a mode of the experiment's supporting framework. At rest, i.e. at normal pumping operation and no human activity, the amplitude of both frequencies clearly amounts to less than 1 μm . When excited manually, the high-frequency vibration shows up to decay within one second, whereas the low frequency mode requires much more time to be damped.

From these results, it can be concluded that the optics design is appropriate for the needs faced here. Its mechanical stability is sufficient for the environment it is operated in. Limitations may originate from the design of the supporting framework. An excellent focus diameter could be achieved in practice, which is much smaller than usually required. These commissioning experiments clearly prove the feasibility of integrating a high-performance optical bench into the ARPES experiment.

5.7. Summary

In this chapter, some difficulties of integrating optics parts into a photoelectron spectroscopy experiment were identified and an approach tolerating these problems was presented. A detailed discussion of basic features was appended to show the feasibility of the solution. Issues concerning static mechanical stability and dynamical properties were covered and could be optimized by numerical simulations. It was demonstrated how electrostatic charge in the system can be tolerated, again by performing a detailed numerical analysis. A simple layout for a beam-shaping optics was introduced. During the work, all components were realized and integrated into the experimental chamber. A versatile method for probing arbitrary light beams at the measuring position of a sample was developed. Extensive testing confirmed the great applicability of the optical setup. The optical performance and the high mechanical stability qualify the device for well-defined, spatially constrained illumination, potentially allowing for spatially resolved experiments working in a scanning mode. By the integration of new light sources, some further projects could already benefit from the setup ([72],[76]), and a high potential for future work is expected.

6. Results

In the preceding chapters, the experimental setup of the photoelectron spectrometer driven in the workgroup was introduced in detail. During this work, several upgrades were implemented in order to provide more comfortable handling and to allow for more flexibility and new operational modes. Chapter 5 was focussed on the development and the calibration of a beam guide with an associated optical system that offers an option of transporting a well-defined light beam to the sample surface in its measuring position. All upgrades were introduced with the intention to carry out quantitative measurements of the SPV effect.

A theoretical model of this effect was introduced in chapter 3.2. Though based on earlier work [8], major changes had to be done in order to obtain an appropriate treatment of an extended range of configurations of the space charge layer. As several new features were introduced for this purpose, an experimental validation of the implications is strongly required. The large number of material constants involved in the model make quantitative measurements of the SPV effect a promising approach to the determination of their actual values.

These topics are subject to the project presented in this part of the work. Using the Rb-covered surface of p-type tungsten diselenide as a model system, an experimental study of the SPV effect was carried out with the experimental setup introduced before. All results are backed with numerical simulations applying a software implementation of the theoretical model. The results obtained here are to be published in an extensive paper which is still in preparation at the present date. It is reproduced in its current state in the following.

Valence band photoemission spectroscopy is used for the quantification of the SPV effect on the surface of $WSe_2 : Rb$. The results are reproduced by numerical simulations, confirming the validity of the theoretical considerations for the examined conditions. In combination with experimental data, the results of the simulation allow for an indirect determination of various material parameters of the sample surface, which cannot be probed by conventional PES. As the experimental station allows for tuning further conditions, future studies extending this work are highly encouraged.

Surface photovoltage effect at the p-WSe₂:Rb - surface: photoemission experiment and numerical model

J. Buck,* J. Iwicki, K. Rossnagel, and L. Kipp

Institute of Experimental and Applied Physics, University of Kiel, 24098 Kiel, Germany

(Dated: June 8, 2010)

It will be shown that a combined experimental and theoretical study of the surface photovoltage (SPV) effect can be utilized for the quantification of a number of material parameters in a semiconductor-adsorbate model system. At the Rb-adsorbed surface of the semiconducting layered transition metal dichalcogenide WSe₂, a large SPV effect of ≥ 600 meV is observed already at moderate photon flux. Using valence band photoelectron spectroscopy and an auxiliary tunable light source, the surface potential and the SPV effect was traced as a function of adsorbate density and absorbed light intensity. The stationary band bending shows a pronounced resonance-like behavior, i.e., a large fraction (50-80%) of the total SPV magnitude rises within less than one order of magnitude of intensity. The effect is reproduced by a numerical model involving semi-classical charge carrier dynamics in the surface space charge layer. Among the parameters determined from the simulation, we find an approximate bulk acceptor density between $0.9 \cdot 10^{17}$ and $2 \cdot 10^{17}$ cm⁻³, a broad adsorbate donor level at ≈ 0.2 eV above the conduction band minimum and electron and hole carrier mobilities $\mu_e = 3.1$ cm²/(Vs), $\mu_h = 6.9$ cm²/(Vs) in the crystallographic *c*-direction.

I. INTRODUCTION

Photoemission spectroscopy (PES) is a potent technique for the characterization of the electronic structure at the surfaces of solids. It has found wide applications in the analysis of occupied electronic bands and chemical composition. Applying these capabilities to surface structures and defects, and providing additional information on charge carrier dynamics, is of potential interest in semiconductor physics, since complex relations between surface states and charge transport near surfaces are known: Considerable electric fields and potentials can be observed in the presence of extrinsic surface states, which are a consequence of charge transfer between the surface and the bulk. Surface states have a high impact on the average lifetime of charge carriers, as they usually represent additional recombination centers.

Despite its excellent capabilities in the determination of the electronic configuration, information on the dynamics of charge carriers near the surface cannot be gained from conventional PES, while the established techniques for the determination of electrical properties based on measurements of the conductivity do not provide detailed data on the electronic structure.

The commonly very low density of states hinders direct measurements of electronic surface states induced by defects or adsorbates using standard PES. Measurements of the conductivity often require considerable minimum dimensions of a specimen, so their application might fail in cases where samples are very thin, anisotropic, or when surface sensitivity is demanded.

An approach to find data on both subjects can be made under certain circumstances: In the presence of a surface potential, semiconductors show a considerable surface photovoltage (SPV) upon illumination, which is a consequence of a stationary redistribution of charges as a function of the creation rate of electron-hole pairs. Since changes of the potential can be measured as a shift in the

photoelectron spectra, this effect can be probed in a photoemission setup equipped with an auxiliary light source. A theoretical interpretation of the measured effect reveals the influence of the electrical material parameters.

Consider a semiconductor surface that gets covered by foreign atoms. Upon deposition, charge is transferred between an appropriate electronic level of the adsorbate and the substrate. Solving Poisson's equation for this configuration directly gives the potential difference to the bulk (the 'band bending').

By the absorption of light with photon energy exceeding the bandgap, i.e., the injection of electron-hole-pairs, this thermal equilibrium-configuration is perturbed significantly. Due to the finite penetration depth of the light, given by the absorption coefficient α , the creation rate of mobile charge carriers $G(z) = G_0 \cdot \exp(-\alpha z)$ ($[G] = \text{s}^{-1} \text{cm}^{-3}$) rapidly decays with distance from the surface z , so a large gradient of the injected charge concentration results. The SPV effect is observed as a decay of the space charge layer, i.e., the surface potential, as a function of the generation rate of mobile charges at the surface $G_0 = G(z=0)$. For a quantitative analysis, an exact model of the charge carrier dynamics including drift, diffusion, and recombination has been formulated. The effect of the adsorbed atoms is not limited to charge donation here as they contribute significantly to the recombination of charge carriers.

As various parameters of charge carriers and the surface state have an influence on the SPV effect, combined numerical simulations and measurements have been proposed as a tool to determine these quantities from photoemission data¹. This approach is pursued here using a well-known model system, which is considered especially suited for the method outlined above:

Tungsten diselenide (WSe₂) belongs to the class of transition metal dichalcogenides (TMDC) and crystallizes, among other known structures, in the trigonal prismatic 2H structure. Like all compounds out of this class,

it basically consists of quasi-two-dimensional layers (the crystallographic *ab*-plane) with internally nearly saturated covalent bonds and small van der Waals-forces acting between the layers.

WSe₂ is known to be a semiconductor with an indirect band gap of 1.2 eV (Refs. 2 and 3). Therefore, it has been considered as substrate for novel solar cells, and remarkable quantum efficiencies could be achieved under laboratory conditions in the past⁴. In addition, excellent carrier mobilities were reported for this material⁵.

Cleaved surfaces of WSe₂ are known to have an extremely low density of states. No band bending is observed in this case, so it can be tuned freely by controlled adsorption. Rubidium atoms adsorbed on the surface of WSe₂ have a donor-like energy level, so the creation of a surface potential leads to a shift of the photoemission spectra to higher binding energy. No penetration of the substrate, i.e., intercalation, is observed for Rb at room temperature and below⁶. The formation of an inversion layer can be observed for a sufficiently large adsorbate concentration.

In this paper, we show how a semi-classical, microscopic treatment of charge carrier dynamics can be used to formulate an appropriate model of the SPV effect. Extending the developments of Trares-Wrobel⁷, the presence of an inversion layer at the surface is explicitly taken into account here. The model is validated for this configuration by comparing numerical simulations to experimental results. It will be shown that the predictions hold for a wide range of the adsorbate concentration, and several orders of magnitude of absorbed photon flux. Since a generally good agreement between the simulations and the experimental data is found, actual values of many participating material parameters are estimated from the combined approach. The sensitivity of the method to these quantities is discussed in detail. An expansion of earlier work¹, the adsorbate state is characterized completely, and self-consistent values for the bulk doping, adsorbate density, recombination rates, mobilities of charge carriers are derived.

This paper is sectioned as follows: Experimental issues, i.e., sample preparation, the external light source, and aspects of data processing, are summarized in section II. The numerical model is outlined in section III. The results are subdivided into two parts: The band bending at increasing Rb coverage in thermal equilibrium is shown in section IV A, followed by the measurements of the SPV effect (section IV B). Comprehensive interpretations and a discussion of the method is given in section V.

II. PHOTOEMISSION EXPERIMENT

A. Sample preparation

WSe₂ single crystals were grown using the chemical vapor transport technique with iodine as transport agent. A small amount of iodine atoms is usually embedded into

the crystal, giving p-type doping². Typical samples were up to 5×5 mm² in area and had a thickness of (30±5) μm.

For the photoemission measurements, the specimen were glued to a copper sample holder using ultrahigh-vacuum compatible, conductive silver epoxy and cleaved *in vacuo* parallel to the *ab*-plane at a base pressure of 3·10⁻¹⁰ mbar.

Simulation predicts band bending effects to occur already at extremely low coverages in the order of 1 % of a monolayer. Thus, an extremely low flux of Rb atoms is required to adsorb a defined, small density of Rb atoms onto the surface. To this end, the samples were exposed to Rb flux from a *SAES Getters* Rb dispenser driven at a heating current of 5 A for fixed periods of Δ*t* = 20 s. An average Rb deposition rate in the range of 10¹⁰ s⁻¹ cm⁻² could be achieved with these parameters, as will be shown later in this paper.

B. Measurements

The photoemission experiments were carried out using a *Specs PHOIBOS 150* electron analyzer and a *Specs UVS 300* He discharge lamp emitting mainly at a photon energy of 21.22 eV (He I_α). A *Specs TMM 302* monochromator was used to suppress undesired satellite lines in the spectrum.

The valence band photoemission spectra were taken at normal emission with an acceptance angle of ±6° and an acceptance area of ≈ 2.5 mm², defined by the spot size of the source. An energy resolution of the electron analyzer of 40 meV was chosen for the measurements.

All photoemission measurements were carried out at constant photon flux, controlled by the sample-to-ground current, which amounted to approximately 1 nA, corresponding to ≈ 6·10⁹ photoelectrons per second. All spectra were taken at room temperature [(300 ± 2) K].

C. Excitation light source

The SPV effect was created using a green laser pointer (λ = 532 nm) with an output power of 5 mW(cw). A pair of polymer polarizers with variable rotation angle was inserted into the beam to provide tunable attenuation of the light intensity. Approximately two orders of magnitude of photon flux could be covered in this way. To provide a focussed, well-defined laser spot on the sample surface with high spatial stability, a specialized beam guide was constructed.

The laser spot diameter was chosen to be well below that of the UV source, typically in the range of (200 – 300) μm. A photodiode was used to calibrate the total transmission of the optical setup, giving an approximate total photon flux of 2.7·10¹⁵ s⁻¹ transmitted through the beam guide, exceeding the photon flux of the UV source by several orders of magnitude. This allows us to neglect the photoemission current in the theoretical

6. Results

model developed below, which would require to include a Schottky back contact of the sample otherwise. Assuming a spot area of $(300 \mu\text{m})^2$ and an absorption coefficient $\alpha = 3.9 \cdot 10^7 \text{ m}^{-1}$ (Ref. 8) at the given wavelength, an estimated maximum photon absorption rate in the illuminated area of $G_0 = 10^{28} \text{ s}^{-1} \text{ m}^{-3}$ could be achieved. In the following, the creation of one electron-hole pair per absorbed photon is assumed.

D. Data processing

Photoemission spectra were taken at successive evaporation steps and excitation light intensity tuned over the full intensity range, giving the surface photovoltage response as function of Rb coverage and photon flux. A higher order binomial filter was applied to the experimental data by convolution with the window $[1, 6, 15, 20, 15, 6, 1] = [1, 2, 1] * [1, 2, 1] * [1, 2, 1]$ prior to further evaluation. Its pronounced low-pass characteristic⁹ leads to optimal smoothing at minimum loss of structures in the spectra.

For each of the discrete adsorbate concentrations prepared here, one spectrum was recorded at thermal equilibrium, which is denoted as $R(E)$ below. It is used as a reference of the spectra showing the SPV effect, which were acquired in the following. The secondary electron background of such group of spectra was normalized (not removed) to a joint level assuming the well-known Shirley background approximation¹⁰.

Due to the fact that the laser focus was chosen to be considerably smaller than the UV spot, the spectra $S(E)$ taken at non-zero bias light intensity contain a broad range of SPV shifts varying locally with the photon absorption rate. This mixture can be separated into components with distinct SPV shift by assuming $S(E)$ to be a linear combination of differentially shifted copies of the reference spectrum $R(E)$ with the physical boundary condition that each coefficient has to be greater than zero:

$$S(E) = \sum_i c_i R(E + i \cdot \Delta E) ; c_i \geq 0 \text{ for all } i. \quad (1)$$

Here, $\Delta E = 10 \text{ meV}$ is the discrete spacing between two datapoints in a spectrum. With the arbitrary choice of $-100 \leq i \leq 100$, the maximum shift amounts to $\pm 1 \text{ eV}$. A least squares solution meeting the boundary conditions $c_i \geq 0$ is determined by an algorithm described in Ref. 11. This method is equivalent to finding a discrete convolution window c with positive components c_i such that the convolution of $R(E)$ with this window gives the 'back bending' spectrum: $S(E) = R(E) * c$.

III. NUMERICAL MODEL

For laterally homogeneous adsorbate distribution and illumination, only the direction perpendicular to the

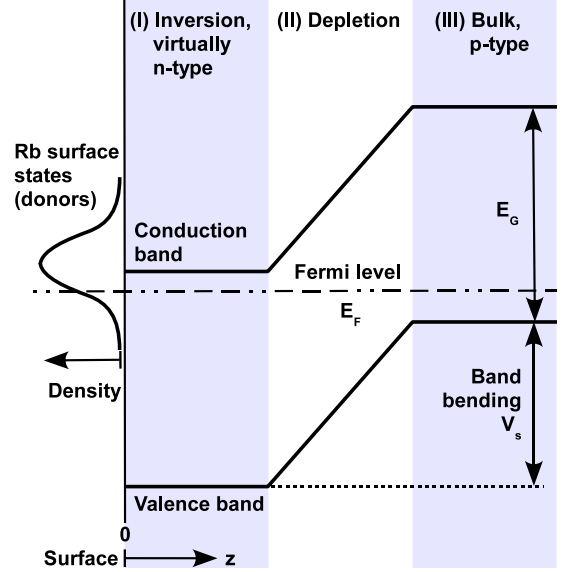


FIG. 1. (color online) Schematic of the space charge layer in thermal equilibrium. It is caused by charge transfer from the donor-like adsorbate state to the substrate. The band bending is described by a solution of Poisson's equation for the resulting distribution of charge. Inversion of the surface is predicted by the simulation for an appropriate choice of the material parameter set of the p-WSe₂:Rb-system.

surface, which is equivalent to the crystallographic c -direction, has to be accounted for in a theoretical model. Its coordinate is denoted as z in the following, which has its origin at the surface and its positive direction pointing towards the bulk (see Fig. 1). All binding energies are referred to the valence band maximum (VBM), $E_{VBM} = 0$.

For given bulk doping and densities of states in the valence and conduction band of the substrate, the bulk Fermi level is determined using Fermi statistics and the claim for charge neutrality in the bulk. In contrast to common three-dimensional crystals, the presence of surface states can be neglected for layered materials, such that a surface dipole need not taken into account for the clean sample.

The transfer of one electron per atom to the crystal surface is assumed upon deposition of Rb at a density N_T , leaving behind an unoccupied state with rather discrete energy E_T . In the model, a Gaussian shaped density of surface states with width σ_T is assumed:

$$D_T(E) = \frac{N_T}{\sqrt{2\pi} \cdot \sigma_T} \exp\left(-\frac{(E - E_T)^2}{2 \cdot \sigma_T^2}\right). \quad (2)$$

The subscript 'T' is motivated by the fact that charge carriers located in the adsorbate state are immobile, i.e., 'trapped'. With positively charged states at the surface, an accumulation of conduction band electrons constitutes in the vicinity of the surface, which is called 'space charge layer' in the following.

The density of mobile charges in the bulk is modeled by the well-known relations for the participating energy bands and the bulk acceptor level¹⁷. All contributions are functions of the corresponding energy levels with respect to the Fermi level E_F , which is a global constant in thermal equilibrium. In presence of an electric potential, the band structure is shifted relatively to the Fermi level, and Fermi statistics requires a non-vanishing space charge density in this case. The space charge density with respect to the bulk is summarized in the space-charge function $\mathcal{F}(u(z), u_b)$ (Ref. 12). Its parameters $u_b = (E_F - E_{ib})/k_B T$ and $u(z) = (E_F - E_i(z))/k_B T$ denote the reduced Fermi levels in the bulk ($z \rightarrow \infty$) and at finite z , respectively.

Quantities with an 'i' in the subscript denote intrinsic values. The intrinsic Fermi level E_{ib} in the bulk is the reference for the electrostatic potential. In this context, Poisson's equation can be formulated in terms of the space charge function¹³. Claiming zero charge density in the bulk, it reduces to

$$L_D \left(\frac{du(z)}{dz} \right) = \mathcal{F}(u(z), u_b), \quad (3)$$

where L_D is the Debye length of the intrinsic crystal. The occupancy of the surface states $D_T(E)$ is governed by Fermi statistics, and the states are considered to be 'floating' on the electrostatic potential at the surface, i.e., the surface charge density is a function of $u_s = u(z=0)$.

The problem can be solved by claiming global charge neutrality, so the electric potential difference between bulk and surface (i.e., the band bending) $V_s = k_B T \cdot (u_s - u_b)$ can be determined numerically. Equation 3 is also used to find the width of the space charge layer by resolving for z , i.e.,

$$z^* = L_D \cdot \int_{u_b}^{u_s} \frac{1}{\mathcal{F}(u, u_b)} du, \quad (4)$$

and integrating numerically.

When light is absorbed at a constant rate G_0 at the surface, a stationary non-equilibrium state results. This configuration is modeled by treating the electrons and holes as separate conglomerates of particles and assuming individual thermal equilibrium. To this end, separate Fermi levels for the electrons, E_{Fn} , and holes, E_{Fp} , are introduced, which are referred to as quasi-Fermi levels¹⁴. The space charge function \mathcal{F} can be generalized for this case simply by replacing E_F by the appropriate quasi-Fermi level. Carrier dynamics will be considered in detail in order to compute the stationary space charge distribution for this scenario.

Assuming laterally homogeneous illumination, and taking into account the processes of carrier generation, carrier recombination, and carrier transport (drift and diffusion), a differential equation for the excess minority carrier concentration can be formulated. Basically two recombination channels have to be included into the model here, i.e., direct recombination of charge carriers

from band to band, as well as, for the surface, transitions involving the surface state.

In a doped semiconductor, the concentration of either electrons or holes strongly prevails. As the amount of photogenerated carriers is balanced, the relative excess charge carrier concentration of the majority can easily be ignored, so carrier dynamics will only be modeled for mobile minority carriers. The presence of the inversion layer must be taken into account here, so if the concentration of holes $p(z)$ dominates the electron concentration $n(z)$ or vice versa depends on z . For $n(z) \gg p(z)$, the one-dimensional transport equation for the excess minority carriers reads:

$$D \frac{\partial^2 \Delta p}{\partial z^2} - \mu \mathcal{E} \frac{\partial \Delta p}{\partial z} - \frac{1}{\tau} \Delta p = -G_0 \cdot e^{-\alpha z}. \quad (5)$$

An analog expression can be formulated for the complementary configuration. The coefficients are the diffusion constant $D = (k_B T/e)\mu$, the carrier mobility μ , the electric field \mathcal{E} , and the average carrier lifetime τ . The right-hand side of the equation accounts for the carrier generation by the absorption of photons, characterized by the surface generation rate G_0 and the substrate absorption coefficient α .

Here, a spatially constant concentration of majority carriers is assumed in order to implement the band-to-band recombination by introducing the average lifetime τ , rendering the equation linear. Since the recombination rate U_s involving the trap state concerns only surface carriers, it is included into the system via a boundary condition at the surface $z = 0$:

$$-\mu \mathcal{E} \Delta n - D \frac{\partial \Delta n}{\partial z} = -U_s, \quad (6)$$

i.e., the surface recombination rate equals the particle flux towards the surface.

The model formulated here follows Shockley's theory¹⁴, modified for surface states^{15,16} and extended by Trares-Wrobel for energy levels with non-zero width⁷:

$$U_s(E) = r_{TV} D_T(E) \times \frac{p_s n_s \left(1 - e^{\frac{E_{Fn} - E_{Fp}}{k_B T}} \right)}{n_s \left(1 + e^{\frac{E - E_{Fp}}{k_B T}} \right) + \frac{r_{TV}}{r_{CT}} p_s \left(1 + e^{\frac{E_{Fp} - E}{k_B T}} \right)} \quad (7)$$

with $U_s = \int U_s(E) dE$ and the surface charge density of electrons n_s and holes p_s . According to Shockley¹⁴, the probabilities for the transition of an electron from the conduction band to the trap state r_{CT} and for the transition from the trap state to the valence band r_{TV} have the dimension $\text{m}^3 \text{s}^{-1}$. They are assumed to be independent from the energy E . This rather general equation still has to be adapted to actual conditions. Our simulation shows that even moderate adsorbate concentration will lead to the formation of an inversion layer (I) at the surface (see Fig. 1). At boundaries between regions with

different types of majority charge carriers, the formation of a depletion region (II) is generally observed and is treated separately here. The bulk (III) is unaffected by the adsorbate. Following Sze¹⁷, the width of region (II) is given by

$$W = \sqrt{\frac{2\epsilon_s}{e} \left(\frac{n_s + N_A}{n_s \cdot N_A} \right) V_s}, \quad (8)$$

with the charge density of the inversion layer n_s and the total band bending V_s . The excess carrier recombination rate is governed by the absolute concentration of charge carriers, which was assumed constant in Eqn. (5). For this reason, the transport equation can be solved individually for regions (I) to (III). In the p-type bulk, the transport of electrons is computed while holes are found to be the minority carriers in the inversion layer (I). In the depletion layer (II), both types of excess carriers are included in the model, because the equilibrium concentrations are found to be very low and nearly balanced in that region. Some simplifications are made here: the potential drop is assumed to be concentrated in the depletion layer (II). Thus, the electric field becomes 0 for regions (I) and (III), and a constant field $\mathcal{E} = V_s/W$ can be assumed in region (II). Furthermore, $\alpha^{-1} \ll z^* + W$ indicates that the bulk (III) is always in thermal equilibrium.

While the non-equilibrium space charge function is solved to find the band bending at a given non-equilibrium configuration, the solution of the transport equation [Eqn. (5)] is required to find the photon absorption rate producing this stationary state. The stationary non-equilibrium state can be regarded as a small perturbation of the equilibrium state, that makes up the stage for the dynamics of a small density of excess minority carriers.

IV. RESULTS

A. Thermal equilibrium

When the concentration of Rb adatoms is increased in defined, commensurate steps, the band bending V_s is seen to increase and saturate at ≈ 800 meV relative to the spectrum of the bare sample (Fig. 2). In order to model this observation with the space charge simulation code, some assumptions about the material parameters of WSe₂ had to be made, or were taken from literature. The used values can be found in Tab. I.

The bandgap is well known from combined direct and inverse angular resolved photoemission experiments. The value of 1.2 eV applied here originates from Ref. 2. From earlier work¹, the density of states in the valence band N_V and the conduction band $N_C = N_V = 10^{19}$ cm⁻³, as well as the acceptor level $E_A = 30$ meV are known.

In accordance with Ref. 18, a dielectric constant $\epsilon_s = 16$ was assumed, which holds for the *ab*-plane of the crystal, i.e., parallel to the cleaved surface. Due to the anisotropic crystal structure, a different value should be expected for the *c*-direction. To our knowledge, it has not been determined reliably yet, so the value stated above was used for the simulation. Only a low variation of the simulation results as a function of ϵ_s was found here, so a precise value is neither necessary nor can be derived from the simulations.

Based on these reference values, the band bending was simulated as a function of adsorbate density, i.e., $V_s(N_T)$, for a large interval of the yet unknown energy level of the adsorbate E_T and the bulk doping density N_A . The results were seen to be unaffected by a variation of σ_T . In order to find a match with the experimental data, the Rb flux η needs to be calibrated. Furthermore, a certain amount of band bending is potentially present before the first evaporation step. This might be caused by surface defect states induced by cleaving, or contamination of the surface. Note that on the bare surface with a total lack of surface states already an extremely low density of charged states will lead to considerable band bending.

Given the simulated band bending curve $V_s(N_T)$, an individual least squares fit of the function

$$V_s((n\Delta t + t_0) \cdot \eta) + V_s(t_0 \cdot \eta) \quad (9)$$

to the experimental data $V_s^{(exp)}(n \cdot \Delta t)$ is found for a set of parameter pairs (N_A, E_T) . The offset t_0 and the deposition rate η are treated as free parameters here, so an appropriate value for η results for every curve.

The fit residual for each examined case is shown in Fig. 3. The elongated minimum in the center suggests a functional relationship between $E_T(N_A)$ for the current experiment, so additional information would be required to derive absolute values. All of the best-fitting curves with parameters chosen from the shaded area in Fig. 3 give an appropriate fit to the experimental data, as they are found to cover the gray-shaded area of Fig. 2.

Boehme⁶ already located the surface state above the direct bandgap, without stating an actual value for E_T . Simulation shows that N_A is constrained to a small range between $0.9 \cdot 10^{17}$ cm⁻³ and $2 \cdot 10^{17}$ cm⁻³ here, independent of the precise energy level. A similar value has also been found by Traving² with Hall measurements on samples grown under identical conditions.

When both E_T and N_A are constrained within these limits, the deposition rate determined from fits of the simulated curves $V_s(N_T)$ amounts to a value (plus/minus standard deviation) of $\eta = N_T/n \cdot \Delta t = (2.232 \pm 0.22) \cdot 10^{10}$ s⁻¹ cm⁻² for a fixed evaporation time $\Delta t = 20$ s. An areal density of $(4.5 \pm 0.5) \cdot 10^{11}$ cm⁻² Rb atoms per evaporation step results. Here, the alignment of the dispenser requires a directed maximum flux of $\eta = (0.5 \pm 0.05) \cdot 10^{10}$ (sr s)⁻¹, provided that every Rb atom hitting the surface sticks. Only sparse reference data on the current-dependent flux of the Rb dispenser is available, but an indirect confirmation can be derived

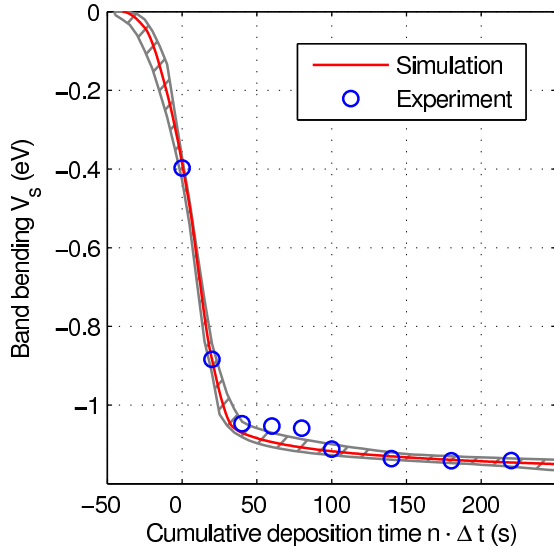


FIG. 2. (color online) Band bending at different stages of Rb deposition on WSe_2 . The red curve is obtained from simulation assuming $N_A = 0.9 \cdot 10^{17} \text{ cm}^{-2}$, $E_T = 1.4 \text{ eV}$, $\eta = 2.232 \cdot 10^{10} \text{ cm}^{-2} \text{ s}^{-1}$, and a density of donor traps after cleavage of $7.6 \cdot 10^{11} \text{ cm}^{-2}$. The gray-shaded area is covered by curves found for alternative choices of (E_T, N_A) pairs (Discussion see text).

from the findings in Ref. 19, where the achieved Rb flux density is stated for a higher heating current. The results were transferred to the actual settings using the additional flux-over-current characteristic of the dispenser given there.

The red curve in Fig. 2 results for $N_A = 0.9 \cdot 10^{17} \text{ cm}^{-3}$, $E_T = 1.26 \text{ eV}$, and an adsorption rate of $\eta = N_T/n \cdot \Delta t = 2.232 \cdot 10^{10} \text{ s}^{-1} \text{ cm}^{-2}$. Offsets according to Eqn. (9) of $t_0 \approx 35 \text{ s}$ and $V_s(t_0) \approx -400 \text{ meV}$ were found from the fit. The actual choice of parameters is commensurate with the mentioned restrictions and is suited best to reproduce the results from the SPV experiments as presented in the following.

B. SPV effect at stationary non-equilibrium

The density of Rb adatoms was increased in well-defined steps. For certain levels of coverage, a series of valence band spectra was taken at increasing laser intensity. The exemplary data set presented in Fig. 4 were acquired at a nominal Rb coverage of 10^{13} cm^{-2} . Since an identical SPV effect could already be simulated for lower coverages, there is evidence that the actual Rb concentration is smaller.

Each experimental spectrum was decomposed into shifted components of the reference spectrum, as de-

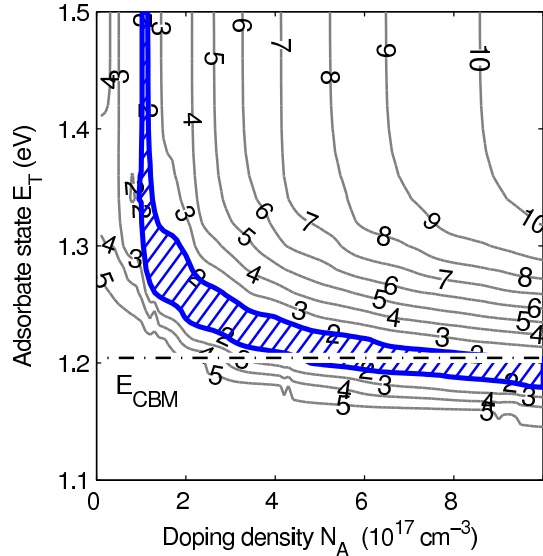


FIG. 3. (color online) Simulation result: The contour plot shows the residual (in arbitrary units) of a fit between simulated band bending and experimental data for a variety of (E_T, N_A) parameter pairs in thermal equilibrium. The elongated 'valley' (shaded blue) indicates that, by an analysis of equilibrium band bending, E_T can only be determined as a function of N_A . Discussion see text.

scribed above. All spectra could be reconstructed well by the component analysis, as can be seen from the thin, dark lines in Fig. 4. The low fraction of unexpected components with negative or very high shift magnitude out of the physically expected range indicates that no other effect accounts for the observation and that those components can safely be considered artifacts.

The results of the spectral decomposition are shown in Fig. 5. It illustrates the intensity-dependent evolution of the decomposed spectra. Each filled circle in the figure corresponds to a non-zero component c_i derived from the algorithm, and the diameter of each circle is scaled with the magnitude of c_i . Components arranged vertically in the figure originate from the same spectrum. The generation rate G_0 stated for a spectrum is derived from the integral light intensity and the estimated spot size. As could be expected, the components are distributed rather broad, with increasing width at higher photon flux.

In the following, only the maximum shift components making up the envelope of the scatter plot will be treated. They originate from the surface region with highest laser flux. For these components, a pronounced SPV effect can clearly be identified. The effect was simulated using the numerical model and the material parameters given in Tab. I. A good agreement between measured and simulated data is found for these parameters, as is illustrated in Fig. 5.

6. Results

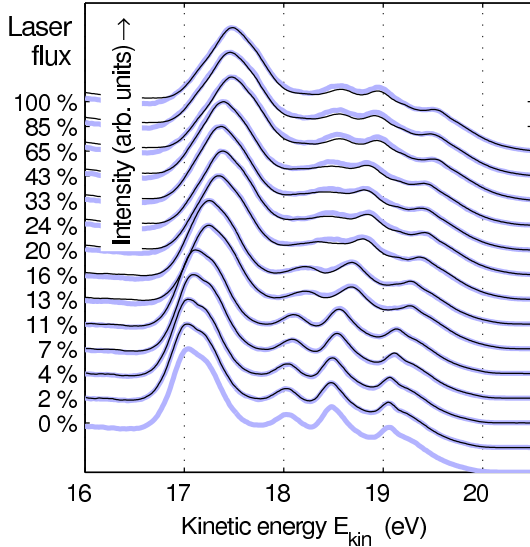


FIG. 4. (color online) Valence band photoelectron spectra of WSe₂ (normal emission, $h\nu = 21.22$ eV, Rb concentration $N_T = 4.6 \cdot 10^{12}$ cm⁻², room temperature) as a function of photon flux: Reference for Rb covered surface in thermal equilibrium (bottom), spectra of inhomogeneously illuminated sample (light blue lines), reconstruction of SPV spectrum from reference (black lines). Details see text.

The envelope shows 'resonance'-like behavior with an extraordinarily large change of the band bending V_s in dependence of the photon absorption rate G_0 in the range between $1 \cdot 10^{27}$ m⁻³s⁻¹ and $2 \cdot 10^{27}$ m⁻³s⁻¹ (Fig. 5), as is also predicted by simulation. The center position of the resonance will be denoted as \tilde{G}_0 in the following. At high light intensity, the elevation is expected to be limited by $1/k_B T$, as derived by Hecht²⁰.

Starting with reference values from the literature (references given in Tab. I), all material parameters were subject to variation in order to find an optimal fit of the simulated curve. Where applicable, the results comply with the boundaries as discussed in the preceding section. The adsorbate density for each case could be found using $N_T = \eta \cdot \Delta t \cdot n$, where n is the integer number of cumulative evaporation steps. To give an impression of the uncertainty of the parameters determined here, the gray shaded area in Fig. 5 shows the variation of the simulation result when all parameters are modified within the limits given in Tab. I.

This procedure was extended to sets of spectra from the same sample at stepwise increased Rb adsorbate density. The findings reported here are confirmed in all examined cases. At resonance, the SPV curve is basically governed by carrier recombination over the adsorbate state. Therefore, the probabilities of electron capture r_{CT} and hole emission ($r_{TV} = r_{CT}$ assumed here)

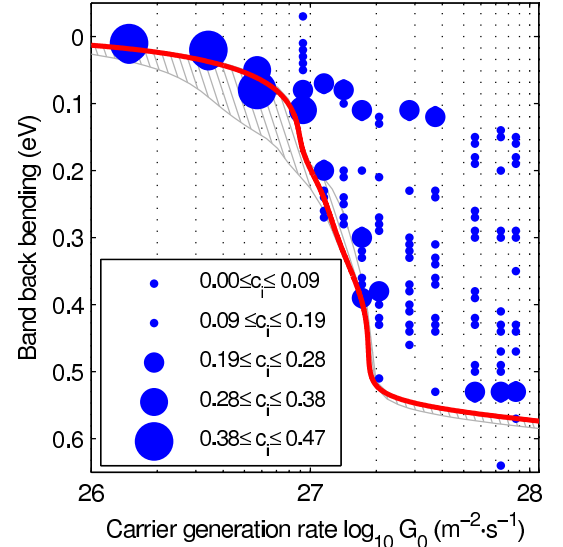


FIG. 5. (color online) Decomposition of the measured SPV spectrum series (blue circles), taken at different light intensities. The red curve is the simulation result for $N_T = 4.6 \cdot 10^{12}$ cm⁻², $E_T = 1.42$ eV, $\sigma_T = 0.115$ eV, $r_{TV} = r_{CT} = 9.9 \cdot 10^{-6}$ m³s⁻¹, $r_{CV} = 2.48 \cdot 10^{-12}$ m³s⁻¹ (symbols see text). The gray shaded area is covered by simulated SPV curves when the material parameters are varied inside the error margins as stated in the text.

determine the critical absorption rate where the resonance appears. Simulation shows that $\log \tilde{G}_0 \sim r_{TV}$ holds approximately. All data can be reproduced by the same mean values and tolerance ranges for the parameters shown in Tab. I. As expected, no significant trends or deviations of material parameters as function of light intensity or adsorbate coverage could be observed.

V. DISCUSSION

Our results allow for a detailed analysis of the effect of individual material parameters on the observed SPV effect. We now discuss the accuracy that can be achieved using the presented method for the involved parameters.

As seen in Fig. 2, we observe a saturation of the band bending at high adsorbate concentration, which can be attributed to Fermi level pinning of the conduction band minimum. This requires the surface charge density to saturate, even at much higher cumulative evaporation time. Ionization of the Rb atoms is expected, as the major part of the surface density of states is found above the conduction band minimum and thus above the surface Fermi level, even at maximum band bending. Furthermore, we find a basically constant resonant generation rate \tilde{G}_0 from the experiments for arbitrary Rb con-

TABLE I. Material parameters of the WSe_2 surface and the surface state as used for the SPV simulation (where referenced) and results extracted from the simulation. Symbols see text.

Symbol	Value	Unit	Ref. Note
E_G	1.2	eV	2
N_V	10^{19}	cm^{-3}	1
N_C	10^{19}	cm^{-3}	1
E_A	0.03	eV	1 h
$\mu_{h,\parallel}$	236	$\text{cm}^2/(\text{V s})$	21 a
$\mu_{e,\parallel}$	105	$\text{cm}^2/(\text{V s})$	21 a
$\mu_{\parallel}/\mu_{\perp}$	40 ... 1205		24 b
ϵ_s	16		21 a
α	$3.9 \cdot 10^7$	m^{-1}	8 c
N_A	$0.9 \cdot 10^{17}$... $2 \cdot 10^{17}$	cm^{-3}	
E_T	1.38 \pm 0.022	eV	h
σ_T	118 \pm 4.2	meV	
η	$2.232 \cdot 10^{10}$ \pm 10 %	$\text{s}^{-1} \text{cm}^{-2}$	d
r_{CV}	$2.52 \cdot 10^{-12}$ \pm 60 %	$\text{m}^3 \text{s}^{-1}$	e
r_{CT}	$1 \cdot 10^{-5}$ \pm 16 %	$\text{m}^3 \text{s}^{-1}$	e
$\mu_{h,\perp}$	6.9 \pm 60 %	$\text{cm}^2/(\text{V s})$	
$\mu_{e,\perp}$	3.1 \pm 60 %	$\text{cm}^2/(\text{V s})$	
$\mu_{\parallel}/\mu_{\perp}$	34.1 \pm 20.4		g

^a In crystallographic ab -plane.

^b Depending on doping concentration.

^c For $\lambda = 532 \text{ nm}$.

^d Average for 20 s evaporation at 5 A heating current.

^e Particularly biased by error of photon flux calibration.

^g Using value for $\mu_{e/h,\parallel}$ from Ref. 21.

^h Relative to valence band maximum ($E_V = 0 \text{ eV}$).

centration, although the surface recombination rate U_s should increase with Rb density, as predicted by Eqn. (7). This indicates that the density of active surface recombination centers does not change much, even though adatoms should contribute to the surface recombination rate, regardless of their charge. Hence, we can conclude that there is a maximum stable density of Rb adatoms of $5 \cdot 10^{12} \text{ cm}^{-2}$, which had been achieved in the course of the experiments, and that the assumption that every surface adatom is ionized holds.

When calibrating the total photon absorption rate G_0 , a rather large error must be taken into account, including reflection losses and drift of the laser module. A noteworthy, though small contribution to the error of G_0 results from the calibration of the absolute absorption rate, which is expected to affect all measurements equally. For the tested cases, the position of the resonance \tilde{G}_0 can be considered constant within these boundaries. Despite the uncertainty of the total absorption rate, it can be concluded that the adsorbate states are very efficient recombination centers compared to the band-to-band recombination probability r_{CV} . With respect to the considerable error of G_0 , we find a ratio of recombination rate param-

eters of $10^4 \leq r_{TV}/r_{CV} \leq 10^6$.

The values found for the mean trap level E_T and energy width σ_T have very small tolerances, because the contribution of a surface state at energy E to the recombination rate is proportional to $\exp(E/k_B T)$ [Eqn. (7)] and hence small changes have a large effect on \tilde{G}_0 . The large σ_T suggests a conglomerate of surface states with different E_T , caused by Rb atoms occupying different adsorption sites, for instance. A closer examination of the surface density of states is motivated by this result.

The in-plane value of carrier mobility μ_{\parallel} of electrons and holes is quite well known^{5,21-23}, but rather unexplored perpendicular (μ_{\perp}). The van der Waals gap that separates layers in WSe_2 is known to suppress charge transport across the layers, leading to a strong anisotropy of carrier mobility. Hu et al.²⁴ report a vast range for the anisotropy ratio $\mu_{\parallel}/\mu_{\perp}$ between 40 and 1205 (depending on bulk doping), so the ratio we find ($\mu_{\parallel}/\mu_{\perp} = (34.1 \pm 20.4) \text{ cm}^2/(\text{V s})$ at $N_A = 0.9 \cdot 10^{17} \text{ cm}^{-3}$) is consistent with this. During the simulation, the same anisotropy factor was assumed for electrons and holes, so this value holds for both types of charge carriers.

Especially with the anisotropy found here, the experimental technique potentially gives biased mobility values due to the fact that a noteworthy fraction of the photo-generated carriers is not transported into the bulk, but parallel to the surface out of the illuminated area. This effect can be neglected here, because either a large concentration gradient of injected carriers or a large lateral electric field would be required. At large SPV effect, the concentration of excess charge carriers and the electric potential can approach lateral differences similar to those achieved in perpendicular to the surface. Anyway, the much bigger spatial dimensions in parallel make the gradients negligibly small: The influence of the adsorbate layer ends at $z = z^* + W$ [Eqns. (4) and (8)] and would hardly ever exceed some ten micrometers, while the distance between the maximum of G_0 and equilibrium is given by a multiple of the spot diameter of several hundred micrometers.

The extreme sensitivity of the SPV effect to the absorbed photon flux in the 'resonant' region is a consequence of the presence of an inversion layer in thermal equilibrium. In this case, a strong reduction of the equilibrium charge carrier concentration results for a small reduction of the surface potential. The deviation from thermal equilibrium can be considered small for a considerable surface photovoltage, so a comparable effect is expected here. A strongly enhanced effect of small changes of the stationary charge carrier generation rate is expected in this case. The observed resonance can be suspected to be caused by this mechanism.

In combination with the numerical model, the extremely low flux of the Rb dispenser could be quantified. Provided the substrate parameters are known with high precision, very precise calibration measurements become possible by evaluation of the equilibrium band bending.

VI. CONCLUSION

In this paper, a quantitative study of the surface photovoltage effect was presented. We demonstrated that the experimental results obtained by photoelectron spectroscopy can be reproduced in detail by numerical simulations. The semi-classical model applied here is based on well-known semiconductor physics and showed up to be a suitable approach to handling a semiconductor surface under extreme conditions. It was shown that the combined experiments and simulations can be utilized for the quantifications of a variety of material parameters, which cannot be determined by conventional photoemission spectroscopy.

The WSe_2 surface appeared to be a well-suited model system for the validation of the presented theoretical model, as it allows almost arbitrary configurations of the space charge layer by controlled deposition of Rb. The extreme sensitivity of the observed surface photovoltage at resonance motivates the application of this material for optoelectronic devices exploiting the locally constrained, pronounced relation between photon flux and surface potential.

The theoretical model outlined here perfectly reproduces the observed effect by combining well-known models of charge carrier dynamics from semi-classical semiconductor physics. It provides an option for the quantitative evaluation of the SPV effect and offers the opportunity to probe a large set of system parameters, including bulk doping, carrier mobility, and properties of the unoccupied surface state such as the (extremely low) adsorbate concentration and the density of states. Although the electronic surface state is unoccupied here,

its energetic distribution could be probed indirectly to some extent, and its contribution to the recombination of mobile charges could be revealed. Especially the basic assumption of a basically local, one-dimensional model, i.e., neglecting lateral charge transport, was confirmed by the experimental results.

In this work, we have shown that the examination of the surface photovoltage effect provides a low-cost, versatile extension of a photoemission environment that offers an option to gain quantitative information on charge carrier dynamics at semiconductor surfaces. By decomposition into its components, information on regions on the sample could be obtained that are considerably smaller than the acceptance area of the photoemission setup.

The precise knowledge of photon-absorption-induced modifications of surface potentials is of high interest when probing semiconductor surfaces, as a reliable quantitative prediction might not only help tolerating an undesired side-effect, but might also be exploited for a characterization of the substrate-adsorbate system. Using high-power lasers and high-brilliance XUV/VUV sources with a small spot diameter, especially at modern micro-focus beamlines, the photoemission measurements might easily be extended to provide spatial resolution by scanning the surface. Furthermore, a modern spectromicroscopy setup equipped with an auxiliary light source offers interesting options for spatially resolved studies, so a high impact of this work on electron spectroscopies applied to semiconductor heterostructures can be expected.

ACKNOWLEDGEMENT

This work was supported by the Deutsche Forschungsgemeinschaft via Sonderforschungsbereich 677.

* buck@physik.uni-kiel.de

¹ L. Kipp, R. Adelung, N. Trares-Wrobel, and M. Skibowski, *Appl. Phys. Lett.* **74**, 13 (1999).

² M. Traving, M. Boehme, L. Kipp, M. Skibowski, F. Starrost, E. E. Krasovskii, A. Perlov, and W. Schattke, *Phys. Rev. B* **55**, 16 (1997).

³ T. Finteis, M. Hengsberger, T. Straub, K. Fauth, R. Claessen, P. Auer, P. Steiner, S. Hfifner, P. Blaha, M. Vögt, M. Lux-Steiner, and E. Bucher, *Phys. Rev. B* **55**, 16 (1997).

⁴ G. Prasad and O. N. Srivastava, *J. Phys. D*, **21** (1988).

⁵ V. Podzorov, M. E. Gershenson, C. Kloc, R. Zeis, and E. Bucher, *Appl. Phys. Lett.* **84**, 17 (2004).

⁶ M. Boehme, PhD thesis, Kiel, (1998).

⁷ N. Trares-Wrobel, PhD thesis, Kiel, (1995).

⁸ R. F. Frindt, *J. Phys. Chem. Solids* **24**, 9 (1963).

⁹ P. Marchand and L. Marmet, *Rev. Sci. Instrum.* **54**, 8 (1983).

¹⁰ D. A. Shirley, *Phys. Rev. B* **5**, 12 (1972).

¹¹ C. L. Lawson and R. J. Hanson, *Solving Least Squares Problems* (Prentice-Hall, New Jersey, 1974).

¹² W. Mönch, *Electronic properties of semiconductor interfaces* (Springer, Berlin 2004).

¹³ R. Seiwatz and M. Green, *J. Appl. Phys.* **29**, 7 (1958).

¹⁴ W. Shockley and W. T. Read jr., *Phys. Rev.* **87**, 5 (1952).

¹⁵ D. T. Stevenson and R. J. Keyes, *Physica* **20**, 11 (1954).

¹⁶ W. H. Brattain and J. Bardeen, *Bell Syst. Techn. J.* **32**, 1 (1953).

¹⁷ S. M. Sze, *Semiconductor Devices: Physics and Technology*, Wiley, (1985, 2002).

¹⁸ B. Davey and B. L. Evans, *Phys. Stat. Sol. A* **13**, 2 (1972).

¹⁹ T. M. Roach and D. Henclewood, *J. Vac. Sci. Tech. A* **22**, 6 (2004).

²⁰ M. H. Hecht, *Phys. Rev. B* **41**, 1 (1990).

²¹ R. Spaeh, U. Elrod, M. Lux-Steiner, E. Bucher, and S. Wagner, *Appl. Phys. Lett* **43**, 1 (1983).

²² K. K. Kam and B. A. Parkinson, *J. Phys. Chem.* **86**, 4 (1982).

²³ M. K. Agarwal, A. R. Jani, J. D. Kshtriya, M. N. Vashi, P. K. Garg, *Cryst. Res. Technol.* **19**, 12 (1984).

²⁴ S. Y. Hu, M. C. Cheng, K. K. Tiong, and Y. S. Huang, *J. Phys.* **17**, 23 (2005).

Part II.

Spatially resolved photoemission spectroscopy

7. Introduction

Research with transition metal dichalcogenides (TMDC), especially WSe_2 , has a long tradition, and many studies were focussed on alkali-adsorbed TMDC surfaces in the past [83]. In most of the reported work, electron spectroscopic techniques using VUV or soft X-ray radiation have been applied. Specific effects like the growth of self-assembled nanowire networks were examined by STM [11],[12]. A broad range of alkali-covered TMDCs was examined by Starnberg et al. ([83],[84], for instance), amongst others, by applying spatially resolved photoemission spectroscopy at beamline 31 at MAXlab (Lund, Sweden) [126],[85]. This and various other experimental stations provide spatial resolution by scanning the sample with a focussed synchrotron beam.

Earlier work on alkali-covered TMDCs revealed a strong tendency of the adsorbate to form self-assembled surface structures and to induce structural modifications of the substrate. Specific effects are known for the $WSe_2 : Rb$ system [12]. While a laterally homogeneous distribution of the adsorbate was assumed in Part I, a considerably more complex configuration can be expected from the findings in related systems. For instance, a lateral accumulation of the adsorbate can be suspected, as it is a common feature in substrate-adsorbate systems. A structured surface could cause interesting implications with respect to the surface potential and the SPV effect. Chemical species in the expected structures can be identified by spatially resolved X-ray photoemission spectroscopy (XPS).

The modern photoelectron emission spectroscopy (PEEM) technique offers the opportunity to obtain spatially resolved data of a complete surface region in parallel. Although well-established today, only few applications to TMDC substrates have been published yet. No WSe_2 -related work using PEEM was reported, except for brief remarks in reference [86]. The Rb-covered surface of WSe_2 shows a large variety of effects concerning the electronic properties (see part I of this work) and self-organized structuring [11]. The possibility of spatially resolved XPS studies using synchrotron radiation allows for tracing structure formation processes with chemical resolution and to reveal potential interactions between all observed effects.

This part of the work is dedicated to PEEM studies of the surface of $WSe_2 : Rb$. First, some experimental issues concerning the preparation of layered crystals for PEEM are discussed (chapter 8). As no detailed experience with handling TMDCs in PEEM was reported yet, it can be seen as a summary of the know-how that was achieved during several beamtimes.

Some technical imperfections of the actual experimental setup usually degrading PEEM data could be compensated prior to data processing, so the full information gathered

during the experiments can be subject to evaluation. In the course of this work, several data pre-processing routines were developed and are presented in detail in chapter 9. The huge amount of data included in a single XPS spectrum acquired with PEEM requires new approaches to data analysis. Some ideas originating from the field of machine learning theory could be adapted to spectroscopic data. A detailed introduction is found in chapter 10. Based on these techniques, data taken at different operational modes of the PEEM could be processed with great success.

Before discussing Rb-induced effects, the clean surface of WSe_2 was studied in detail in order to provide a solid reference for the following measurements (chapter 11.2). The large scale distribution of adsorbed Rb was probed with photoemission spectra subsequently. Results are presented in chapter 11.4. Spatially constrained adsorption of Rb was carried out in order to probe the mobility of Rb adatoms qualitatively. The relevant findings are outlined briefly in chapter 11.6. Self-organized nanostructures were subject to dedicated X-ray absorption measurements presented in chapter 12.

8. The (S)PEEM experimental station at beamline UE49/PGMa at BESSY II

8.1. Beamline

The experiments discussed in this part of the work were carried out using soft X-ray radiation at the *BESSYII* synchrotron facility. Its major component is a circular storage ring of 240 m circumference, in which electron bunches at relativistic energy (1.7 GeV/e⁻ for BESSY II) are kept on a circular trajectory by strong magnetic fields. As the storage ring is kept under ultra-high vacuum in the range of $1 \cdot 10^{-10}$ mbar, inclusion of electron bunches in this orbit succeeds with extremely low loss. Typical decay constants range between 6 and 10 h. A crucial parameter of the storage ring is the 'ring current' made up by the orbiting electrons. At *BESSY II*, its maximum value amounts to 300 mA.

Modern synchrotron facilities use dedicated devices, the undulators, to produce synchrotron radiation. These are located along the circumference of the storage ring such that the electron beam transits them longitudinally. An undulator consists of at least two parallel rows of permanent magnets, aligned with alternating orientation of the magnetization. Basic electrodynamics predicts the emission of electromagnetic dipole radiation for a beam of charged particles crossing the alternating magnetic field created by the magnetic structure [87]. Because the radiation is produced in the particle's frame of reference, an observer at rest observes the extremely Lorentz-contracted directional characteristic of the radiation, so it appears strongly directed. Synchrotron radiation has a broad spectrum, and its emission characteristic is determined by the parameters of the undulator. The photon energy with highest photon flux grows as particle energy, the periodicity of the magnetic structure, and the magnitude of the magnetic field increase [88]. In practice, the undulator gap, i.e., the distance between the rows of magnets is tuned to maximize the flux at the desired photon energy.

The data presented in this part was acquired at the end station *PGMa* of beamline *UE49*, located at the *BESSYII* storage ring. It is equipped with an undulator of the *APPLEII*-type [123],[89],[90],[91],[92]. This undulator design does not, as usual, consist of two rows of permanent magnets with alternating magnetic orientation, but four (figure 8.1). The purpose of this layout is to establish the capability of selecting

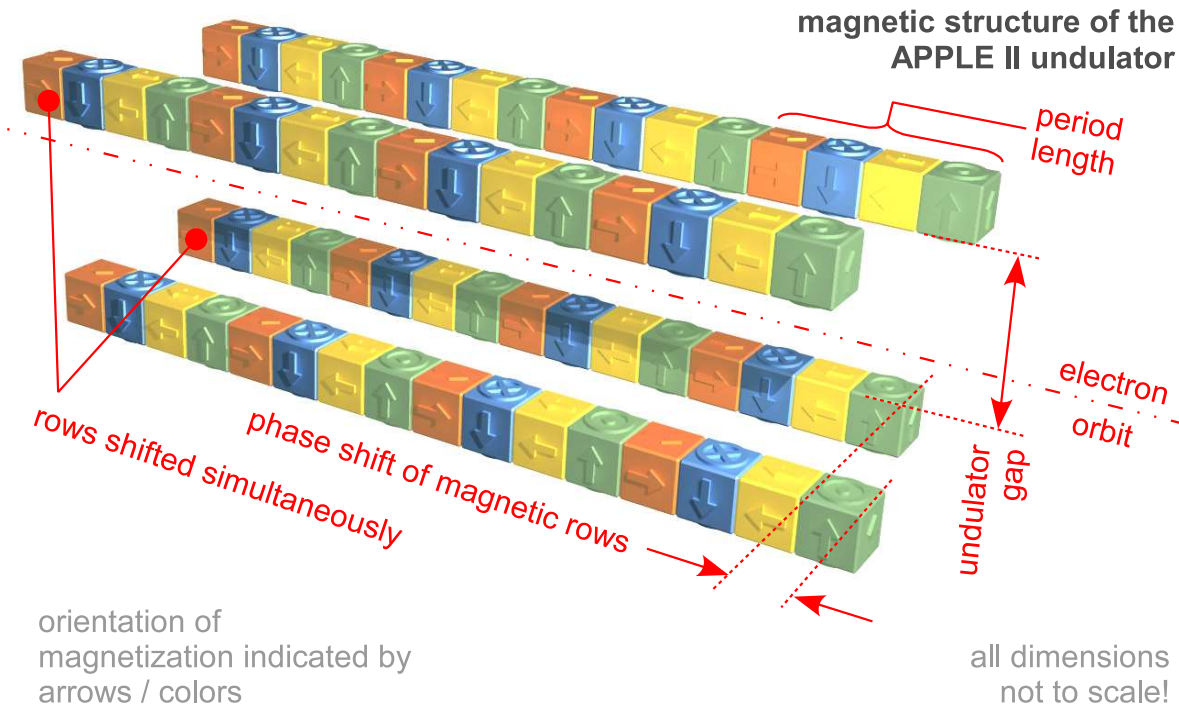


Figure 8.1.: Magnetic structure of the APPLE II undulator design [123] as realized at beamline UE49 (BESSY), for instance. The rows consist of permanent magnets with periodically rotated magnetization (indicated by the arrows). The phase difference of the magnet rows can be aligned free, so radiation with arbitrary polarization can be produced.

a particular type of polarization of the synchrotron radiation. By altering the shift between the rows as depicted in figure 8.1, the creation of linear polarized light with arbitrary orientation is possible. In an alternative mode, the shift can also be configured to create a helical magnetic field in the undulator gap, so circularly polarized light is emitted. Both left-handed and right-handed orientation can be achieved here, as well as intermediate states, i.e. elliptical polarization. Spin-resolving techniques such as X-ray magnetic circular dichroism (XMCD) are based on the spin-dependent interaction of circular polarized soft X-ray radiation with matter. The measurements presented here were carried out using the linear horizontal polarization mode of the undulator.

The specifications achieved at the beam line including this undulator design are presented in the following. A compilation of crucial features is shown in the table in figure 8.2. When the storage ring is driven with typical parameters, a beam divergence as low as 2.3 mrad horizontally and 0.79 mrad vertically are achieved at the beamline.

The beamline is equipped with a reflective plane-grating monochromator (PGM), so monochromatic light is supplied to the experimental station. A grating with 1200 lines

(S)PEEM experimental station @ beamline UE49/PGMa, BESSY

undulator	APPLE II-type		
photon energy range	100 ... 1800	eV	
photon flux	10^{11} ... 10^{13}	$(s \cdot dE)^{-1}$	@ ring current of 100 mA
polarization	variable linear, circular, and elliptic		
energy resolution	$1.5 \cdot 10^4$		@ $h\nu = 300$ eV
monochromator type	plane grating	300 or 1200 lines / mm	
beam divergence	2.3	mrاد	horizontal
	0.79	mrاد	vertical
spot diameter	≤ 30	μm	at sample
operating temperature	110 ... 2000	K	at sample

Figure 8.2.: Typical parameters of beamline UE49/PGMa at BESSY II (following [124],[125])

per millimeter was used during the experiments. The width of the monochromator exit slit can be tuned for an individual trade-off between photon flux and achieved energy resolution. An energy resolution $E/dE \geq 13000$ is found for a $30 \mu\text{m}$ slit in the relevant photon energy range $90 \text{ eV} \leq h\nu \leq 300 \text{ eV}$. When using these settings, the photon flux exceeds 10^{11} photons $\cdot (s \cdot 100 \text{ mA} \cdot dE)^{-1}$, referenced to a beam current of 100 mA kept in the storage ring. In general, a photon energy range between 90 eV and 1800 eV is accessible.

The size of the synchrotron light spot is focused down to $\approx 30 \mu\text{m}$ in the experimental chamber using a reflective focussing mirror setup. It provides an image of the monochromator exit slit at the measuring position, so the beam profile appears Gaussian in one direction and has nearly boxcar-shape perpendicular to the exit slit. As a consequence, the size of the synchrotron spot on the sample will vary as the monochromator slit width is changed.

In electron spectroscopy, intensity monitoring of the incident beam is desirable for referencing the acquired signal, basically because the ring current decays with time and the synchrotron yield at the end station is a function of the desired photon energy. As a direct measure of the total amount of incident photon flux, a reference specimen such as a gold mesh, inserted into the beam, is normally used in photoemission spectroscopy.

At constant spatial arrangement of all components, the photoemission current from the reference is proportional to the incident photon flux at the sample. A direct measure of the total photoelectron yield is given by the photoemission-generated current from the sample holder to ground. Due to the high voltage applied to the sample with respect to the ground, this would not be feasible for the PEEM setup, and a gold mesh might disturb the microfocussing of the beam. Instead, the small amount of absorbed radiation on the last bending mirror of the beamline is measured (the 'mirror current') by the resulting photoemission current. Referencing the flux at different photon energies by the photoelectron yield is problematic in general, as the photoemission cross section strongly varies with photon energy [60]. If this effect needs to be included, using a well-known material like gold is indicated.

The high flux achieved by its small focus size and the vast energy range make the beamline ideally suited for X-ray photoemission and absorption experiments. The optional polarization is a crucial part of experimental methods probing magnetism like the XMCD technique.

8.2. Photoemission Electron Microscopy (PEEM)

In this section, features of the photoemission electron microscopy setup at the end station *UE49/PGMa* are summarized. As in conventional photoemission spectroscopy (PES) (see chapter 4), photoelectrons emitted from a sample specimen are analyzed when using PEEM. In contrast to a conventional photoelectron spectrometer, a photoemission electron microscope includes an imaging stage such that the origin of photoelectrons is imaged with nanometer resolution. It combines electron spectroscopy and microscopy to provide spatially resolved PES spectra.

The actual PEEM setup is made up by the commercially available *PEEM III* (Elmitec GmbH), which is also found today at various synchrotron facilities, among them ELETTRA [93], SPring8 [95], and beamline 11ID-2(VLS-PGM) of the Canadian Light Source (CLS) [127].

Figure 8.3 shows a principle sketch of the complete optical setup. The sample is usually considered part of the optical system, so it was included in the image. Some features of relevant components will be introduced now.

The sample is transported into the experimental main chamber on a dedicated clamping system, where it is fixated on the sample manipulator. Its surface must be aligned precisely with respect to the microscope to grant best imaging quality. For this purpose, the manipulator provides 5 degrees of freedom, 3 translational and a tilt mechanism to match the sample normal with the optical axis of the imaging column. Distance gauge heads give feedback about the transverse manipulator position with respect to the optical axis within micrometer precision. All components of the experiment are kept under ultrahigh vacuum (UHV) conditions with a base pressure $\leq 5 \cdot 10^{-10}$ mbar.

In measuring position, the synchrotron beam approaches the sample at an angle of 16°

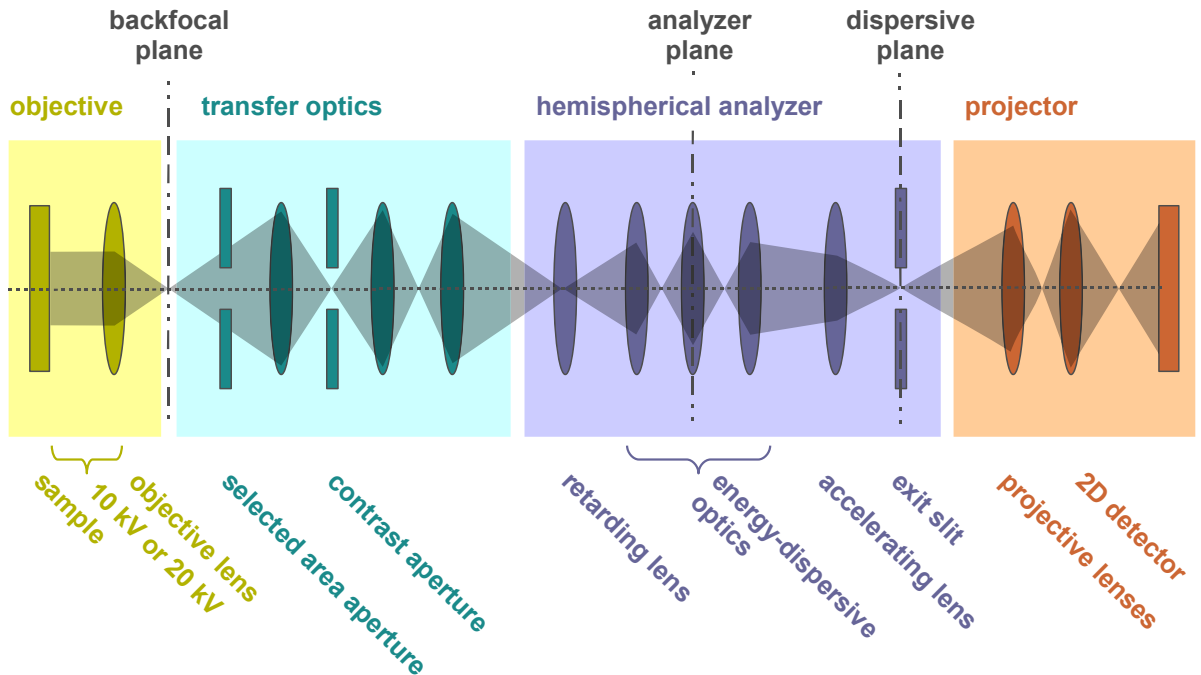


Figure 8.3.: General layout of the optical components of the Elmitec PEEM III photoemission microscope (following [93],[94]).

towards the surface. For alignment tasks, a mercury-arc lamp illuminating the sample at a photon energy of 4.9 eV at the same angle of incidence is used. During measurement, the sample is usually held at a potential of -20 kV against the imaging column (and ground), so the emerging photoelectrons are accelerated and redirected, so all trajectories approximately match the optical axis. The imaging column is made up by a set of magnifying magnetic lenses and several stigmators (not shown in the figure) for image correction. The lenses basically consist of coils and can be tuned by altering the current. This layout has the side effect of rotating images when tuning the lenses, especially when switching the total magnification. One out of a set of contrast apertures can be inserted into the focal plane to limit the angular acceptance of the microscope [96]. This measure is especially important for spectroscopic studies to provide defined energy resolution [97]. Energy dispersion is achieved by means of the hemispherical energy analyzer. For optimal energy resolution, the electrons are decelerated by the retarding lens to a typical pass energy of $E_{pass} = 1250\text{ eV}$. For spectroscopic applications, an exit slit in the dispersive plane is set to define the energy resolution of the analyzer. After passing the analyzer, the electrons are re-accelerated to 20 kV . The projective lenses perform the last stage of magnification and project the image plane onto the detector. Incident photoelectrons are detected by the familiar combination of stacked multichannel plate

(MCP) in a Chevron configuration and phosphor screen (chap. 4.2). The intensified image is digitalized by a low-noise CCD camera. For spin-resolved studies, the electrons can be redirected to a dedicated spin detector using a set of deflectors (blue trajectory in figure 8.4). Further information on design and performance of the *PEEMIII* experiment can be found in [94],[93].

The data that is presented in this part of the work was acquired by using the operating modes that are introduced in the following. The control software basically allows for two different modes.

In the first case, a series of two dimensional images ('image stack') of the surface is recorded at constant photon energy and variable kinetic energy of the photoelectrons ('analyzer scans'). The resulting data represents spatially resolved X-ray photoemission (XPS) spectra. Here, photoemitted electrons emerging from a certain atomic core level or the valence band of the sample are detected to give a measure of the density of electronic states in the sample as a function of binding energy. The signal yield is rather low in this case, as only electrons within a narrow kinetic energy range are detected at a time. The energy resolution is defined by the analyzer settings here and is specified as ≈ 200 meV [128], i.e., considerably worse than achieved with dedicated XPS spectrometers. The best value at suitable flux found during the experiments was only slightly above this.

As the exit slit of the analyzer does not have a distinct position and must be removed for sample alignment, offsets up to 1 eV on the kinetic energy scale are observed after re-inserting or changing slits. Therefore, referencing energies is feasible only among spectra taken at identical slit settings. When scanning large ranges of kinetic energy, chromatic aberration must be taken into account. First, the focal length of the objective lens changes as a function of kinetic energy. In consequence, the lens current must be readjusted when scanning large intervals of kinetic energy. Such feature is not supported by the data acquisition software. Reference [127] gives an impression of the magnitude of correction that would have to be applied. Second, the magnification of the microscope changes as a function of kinetic energy. If an image stack covers a wide range of kinetic energy, pixels off the center of the image do not map a constant point of the sample surface, which would make the data extremely elaborate to interpret. The mirror current gives an acceptable reference of total photon flux in this case, but one should be aware of additional noise being introduced to the data when normalizing. The current ranges in the low nA range and thus includes relative high noise.

The second mode exploits the capability of the monochromator to continuously change the photon energy ('monochromator scans'). The basic idea is to detect the absorptivity of the sample as a function of the photon energy. This would also give access to the spatial distribution of chemical species across the surface, because elements can be identified by their specific absorption edges.

As a measure of absorption, the total secondary electron yield is recorded. Secondary electrons are created by inelastic scattering of a photoelectron traveling to the sample surface, i.e. before emission from the sample. Part of these scattered electrons has sufficient kinetic energy to escape from the sample and to give a characteristic energetic

distribution (the 'secondary electron background'), a roughly exponential decay of intensity with kinetic energy. The energy-integrated secondary electron signal is usually much larger than that from direct photoemission. At constant incident photon rate, the secondary electron yield is proportional to the total absorption coefficient of the sample. Referencing the total photon flux by the mirror current appears to be problematic here as the mirror itself is expected to show energy-dependent absorption. This does not matter in the case of XPS measurements, as the photon energy is kept constant there.

The major part of the emitted photoelectrons is included in the secondary electron background. It has a characteristic, constant shape, so changes of its magnitude are also found when detecting a constant interval in the distribution. As no specific features are found in the secondary electron background, no particularly good energy resolution has to be established in the electron analyzer.

Instead, the total resolution is defined by the monochromator. In this case, it is at least as good as the resolution that could be achieved with the analyzer. Besides the larger signal compared to XPS spectra, the drawbacks of aberrations in the imaging system when scanning the kinetic energy do not occur here, because the imaging column is held at constant settings during a scan. The creation of secondary electrons from absorption of X-rays involves a complex mechanism that includes penetration depth of the sample and escape depth of the photoelectrons, both depending on energy, so a quantitative analysis is hindered for this case. However, the large signal obtained here makes it the method of choice for relative measurements when using the PEEM setup.

8.3. Environment

The PEEM setup is born by a massive, solid aluminum plate to provide maximum flexural stability and inertia. The plate is hooked up into the chassis at its four corners by a combination of tension belts and pressure springs. This construction is meant to grant maximum vibrational decoupling of the microscope from the ground. The chassis consists of a framework made of heavy-load aluminum construction profiles built on an ashlar of solid granite.

As the focus of the beamline measures only $\approx 30 \text{ } \mu\text{m}$, a stable alignment of the sample position relative to the beamline has to be kept up during measurements. For this purpose, the relative position of the experiment's base plate is measured in real time at the bellow connection between experiment and beamline by means of capacitive sensors within nanometer precision. Optionally, an automatic feedback system can be used to align the plate by readjustment of the belt tension.

An photograph of the experimental station and an appropriate schematic are shown in figure 8.4. It is equipped with a dedicated sample preparation and storage chamber. As commonly required for surface analysis, the chamber is kept under ultra-high vacuum. A system of transfer rods allows for transferring samples under UHV into the PEEM. Connected to the preparation chamber, a fast lock load chamber is used to

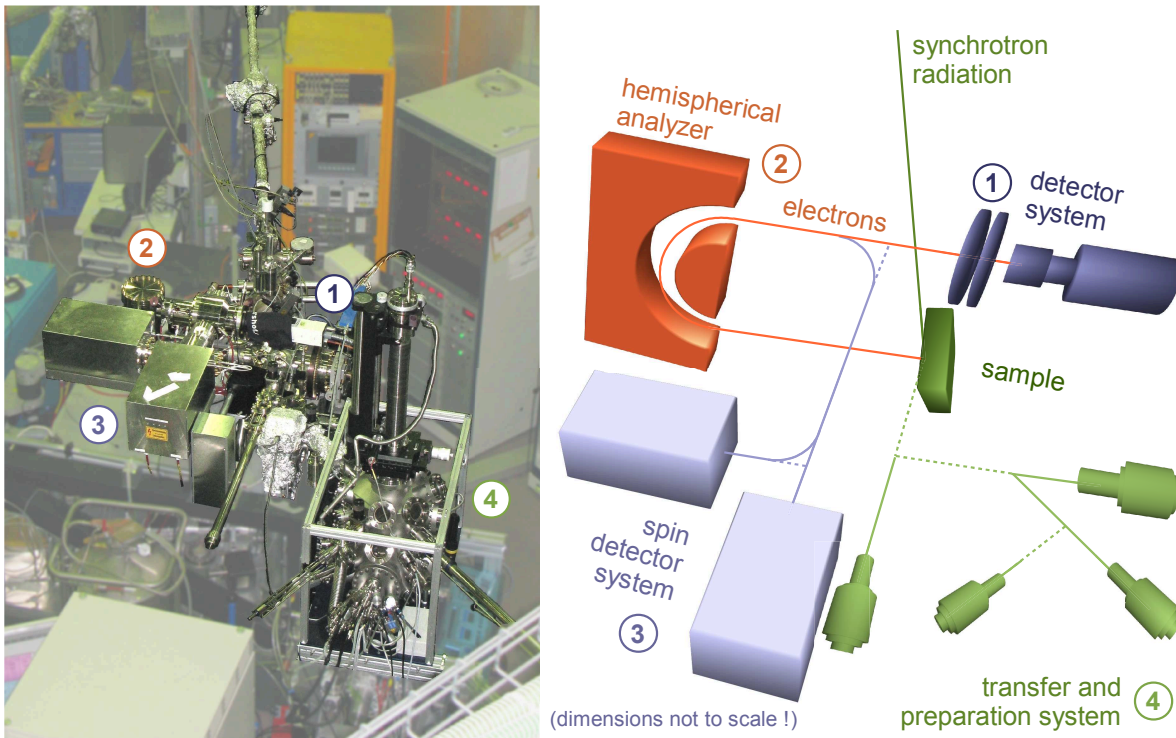


Figure 8.4.: **Left:** Photograph of the experimental station with highlighted components of the experimental chamber. **Right:** Schematic of electron trajectory inside the vacuum chamber as seen in the photograph.

transfer samples into the vacuum system. Sample preparation techniques located in the preparation chamber include sputtering, evaporation of various metals and a device for switching magnetization of appropriate materials. For the experiments discussed here, *SAES Getters* Rb dispensers were mounted to this chamber to give two options. The first one allows for homogeneous Rb deposition on the full area of the sample surface.

Tim Riedel and Dirk Rahn designed a device for locally constrained adsorption of Rb (see figure 8.7) and [98]). It is based on the standard *SAES Getters* Rb dispenser that is enclosed by a housing such that most of the evaporated Rb is screened from the recipient. From [99], it is known that Rb hitting a surface cannot desorb again if the surface is cooled down well below room temperature. All components of the housing are cooled by liquid nitrogen to assure that incident Rb atoms are captured. During operation, the temperature is monitored by a *PT100* resistor that is glued to the device with thermal conductive epoxy, so good thermal contact is granted. The minimum temperature that was achieved amounts to ≈ 100 K, as the heat is dissipated via a flexible copper cord with reasonable thermal resistivity. Even during operation of the dispenser, the temperature does not rise by more than a few *K/min*. When cooled down, the only possibility for Rb to leave the housing is on a straight path from the

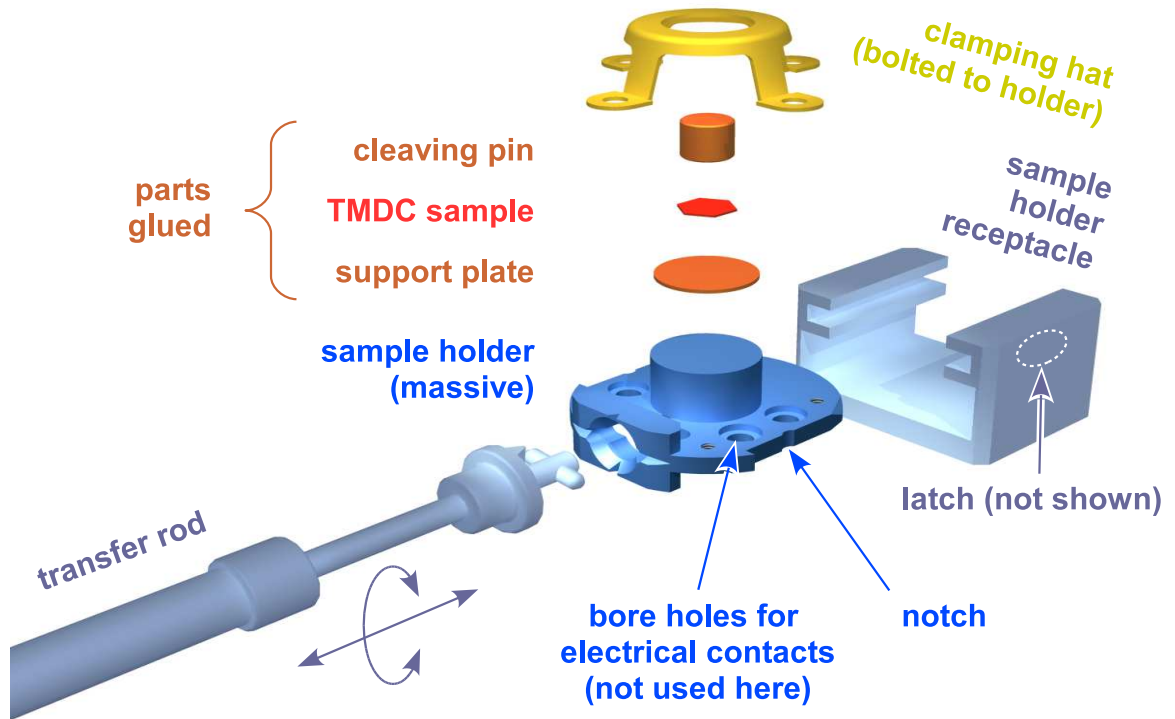


Figure 8.5.: Sample holder system used with the PEEM system with individual modifications. The sample holder has been rebuilt in a massive version to carry platelets with TMDC samples glued on top. Samples prepared in this manner are cleaved in ultra-high vacuum by shearing off the cleaving pin.

dispenser through the slit aperture at the tip of the housing. It is constrained by two aligned silicon wafers with well-defined breaking edges. If broken along a high-symmetric direction of the Si crystal, extremely sharp edges can be obtained [100].

The dispensers are known to evaporate from a well-defined region, which is recognizable as a small trench on the side of the dispenser body. The aperture at the tip has a width of $\approx 200 \mu\text{m}$ and is located $\approx 50 \text{ mm}$ away from the source, so the setup gives a narrow, low-divergent Rb beam. When aligned at most $500 \mu\text{m}$ from the aperture, a defined region on the sample surface is exposed to Rb exclusively. Due to the small Rb-emitting area at the dispenser, the flux density passing the front aperture is not attenuated there. Considerable screening of the evaporating region is found by the circular aperture close to the dispenser (See figure 8.7). The flux density obtained outside the housing is therefore clearly reduced with respect to the unscreened evaporator.

Samples to be probed in the PEEM must be prepared to fit the sample holder system. The systems to be tested here are usually prepared on substrate platelets which are clamped between the body of the sample holder and a tin hat. An outline drawing of the system is shown in figure 8.5. The tin hat is particularly necessary to screen sharp

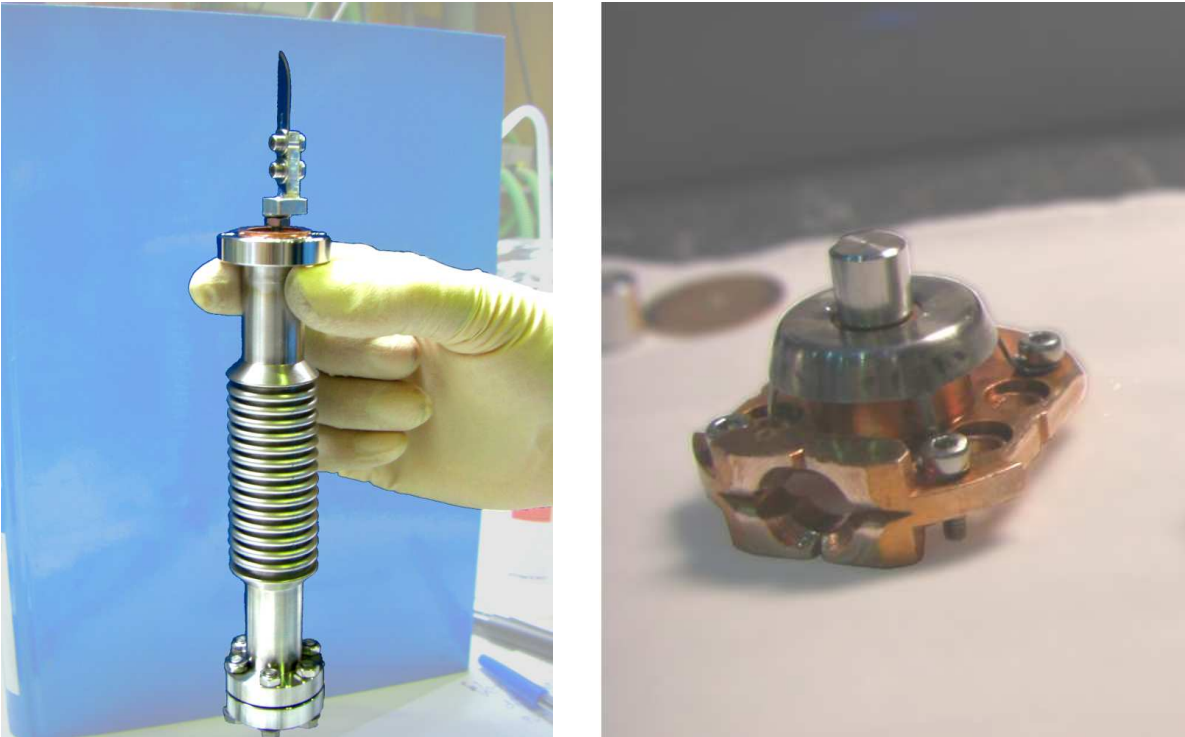


Figure 8.6.: **Left:** Photograph of the scalpel mounted to an improvised wobble stick. The device allows for removal of flakes at the sample surface after cleaving. **Right:** Prepared TMDC sample on the holder system. The cleaving pin on top covers the sample and is sheared off in ultra-high vacuum.

edges of the substrate, as these could cause electric breakdown when exposed to the high voltage in the PEEM. Receptacles for these samples consist of parallel rails, equipped with latches to fit the lateral notches at the sample holder. Additional fixation is achieved by the underneath elastic electrical contacts. The general design of the holder system allows for various features, as four electric contacts can be addressed individually. An available option is a dedicated high-temperature version of the sample holder. It is made of tungsten and provides in situ electron-beam heating of the sample back side. This holder is capable of standing short-term temperatures of 2000 K . For the experiments presented here, some specimen of a simplified version of the sample holder system were fabricated in the mechanical workshop of the Institute of Experimental and Applied Physics (IEAP) at the University of Kiel.

Besides WSe_2 , experiments with further transition metal dichalcogenides have been made at the PEEM experimental station in the past beamtimes [101], [102], [98]. Beforehand, the well-known in vacuo cleaving technique for surface preparation had to be adapted to the PEEM sample holder system. An appropriate solution was found by fixating the samples on sheet metal disks using UHV compatible, conductive epoxy and

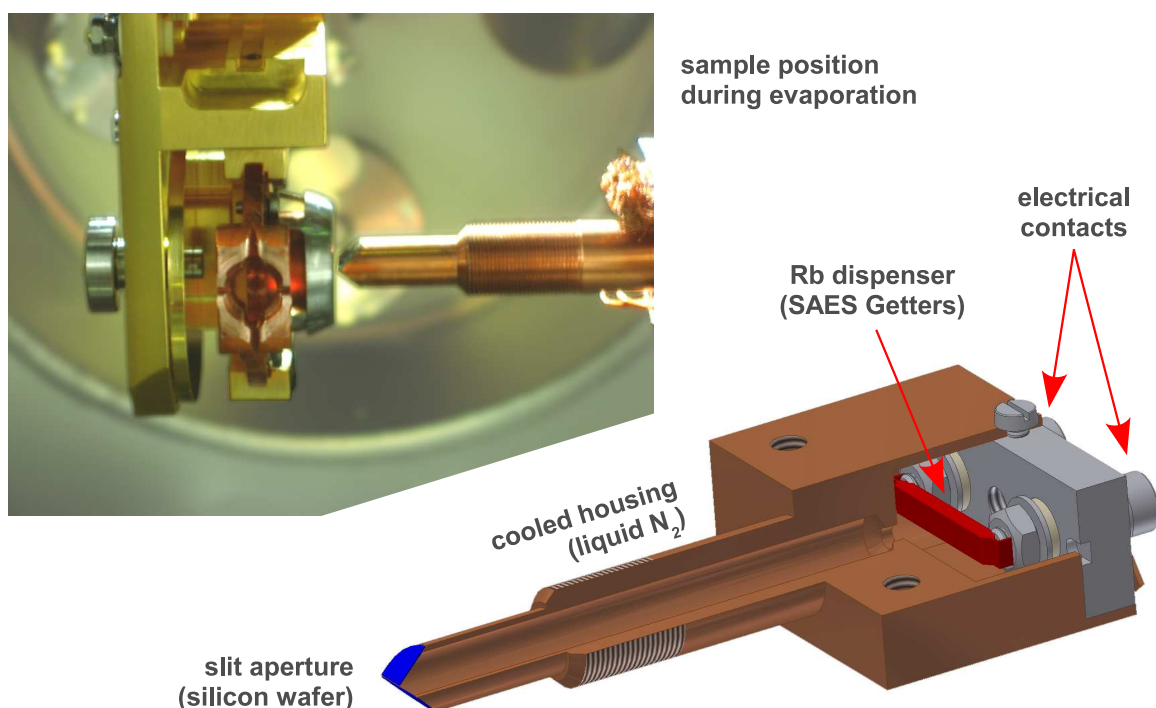


Figure 8.7.: Rb dispenser with slit aperture for spatially confined adsorption of Rb. The device was designed and implemented by D. Rahn and T. Riedel. **Upper left:** In situ photograph during evaporation. **Lower right:** Cross section sketch showing the aperture setup. The slit aperture at the tip constrains the Rb flux. Image by courtesy of T. Riedel.

gluing cylindrical cleaving pins on top (figs. 8.5 and 8.6(right)). The metal disks were designed to fit into the clamping hats of the sample holder system. Several materials were tested, including copper, tantalum, and phosphor bronze. The samples are cleaved *in vacuo* by shearing off the cleaving pins.

Although simple in concept, the adapted cleaving technique requires careful preparation to give suitable results. Glue layers must be kept as thin as possible. Otherwise, the crystal might be bent when pressing it on the metal plate. Bent surfaces significantly reduce the maximum achievable spatial resolution in the microscope as long-range distortions of the accelerating electric field might occur. As the local sample normal must be matched exactly to the optical axis, moving to another site at the sample becomes an elaborate task when the sample is not flat. Despite its lack of flexural stiffness, some specimen showed cracks at the micrometer scale and below after being exposed to high flexure. When preparing samples, establishing a connection between the upper and lower glue layer must be avoided at all costs, as this will cause irregular cleaving and flakes remaining at the surface. Even when taking care of all these recommendations,

small flakes are found quite often remaining at the surface, such that breakdowns in the PEEM occur when ramping up the operating voltage. Small flakes can be removed carefully using a knife edge that is located in the fast load-lock chamber and mounted to an improvised wobble-stick (figure 8.6) without harming the homogeneous parts of the surface.

Florian Kronast (BESSY, Berlin) defined a modified set of PEEM settings, so it can work with a reduced operating voltage of only -10 kV . This measure showed up to be crucial for samples prepared in the manner discussed before. Concerning spatial resolution, the microscope finally showed up to perform almost as good as with the -20 kV setting. Examples can be found in the following chapters. The main limiting factor to achieving the design resolution of the microscope still originates from sample homogeneity, flatness, and size.

When the mentioned topics are dealt with, the PEEM technique can be applied successfully to transition metal dichalcogenides and satisfactory results are obtained.

9. Raw Data Processing

The capability of PEEM to provide photoemission data with spatial resolution results huge amounts of data due to the fact that, potentially, one XPS spectrum is acquired per detector pixel. While the evaluation of a small area in the detector image is sufficient for many applications, the intention of this work is to evaluate as much of the acquired information as possible. For studies exploiting spectral data from the complete detector plane, it must be assured that the obtained signal is not degraded by imperfections of the experimental setup. Though operating the experiment near its optimal settings, some basic limitations cannot be circumvented at the stage of data acquisition.

The origin and the effect of several perturbations of the measured signal could be identified in the experimental data. In this chapter, some methods aiming at the quantification and elimination of these influences are presented. A significant improvement of the data quality by applying these techniques prior to a quantitative analysis is demonstrated. In many cases, the perturbations could be reduced below the threshold of measurability. No further device-dependent, undesired effects were found in the spatially resolved spectra. As a consequence, spectroscopic data from the complete detector image was analyzed in the following.

Many of the methods apply to special circumstances, so they are not considered mandatory. A discussion of the individual preliminaries is found in the corresponding chapters. All methods introduced here were designed and implemented in the course of this work.

9.1. Removal of hot pixels

The magnified and intensified photoelectron image is captured by a scientific CCD camera system, the Sensicam built by PCO systems. Even such high-end devices do not show perfectly uniform sensitivity to light over the detector area. As an effect of aging, single pixels start pretending more or less constant, high incident light intensity, which are usually called 'hot pixels'. They appear as artifacts in every PEEM image at a constant position, so the first step in PEEM data processing is the equalization of these pixels. Beforehand, a reliable identification scheme has to be defined in order to create a list of hot pixels for the current state of the camera. Detecting the brightest hot pixels is trivial, as they show full measured intensity at zero light intensity. A larger set of pixels will show up only occasionally and not as clear as in the extreme cases. In other cases a pixel might have a deviation of the yield factor, so the difference would only show up

at non-zero incident signal. All relevant pixels can be identified from experimental data when referencing the signal of a pixel by its direct neighborhood. A pixel is considered 'hot' when its measured signal exceeds the average signal of the neighbors by a user-defined threshold. In an image stack, if this criterion is met for a certain percentage of all images by one pixel, it is identified as a hot pixel and is added to a list. Once on the list, its measured intensity will be corrected in all images of a series without repeated identification.

Correction of a hot pixel simply means replacing its intensity by the average signal of the pixels in the next neighborhood on the CCD detector. There are two scenarios in which this technique does not give sufficient equalization: First, a hot pixel might virtually have such high incident intensity that the signal measured in the next neighborhood is also increased, an effect called 'blooming'. Second, a locally increased intensity might not originate from the CCD sensor, but from the multichannel plates showing single hot channels, so the CCD detector works correctly, but the MCP stack does not. In both cases, the corrupted intensity measurement is not localized on a single pixel. Whenever several neighbored pixels are affected, this method cannot provide complete validation and it is safest to exclude the affected detector region from further processing by a modified region of interest. Reliable removal of hot pixels showed up to be a crucial measure to prevent further data processing routines from failing. Especially all methods involving data correlation, as applied during the removal of sample drift, for instance, are extremely sensitive to single pixels with extreme measured signals.

9.2. MCP normalization

Besides inhomogeneities of the CCD detector as discussed in the previous section, the image acquisition system shows a lateral variation of sensitivity on a larger scale and a small-scale modulation in a regular pattern. This originates from large-scale inhomogeneity of the gain factor that is achieved with the MCP stack. The effect can easily be seen when operating the microscope with unadjusted objective current such that the imaging optics is unfocussed and a homogeneous incident signal is to be detected. Furthermore, the hexagonal arrangement of the microchannels on the plate leads to a Moiré pattern of variable gain factor if the MCPs are not rotated against each other at an appropriate angle of $\approx 20^\circ$. In order to achieve a homogeneous image, these effects have to be removed by means of a normalization image before proceeding with data analysis.

For this purpose, an image is acquired with unfocussed optics from a region on the sample that must not show large-scale structure. Appropriate images are best acquired using the UV source as it has a very large spot diameter, so no lateral dependence of photoelectron intensity can bias the determination of the lateral detector sensitivity. Because of the strong, non-linear dependence of the MCP gain factor from the applied operating voltage, the magnitude of its variation is expected to depend on that voltage. Therefore, the actual data and the normalization image have always to be acquired at

identical MCP voltage. Normalization can then be applied to each image by dividing the measured intensity by the intensity in the normalization image pixel by pixel. Overall brightness in the image is equalized hereby, except for one kind of artifact. As an effect of wear, individual channels on the plate become 'hot', i.e., they show a significantly increased, roughly constant signal. These defects are usually recognized by an increased measured intensity in an area of some neighbored pixels at constant position. As these pixels do not reflect a real photoemission signal, normalization will not reliably equalize the data. As the hot pixel-detection introduced in the preceding section is not capable of detecting multi-pixel defects in the detected image, it is best practice to exclude such areas from further processing by reduction the region of interest. Brightness equalization was mandatory for all PEEM data presented in this work and has always been applied before analysis unless stated otherwise.

9.3. Beam profile normalization

The microfocus beamline *UE49/PGMa* provides a synchrotron spot with dimensions in the range of a few $10\ \mu\text{m}$. At optimal alignment, the incident beam has a two-dimensional Gaussian profile with a full width at half maximum (FWHM) of approximately $30\ \mu\text{m}$ at the measuring position of the sample. As the spot is made up by the demagnified image of the monochromator exit slit, the Gaussian appears truncated in the vertical direction. In the horizontal direction, the spot appears elongated because of the low angle of incidence of only 16° towards the sample surface. Anyway, its Gaussian shape is clearly visible when operating the PEEM with large field of view. Even at high magnification, an inhomogeneous photoemission signal will be visible due to the beam profile. When analyzing the complete detected image, the lateral brightness variation has to be equalized before data evaluation in order to get a constant signal amplitude from equivalent regions of the image. During acquisition of spatially resolved spectral data, the situation might even get worse when relative motion of the experimental station against the beamline causes a virtual shift of the beam position on the sample surface. Usually, data including beam drift cannot be used for spectral analysis, as it would lead to virtual distortion of spectra from small regions of interest.

9.3.1. Local approximation of the beam profile

In this section, a method will be presented to deal with the inhomogeneous distribution of signal intensity and beam drift. It shows up to be applicable as long as both effects are not too pronounced. Provided the microscope is operated at high magnification with a field of view of $10\ \mu\text{m}$ and below, and the beam drift does not affect the cumulative signal in the image too much, the data can be homogenized.

As the synchrotron spot is much larger than the field of view in this case, the observed photoemission intensity is modulated by only a small section of the two-dimensional

Gaussian, which basically appears as roughly linear position-dependent intensity with a small quadratic contribution. The exact beam profile is not known, because its parameters cannot be determined reliably here. For normalization, taking a reference beam profile has shown up to be pointless, as beam damage will quickly degrade the local emissivity of the sample, such that the spatially detected photoelectron distribution is not proportional to the incident photon flux. As an alternative, a local approximation to the Gaussian is proposed here. Given a region of the sample surface without large-scale spectral features, the intensity distribution $I_0(x, y)$ can be approximated by fitting the two-dimensional image data to the biquadratic function

$$I(x, y) = a_1x^2 + a_2y^2 + a_3x + a_4y + a_5xy + a_6 \quad (9.1)$$

by means of a least-squares minimizer. The complete image is equalized by dividing the signal by the approximate large scale brightness function I then. Afterwards, the complete image is renormalized by a factor such that $\Sigma_{x,y} I(x, y)$ is retained. For a spectroscopic image series, this guarantees that the shape of the spectrum from the total image is retained. As the camera image usually consists of 512×512 pixels, a large amount of noise in the signal of the individual pixel will be tolerated by this procedure. I gives an acceptable approximation to arbitrary sections of a two-dimensional Gaussian within the diameter of the applied field of view. Whenever the statistical noise level is of importance, this procedure has to be handled with great care, as Poisson statistics does not hold any longer for the normalized image. This limitation forbids treating large brightness differences in an image.

As the brightness correction works for a single image, it can also be used well for a spectroscopic image series by individual normalization of each image. The effect of slight drift of the beam during a long term measurement can be ignored after brightness correction.

Although several drawbacks of the procedure are known, and some of them are severe, a method of image homogenization is mandatory for some steps of the data processing chain. The drift correction for the sample (chapter 9.5) is based on cross correlation of images. Whenever it cannot be granted that the image signal is stationary, i.e., no large scale variation of the local mean image signal is found, determination of the relative shift of two images by finding maximum correlation will give a biased result. Stationary data is also required for the data classification scheme introduced in chapter 10 as it tends to discriminate the most dominant features of a data set. This would be intensity in case of unnormalized image data. The absorption spectra discussed in chapter 12 have proven to meet the prerequisites for the normalization method presented here. The algorithm has been applied to that data successfully, so the extremely low contrast of the included features could be classified well into regions near nanostructures near the resolution limit and remote ones.

9.3.2. Referencing at large field of view

Homogenization of the brightness distribution in a PEEM image can be extended to a larger field of view under special circumstances. Then, a simple approximation of the Gaussian profile by equation 9.1 has too low accuracy. A method of dealing with this case will be introduced now. It is especially designed to tolerate moderate beam drift. The demand for a constant position of the synchrotron spot and homogeneous photon flux over the complete field of view cannot be satisfied in most cases, because of the observed drift and a small, systematic shift of the beam position as a function of photon energy. Nevertheless, the signal of two images or spectra acquired at slightly different beam position can still be compared quantitatively when making some assumptions.

As stated above, the beam profile can be described by a two-dimensional Gaussian

$$I(x, y) = \frac{I^T}{\sigma_x \sigma_y \cdot 2\pi} \cdot \exp \left[-\frac{1}{2} \left(\frac{(x - x_0)^2}{\sigma_x^2} \cdot \cos^2 \Theta + \frac{(y - y_0)^2}{\sigma_y^2} \cdot \sin^2 \Theta \right) \right] \quad (9.2)$$

with I^T denoting the 'total' flux which is defined by the beamline and monochromator settings. Values for the complete photon energy range are tabulated and also supervised in situ by recording the 'mirror current' (see chapter 8.1). 'True' values of σ_x , σ_y cannot be stated unless the microscope's field of view is calibrated precisely. According to actual data, the main axes of the beam profile are assumed to have a tilt Θ against the coordinate axes of the image. Finding these parameters in the image might be subject to an appropriate fitting routine, but showed up to have low accuracy and poor overall convergence.

In the following, it is assumed that the beam dimensions are constant, and only the magnitude and center changes between two images. Again, the sample surface has to show up low variation, especially at large scale, so the signal from most of the image area can be considered equivalent.

The task is to find the ratio of intensity-normalized signals I_1^0/I_2^0 from two images or spectra with lateral resolution given the ratio of measured intensities I_1^m/I_2^m . Assume the synchrotron spot has shifted by the vector $(x, y) = (2\alpha, 2\beta)$ between the acquisition of two images. Then the required relation reads:

$$\frac{I_1^m}{I_2^m} = \frac{I_1^0}{I_2^0} \cdot \frac{I_1(x - \alpha, y - \beta)}{I_2(x + \alpha, y + \beta)}. \quad (9.3)$$

Inserting the definition of I from equation 9.2 and simplifying the resulting expression, the beam profile-dependent part of the equation can be written as

$$\frac{I_1(x - \alpha, y - \beta)}{I_2(x + \alpha, y + \beta)} = \exp \left(\frac{2\alpha \cos^2 \Theta}{\sigma_x^2} (x - x_0) \right) \cdot \exp \left(\frac{2\beta \sin^2 \Theta}{\sigma_y^2} (y - y_0) \right). \quad (9.4)$$

Note that the quadratic contributions to the exponent cancel, so the lateral intensity modulation caused by a mismatch between the beam center positions leads to an exponential trend in the signal ratio as function of the coordinates (x, y) . Finding the profile

parameters $x_0, y_0, \sigma_x, \sigma_y, \alpha, \beta, I_1^T, I_2^T, \Theta$ is elaborate and not necessary here, as only the prefactors $2\alpha \cos(\Theta)/\sigma_x$ and $2\beta \sin^2(\Theta)/\sigma_y$ need to be determined from equivalent regions in the data. Rewriting equation 9.4 as below (eqn. 9.5), it can be treated as an optimization problem such that optimal values of a, b, C are found. Due to the large number of pixels that are typically used here, a certain amount of measuring uncertainty will be tolerated.

$$\log \frac{I(x - \alpha, y - \beta)}{I(x + \alpha, y + \beta)} = ax + by + C \quad (9.5)$$

$$\text{with } a = \frac{2\alpha \cos^2 \Theta}{\sigma_x^2}$$

$$b = \frac{2\beta \sin^2 \Theta}{\sigma_y^2}$$

$$C = ax_0 + by_0$$

$$\text{Define } s = \log \frac{I_1^0}{I_2^0}$$

In this representation, a linear relationship between quantities representing measured data and normalized photoemission yield (s) is obtained. Fitting a linear function is naturally much more effective than fitting a Gaussian profile with many more free parameters. The number of degrees of freedom of the fit function is reduced strongly, as the parameters of the Gaussian are united in only three parameters (a, b, C). As a consequence, the true values of the parameters of the Gaussian in equation 9.2 cannot be determined from the fit result. Once the parameters in equation 9.5 are known, all signal ratios in the image can get referenced by normalizing the signal-to-signal ratio with the factor below

$$\frac{I_1^0}{I_2^0}(x, y) = \frac{I_1^m}{I_2^m} \cdot \frac{I_2^T}{I_1^T} \cdot \exp(-ax - by - C) \quad (9.6)$$

to derive information on the relative photoelectron yield at normalized flux. This method showed up to be especially useful to recognize relative changes of the chemical composition of a surface by means of the XPS emission signal ratio of core levels of different atomic species. With this intention, removal of the beam profile from the data was applied to the data presented in chapter 11.2.

9.4. Calibration of the lateral variation of the photon energy

Synchrotron radiation has a broad photon energy distribution when produced in an undulator. Spectroscopic techniques based on the photoemission process require monochromatic light, so a narrow interval of the broad spectrum has to be picked by means

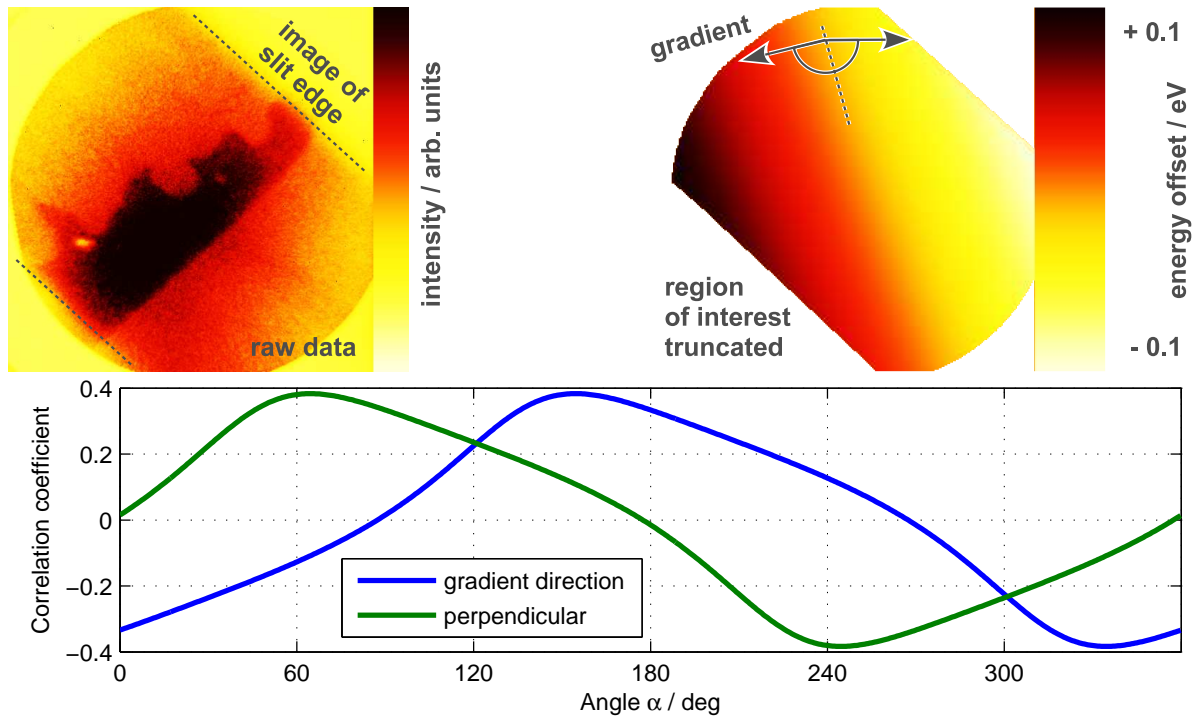


Figure 9.1.: The dispersion of the monochromator causes a small lateral variation of the photon energy, which results in a small virtual shift of substrate core levels across the detector image. After the magnitude and direction of the gradient has been estimated from actual data (**upper right**), this effect can be eliminated from experimental data assuming a linear dispersion. A certain amount of structures, as seen in the raw data image (**upper left**), is tolerated by the procedure. **Bottom**: Cross correlation function of the measured binding energy of a core level with the position in the detector image as a function of the direction (see text). Raw data: XPS spectrum of $W\ 4f$ core level, $h\nu = 147\text{ eV}$, $\text{FOV} \approx 25\ \mu\text{m}$.

of a monochromator. In the case of beamline $UE49/PGMa$, a plane grating with a line density of 1200 mm^{-1} is used as dispersive element. Incident at a small angle versus the grating surface, the 'white' light is split into its spectral components by diffraction, so the mean photon energy of the diffracted beam becomes a function of its angle versus the grating surface. The width of the exit aperture defines the small photon energy range, i.e. a small fraction of the total photon flux, that is transmitted through the monochromator. Adjusting the width allows for finding an individual tradeoff between monochromaticity of the transmitted beam and the flux.

As the size of the radiation source is finite, a photon energy distribution with finite width is found for every diffraction angle at the grating. Its dependency from the exit

angle causes a slight variation of the mean transmitted photon energy across the exit slit. As already discussed before, a demagnified image of the exit slit is projected on the sample surface, so the synchrotron spot includes noteworthy dispersion. Therefore, a small virtual shift of the resulting photoelectron spectra with position is observed. At a mean photon energy of 150 eV and a moderate slit width of 0.5 mm, a variation of ≈ 200 meV is found across the synchrotron spot. This value is in the range of the analyzer resolution. For studies at small regions of interest, when only an excerpt from the total detector image is processed, or when working at high magnification, it can easily be ignored. Otherwise, a correction technique that is presented in the following might be applied.

The observed dispersion includes only a small percentage of the photon energy, so it can be assumed linear here. Although the orientation of the slit apertures can clearly be identified in the image, the photon energy gradient is not necessarily perpendicular to the edges of the aperture, which would be the ideal case. Thus, both the direction and the magnitude of the monochromator dispersion have to be calibrated from photoemission data. Given a spatially resolved core level spectrum of an arbitrary substrate core level, its peak kinetic energy is determined with one-pixel spatial resolution using the data reduction and reconstruction technique introduced in chapter 10.2. Assuming lateral homogeneity of the sample surface, the peak kinetic energy only depends on the excitation photon energy.

The direction of the dispersion gradient is determined as follows: After data reconstruction, the lateral distribution of peak kinetic energy (E_j at positions (x_j, y_j)) is known for typically $N = 45000$ data points (at 256×256 pixel resolution of the detector image). Although the reconstruction technique is known to provide smooth spectra, even at low signal, a remaining amount of statistical uncertainty of E_j has to be tolerated. Therefore, correlation is a suitable measure here. The direction α^* of the gradient is found by maximizing the correlation coefficient between E_j and $p_j(\alpha) = x_j \cdot \cos(\alpha) + y_j \cdot \sin(\alpha)$ subject to α . The huge number of data points results in an extremely smooth estimate of the correlation coefficient as a function of α with pronounced maximum, so the experimental direction α^* of the gradient can be determined within a precision of $\leq 1^\circ$. Once α^* is known, the magnitude of the dispersion is found by fitting the data points $(p_j(\alpha^*), E_j)$ by a linear function using least-squares minimization.

The statistical approach of maximum correlation showed up to be suited well for realistic cases. No dedicated calibration spectra are required to apply this method and even a non-homogeneous signal in the image will be tolerated as long as the sample does not show a large-scale gradient of binding energy for the chosen core level. For instance, the spectra discussed in chapter 11.4 were corrected using the presented method. They were acquired during a beamtime in December 2008, when the beamline had a known misalignment. For this data, the photon energy variation as found from the fit procedure is shown in figure 9.1. The calibration data was acquired at an exit slit width of 500 μm , a field of view of the microscope of ≈ 25 μm , and an acceleration voltage of -10 kV.

Here, a direction of the photon energy gradient against the positive horizontal of 158.7° was found. The magnitude derived from the data amounts to $8.46 \cdot 20^{-4} \text{ eV} \cdot \text{pix}^{-1}$ for a reduced resolution of the raw data image of $256 \times 256 \text{ pix}$. As can clearly be recognized, the dispersion direction is tilted by some degrees against the normal of the slit edges. The magnitude of the dispersion is correct only for the photon energy of $h\nu = 147 \text{ eV}$ used here. The direction can be considered constant as it presumably originates from the relative alignment of the monochromator grating and slit aperture.

Single-pixel data discussed in the following chapters was corrected with a kinetic energy offset as found from the linear dispersion calibration data. Whenever a set of pixels is accumulated, the mean shift of all participating pixels is used as offset. Before intensities are summed up to the total signal, the individual offsets are rounded to the discrete steps of the energy scan. The error introduced hereby potentially affects spectral properties such as the measured full width at half maximum of peaks. This effect is considered negligible for the data discussed in this work, as the energy steps usually amounted to 100 meV , while the combined energy resolution of the beamline and the electron analyzer ranges between $\approx 200 \text{ meV}$ and $\approx 500 \text{ meV}$, depending on the actual settings.

9.5. Drift correction

Acquisition of large sets of PEEM images takes a rather long time. For spatially resolved spectra, it takes between 30 and 90 minutes to gather sufficient signal for an appropriate number of energy steps, even at moderate magnification. The signal per unit detector area obtained at smaller fields of view require even longer acquisition time. During this interval, the sample position usually cannot be kept constant with respect to the imaging column within the required precision of some 10 nm . The reasons for the drift of the sample can be found when the mechanical setup of the sample manipulator is taken into account. As the system can never be decoupled completely from the environment, even small external mechanical shocks transmitted via the chassis to the PEEM setup can lead to minimal misalignment of the sample. Hence, long scans are recorded with much higher stability during night shifts, when the operation of large machines like the overhead crane is reduced to a minimum level. Second, and even worse, another reason for sample drift is found when switching between the photoemission light sources. The UV arc lamp has a nominal power of 100 W . Even though only a small amount of this is irradiated in the UV range, and transmission of the light into the experimental chamber is constrained by an iris aperture, the small heat load at the sample and its holder by UV absorption is suspected to cause small, yet visible thermal deformation of the manipulator. Strong drift occurring after switching the UV source on or off, i.e., changing the stationary heat load of the sample holder system, gives a strong hint for the significance of this mechanism. When spectroscopic data is to be evaluated at one-pixel precision, the drift motion of the sample has to be corrected before extracting

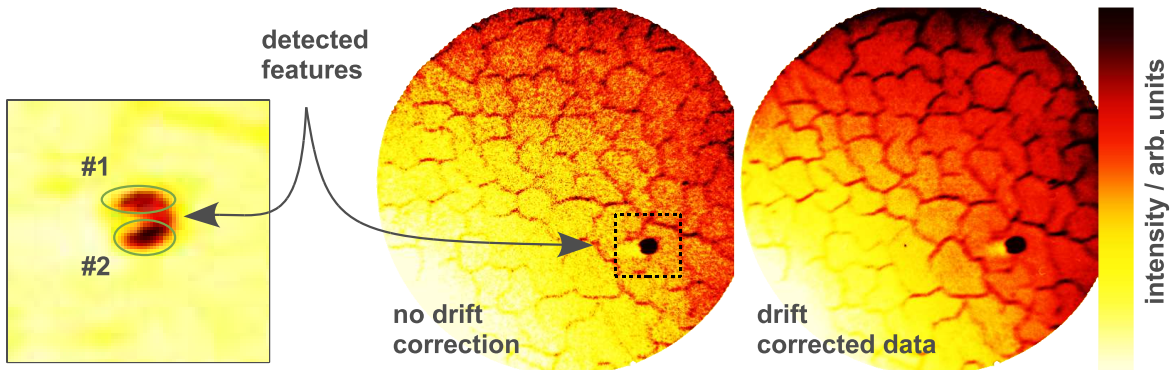


Figure 9.2.: Cumulative raw data images of a series (83 images) detected under identical settings of the system (UV source, $h\nu = 4.9 \text{ eV}$, $\text{FOV} \approx 25 \mu\text{m}$). Drift removal by tracing distinct features clearly improves the match between the single images. A clear reduction of the blur and an enhanced contrast of the cumulative intensity result.

the signal from single pixels in the data. The mechanical drift motion can hardly ever be suppressed completely, so an approach to find and correct the motion of the sample is motivated here. For this task, specialized algorithms have been developed and are presented in the following.

9.5.1. Feature tracing

Whenever the signal from the sample has sufficient spatial structure, i.e., the signal includes low statistical noise and features such as point defects, step edges etc. can be identified in every single image of a stack, the following algorithm is best suited. Small particles on the surface are quite common, so the technique will be introduced assuming point defects as reference. First of all, the position of a feature has to be identified within each image, so the relative shift can be nullified by the correction algorithm. A feature is made up here by a locally confined deviation of the signal amplitude from the surrounding region. Combined contrast enhancement and smoothing by applying a linear image filter (section 14.2) showed up to result stable discriminators for feature identification.

A feature is identified by simply applying a custom brightness threshold, turning the gray-scale image signal monochrome. In this representation, a feature consists of a cluster of interconnected pixels of one color. Artifacts originating from statistical noise can be suppressed by claiming a minimum cluster size. The feature position is found by computing the center of mass of all pixels in a cluster and is thus a real number. In the general case of more than one feature per image, a criterion for assigning features of two subsequent images is required. Here, the lowest possible shift between two images is assumed. Hence, between members of two sets of features from two images, clusters

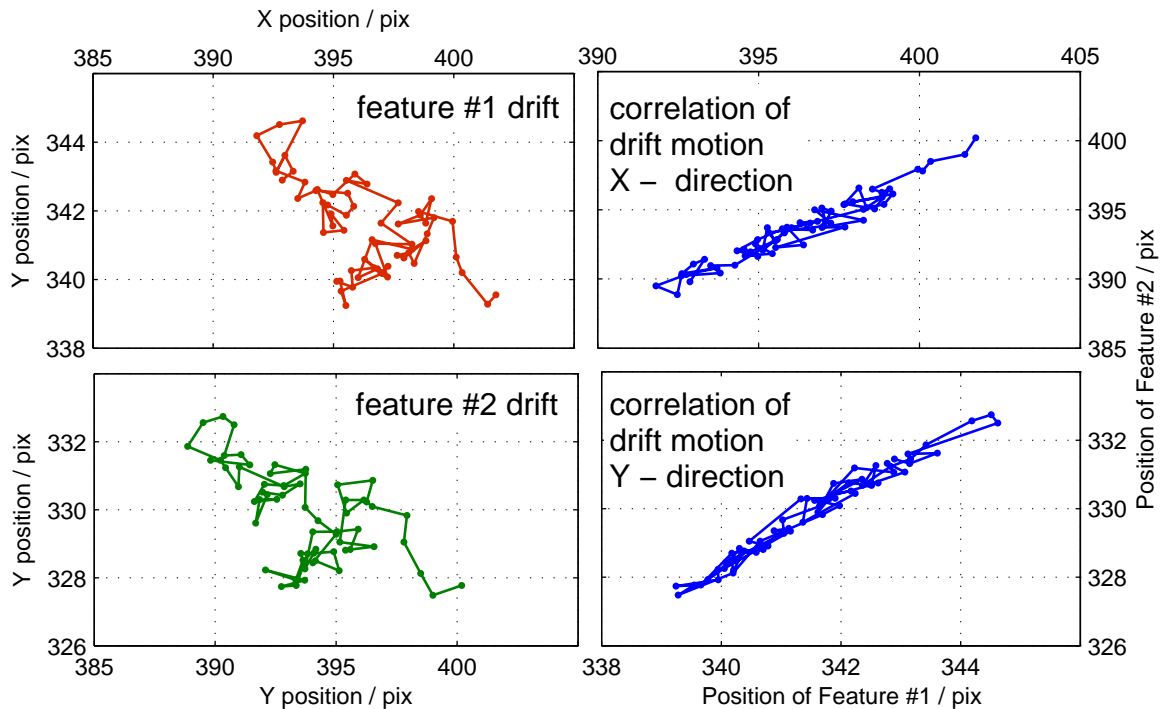


Figure 9.3.: **Left:** Trajectory of the features shown in figure 9.2. Each data points originates from one image in the raw data series. Removal of this drift results highly improved contrast in the cumulative raw data. **Right:** The data from both features shows up to be highly redundant, as nearly identical information is obtained from both trajectories.

with the smallest Euclidean distance are assigned and considered to represent the same feature in both images.

Applying this technique to an image stack gives the individual drift trajectory of every feature. Neglecting tolerances of the data processing procedure and noise in the data, all trajectories are assumed to include identical relative shift, so the information in a single trajectory would be sufficient for drift removal. The conclusion is valid provided that a constant magnification factor is found for the complete field of view. This preliminary might be violated when using a large field of view with diameter $\geq 50 \mu m$. Here, a considerable distortion of the image is usually found with increasing distance to the optical axis, i.e., the center of the image. Under these circumstances, the drift correction found for one feature is not valid for the complete image.

When applied to data with negligible imaging error, the technique is highly redundant and proved to be stable even for noisy data, when not every feature can be detected reliably in every image. The spread of several feature trajectories might be analyzed to gain an impression of the uncertainty of the results. As relative shifts $(\Delta x_j, \Delta y_j)$ between

subsequent images j and $j + 1$ in a series of N images are determined by this procedure, the actual drift correction is done by shifting images $j + 1, \dots, N$ by $(-\Delta x_j, -\Delta y_j)$. As the interpolation between pixels should be avoided, the relative shift is always rounded to integer values.

An example of the performance of the algorithm is depicted in figure 9.2. It was applied to a series of 83 images taken at constant PEEM settings using the UV source. In the left panel of the figure, the cumulative intensity of the uncorrected data is shown. The right panel shows the result after correcting the images by the drift trajectory shown in figure 9.3, which has been derived by tracing a single feature (see inset of the figure). Comparing the images before and after drift correction, it is clearly found that all structures get more pronounced and reveal sharper boundaries as the drift is compensated. Although there is no proof that the drift is removed completely from the data, the example at least indicates a strong reduction.

9.5.2. Drift correction for low signal level

The algorithm presented in the preceding section requires a rather large signal, such that features are recognizable within every single image of a scan. Here, an alternative method of drift correction is introduced, that is also capable of dealing with low-signal images. Whenever a region of the sample does not show localized structures, the statistical approach made here is still feasible. Even at a high level of statistical noise in the data, the cross correlation between the pixels of two images as a function of the relative shift will still have a sharp maximum with a typical full width at half maximum (FWHM) of ≤ 2 pixels at the most likely shift. In order to derive meaningful values of the cross correlation function, the statistically distributed intensity of pixels mapping equivalent regions of the sample surface should have constant expectation value and standard deviation throughout all images in a series. This is of particular interest for intermediate to large fields of view, where the spot profile of the synchrotron radiation usually gives a brightness gradient. Finding the largest correlation would yield a fit of the spot profile, not of the structures found on the sample. Therefore, the data must be referenced to its direct environment by a linear filter as discussed in chapter 14.2. The result of applying the filter to the raw data can be regarded as kind of smoothed second derivative. Assuming that the brightness gradient caused by the spot profile is much smaller than the gradients found by structures on the surface, the effect of inhomogeneous brightness can be reduced to a tolerable level.

Once the beam profile is eliminated from the data, the cross-correlation function is computed for finite, integer steps of relative image shift $-N \leq \Delta x \leq N, -N \leq \Delta y \leq N$. For improved stability, the optimal shift is found by the weighted mean of the shift values showing highest values of the cross correlation function. The weights are found as a function of the cross correlation coefficients. As this technique is designed to work with low signal, the significance of correlating two subsequent images in a series might be too low for a reliable determination of the shift.

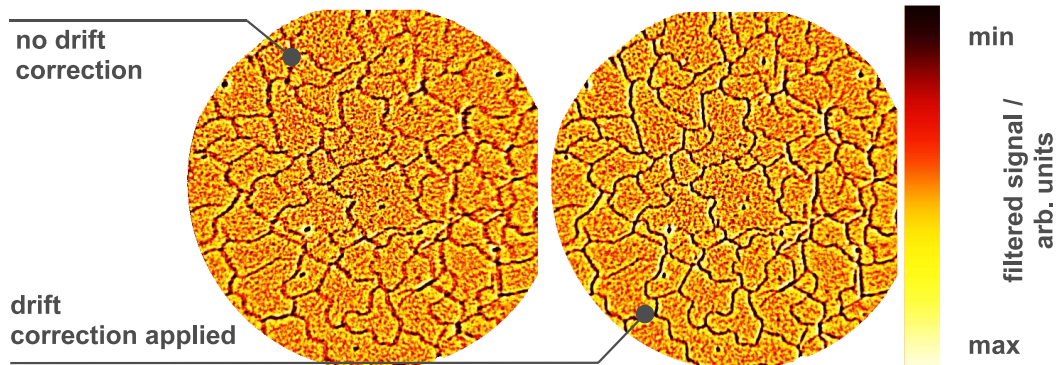


Figure 9.4.: Result of drift correction by image cross correlation for low intensity image stacks. The data consists of a series of images acquired under constant conditions using the UV source ($h\nu = 4.9 \text{ eV}$) and a FOV of $\approx 10 \mu\text{m}$. The shown images represent the cumulative intensity of the complete series. Both images were filtered (section 14.2). The drift corrected data set clearly shows pronounced structure and enhanced contrast.

Instead, the following strategy is pursued: The drift trajectory of the sample can be assumed continuous and in common cases, it will show monotonous behavior. Here, an approach operating on the complete image series can be made to reduce, not remove, the drift motion stepwise. The significance of cross correlation can be enhanced by correlating the cumulative intensity of images $1, \dots, j$ and $j + 1, \dots, N$ and then correcting the relative shift of images $j + 1, \dots, N$. Arbitrary drift trajectories can be found successively when repeating this process for an alternative choice of values of $2 \leq j \leq N - 1$. After having removed the drift partially by correction for a single value of j , the overall sharpness of the cumulative images for the alternative choice is increased, so a smaller FWHM value of the cross correlation function is found as the procedure is repeated. Thus, the precision of relative drift determination is increased in subsequent steps. The current implementation of the algorithm uses a series of $j = N \cdot (\frac{1}{2}, \frac{1}{4}, \frac{3}{4}, \frac{1}{8}, \frac{3}{8}, \frac{5}{8}, \dots)$. In practice, all segmentations j of the image series must be tested in several repeated runs until the determined shift has converged.

One type of artifact in the data has shown to be remarkably important for proper drift correction: Although most of the camera's hot pixels can be identified and removed by the dedicated hot-pixel removal algorithm (section 9.1), the most probable reason for this drift correction algorithm failing is the presence of hot pixels with only slightly increased intensity or just occurring occasionally. Both cases have been observed when using the Sensicam CCD camera. Naturally, these pixels always appearing at a constant position on the detector leads to an artificially pronounced correlation between images at zero shift. This effect showed up to bias the drift correction technique significantly, so the correlation coefficient at zero shift has to be excluded from computing the most likely shift.

A profound validation of the method presented here was carried out with the dedicated measurement of an image series at constant settings of the PEEM. As no further side effects were expected here, the effect of drift compensation becomes clear. Referring to figure 9.4, the contrast of the cumulative intensity of the image stack is increased significantly and the sharpness of the structures is improved strongly by applying the algorithm. The correction technique could be applied successfully to the XPS absorption spectra presented in chapter 12, although the high magnification applied there lead to a pronounced effect of the drift and a very low average signal level. The imaged structures were found to have extremely low contrast, such that an identification with the naked eye is almost pointless. Nevertheless, application of the drift correction routine discussed here gave a robust estimation of the sample drift, so that the structures could easily be identified in the corrected data.

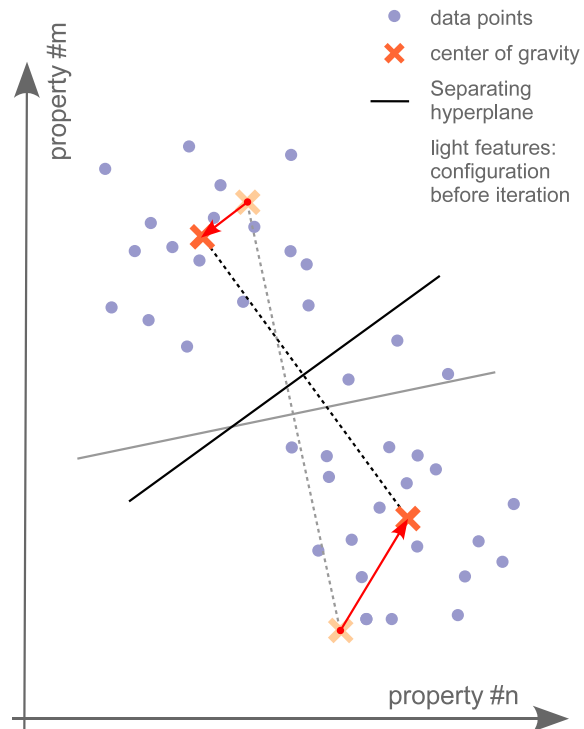
10. Data classification scheme for PEEM data

In comparison to conventional XPS spectroscopy, the PEEM technique potentially yields much more information by supplying spatial resolution down to a theoretical resolution of 20 nm in case of the Elmitec PEEM III. Using standard settings, the detector system acquires images at a resolution 512×512 pixels, giving ≈ 200.000 data channels within the circular region of interest, which is defined by the outline of the MCP stack. From each pixel, a complete spectrum can potentially be extracted, so a huge number of data channels is usually detected in parallel.

The total amount of information found in the set of data channels might not be obvious. Although the microfocus beamline *UE49/PGMa* supplies very high flux, the signal found in a one pixel-channel will usually have an insufficient signal-to-noise ratio for quantitative evaluation. The usual way to increase the signal quality is to introduce a binning of the signal from channels that are considered equivalent. In general, this casts the new complication of recognizing equivalent regions. A novel strategy dealing with the extremely high number of data channels with rather low quality is pursued here. As will be shown, it is especially suited to exploit the full potential of spatially resolved electron spectroscopy. An approach originating from the field of machine learning theory is presented in this chapter. It works for XPS and absorption spectra as well as for arbitrary multichannel data. The results derived from actual experimental data (chapter 12) were found using this technique and several application examples can be found there besides the demonstration data discussed in this chapter.

Here, the case of *XPS* spectroscopy will be treated, but the equivalent holds for an absorption spectrum. The considerations are based on an alternative representation of the image stack, i.e., the spatially resolved spectra, which is introduced in the following. As a spectrum consists of a series of signal values $I(E_i)$ at distinct kinetic energy E_i , $i = 1..N$, it can also be represented as a vector in N -dimensional space with components $(I(E_1), I(E_2), \dots, I(E_N))$. Then, the information gained from all M pixels during a scan is represented by a set of M discrete points in that space, called 'spectral' space in the following. Without further constraints, this space includes all possible spectral distributions with no respect to their physical origin. The data in channel k is denoted by I^k ($k = 1, \dots, M$) below.

Figure 10.1:
 Determination of a hyperplane in parameter space such that a set of data points is separated along the axis of maximum variance. The features show the configuration before an iteration step (light colors) and after (dark). The procedure can easily be generalized to process an arbitrary number of dimensions.



10.1. Separating Hyperplane

Although the low signal-to-noise ratio of the individual data channel makes the interpretation of its spectrum nearly impossible, valuable information can be obtained by referencing its position in spectral space to the distribution of all M data channels. The first thing to do is to figure out the vector in spectral space with maximum dynamic range of the projection of all data points to this vector. Geometrically speaking, this means to find the main axis of the distribution of points. This task is performed by a simple iterative algorithm, whose pseudo code representation is shown below. Assume the data is enclosed by the N -dimensional interval

$$Q = \{x \in R^N \mid \min \{I_j^k, k = 1, \dots, M\} \leq x_j \leq \max \{I_j^k, k = 1, \dots, M\}\} \quad (10.1)$$

for all $j = 1, \dots, N$, i.e., Q is the bounding box of the complete data set with edges aligned to the coordinate axes. The algorithm reads:

- (1) r_0, s_0 : random vectors out of Q
 $R_0, S_0 = \{\}$ // empty set
 $i = 0$
- (2) find Hessian representation of affine hyperplane
 $(x - b) \cdot m = 0$
 with
 $b = (r_i + s_i)/2$
 $m = (s_i - r_i)$
- (3) separate all points into two sets R_i, S_i such that
 $(I^k - b) \cdot m < 0$ if $k \in R_i$
 $(I^k - b) \cdot m > 0$ if $k \in S_i$
- (4) if $(I^k \in R_i) \oplus (I^k \in R_{i-1})$ for all $k = 1, \dots, M$
 \Rightarrow done
- (5) set r_{i+1} = center of gravity of points in R_i
 set s_{i+1} = center of gravity of points in S_i
- (6) increment i
 proceed with (2)

Starting at random positions, an affine hyperplane H in spectral space, the so-called separating hyperplane, is found. For two dimensions, the separating hyperplane is depicted in figure 10.1, but the following holds for an arbitrary number of dimensions. It is oriented such that the vector $m_i = s_i - r_i$ is perpendicular to the plane and a supporting vector is given by $b = (r_i + s_i)/2$. The Hessian representation of H , $(I - b) \cdot m = c$ is used then to separate the data points into two subsets which can be interpreted to be located 'left' ($c < 0$, elements of R) and 'right' ($c > 0$, elements of S), respectively, of H ($c = 0$). Then, the procedure is iterated with updated r and s until the assignment of points to the sets R and S has converged. Convergence is reached when the sets R and S did not change during an iteration step. The \oplus in step (4) represents logical exclusive disjunction (XOR). The algorithm is likely to separate the data along the direction of maximum variance [103].

After converging, the vectors r and s , representing the cumulative spectra from the two subsets R and S , can be seen as a solution of the problem of partitioning a set of M points into two disjunct subsets such that the difference between the sets is maximized. In general, such problems are extremely difficult to solve by a combinatorial approach, as this potentially requires to check 2^M configurations. With respect to the problem of

identifying regions with equivalent signals, the solution found here can be regarded as a reduction of that problem.

As r and s contain the combined signal of approx $M/2$ data channels, they will usually be very smooth. This property can be exploited when evaluating spectroscopic data. Some implications on the application are discussed in the following.

10.2. Data Reduction

The concept of finding the main axis of a distribution of data points in spectral space can be generalized to find a system of main axes. To find further main axes by means of the algorithm introduced in the preceding section, a reduced representation of the data set needs to be derived. Therefore, each data point (i.e. spectrum) $I^k \in Q$, $k = 1, \dots, M$ is transformed to the combination of its projection $I_{(1)}^k$ onto the first main axis m_1 and its projection $J_{(1)}^k$ into the $N - 1$ dimensional hyperplane H_1 .

$$\begin{aligned} I^k &= m_1 \cdot I_{(1)}^k + J_{(1)}^k \\ J_{(j)}^k &= m_{(j+1)} \cdot I_{(j+1)}^k + J_{(j+1)}^k \end{aligned}$$

Then, a separating hyperplane H_2 is found for all data points $J_{(1)}^k$; $k = 1, \dots, M$, which are elements of H_1 . As the separating hyperplane H_1 is perpendicular to the first main axis m_1 , the two main axes m_1 and $m_2 \in H_1$ are also perpendicular. When this procedure is iterated $j \leq N$ times, j main axes m_j are determined. For $j = N$ steps, a new affine basis with orthogonal base vectors of spectral space is made up by the vectors m_j , so the data can be represented in an equivalent way using this basis without loss of information:

$$I^k = b + \sum_{j=1}^N m_j \cdot I_{(j)}^k \quad (10.2)$$

It can be shown that the supporting vector b is constant for all projections and represents the center of gravity of all I^k . As stated above, the separating hyperplanes found in each step will be oriented such that maximum variance of the data points is found along the accordant main axis.

For actual data, the variance of the projections $I_{(j)}^k$ shows up to decrease rapidly with j (assumed the vectors m_j are normalized to unity), so higher terms of the linear combination in equation 10.2 do not contribute much to the sum. This can be exploited to derive an approximate representation of the data points in spectral space by neglecting higher terms. This approximate representation has some remarkable properties: Spectral space usually has a huge number of dimensions in the order of 10^2 , making data handling quite laborious and overestimating the number of degrees of freedom in a spectrum by far. Taking into account only the first few terms in equation 10.2 (in practice: $N \leq 5$) reduces the dimensionality a lot, but still gives a good estimate of the original data

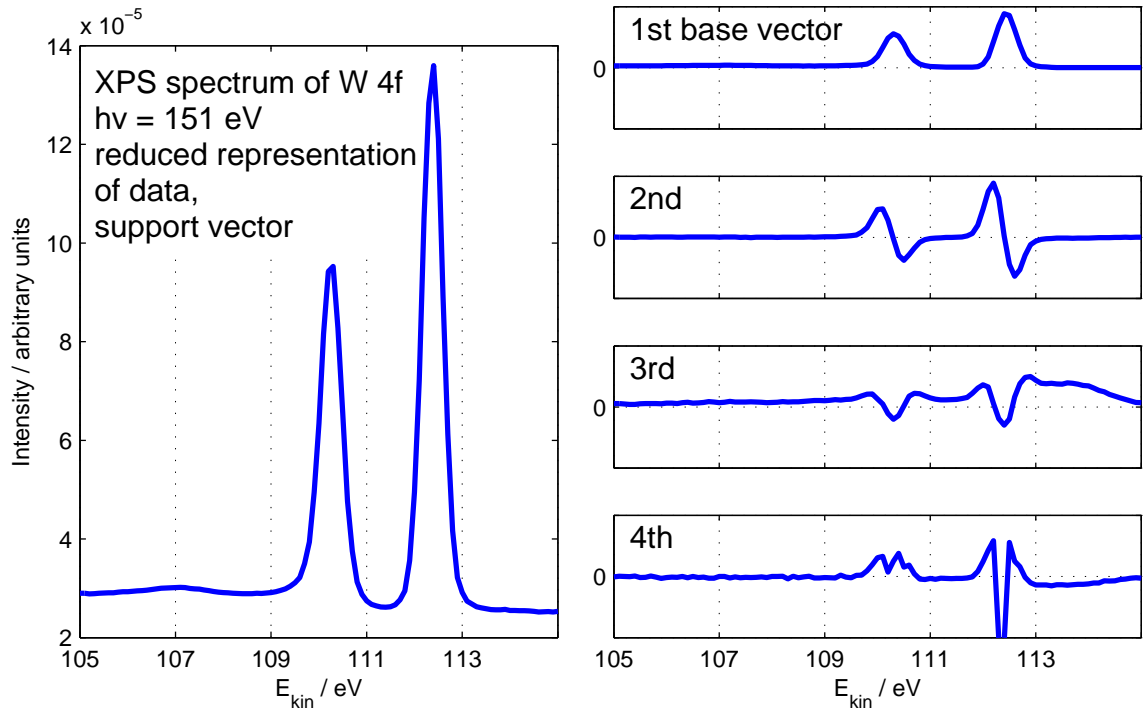


Figure 10.2.: **Left:** Mean XPS spectrum of W 4*f* as found on the cleaved surface of WSe_2 (chapter 11.2). The mean spectrum appears in the mathematical description as the supporting vector b . **Right:** First base vectors m_1, \dots, m_4 of the basis determined by the data reduction algorithm. As the full signal is involved in the determination of the base vectors, they show very low noise. Here, an interpretation of the feature modified in the first directions can be given : 1. Amplitude, 2. Peak kinetic energy, 3. Extra feature from step edges as discussed in chapter 11.2 plus peak broadening.

point. As seen above, the base vectors of the main axes system are differences of points in spectral space (r, s) including the sum over half of the data set each. As a consequence, the base vectors include extremely low noise and the approximate representation of a data point will also be rather smooth.

This allows to create an individual reconstruction of the signal from a single data channel (i.e. pixel) from only a few coefficients $I_{(j)}^k$ by exploiting properties of the complete data set. The reconstruction is a point in a low-dimensional hyperspace, which is made up by the first main axes, so the amount of data to be processed is reduced strongly. As an orthogonal system is determined from the procedure, each representation in reduced spectral space is found to be the optimal approximation in reduced space. Representing a data point by a linear combination of a small number of smooth base vectors (i.e. difference spectra) can be regarded as the 'optimal' smoothing algorithm

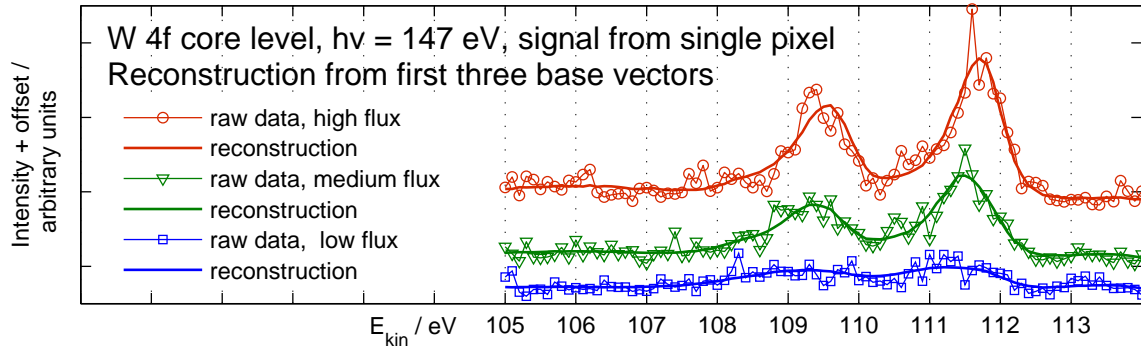


Figure 10.3.: Representation of single-channel (2×2 pixel) spectra including the first three components of the basis shown in figure 10.2. The reconstruction works well for a wide variety of spectra (variation shown here: total intensity). As only general properties of all spectra can be reconstructed here, smooth representations of the raw data are found. The statistical noise included in the individual channel is eliminated by reducing the number of dimensions of the 'spectral' space.

with respect to the individual data set.

Figure 10.2 shows an application example for the data reduction technique developed here. The dataset was acquired using *XPS* spectroscopy from tungsten diselenide, as it is also discussed in chapter 11. Here, selected properties of the basis of main axes are presented. The left panel of the figure shows the supporting vector of the affine subspace found for the core level photoemission from the $W 4f$ core level. As can be seen from the equations given above, it is the mean spectrum derived from all pixels found in the image. In the right column of the figure, the components of the first four base vectors are depicted.

In this case, the main axes can directly be interpreted as spectral features. The first base vectors representing the strongest variation in the image just gives a change in magnitude when added to the base vector. The data set was acquired at quite low magnification, so the spatially resolved photoemission data is modulated by the profile of the synchrotron beam making the largest variation in the data set. Second, a small lateral change of photon energy can be observed at the beamline (see section 9.4), giving a small shift in the peak emission intensity. This feature is represented by the second base vector. The third main axis contains information on lateral variation of the sample surface: For some reason, a small extra feature is found near the $W 4f_{7/2}$ emission line, and the appearance of this feature is accompanied by a small growth in peak width. Figure 10.3 shows the typical signal obtained from a single pixel in the emission spectrum of $W 4f$. In addition, the reconstruction of the spectrum from the first four components of the reduced representation is shown, giving the optimal shape-preservative smoothing.

10.3. Data Clustering

One crucial step when analyzing large amounts of heterogeneous data is to find an appropriate classification of the data sets by means of typical properties. At first, it is necessary to identify properties that allow for reliable discrimination among those that don't. In the previous section, a method was introduced to reduce the amount of data required to represent a single instance of a large set of photoemission spectra. A single data point is represented by typically 4 – 6 real numbers (i.e. the coordinates in the reduced space) then, which are made up by the components of a vector in a real vector space with the appropriate number of dimensions. This space is called 'parameter space' in the following. Whenever an abstract numerical representation of the data is given as defined in the previous section, classification of data points is equivalent to identifying joint regions in the parameter space that make up a class. Data points found inside these regions are considered members of the associated class. When the segmentation of the parameter space into classes cannot be given a priori, the configuration has to be determined from the experimental distribution of data points.

Deriving an appropriate class assignment from actual data is a basic problem in machine learning theory. To some extent, it can be considered complementary to the problem of generalizing the class assignment from a given set of data points with known class affiliation for the complete parameter space, which is known as 'supervised learning'. The term 'supervised' indicates that the group assignment of data points is known. Here, the generalization for the complete parameter space means finding kind of a scalar function of all parameters such that, for instance, two classes can be discriminated by the function value. The simplest example of an appropriate function is the separating hyperplane (see previous section) in the Hessian representation. A variety of methods also deals with non-linear functions [104]. When the segmentation of the parameter space is known, arbitrary new data points can be assigned to a class. In this context, the process of finding a discriminator for classes is called 'learning' and the experimental data used here is referred to as 'training set'.

Machine learning techniques have successfully been applied to a large variety of problems. It proved great performance whenever an imitation of primitive cognitive tasks is required. Learning algorithms are applied in the large field of data mining or for highly specialized tasks like overhead character recognition (OCR), where the identification of characters from noisy, bitmapped data is performed automatically and with high tolerance.

The problem to be solved for the reduced representation of spectroscopic data as derived in section 10.2 is to find a meaningful segmentation of parameter space in order to reveal features of large data sets that would not be accessible otherwise. An unbiased classification of data channels (i.e. pixels in the detector image) is to be found by means of the included spectral data. Here, the classification aims at an objective recognition of data channels from the vicinity of surface structures.

The critical properties of the reduced representation have to be worked out first as well

as the actual number of classes to be created. An algorithm that is well known in machine learning theory is capable of finding solutions of this problem, provided the parameter space is real, i.e., the data can be completely expressed as a set of real numbers. Details of an individual implementation of this algorithm will be described in the following. First, some basic concepts of the algorithm are introduced. As mentioned above, a class is defined by a well-defined region of the parameter space. In the algorithm, the primitive representation of a class is given by a point in that space, the 'class center'. It does not represent kind of geometrical center, but is used to find the associated volume for a given configuration of cluster centers.

Given two data points r_0, r_1 in N -dimensional parameter space (i.e. R^N), the space can be subdivided into two associated regions by the $N - 1$ -dimensional hyperplane $H, x \in H$ where $(x - b) \cdot m = 0$ with $m = r_1 - r_0$, $b = \frac{1}{2}(r_0 + r_1)$. This definition is equivalent to that of the separating hyperplane used in the previous section and can easily be interpreted as a plane oriented perpendicularly to the vector $\overline{r_0 r_1}$ and dividing the distance between the two points into identical parts.

In order to generalize this concept for an arbitrary number of points, knowledge of next-neighbor-relations between the points is required. For an irregular configuration of points, this relationship can be defined by the edges of the Delaunay tessellation [105], [106]. A simplex is the most primitive body in N -dimensional space with non-zero volume, which is the convex hull of $N + 1$ non-collinear points. These points are called vertices. For a set of $k \geq N + 1$ vertices, the Delaunay tessellation algorithm determines a set of simplices such that no vertex is found in the interior of any simplex. The result can be interpreted as a graph that has edges between all pairs of vertices that share at least one contribution to a simplex. All vertices with a direct interconnection are considered next neighbors with respect to the total configuration here.

The region associated with a point is therefore made up by the intersection of all segmentations of space given by the separating hyperplane between that point and its next neighbors. The graphical representation of the class borders derived here is called Voronoi diagram [105]. For the two-dimensional case, an example is shown in figure 10.4. Based on its definition, it can be regarded as a generalization of the Wigner-Seitz cell for an irregular set of points. The faces of a cell in the Voronoi diagram are made up by separating hyperplanes. As the region around a point is the intersection of convex subsets of parameter space, the region is convex. A region does not necessarily have finite volume.

Using these definitions, every point in parameter space can be assigned uniquely to a class. Precisely speaking, this does not hold for data points located on the border of a region, but, as the parameter space is quasi-continuous in reality, this case appearing is unlikely and has thus no practical relevance. Two preliminaries to a set of points used to derive a classification scheme exist. First, the convex hull of the set must have non-zero volume. Second, the set must include at least $N + 1$ data points, which is an implication of the first preliminary. No simplex can be formed with less than $N + 1$ points. Given exactly $N + 1$ points, exactly one simplex can be formed and every point

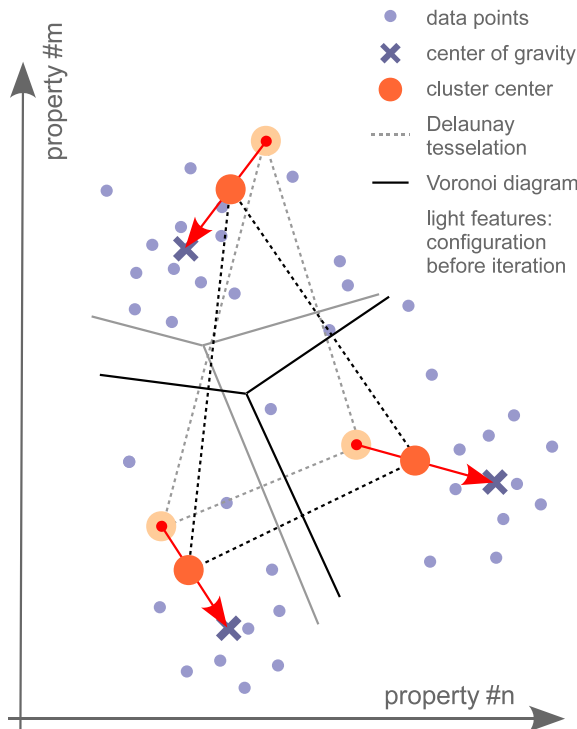


Figure 10.4: Demonstration of an iteration step of the data clustering algorithm. Starting with the configuration depicted by the light components, every cluster center is shifted towards the center of gravity of all data points found inside its associated cell of the Voronoi diagram. The borders of the Voronoi diagram are defined in analogy to the separating hyperplane as shown in figure 10.1.

is a next neighbor of any other.

Routines for handling simplices in N -dimensional space are part of a dedicated MATLAB toolbox which basically is a wrapper of the QHull library [129], [107]. Here, algorithms for the determination of the Delaunay tessellation, the Voronoi diagram, and convex hulls are implemented. It also provides routines for the runtime-efficient search of point-to-simplex and face-to-simplex relationships. The library is designed to work with any number of dimensions $N \leq 10$. Runtime of these algorithms grows exponentially with N , so the data sets discussed later (chapter 12) showed up to best processed using at most 6 dimensions. In that case, the runtime was limited to a few minutes when handling ≈ 45000 data points on a 2 GHz single-core machine. The need to keep the number of dimensions small pronounces the importance of figuring out the essential properties of the data by reduction as shown before.

Now that a representation of classes has been derived for N -dimensional data, an algorithm can be formulated to provide kind of 'optimal' segmentation of training data, i.e., to implement the learning process. The aim of the algorithm presented now is to reveal the inherent structure of a given data set, i.e., to place class centers wherever a concentration of data points is found, so separate regions with high density of data points can be distinguished by their class. In terms of the actual data, this means to separate clusters of data points with relatively low variance from the rest. The technique implemented here is well-known in the literature on machine learning [103],[130]. Though accepted in general, it is found with several variations in detail.

Basically, the distribution of data points inside a class is analyzed for a given configuration of class centers. Depending on the result, the cluster center is modified by means of simple rules described below and the process is iterated. It is completed when no data points have changed their class after an update. The topology of the next-neighbor network and the spatial segmentation are potentially affected at each step, so all have to be recomputed at each step. Modifications of the class configuration are based on operations on single class centers. One of three rules is applied at each iteration step to every class center:

First, if the size of a region exceeds a user-defined threshold, the class will be split by introducing a new class center somewhere inside the associated region. In the actual implementation, a measure for the 'size' is given by the maximum distance of a data point associated with the class from its center. New class centers are placed at the coordinates of the most-distant data point.

Second, if two class centers approach each other to less than a user-defined threshold, it is not suitable to treat the data points in both classes separate. In that case, two classes are united by removing the class centers from the configuration and introducing a new one located in the center of the old positions.

These two measures are meant to implement a certain variability with respect to the given data. By introducing these two rules, no assumption about the final number of classes is required a priori. The actual adaptation of the structure in the data is introduced by the third operation:

The class center point r as introduced above does not necessarily match the center of gravity C of the data points located in the associated volume. The center of gravity is considered as the 'optimal' point for the definition of a class center in this context. When a class is not split or united during an iteration step i , its center is shifted along the vector \overline{Cr} in order to find an improved representation of the data points of the current class (see also figure 10.4):

$$r^{(i+1)} = r^{(i)} + \epsilon \cdot (C^{(i)} - r^{(i)}) \quad (10.3)$$

Here, the 'learn rate' $\epsilon \in [0, 1]$ is introduced. It is a measure of the 'speed' by which the optimal representation of the data points by a class center is approached, where $\epsilon = 0$ would obviously result in no updating at all. The maximum learn rate $\epsilon = 1$ is not suitable in common cases, as updating the cluster centers affects the segmentation of the parameter space. This implicates that data points located at the border of a class might change class membership upon shift of the class centers. As class membership needs to be recomputed at each iteration, the center of gravity C of a class is not constant throughout the process (indicated by the superscript ' i ' in equation 10.3). In practice, $\epsilon \approx 0.3$ showed up to be a good choice.

Given a set of constant parameters, the algorithm is applied to training data until a class configuration is found such that no data point changes membership during an iteration step. This implicitly requires that no classes were created or combined during

this step. Finding suitable parameter settings for the learning rules discussed above requires some assumptions about the actual data set and the expected structure of the occupied volume in parameter space. Hence, a subsequent analysis of the class configuration determined by the algorithm is obligatory. Especially the number of classes to detect strongly depends on the actual distribution of data points. When the data is classified into a large number of sets, every data point will be represented well by means of the class centers, as low variance inside the class results. On the other hand, introducing a large number of classes does not give a good generalization and interpretation of the result is complicated. When the number of classes is chosen too small, the variance of the actual data associated with a class increases, and no proper discrimination of qualitatively different data points might result.

The number of classes to cover the parameter space is restricted by the choice of further parameters of the algorithm such as minimum distance between class centers. Therefore, the approximate volume occupied by the actual data must be known and the settings need to be modified for the individual case. As the classes are represented by convex sets with approximately equal length in all dimensions, more complex structures usually need to be represented by sets of classes. Choosing an appropriate subset of the classes in this case is up to the user and requires additional assumptions about the data. More sophisticated machine learning techniques were developed for these cases [104]. Typical approaches make use of non-linear transformations of the parameter space in order to find a linear data separation in the imaged space.

The question if a class configuration found by the machine learning algorithm contains significant information can be decided by analyzing the results of several independent runs with slight modifications of the parameter set or with random start values. For the cases discussed later (chapter 12), great reproducibility was found despite the low difference between structures and the background.

As the machine learning technique introduced here is basically intended to provide a generalization of arbitrary data, the classification scheme determined this way might also be applied to repeated recordings of data of the same type without further modification. For instance, recognition of nanowire structures as shown in chapter 12 from a new region of the sample should be possible using the classes in parameter space that have been determined from a training set before.

Machine learning is a powerful technique whenever structure needs to be extracted from large amounts of data. In the context of this work, it was introduced for the analysis of large amounts of spectroscopic data (absorption of nanowire structures in chapter 12). In that case, the recognition of structures 'by eye' showed up to be extremely difficult. Machine learning is an unprejudiced method that does not require sophisticated assumptions on the expected result a priori. Here, it could be used with great success in order to detect structures only by grouping data points with relative high similarity.

11. PEEM spectroscopy of WSe_2 : Rb

Besides crucial effects on carrier transport dynamics (see Part I of this work), Rb adsorbed on the cleaved surface of WSe_2 leads to further effects, which can be probed with photoemission electron microscopy (PEEM). Here, electron spectroscopic studies of the self-organized arrangement of Rb atoms are presented. From spatially resolved XPS data, a deeper insight into the microscopic interaction between the adsorbate and the substrate will be derived. Applying the methods introduced in chapters 9 and 10, a profound analysis of the observed spatial structures will be given. It will be demonstrated that the algorithms can be applied for an unbiased identification of spatial and spectroscopic structures and provide an efficient way of data refinement. Hence, the full detector image can be processed here without a loss of resolution.

The data presented here was acquired during several beamtimes at the PEEM experimental setup at beamline UE49/PGMa at BESSY II (Berlin), which has been introduced in detail before (chapter 8). Details of the experimental procedure are given in section 11.1. Prior to the results obtained from the Rb-covered surface in sections 11.4 and 11.5, a comprehensive PEEM study of the bare WSe_2 -surface is presented and discussed (sections 11.2 and 11.3) and acts as a reference for the conclusions given later.

11.1. Experiment

At the beginning of each beamtime, the PEEM setup based on a reduced sample high voltage of -10 kV was refreshed using a reference specimen. This procedure becomes necessary as the optimal settings of the PEEM are expected not to be exactly constant over the period of up to 6 months between two beamtimes. Especially the magnetic lenses of the imaging column are known to show a small hysteresis. Large changes of the lens currents are only necessary when switching the PEEM between standard operation and the -10 kV setup, so effects of hysteresis are expected to occur in particular then. Furthermore, modifying the lens currents strongly means changing the heat load and thus potentially affects the mechanical alignment of the imaging system, so readjustment of the system after some hours of re-equilibration becomes necessary.

The WSe_2 samples were prepared in the way discussed in section 8.3. The samples show up to stand the reduced high voltage of -10 kV of the PEEM when larger flakes have been removed manually. After being transferred into the main chamber of the PEEM, the sample was adjusted by means of tilt angle and distance to the imaging column. This procedure was monitored by the photoemission signal obtained from the

UV lamp in real time. Details can be found in [127]. A UV survey of the complete sample surface was carried out with optimized settings using the lateral shift option of the sample manipulator. The general sample quality and its overall flatness were estimated and the best candidates were chosen for the measurements.

The *Rb* dispenser was mounted to the preparation chamber one week before the beam-time. After bakeout, it was degassed carefully by ramping up the heating current, starting at $\approx 0.5 A$ up to $2.5 A$ over up to $18 h$. Each time the current is increased, a considerable rise in pressure is observed, indicating desorption of contaminants from the dispenser and its support. After reaching $2.5 A$, further degassing is carried out by repeated short-term ($2 - 3 min$) increases of the heating current. This strategy is meant to avoid excessive heating the dispenser support, so the pressure rise in the vacuum chamber is limited. During the last step, the peak current was increased stepwise to a maximum of $6 A$. At the operational current of $5 A$, the well-degassed dispenser did not produce a significant rise of the base pressure inside the preparation chamber, which usually resides in the low $10^{-10} mbar$ region.

After alignment of the sample in the PEEM, XPS spectra were acquired from the *W 4f* and *Se 3d* substrate core levels and the valence band and, after evaporation, also from the *Rb 3d* core level. Within the used photon energy range between $110 eV$ and $225 eV$, the mentioned core levels are known to have the largest photoionization cross sections [60], so they are expected to give the largest signals. For imaging, an approximate field of view of $25 \mu m$ was chosen such that the photoemission signal covers nearly the complete detector area. As the width of the monochromator exit slit defines the synchrotron spot dimensions (section 8.1) in one direction, it was set to $300 \mu m$, giving a contribution to the total energy resolution of the system of $147 meV$. With these settings, the mirror current (see section 8.2) amounts to $2.47 nA$ at a storage ring current of $\approx 300 mA$ and a photon energy of $169 eV$. The small measured mirror current indicates a relatively low photon flux, which was chosen intentionally to reduce cumulative beam damage and/or localized carbon contamination originating from synchrotron-cracked carbon compounds found in the experimental chamber [108]. In order to have a sufficient signal level, the large contrast ($70 \mu m$) aperture of the imaging column was set. The energy resolution of the electron analyzer is basically defined by the width of its exit aperture, so the smaller one ($12 \mu m$) was chosen. The MCP image intensifier was operated near the maximum voltage between $1300 V$ and $1375 V$ and each image was acquired with an exposure time between $2 s$ for the substrate core levels and $5 s$ for *Rb 3d*.

In common XPS spectroscopy, a photoelectron spectrum of the sample would be acquired using a fixed photon energy and scanning the measured kinetic energy over the full available range. When using PEEM spectroscopy, the chromatic error of the imaging optics has to be taken into account. First, a variation of the focal distance as function of the energy of the transmitted photoelectrons is found [127], the so-called longitudinal chromatic aberration. For a fixed objective current, this means that a sharp image of the surface is found for only one discrete kinetic energy. Second, the lateral chromatic aberration results in an energy-dependent image magnification. Missing cal-

ibration measurements of these effects make an individual correction for each kinetic energy impossible, and the automated data acquisition software does not provide a related feature. Reference [127] gives an impression of the magnitude of correction required here. Furthermore, readjustment of the objective current, would have severe side effects. Imaging by means of a magnetic lens always involves a current-dependent rotation of the image, so a point on the sample surface would not be imaged to a constant position on the detector screen unless located on the optical axis.

In order to minimize the imaging errors during the acquisition of spatially resolved XPS spectra, only small kinetic energy intervals can be scanned. Therefore, every core level spectrum was acquired using an individual photon energy, so the resulting photoelectrons were always found in a fixed kinetic energy interval $100 \text{ eV} \leq E_{kin} \leq 120 \text{ eV}$. The photon energy was chosen with respect to the tabulated binding energy [109], so the expected peak photoemission signal is found around $E_{kin} = 110 \text{ eV}$. Here, $h\nu = 147 \text{ eV}$ was chosen for $W 4f$, $h\nu = 169 \text{ eV}$ for $Se 3d$, and $h\nu = 225 \text{ eV}$ for $Rb 3d$. This ensures that the pixels in photoelectron spectra from core levels with large difference in binding energy still map identical positions on the sample surface.

For Rb evaporation, the sample had to be transferred into the preparation chamber and back, requiring a complete realignment of the manipulator afterwards. For the data presented in section 11.4, the sample surface was moved into a position $2 - 3 \text{ cm}$ apart from the dispenser. The dispenser was driven at a heating current of 5 A for a duration of 4 min . As the Rb emission is not directed significantly, a homogeneous coverage of the surface was achieved this way. Compared to the evaporation time used for the experiments in chapter 6, the surface Rb concentration achieved here exceeds the amount needed for the saturation of surface band bending by far. For the locally constrained Rb adsorption discussed in chapter 11.6, the dispenser equipped with a slit aperture was operated at a heating current of 5 A for 4 min , i.e., identical settings as above.

Prior to evaluating the experimental data, standard preprocessing routines were applied. All procedures are presented in the methodical chapter 9. For the actual data discussed in this part, this includes

- clipping the camera image such that only the active, circular detector area remains,
- removal of hot pixels (section 9.1),
- MCP normalization (section 9.2),
- normalization of the spectra by the photon flux (i.e. the mirror current),
- data downsampling by binning square regions.

As the chosen field of view is rather large in this case, no explicit beam profile normalization could be applied. Furthermore, the drift of the manipulator is negligible for low magnification, so no drift correction was made. Potential intensity-dependent shifts of

the core level positions, like charging or the SPV effect, complicate the safe determination of the monochromator dispersion here, so the reader should be aware of a small lateral photon energy variation included in the data.

11.2. Results: The clean surface of WSe_2

After cleaving in ultra-high vacuum, the WSe_2 sample was aligned in the microscope and a survey scan of the surface was made. Typical samples show very low emission at the homogeneous surface when illuminated with the UV lamp, which is expected for semiconductor specimen. Defects, especially step edges and small particles remaining from the cleaving process, are the only features that were found on the clean surface. On a well cleaved crystal, these defects have a very low density, so that it is easy to find regions with areas of several thousands μm^2 without a single defect that is visible in PEEM. At a closer look, a small unspecific variation of photoelectron yield is found for sharply bounded areas of the approximate dimensions of some $10 \mu m$.

The origin of this contrast is to be clarified, as it might help getting a deeper insight into the structure formation processes after Rb deposition as discussed in section 11.4. The basic question is if adsorbates of arbitrary origin might also be found prior to Rb deposition. A potential source for non-crystalline adsorbates is the crystal itself, as it is known that layered dichalcogenides tend to intercalate its precursors during growth. Intercalated excess material is expected to be located in the van der Waals-gap, so it would be found at the surface after cleaving. Especially tungsten diselenide crystals grown with iodine as transport gas are known to have p-type doping, which is an effect of the transport gas getting partially incorporated into the crystal during growth. Furthermore, potential contamination of the surface might also originate from the vacuum system.

The intention of the reference measurements presented here is to estimate potential deviations of the surface from ideal stoichiometry and to reveal potential precursors of the Rb-induced structures presented in section 11.4. For the experiment, a sample position was chosen that includes both contrast levels in order to provide comparable data. At this site, core level spectra of the substrate levels $Se\ 3d$ and $W\ 4f$ were acquired in a field of view of $\approx 25 \mu m$. The same, small contrast is found from the total photoelectron yield (upper left panel in figure 11.3) when using synchrotron radiation. The photoemission data was binned in square regions of 8×8 pixels, giving an image of 64×64 data channels, of which ≈ 3200 contain data.

The cumulative signal of each channel was fitted by a theoretical profile of the photoemission line. For both core levels, the signal is composed of two spin-orbit split lines with fixed difference in binding energy and amplitude ratio. Although tabulated values are available for these parameters, they were held variable during the fit. Atomic physics requires that these values are constant for all data channels, so the results can serve as a criterion to check the consistency of the theoretical profile with the experimental data.

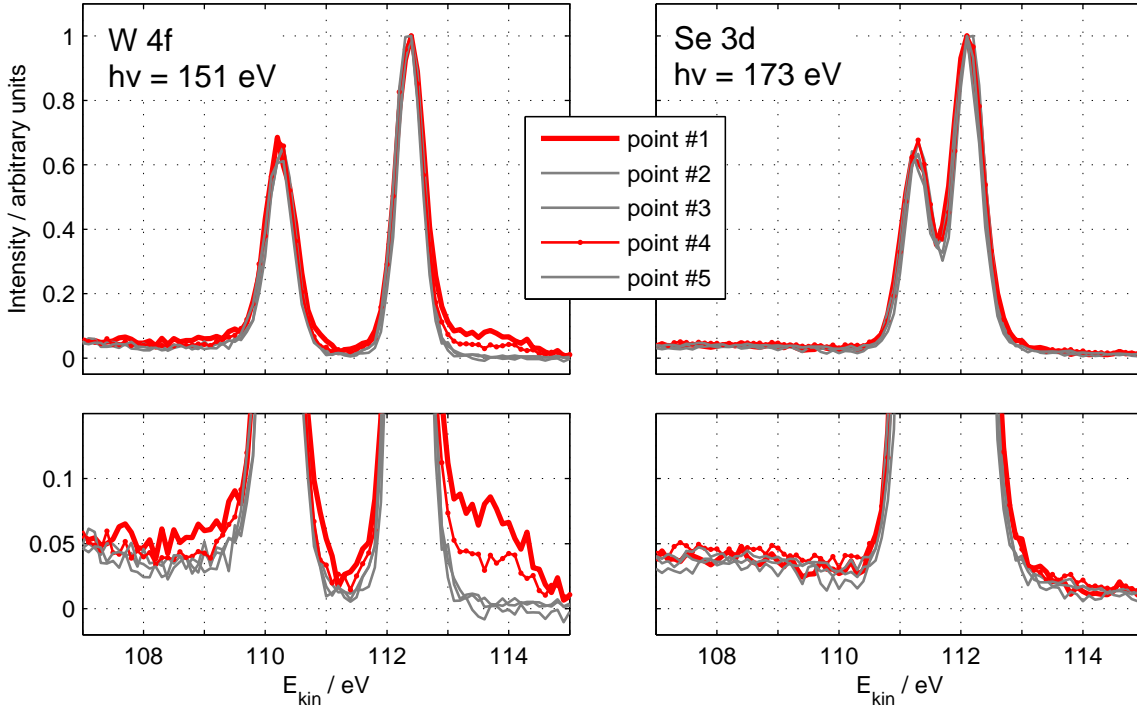


Figure 11.1.: Core level photoemission spectra from selected points in a detector image (see figure 11.3, FOV $\approx 25 \mu m$) on the cleaved surface of WSe_2 . No major modifications of the peak parameters are found, except for a small extra feature near the $W 4f$ core level doublet. This feature is found exclusively in regions near step edges (red lines).

Especially the realistic amplitude ratio is known to show a strong deviation from the values expected from theory, i.e. $2 : 3$ for the $Se 3d_{3/2}/Se 3d_{5/2}$ spin-orbit doublet and $3 : 4$ for $W 4f_{5/2}/W 4f_{7/2}$, so it would have to be determined from the data anyway. The profile of the individual photoemission line is known to be composed of an intrinsic and a device-dependent contribution. The intrinsic line shape can be modeled by a Lorentzian function in case of a semiconductor. The device dependent part of the peak profile is usually given by a Gaussian function, introducing the effect of finite combined energy resolution of radiation source and electron analyzer to the peak profile. The actual line shape is obtained by a convolution of both profiles, giving the Voigt profile. In the general case, a suitable approximation of this function is required, because a general analytical expression is not known. Here, the Gaussian part of the theoretical peak profile dominates the intrinsic Lorentzian contribution in width, so the experimental profile is approximated well by a Gaussian. Both peaks were assumed to have identical width, which was determined by the fitting routine.

The binding energy of electrons in a certain core level are known to be affected by

changes of the chemical environment of the associated atomic species. In XPS spectroscopy, this effect is usually used to identify the environment, so the kinetic energy of peak photoemission includes valuable information and is thus the most important feature to find from fitting.

The experimental spectra include an energy-dependent background of inelastically scattered photoelectrons. The standard procedure of subtracting a Shirley background [110] from the data prior to fitting requires a large interval of background recorded around the emission line. Due to the limited stability of the system and the need to scan relatively small kinetic energy intervals, spectra must be kept as short as possible. Instead of removing the background from the experimental data, it was estimated by applying Shirley's approach to the theoretical line shape. When derived from real data, the background function still has to be scaled, so the Shirley contribution was designed to have unit amplitude and an additional prefactor that was subject to optimization during the fit.

By this approach, only the fraction of inelastically scattered photoelectrons emitted from the currently scanned core level is found. In the Shirley model, also inelastically scattered photoelectrons emerging from levels at lower binding energy contribute to the total background. For the spectra covering a limited kinetic energy range around the substrate core levels, such electrons are found as a constant offset of the signal. This offset scales with total photon flux, so an individual treatment for each data channel is required. Especially at low signal levels, another small offset is introduced by the noise of the detector unit which is assumed not to depend on the total photon flux. Both influences are implemented in the theoretical spectrum by an additional fit parameter.

Using this model of the experimental data, the actual values of all parameters were determined by least-squares fitting the experimental data from each channel. The table in figure 11.2 gives an overview of the average parameters found for all data channels. The parameters of the spin-orbit doublet, splitting and amplitude ratio, were found with low variance, so it can be concluded that the theoretical profile is in good agreement with the data. As could be expected, the Gaussian width of both core levels is found to be almost identical. Low variance was found over the complete sample.

In figure 11.1, the XPS spectra from five selected data channels are shown. No obvious difference in their features could be found, except for a small modification of the background at the high kinetic energy side of the $W4f$ core level for spectra 1 and 4. These two were taken from positions that show modifications of the surface, which can be interpreted as step edges. As no obvious evidence for variations of the homogeneous part of the surface is found, the parameters determined by fitting are evaluated in detail. In the panels of figure 11.3, the data obtained for the individual data channels is transformed back into a low-resolution representation of the raw data image. The spectra shown in figure 11.1 originate from the positions marked by green circles. Some artifacts of the fit procedure can be seen in the image. These can easily be identified by vertical stripes of relative strong deviation from the channels in the environment.

The stripes originate from the fitting algorithm that processes all channels in the order

	parameter	mean value	\pm	std. dev.	unit
Spin-orbit doublet $W\ 4f_{5/2} / W\ 4f_{7/2}$	spin-orbit splitting	2.1270	\pm	0.0049	eV
	amplitude ratio	0.6305	\pm	0.0126	
	Gaussian width σ	0.2152	\pm	0.0053	eV
	prefactor Shirley fcn.	0.0422	\pm	0.0060	
Spin-orbit doublet $Se\ 3d_{3/2} / Se\ 3d_{5/2}$	spin-orbit splitting	0.8414	\pm	0.0042	eV
	amplitude ratio	0.6200	\pm	0.0132	
	Gaussian width σ	0.2297	\pm	0.0059	eV
	prefactor Shirley fcn.	0.0268	\pm	0.0050	

Figure 11.2.: Optimal parameters of the simulated peak profile for both substrate core levels found by least-squares fitting to all ≈ 3200 data channels. The profile consists of a spin-orbit pair of Gaussian profiles with simulated Shirley background. The given standard deviation of the parameters was determined from the complete image, so a certain contribution to its magnitude is owed to variations of the sample surface.

of appearance in the image column by column. In order to optimize the performance of the algorithm, the start parameters of the fit are given by the fit result of the preceding channel. The algorithm is known to converge incorrectly on occasion, so invalid start parameters are passed to the next iteration, increasing the likelihood of the fit failing once more. All shown images reveal a strong contrast at the imperfections of the surface and a more or less pronounced contrast between homogeneous areas. All color scales of the panels in figure 11.1 are normalized to the mean values of the fit found in table 11.2. The homogeneous parts of the surface can be classified by the Gaussian width of the fit, where slightly increased values are found for the upper and lower parts of the image. A physical reason for an increased peak width is not expected. Due to the rather low energy resolution of the electron analyzer, the broader structure could be explained by the superposition of two or more spectra with small energetic shift.

Further information is found from the spatial dependence of the relative secondary electron yield of a specific core level. It is found by computing the ratio of the com-

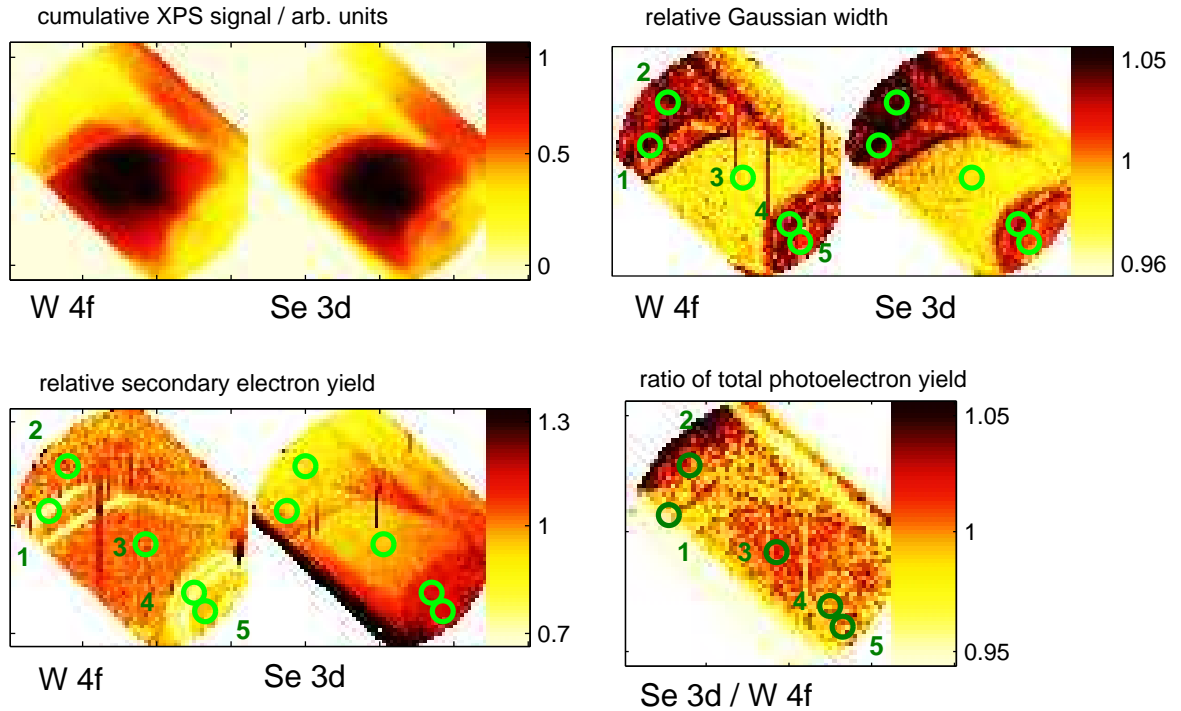


Figure 11.3.: Spatially resolved analysis of the clean surface of WSe_2 : $h\nu = 151\text{ eV}$ ($W\ 4f$), $h\nu = 173\text{ eV}$ ($Se\ 3d$), $FOV \approx 25\ \mu\text{m}$. **Upper left:** Raw data image of the cleaved surface of WSe_2 . **Lower left:** Lateral distribution of secondary electron yield found for XPS photoemission for both substrate core levels. **Upper right:** Lateral distribution of the Gaussian width with systematic broadening in the regions off the image center. **Lower right:** Photoemission yield ratio of $Se\ 3d$ over $W\ 4f$. Using the beam profile normalization technique from chapter 9.3, it can be concluded that the stoichiometric ratio of W and Se is constant within a precision of 2%. The small deviation possibly reveals a small excess of W in the region around point # 2.

bined photoemission amplitude and the prefactor to the Shirley part of the simulated spectrum. Again, a pronounced correlation with the step edges is found, revealing a lowered likelihood of photoelectrons emerging from the $W\ 4f$ core level suffering inelastic scattering. For $Se\ 3d$, no clear statement can be given. The broad stripe of virtual high secondary electron yield at the lower boundary of the image is assumed to be an artifact obtained from the low signal level found there. Step edges are not pronounced here, and although a systematic spatial variation is found, the classification obtained from the map of Gaussian width is only reproduced roughly.

In order to find potential deviations from perfect stoichiometry, the ratio of the total

emission signals obtained from the substrate core level was analyzed as a function of position in the image. When a constant position of the incident synchrotron beam is assumed, the magnitude of the local photon flux would cancel out and the ratio can be interpreted. Here, the modulation of the result by a small offset of the beam position between the two spectra had to be removed by using the technique described in chapter 9.3. This is known to work only for a Gaussian beam profile, so the peripheral parts of the image are corrupted by normalizing and should be ignored. In the valid area, a very small change of the signal-to-signal ratio between the larger regions identified by the Gaussian width map can be suspected.

A map of the peak positions was also created for both core level spectra. The suspected presence of adsorbates should be detectable by the resulting modification of the chemical environment of surface atoms. Determination of the precise peak position requires that the influence of the excitation source can be ruled out. This concerns both the lateral variation of the photon energy and the effect of high photon flux, which might result in a small charging of the surface or, in case of an adsorbate-covered semiconductor, a surface photovoltage effect (see chapter 3.2 in part I). For the current case, these effects cannot be separated reliably from a suspected chemical shift.

11.3. Discussion: Clean surface

From the results presented in the preceding section, some qualitative statements about the cleaved surface of WSe_2 can be derived. First of all, the surface is found to be homogeneous except for small deviations found in regions like the one presented before. The abundance of these regions was found to vary with the specimen, but showed up to be typical features. A detailed analysis was motivated by the fact that these small deviations are structured and are found concentrated in specific areas. The analysis of the spatially resolved XPS spectra revealed a systematic variation of spectral features over the sample surface. An interpretation of the observed effects will be given here.

The most pronounced variation was found for the Gaussian width of the fitted peak profile. Here, the examined region can clearly be divided into two parts with relatively narrow (point # 3 in fig. 11.3) and relatively wide (points #2, #5) photoemission lines. Due to the low energy resolution of the electron analyzer, this finding is attributed to the existence of a small chemical shift for part of the substrate atoms found in regions with wide peaks. For Se, atoms located directly at the surface contribute to the photoemission signal as well as those located in the second layer. A small shift affecting the topmost layer might be caused by a small concentration of adsorbate atoms, so some evidence for a lateral variance of adsorbate concentration is given here. The effect is less pronounced for W, as its first layer is not exposed directly to the surface. This leads to the conclusion that the region around point #3 has no, or relatively low contamination. In general, the existence of a chemical shift should be visible directly when the binding energy of the emitting core level is analyzed. The precise determination of binding energy for

the individual spectrum is biased by the linear lateral variation of photon energy of up to 150 meV across the image. Although eliminated for the most part (chapter 9.4), some artifacts remain. In addition, a potential slight intensity-dependent shift caused by charging should be taken into account. The existence of an adsorbate could also potentially lead to band bending and an SPV effect-induced shift in case of a charge transfer from the adsorbate to the substrate. If present, the magnitude of such effects is limited to less than 100 meV . No additional level shifts above the magnitude of the mentioned effects could be observed. Thus, it can be concluded that adsorbates either have very low density or are uncharged.

XPS spectra of an adsorbate-covered surface are expected to reveal an enhanced secondary electron background at the substrate core levels. As can be seen in figure 11.3, no clear correlation of this effect can be found with the suspected adsorbate coverage. While no contrast is found for the W 4*f* core level, there is an effect for Se 3*d* for part of the examined region. The fact that the secondary electron background is only partially affected by adsorbates could only be explained if the concentration of foreign atoms is assumed very small, however, the clear effect on the chemical shifts indicates a considerable concentration of surface atoms. Therefore, it might be concluded that the surface is partially covered by unbounded atoms of the same species as the substrate, i.e., W or Se . Unbounded atoms are expected to show a slightly different electronic configuration, which might explain the observed variation of binding energy. Indeed, a small deviation of the stoichiometry is indicated by small lateral variations of the signal-to-signal ratio (figure 11.3), although many artifacts are included there. Assuming that the ratio found around point #3 represents the exact stoichiometry of the substrate, a small excess of W atoms is found near points #2 and #5. A considerable higher contamination of the surface cannot be excluded here, as long as the contamination is assumed to have the stoichiometric ratio of the crystal. The adsorbates found here are assumed to originate from the growth process. It is well known that transition metal dichalcogenides show a tendency to intercalate excess material when the exact stoichiometric ratio of transition metal and chalcogen is not kept up during growth. After cleaving the crystal, the surface is made up by a former van der Waals-gap, where intercalates are assumed to be located in the bulk crystal.

11.4. The Rb covered surface of WSe_2

After deposition of Rb, the WSe_2 surface turns extremely inhomogeneous. As was found in an UV survey, it is textured with sharply bounded areas of very high photoemission yield compared to the rest, whereas low variation is found inside these areas. The parts of the structure have typical dimensions of some 10 μm up to several 100 μm . To give an overview, part of the surface is imaged in figure 11.4. The image was assembled of 19 raw data images using the method introduced in chapter 14.1. In general, the bright areas are found to have one side with a straight border and another where it is serpentine. The

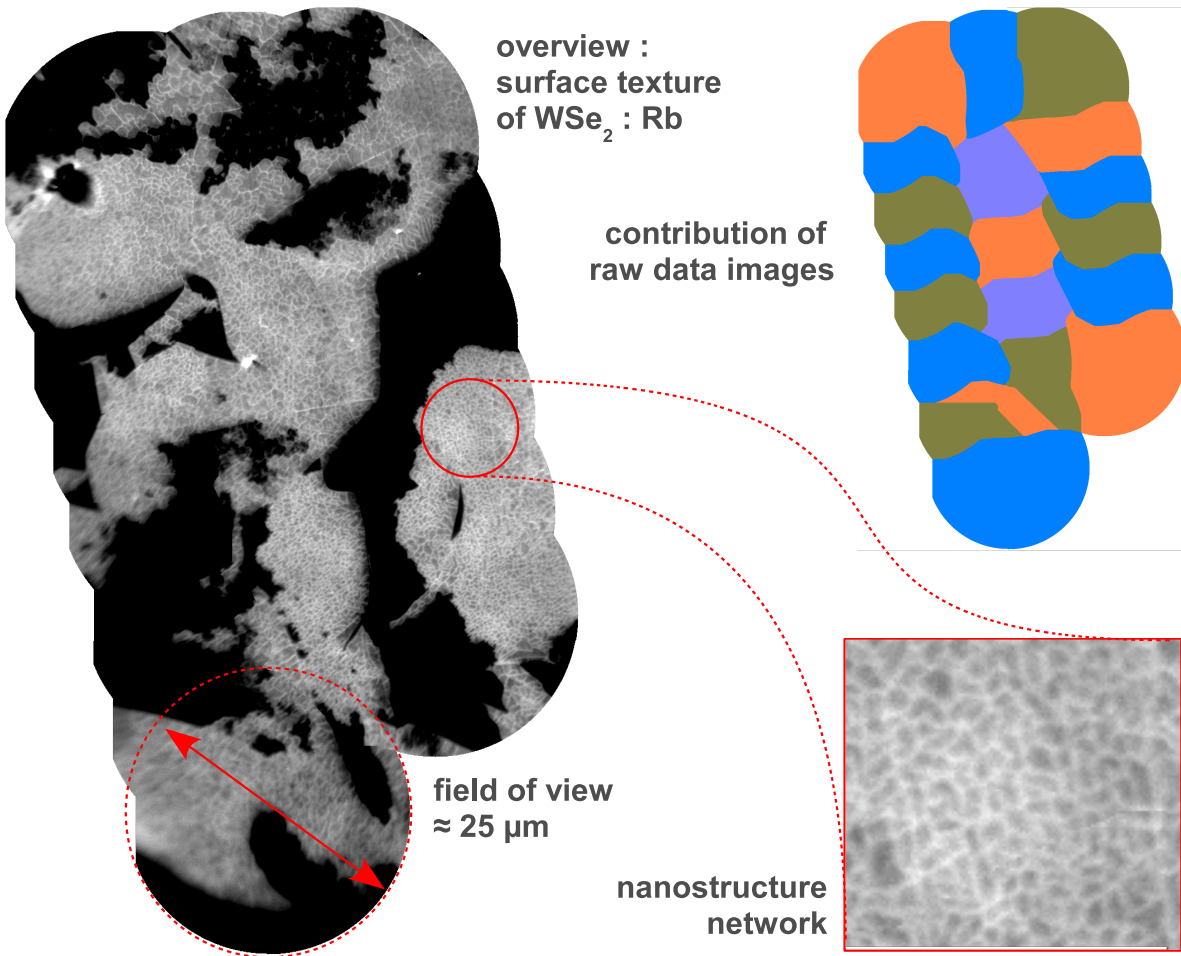


Figure 11.4.: Overview image of the Rb covered surface of WSe_2 . Assembled from 19 raw data images acquired using the UV source ($h\nu = 4.9 \text{ eV}$) and a field of view of $\approx 25 \mu\text{m}$. The contribution of the raw data images is indicated by the colored map to the upper right. The brighter part of the surface texture is covered by a microscopic network. Here, only issues of the large scale texture are presented. For a discussion of the observed network structure, refer to chapters 12 and 15.

straight borders suggest that the 'bright' regions are delimited by step edges there, which were also found to have relatively straight sections, but no favored direction at a larger scale. As can be seen from figure 11.3, the bright areas have a distinct substructure. This is assumed to be a network of Rb induced nanostructures. These were also examined using the PEEM technique in subsequent experiments. Results are reported in chapter 12 and 15. Although these structures only become visible within the bright areas here, they are supposed to exist on the complete surface. For the darker regions, auxiliary

experiments proved that the structures can also be found there. It can be concluded that the formation of the surface texture is independent of the nanostructure creation process.

The measurements presented in this chapter are intended to unveil spectroscopic features that show the difference between the two observed types of domains. A representative region of the surface was chosen, and a set of core level spectra was obtained. A raw data image showing the borders of the image is shown in figure 11.5. It was acquired at a photon energy $h\nu = 169 \text{ eV}$ and a kinetic energy $E_{kin} = 111 \text{ eV}$, so the emission signal originates from the vicinity of the *Se 3d* core level. The identical shape is found throughout the spectrum, though with attenuated contrast. A set of XPS spectra was acquired from this surface region, again covering the major components of the photoemission signal. In order to provide best spatial resolution, an alternative approach was made when processing the data. The raw data was binned into channels of only 2×2 pixels here, resulting an image of 256×256 pixels with ≈ 45000 including a photoemission signal.

The spectra obtained in these data channels include much statistical noise, such that a direct interpretation is pointless. Instead, the data reduction technique introduced in chapter 10.2 was applied to the complete data set. Using the basis of the reduced data, a smooth representation of the spectrum in every data channel was derived, so a detailed analysis of the spectral components became possible for a signal taken from only 4 pixels.

Prior to spectral analysis, the actual shape of the island was determined by applying the automated classification algorithm discussed in chapter 10.3 to the data. For this purpose, each data channel was represented by its most obvious features, the signal-to-background ratio of the photoemission spectra of *W 4f*, *Se 3d*, and *Rb 3d*, which was determined from the reconstructed spectra with low error. Data channels containing signals from one type of surface showed up to be well separated from channels belonging to the other type in that parameter space, so a precise and self-consistent assignment of the data channels to the surface type was derived. The results can be seen in figure 11.5. The red regions, denoted with (I), indicate the part with high overall photoemission signal.

For every data channel, the Euclidean distance to the nominal border found this way was determined. Using the distance to classify the data, gradual variations of the features discussed below are expected to become visible if existent. The distance to the border is used as a measure to provide binning of multiple data channels that are expected to contain equivalent spectra. Cumulative raw data spectra created from binning channels within small distance intervals were obtained from the regions indicated as stripes in figure 11.5. The results are shown in figure 11.6. Note that the spectra are sorted by mean distance of the contributing channels in the waterfall plot. In order to obtain an increasing scale, a minus sign was assigned to the distance of bins inside region (I). From the raw data spectra, it can be seen that the high photoemission signal inside region (I) (figure 11.5) is not limited to certain spectral features. In general, a relatively high

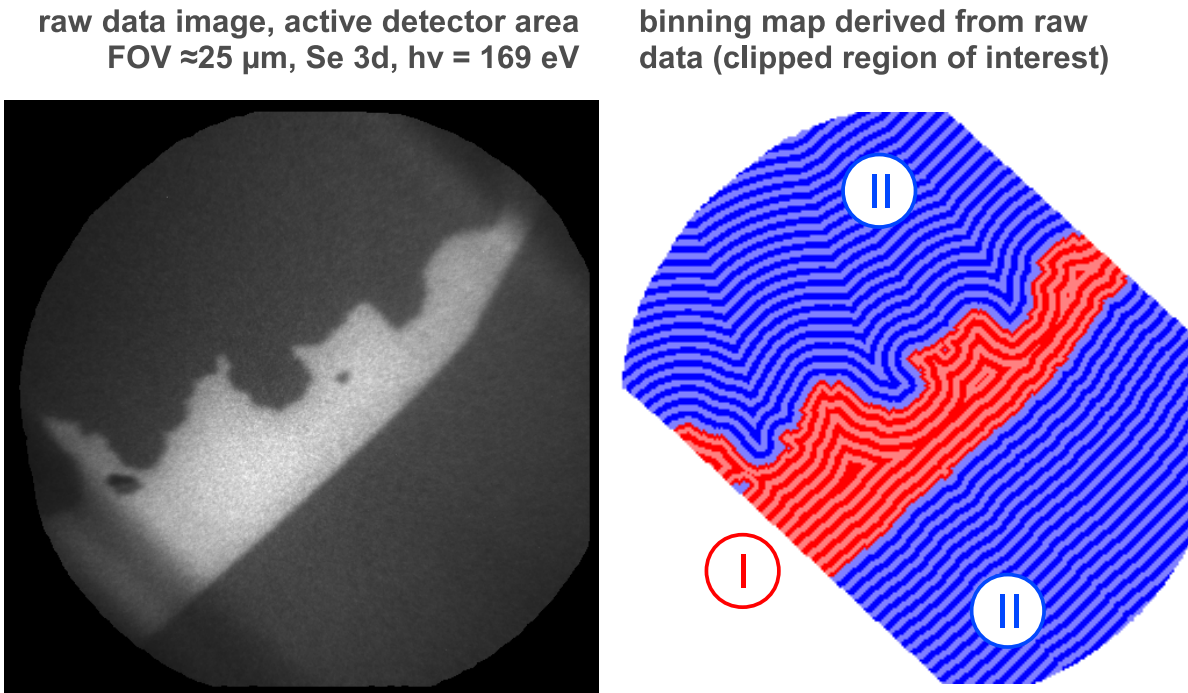


Figure 11.5.: **Left:** Raw data image of the textured surface. XPS signal from the $Se\ 3d$ core level, field of view $\approx 25 \mu\text{m}$, $h\nu = 169 \text{ eV}$, $E_{kin} = 111 \text{ eV}$. **Right:** Data binning by distance from border between bright and dark regions. The border was determined using the data classification algorithm presented in chapter 10. Here, the signal-to-background ratio found in the XPS spectra of all three core levels was processed giving a reliable and self-consistent representation of the border. Settings: FOV $\approx 25 \mu\text{m}$, $256 \times 256 \text{ pix}$, $1 \text{ pix} \cong 90 \text{ nm}$.

cumulative signal is found for the substrate core levels, while a lower signal is found for Rb.

Strong spectral differences are found between the two types of texture. These are analyzed in detail during the following paragraphs. Here, the reconstructed representations of the spectra were processed in order to keep up the high spatial resolution. All results were plotted versus the distance to the border of the structure. The results are shown in figures 11.7 and 11.8. Every gray point represents one data channel. For better orientation, the median of the distribution for data points within distance bins was added to the figures. The intervals drawn for each interval range from the 25% quantile to the 75% quantile of the distribution, i.e., the central 50% of the data points are found inside the marked interval.

In figure 11.7, the kinetic energy of maximum photoemission is drawn for all core

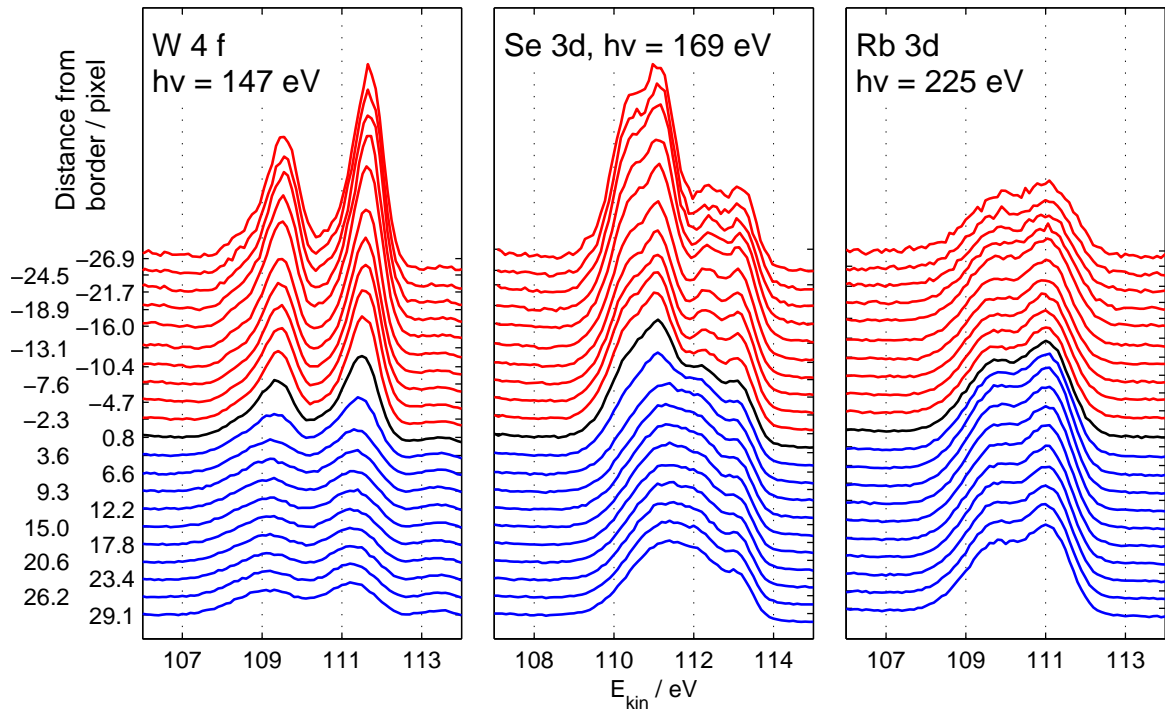


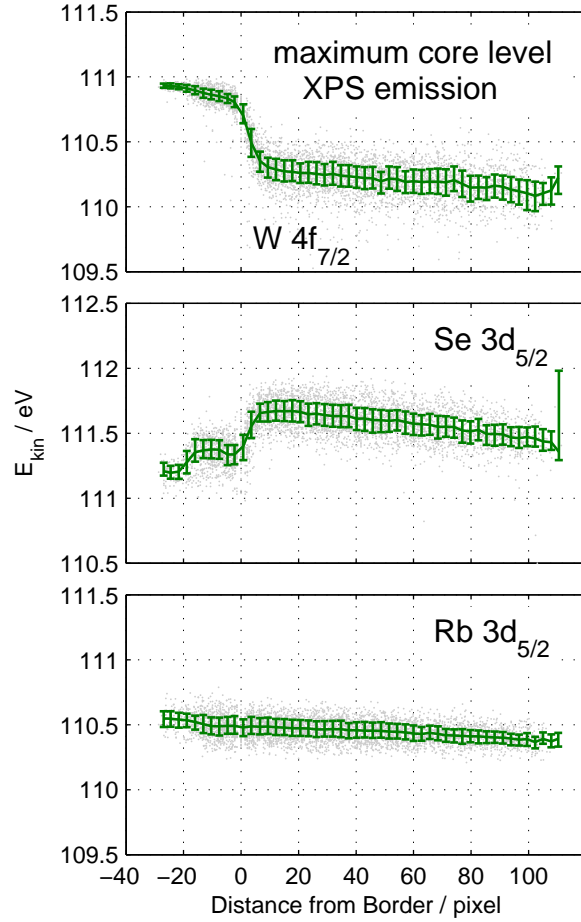
Figure 11.6.: Spatially resolved core level spectra. Derived by binning data from pixels with nearly constant distance from the border as shown in figure 11.5. A clear variation of spectral features is found near the border. No modifications were applied to the data, except for normalization of the bin size.

levels examined here. A clear evolution of the peak position of W $4f$ with distance to the border can be found, indicating a lower binding energy on the center region in the image. Variation is predominantly limited to the region around the border. A small trend on a larger scale is supposed to originate from a small remaining lateral variation of photon energy. As the incident photon flux falls off with increasing distance, a small synchrotron-induced SPV effect might also be found in the data, but the observed trend is too small for a quantitative analysis. The binding energy of the Se $3d$ core level virtually shows significant evolution along the total scale, but the spectrum shows significant modifications with respect to the spectra obtained from the clean surface, so a more sophisticated analysis had to be performed here and is presented below. Up to now, it can be suspected that the measured spectrum consists of a superposition of Se $3d$ doublets with relative chemical shift. From figure 11.7, it can only be concluded that a variation of the weights in such combination is likely. No evolution was found for the Rb $3d$ core level except for the side effects discussed above.

The total rate of photoelectrons emitted from a certain core level depends on the concentration of the associated atomic species, the photoionization cross section of the

Figure 11.7:

Results from evaluation of reconstructed XPS spectra (W 4f, Se 3d and Rb 3d core levels) for every pixel (10% of ≈ 45000 data points shown). The gray dots mark the results obtained from the individual data channels. The solid line indicates the median value found at certain distance from the border ($1 \text{ pix} \cong 90 \text{ nm}$). The colored intervals reach from the 25% quantile to the 75% quantile, such that the center 50% of the distribution is found inside this interval. **Shown here:** Kinetic energy of maximum photoemission signal.



atomic orbital [60], and the average depth in the sample. In general, the depth sensitivity of XPS is governed by a combination of the penetration depth of the exciting radiation, i.e., the photoionization cross section, and the escape depth of photoelectrons that depends on the kinetic energy [61]. Here, the effect of finite escape depth dominates, and the information depth of XPS amounts to $\approx 7.5 \text{ \AA}$ for photoelectrons with a kinetic energy of 110 eV . As the unit cell of WSe_2 measures $\approx 6.8 \text{ \AA}$ in the c -direction (chapter 2), most of the photoemission signal originates from the topmost layer of the crystal here. Furthermore, the rather low absorption of the radiation means that all atoms of one specific species can be assumed to emit photoelectrons at the same rate, regardless of their individual distance from the surface. As the experimental setup was configured to acquire all spectra inside the same range of kinetic energy, the value stated for the information depth is assumed to hold throughout the data discussed here.

Therefore, the ratio of cumulative photoemission signal from different core levels originating from the same spot on the sample surface is proportional to the ratio of densities of atomic species. The ratio of photoionization cross sections is part of the proportion-

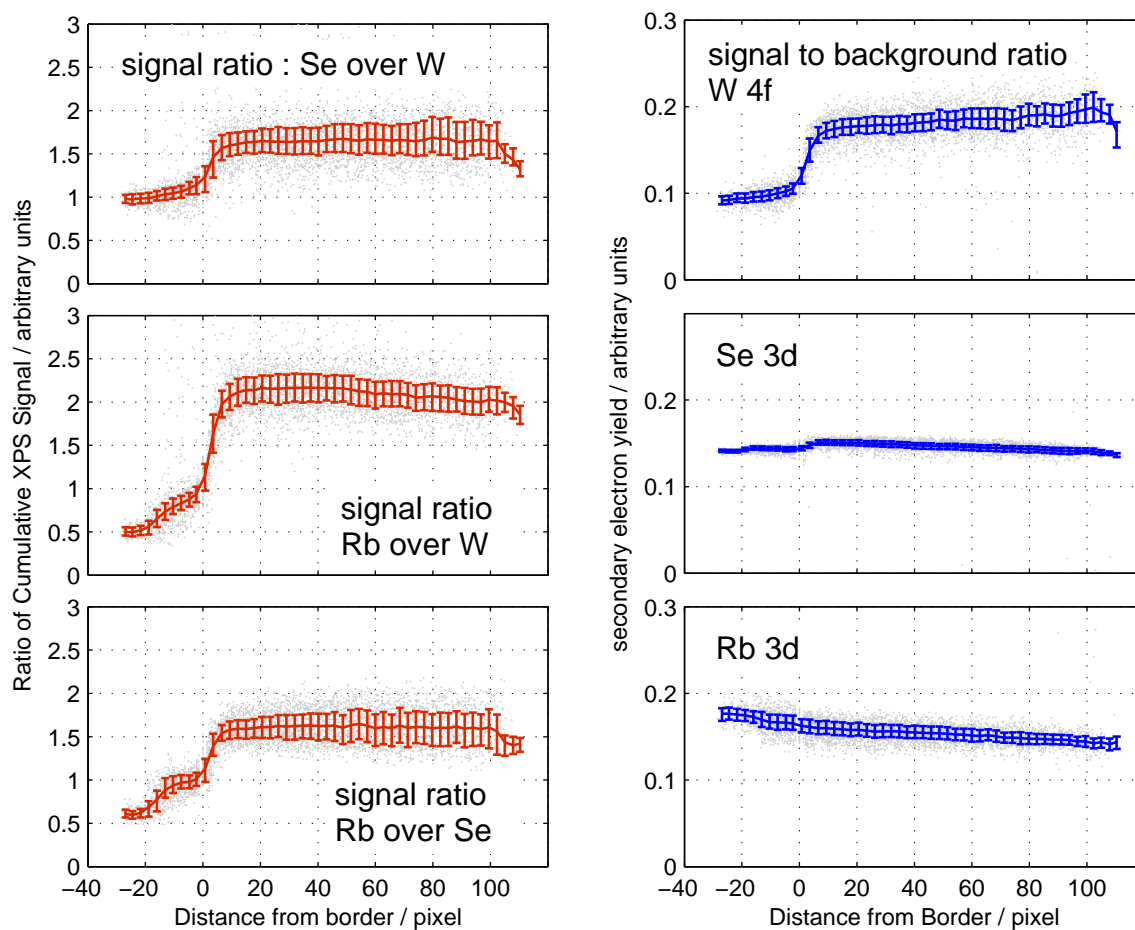


Figure 11.8.: Spectral features found for all data channels (continued). The meaning of the depicted features is identical to figure 11.7 (Parameters of the experimental data found there). **Left:** Ratio of cumulative photoemission signal of the examined core levels. **Right:** Secondary electron yield of electrons being emitted from specific core levels.

ality factor, and for the crystalline substrate, a correction factor owed to the spatial configuration of the unit cell would have to be introduced for a quantitative analysis. Here, only the ratio of the cumulative signals is presented (figure 11.8). Beforehand, a Shirley background was subtracted from the spectra. The effect of a shifted synchrotron beam was eliminated using the technique presented in chapter 9.3 for a large field of view.

As the substrate is composed of a fixed ratio of W and Se atoms, a constant relative signal is expected here, independent of adsorbate coverage. The upper left panel of figure 11.8 clearly shows a systematic deviation from a fixed ratio, clearly indicating a

non-stoichiometric composition at either part of the surface texture. As could also be seen from the spectra in figure 11.8, a lower concentration of Rb is found for region (I) (fig. 11.5), independent of the reference.

The probability of a photoelectron suffering inelastic scattering increases with the distance it has to travel through the sample before it can escape. Thus, the amount of inelastically scattered electrons emerging from a certain core level can be used as a measure of the average escape depth. As the surface is covered with an adsorbate, the secondary electron background of substrate core levels is expected to increase. Because electrons never gain kinetic energy when scattered, the Shirley background function always shows steps at the energy of atomic levels and is nearly constant in between. Thus, the height of a step in the Shirley function is a level-specific measure for the rate of scattered photoelectrons. Using these assumptions, the individual signal-to-background ratio can be computed for a core level. In the actual data, the only pronounced effect that can be correlated with the border is found for $W 4f$ (see figure 11.8).

As mentioned above, the strong deviation of the spectrum obtained from the $Se 3d$ core level from a doublet spectrum requires a special analysis. Here, the spectrum will be interpreted as a linear combination of an a priori unknown number of doublets with chemical shift, indicating a mixed environment of the Se atoms contributing to the photoemission signal. The spectra obtained from the clean surface (section 11.9) are fitted well by a theoretical profile with the parameters found in table 11.2, so a valid model of the pure doublet structure is known for the current experimental setup.

From these findings, a fit template can be derived which is used to decompose the spectrum into a linear combination of energy-shifted versions thereof. This task is technically identical to the decomposition of photoemission spectra including a mixed magnitude of SPV effect, so the algorithm presented in chapter 6(part I) can also be applied here. In the upper left panel of figure 11.9, the fit template for the $Se 3d$ doublet is shown. Here, a modified Gaussian width of $520 meV$ was used instead of the tabulated value. The increased width was introduced here because the observed spectrum is not expected to consist of discrete components, but found to be distributed with finite width around a set of shifted energy levels.

The decomposition algorithm was applied to the spectra seen in figure 11.6. The results are found in the lower left panel of figure 11.9. The gray dots mark non-zero components of a spectrum found at given mean distance to the border (x -axis) and at given energy shift (y -axis). In consequence, a measured spectrum is found to be the combination of all components arranged vertically, i.e., at constant distance in the plot. The magnitude of a component is represented by the size of a dot. The binding energy is referenced to the binding energy of the $Se 3d$ doublet (i.e., the maximum of the $Se 3d_{7/2}$ component) of the clean surface.

In this overview, basically three components of the $Se 3d$ core level can be identified (A-C). At 'negative' distance to the border (i.e. in region (I) of figure 11.5), the spectrum clearly consists of only two components (A,C) with at relative shift of $\approx +1.1 eV$ and $\approx -0.9 eV$. No evolution of these two levels is found across the surface. At positive

distance, a third component appears (B) at a relative binding energy of $\approx +0.3$ eV. No clear evolution can be identified for this feature, too. Note that the magnitude of this component is very small at 'negative' distance, so the effect seen at the border is considered virtual. For a detailed analysis, all components were binned into the relative binding energy ranges A to C. The right panels of figure 11.9 show the mean binding energy of the binned components and the relative weight of these regions. Here, a substantial difference is found between the types of the surface texture, indicating a larger variety of chemical environments of *Se* in the blue regions (fig. 11.5).

11.5. Discussion: Rb covered surface

From the results derived in the preceding section, it can be concluded that the Rb-covered surface can be classified into two types. Except for the observed border between the regions (I) and (II) (fig. 11.5), a closer examination of the spectral features of the substrate and the adsorbate resulted no further lateral variation that could be attributed to the sample. All spectral features evaluated here show a smooth change when crossing the border, which is delimited to an interval of 5-10 pixels, equivalent to 500 – 1000 nm for the actual settings. A certain tolerance level must be accounted for when deriving the border from the raw data, so the true width of the intermediate region is expected to be ≤ 500 nm.

A clear deviation of the stoichiometric ratio of the substrate on at least one of the regions is indicated by the change of the signal-to-signal ratio of *W* and *Se*. This difference is much more pronounced than found for the clean substrate in chapter 11.2. Furthermore, the regions can be discriminated by the relative Rb coverage, regardless of the used reference (*W* or *Se*). From the signal ratio, relative coverages between the regions (I) and (II) may be derived. Depending on the reference, a value near 1 : 3 (*Se*) or 1 : 4 (*W*) is found.

From the raw data in figure 11.6, no modification of the XPS spectrum of *Rb 3d* is found, so it is well approximated by a typical spin-orbit split doublet for the complete surface. At low concentration, Rb adsorbed on WSe_2 is known to donate its valence electron to the substrate, creating a space charge layer near the surface (see part I). Unless the binding energy of the valence electron is smaller than the conduction band minimum of the substrate, the ionization of adsorbed Rb is expected to saturate at higher density. Neutral Rb atoms should be distinguishable from ionized ones by means of the chemical shift of its core levels. As the core level apparently consists of only a single component, all atoms of the adsorbate must be ionized. At saturation of the Rb-induced band bending, this configuration is only possible for a valence level located at a smaller binding energy than the conduction band minimum of WSe_2 . This confirms the results found from numerical simulations of space charge layer formation discussed in part I.

The intercalation of alkali metal adsorbates is well known for a wide variety of tran-

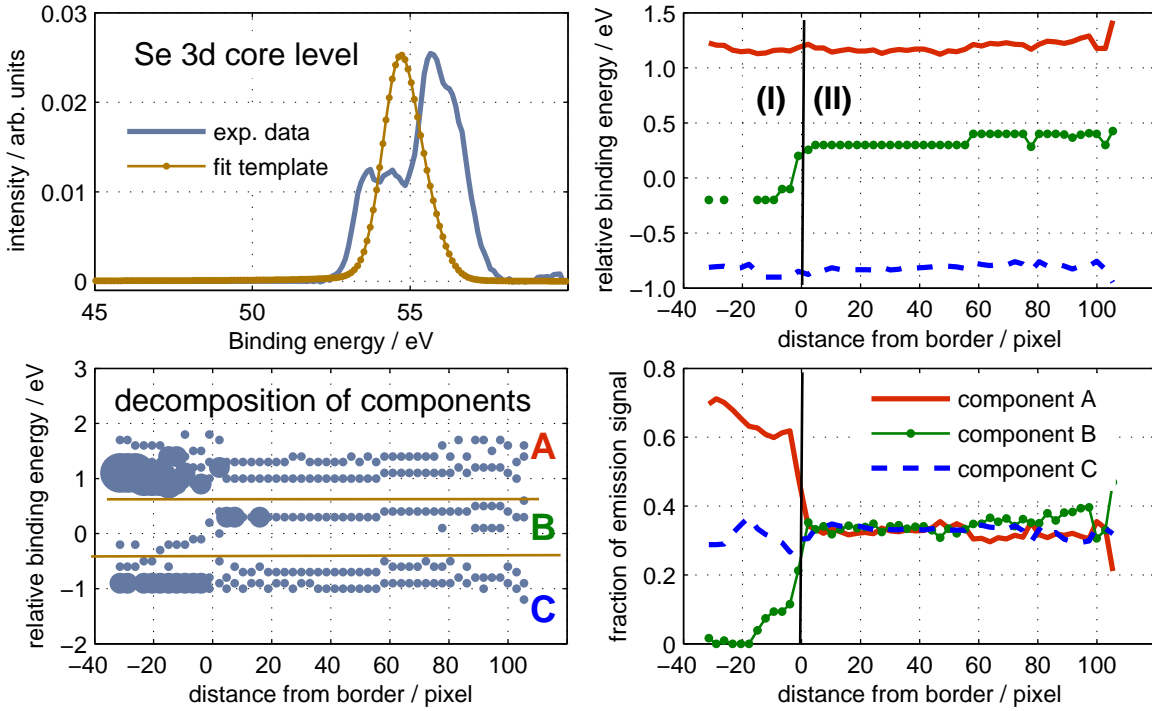


Figure 11.9.: Detailed analysis of the measured XPS spectrum of $Se\ 3d$ ($h\nu = 169\ eV$, $FOV \approx 25\ \mu m$). **Upper left:** Selected raw data spectrum and simulated template derived from fitting the spectrum obtained from the clean sample (fig. 11.3) including an increased Gaussian width of $520\ meV$. **Lower left:** Decomposition of the components. The spectra found at distinct distance to the border consist of a linear combination of shifted copies of the fit template with coefficients as indicated by the gray dots. The size of a dot represents the magnitude of its associated component (vertical position of the dot). Basically three separated contributions (A-C) can be identified. **Upper right:** No variation of the basically three components (A-C) is found with distance to the border. **Lower right:** Regions (I) and (II) in figure 11.5 can be distinguished by a change of contributions from regions A-C.

sition metal dichalcogenides [83], [84], [111]. Usually, intercalated atoms show a clear chemical shift with respect to atoms located at the surface of a substrate and can thus be identified easily. The information depth defined by the inelastic mean free path of photoelectrons is expected to include at least the first van der Waals-gap of the crystal, so intercalates would potentially be detectable, though at an attenuated signal level. As no additional components of the Rb 3d core level can be found here, intercalation of Rb in WSe_2 does not occur at room temperature. This result is in agreement with the

findings in [54].

Component A of the spectrum of Se 3d in figure 11.6, which is the major component of the spectrum in region (I) is found at the common binding energy for WSe_2 . It has a relative shift between 1 and 1.2 eV with respect to the position found for the clean substrate. This shift is caused by the electrostatic potential of the Rb-induced space charge layer near the surface, which is known to have a maximum magnitude around 1.1 eV when saturated (see part I). The thickness of the space charge layer is known from simulation (chapter 3.2) and has typical values in the range of some 10 nm up to 100 nm. As the information depth of the XPS technique is considerably smaller, the depth-dependence of the potential cannot be seen here.

The spectral components B and C have lower binding energy, revealing the existence of Se specimen with reduced oxidation state. In region (II), the relatively high abundance of reduced Se is accompanied by a higher oxidation state of W, as can be seen in figure 11.7. Taking the increased surface density of ionized Rb atoms in region (II) into account, an explanation of these results can be proposed. Usually, the Se atoms basically have covalent bonds with the W atoms of the same crystal layer. Here, the presence of positive charges in the direct vicinity of the Se atoms might cause a polarization of the bonds such that negative charge is shifted from the W atoms towards Se effectively.

For the complete surface, only distinct oxidation states without lateral variation are found. Especially the increased Rb density in region (II) does not increase the chemical shift in magnitude, but causes a transfer of relative weight between the distinct states (figure 11.9). The existence of discrete shift levels here can be explained when Rb is assumed to occupy special sites of the surface lattice of Se atoms preferentially. At low Rb concentration, as found in region (I), only equivalent sites are occupied and a chemical shift as found for the spectral component C results. At higher concentration (region (II)), an additional type of adsorption site gets occupied (component B). As the surface potential of the substrate is periodic due to the periodic arrangement of the topmost layer of Se atoms, the Rb atoms are expected to form a periodic lattice as well when located at well-defined positions. For $TiSe_2$, the formation of a periodic adsorbate lattice was reported by Starnberg [83], so a defined adsorbate lattice can be postulated for WSe_2 as well.

For the estimated escape depth of the photoelectrons, a contribution of approximately one third of the total Se emission signal is expected to originate from the back Se layer of the first crystal layer. As intercalation was excluded for this system, this contribution is expected to show an unmodified binding energy and therefore to be found in peak component A. Attenuation of the signal by the adsorbate affects all photoelectrons equally, so the stated fraction is kept up for the covered surface. In region (II), the total contribution of component A is hardly greater than the contribution expected from the back Se layer, so almost no unmodified Se is found in the topmost layer there. This means coverage of at least one monolayer of Rb for region (II). The coverage in region (I) is found well below this value.

As a consequence of lattice formation, the mobility of Rb atoms is expected to be

lowered drastically compared to the individual atom. Thus, lattice formation might be the reason for the observed stability of the border between the regions. Furthermore, the Rb stripe deposited on a clean surface (chapter 11.6) could get stabilized by this mechanism. In that case, no impurities of the surface were found to explain the sharp limitations of the adsorbed stripe.

An ultimate answer to the question why the observed structures have this good stability, even though basically consisting of mobile Rb, cannot be given here. The reason for the existence of regions with well-defined Rb density is regarded to be a result of lattice formation. In that case, two different types of sublattices would coexist on the surface.

The actual type of lattice formed at a certain position might be determined by the density of excess atoms found there after cleaving. The results in sections 11.2 and 11.3 proved the existence of sharply-bounded regions with deviating stoichiometry of the substrate, presumably made up by excess tungsten. The drastically increased concentration gradient found for the Rb-covered sample poses the question of the origin of the extra material and the reason for its accumulation. Tungsten atoms might get superseded from the high-density Rb-superlattice, so an outward increase in concentration results, but as no further information about the deposition process can be extracted from the data, this hypothesis cannot be tested here.

The self-assembled inhomogeneous distribution of Rb at a concentration near one monolayer has been shown here. Basically two distinct types of the surface were found and typical spectral features could be identified. Basic components of the structure formation mechanism could be identified, but not all were explained with absolute certainty, so parts of this section must be considered postulates. The existence of stable conglomerates of individually mobile atoms results in a fascinating system allowing for many more exciting experiments. Some evidence was found for the formation of superlattices of adsorbate atoms. Future experiments, providing spatially resolved information on the crystal structure, especially LEEM (low energy electron microscopy), are highly motivated by the results presented here.

11.6. Laterally confined adsorption of Rb

The Rb adsorbed surface of WSe_2 has revealed pronounced surface structures at the scale of some $10\ \mu m$, as was presented in detail in chapter 11.4. In order to gain a better insight in the structure formation process, some basic questions concerning the behavior of Rb atoms adsorbed on the surface of WSe_2 need to be answered. Here, a statement about the room temperature mobility of the adsorbate is of special interest.

A WSe_2 sample was prepared as usual (see chapter 8.3), cleaved in ultra-high vacuum and transferred into the PEEM. No unusual features were found for the clean sample. Afterwards, the sample was exposed to Rb flux using the dispenser equipped with a slit aperture. The sample was positioned at an approximate distance of $300\ \mu m$ from

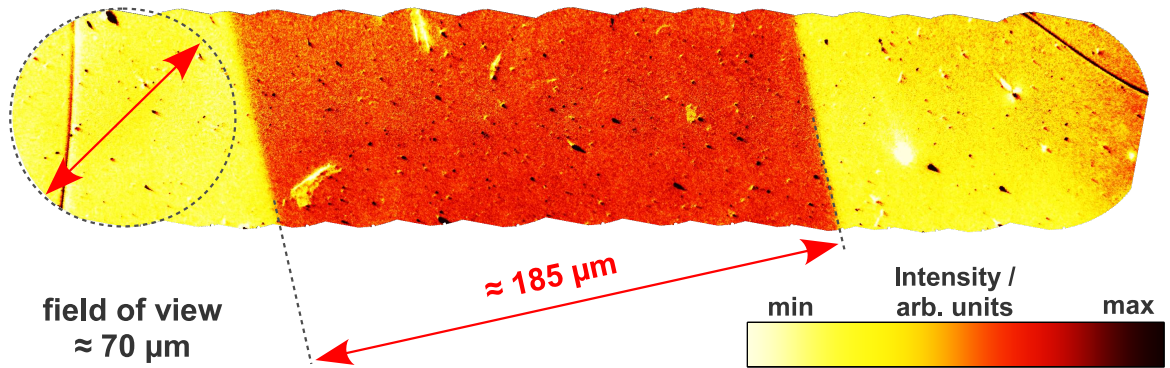


Figure 11.10.: UV image ($h\nu = 4.9 \text{ eV}$) showing a sharply-bounded stripe of increased photoemission signal on WSe_2 . Created by using a Rb dispenser with slit aperture as presented in chapter 8.3. At room temperature, the sharp contrast is kept up for at least some hours after deposition, although part of the adsorbed Rb is expected to be mobile.

the tip of the dispenser housing. Then, a heating current of 5 A was applied to the dispenser for a duration of 4 min . Identical parameters were used for the experiments discussed in chapter 11.4. During treatment and measurements, the sample always had room temperature ($\approx 300 \text{ K}$). After realigning the sample in the manipulator, a PEEM survey of the surface was made using the UV source and a large field of view of $\approx 70 \mu\text{m}$ in diameter.

The sample was found unchanged over the better part of the surface. The part of the sample that had been unscreened during evaporation could be identified easily: A broad stripe of relatively high photoemission signal could be found over a length of $\approx 2.5 \text{ mm}$. A series of images with large overlap was taken at subsequent steps crossing the stripe by moving the sample manipulator. The rather high abundance of point-like defects allowed for unequivocal determination of their relative positions, so the complete series could be assembled to a single overview image showing the full width of the stripe. For details of the image assembling technique, refer to section 14.1. The result is shown in figure 11.10.

A closer examination reveals that the stripe matches the dispenser slit in orientation and also, though roughly, in width. The actual slit width, which was stated to be $\approx 200 \mu\text{m}$, cannot be found exactly in the data, as length measurements were referenced to the diameter of the field of view here. Unfortunately, the nominal values are not achieved precisely for the -10 kV setup. Because there is no reason to expect a Rb stripe with smaller width than the slit aperture, the stated value of $185 \mu\text{m}$ should be explained by a somewhat larger field of view. The stripe width found using the position monitor of the manipulator also indicates a larger value.

The stripe was found to remain stable for at least some hours, and even its well-defined border showed up to remain as sharp as shown. Although Rb is usually assumed to have

very high room temperature mobility at surfaces, this clearly indicates that part of the deposited material is immobilized. First absorption measurements carried out at the border of the stripe reveal that Rb can also be found in the regions next to the stripe, but a quantitative statement cannot be given. From this result, it can be concluded that the adsorbed Rb remains mobile immediately after adsorption with a mean free path exceeding some μm . No evidence was found that the Rb will ever settle at room temperature. Finding the long-range surface Rb distribution as a function of distance from the stripe edge might answer this question and is an interesting subject of future XPS studies.

At the current stage, it cannot be excluded that the stripe is formed by contaminants from the dispenser. During similar experiments using TaS_2 as substrate [112],[98], the stripe could be reproduced several times. Furthermore, typical Rb induced features were found exclusively on the stripe, though a small surface concentration could also be detected in the vicinity as well.

This gives rise to the conclusion that the formation of the stripe is a consequence of direct Rb exposure and the achieved Rb concentration at least contributes to the stripe. On the TaS_2 -substrate, it is well-known that Rb is immobilized by intercalation [112], which is not expected for tungsten diselenide [54]. in accordance, no evidence for Rb intercalation was found in the XPS spectra recorded during this work. Further experiments will have to reveal the actual distribution of elements and find hints for a potential mechanism of Rb immobilization for a WSe_2 substrate.

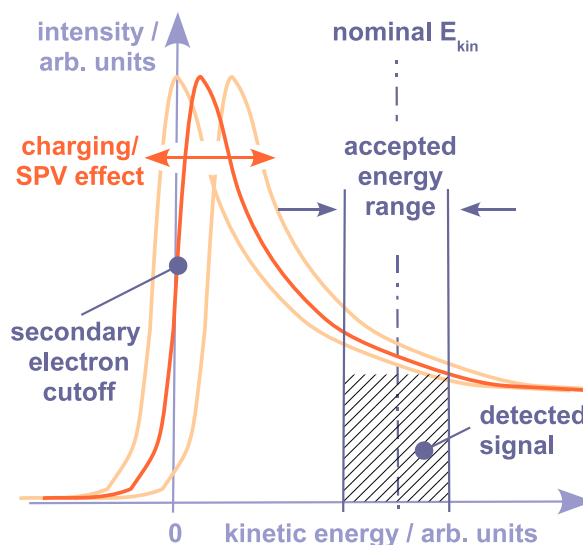
12. Absorption spectra of self-organized nanostructures

Besides the large-scale texture of the Rb-covered surface of WSe_2 , further Rb-induced structures can be identified in the UV survey shown in figure 11.4. At least on the part of the surface that shows a relatively high photoemission signal, a network of linear nanostructures is found. Similar features have been reported by Adelung to occur in this system [11],[12], and were denoted as nanowires there. In the STM study discussed in that paper, basic properties were examined, revealing insight into the creation process. At an early stage of nanowire growth, a network of trenches was found as a precursor. These were interpreted as cracks, induced by adsorbate-induced lateral tension, located in the topmost crystal layers. After further deposition of Rb, the trenches appeared to be partially filled up with material. Although it can be suspected easily that this material mainly consists of adsorbed Rb, no experimental proof of this hypothesis could be given, as the STM technique does not provide information on the chemical composition of a specimen.

In the cited work, nanowire networks showed up to have mesh sizes in the large range between some 10 nm up to $\approx 1 \mu m$. The observed width of the wires amounts to a few nanometers. The network structures found in figure 11.4 are considered to correspond to the largest components of a nanowire network as reported by [11] and motivate a spectroscopic study dedicated to the composition of nanowires. Even the largest reported nanowire width was found to be clearly smaller than the best spatial resolution of the photoemission microscope (20 – 30 nm). Nevertheless, an attempt is made here to obtain specific spectroscopic data from features of the wire network, unavoidably including its close vicinity.

The signal obtained from direct photoemission is expected to be very low when operating the microscope with an appropriate magnification. As an alternative, spectroscopic data was acquired in the form of absorption spectra here. In contrast to common XPS spectroscopy, the electron analyzer is configured for detection of electrons at low kinetic energy between 2 eV and 3 eV constantly and the photon energy is tuned by means of the monochromator. The signal in this kinetic energy range is dominated by the background of inelastically scattered photoelectrons. Because the escape depth of photoelectrons is confined to a small range beneath the sample surface, the signal level obtained from the secondary electrons is a function of the rate of photoelectrons created near the surface. The obtained spectra therefore basically represent the absorption coefficient of the sample as a function of photon energy. The major advantage of this technique is a much

Figure 12.1:
Principle sketch of the photoelectron signal near the secondary electron cutoff. The detected kinetic energy for the absorption spectra is chosen such that stationary modifications of the surface potential (SPV effect) do not bias the measured spectrum much.



stronger signal compared to XPS, so the PEEM can be operated at high magnification.

The data presented here was acquired using a field of view of $\approx 10 \mu m$. In general, absorption spectra are obtained by detecting electrons near the maximum of the secondary electron background near the low-energy cutoff in order to maximize the measured signal. The shape of the secondary electron background is expected not to change its shape, so an equivalent signal can also be obtained at alternative kinetic energy in the background spectrum. As a finite kinetic energy interval is detected, small shifts of the background spectrum caused by charging or the SPV effect can lead to a variation of the detected signal when the secondary electron cutoff is included in that interval. As scanning the photon energy also yields variable photon flux, the influence of such effects needs to be suppressed by choosing an energy range with sufficient energetic distance from the cutoff (see figure 12.1). As the signal is meant to represent a constant fraction of the total secondary electron yield, no particularly good energy resolution of the electron analyzer is required here, so the measurements were carried out using the large analyzer aperture (width: $60 \mu m$). In this configuration, the total energy resolution of the system is defined by the monochromator. Its exit slit was chosen such that an energy resolution of $\approx 150 meV$ was obtained, a value well below the common scanning step size of $0.25 eV$. At the resulting photon flux, no synchrotron beam-related modifications of the examined position at the sample surface could be observed after some hours of data acquisition. Large energy ranges were scanned so that specific absorption features of many core levels of the substrate and the adsorbate are covered. An overview of the core levels found in the scanned range is given in the table in figure 12.2.

All absorption spectra were preprocessed using the common techniques, i.e., normalization of the MCP sensitivity and masking of the active area of the detector. The resolution of the raw data images was reduced by binning areas of 2×2 pixel. Due to

12. Absorption spectra of self-organized nanostructures

Binding energy eV	Element/ orbital	Photoionization cross section* Mb (10^{-22} m ²) @ eV		Binding energy eV	Element/ orbital	Photoionization cross section* Mb (10^{-22} m ²) @ eV	
112.0	Rb 3d _{5/2}	4.5	200	229.6	Se 3s	0.15	250
113.0	Rb 3d _{3/2}	4.5	200	243.5	W 4d _{5/2}	0.70	550
239.1	Rb 3p _{3/2}	0.9	250	255.9	W 4d _{3/2}	0.70	550
248.7	Rb 3p _{1/2}	0.9	250				

* max. value at energy

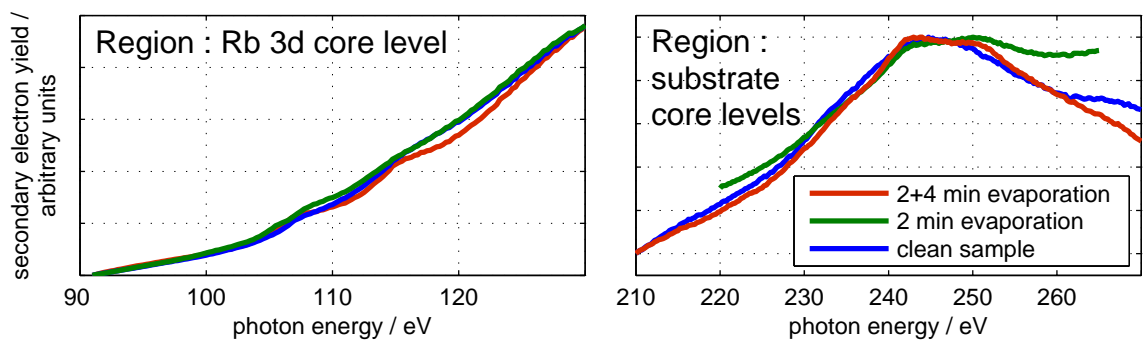


Figure 12.2.: **Top:** Table of core levels found in the scanned energy range. The binding energy was taken from [109]. The maximum values of the photoionization cross sections originate from [60] and are found at photon energies as given in the table. **Bottom:** Raw data absorption spectra from two different photon energy intervals (cumulative signal at $\text{FOV} \approx 25 \mu\text{m}$). Left, basically the Rb 3d core levels are covered. A clear effect is seen upon higher Rb coverage. Numerous core levels of the substrate are found in the right panel, revealing only unspecific features.

the relatively large step size and the small field of view, the effect of lateral variable photon energy is negligibly small here, so no related correction was applied.

While the network can easily be identified in images acquired using the UV excitation source, very low contrast is found in the X-ray absorption spectra. Even at long acquisition time, contrasts exceeding the level of statistical noise can hardly be achieved, so a safe visual identification fails. In the following sections, it will be shown that the application of the data classification scheme introduced in chapter 10 provides a robust discrimination of the structures from the spaces in between. As a result, part of the network structure is recognized by the algorithms with single-pixel precision by means of properties of the individual absorption spectra.

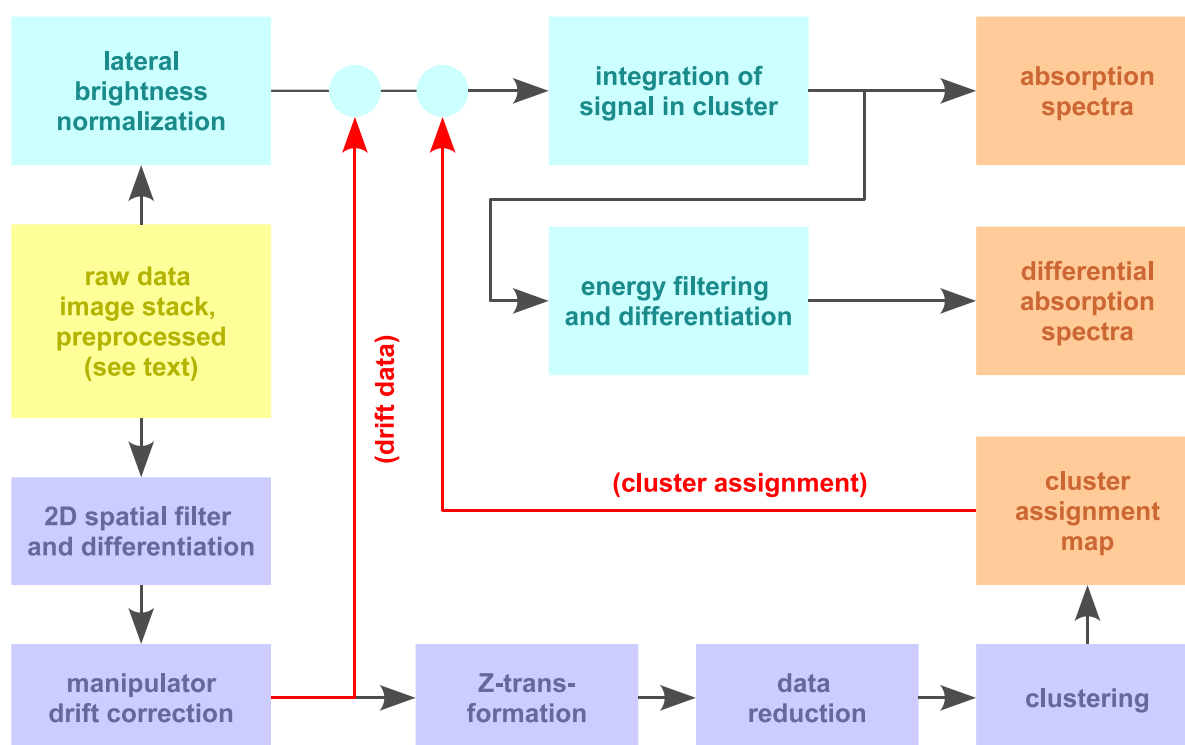


Figure 12.3.: Flux diagram for processing of absorption spectra. The requirements of the correction techniques are met by treating the data in two parallel branches. This layout allows for a minimum number of operations being applied to the data when deriving the absorption spectra. **Lower branch:** The smoothed and differentiated data is used to find and correct the drift trajectory of the manipulator. Further processing steps provide the cluster assignment map, from which pixel groups representing nanowires can be identified. **Upper branch:** The image of the preprocessed data is normalized for brightness. Intermediate results derived from the differentiated data are applied. Integration over the groups gives the final absorption spectra. Optionally, a smoothed and differentiated representation of the absorption spectra is derived.

12.1. Data Processing

In order to identify regions near nanowires, the absorption spectra were treated as shown in the scheme in figure 12.3. As the signal contained in a single detector image (i.e., at distinct photon energy) has rather high statistical noise, direct identification of the nanowire structures in the absorption spectra is not possible. In order to obtain a smoothed image with enhanced contrast, the spatial filter presented in chapter 14.2 was applied to each image. Large-scale inhomogeneities, in particular the beam profile, can

be ignored then, so the drift correction technique from chapter 9.5 can be applied to the data. The following steps aim at the identification of features in the image representing nanowire structures.

A reduced representation of the absorption spectrum in every pixel of the image was determined for each absorption spectrum using the algorithm introduced in chapter 10.2. The signal at every data point in the spectrum is meant to contribute equally to the reduced representation, so every image was z-transformed before finding the reduced representation of the data. In this context, applying the transformation to an image means subtraction of the mean signal in the image and normalization by the standard deviation. Subtraction of the mean value is redundant, as the two-dimensional image filter is supposed to yield zero-centered values. Normalization of the standard deviation becomes necessary, because the pixel-resolved data has considerable statistical noise. Assuming Poisson statistics, the standard deviation of the data grows as the absolute signal grows. As a consequence, images (i.e. data points in each absorption spectrum) recorded at high flux would dominate during the data reduction process if not normalized.

Using the reduced representation of the data, the clustering algorithm (see chapter 10.3) combines the absorption spectra from each pixel into groups with relative homogeneity. As the pixels are colored according to their associated group, the lateral arrangement of the groups becomes visible and groups representing nanowire structures can be identified by the shape of the covered region.

The actual absorption spectra are derived from the raw data with a minimum of processing steps. The beam profile can be approximated here using the technique for a small field of view as discussed in chapter 9.3 and a corresponding correction was performed for the complete data. In order to suppress a potential bias in drift correction by remainders of the beam profile, the drift trajectory determined from the differentiated data is applied here. The cluster assignment map, derived following the lower branch of the flux diagram in figure 12.3, is used to group pixels of the raw data. Integration of the data in the clusters gives the resulting spatially resolved absorption spectra. As these show relatively low variation throughout the examined region, differential absorption spectra are determined from this result by binomial smoothing and subsequent numerical differentiation.

12.2. Results

Absorption spectra were acquired for the clean surface of WSe_2 and two levels of Rb coverage. For the first deposition, the cleaved WSe_2 surface was exposed to Rb flux from the dispenser driven at a heating current of 5 A for 2 min. For the second step, an evaporation time of 4 min at the same heating current was chosen. After the first deposition step, 30 – 50% of the sample surface was found covered with a network of nanowire-like structures. The reference images seen in figure 12.4 of the inspected regions were acquired for both steps using the UV source. In contrast to the data presented

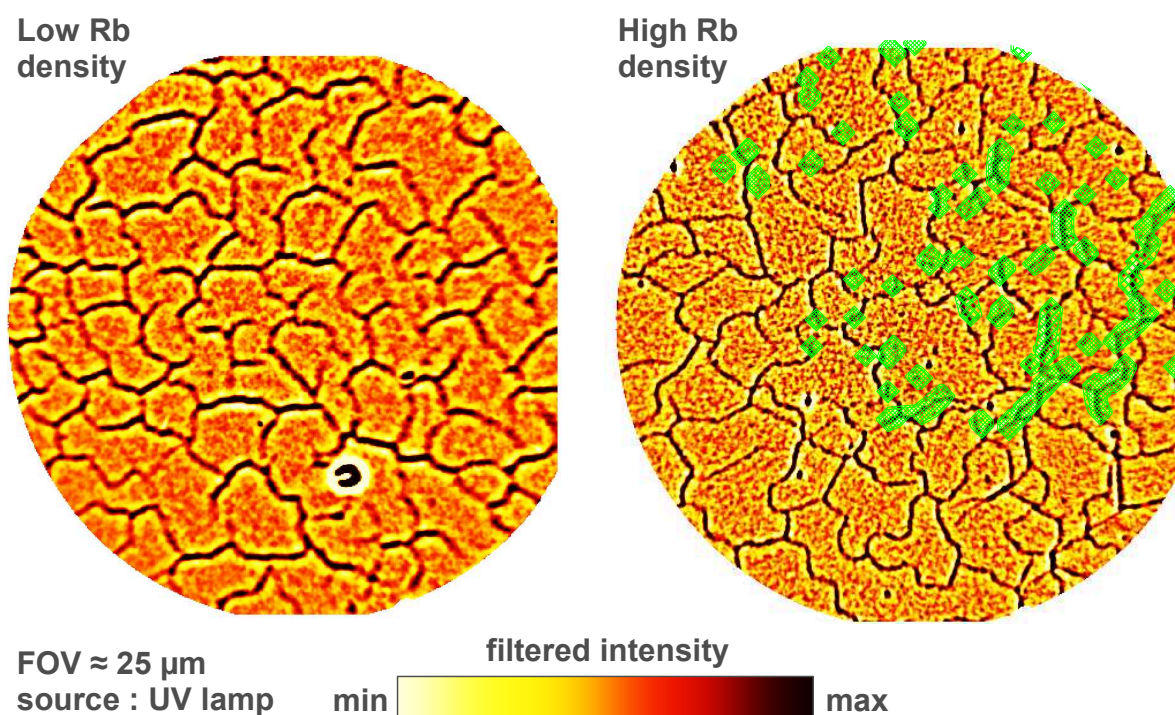


Figure 12.4.: Filtered UV images ($h\nu = 4.9 \text{ eV}$) of the examined sites showing pronounced nanowire structures. Both images were acquired from the same sample at different positions and at different nominal Rb coverage. The data was smoothed and the contrast was enhanced by application of the spatial filter introduced in section 14.2. The shaded structures of the right image are reproduced by spectral features, as will be discussed in the following.

in figure 11.4, the network appeared to have a relatively large fraction of open ends. If this can be interpreted as an intermediate step towards a closed network covering the complete surface, as reported in [11], could not be clarified, as no more evaporation steps were made. From the data presented here, no statement about a possible evolution of the nanowire network can be derived.

The energy range of the absorption spectra was chosen such that as many core levels as possible were covered. The table in figure 12.2 shows the binding energy and maximum photoionization cross section of all core levels of the substrate and the adsorbate that are found inside the scanning range of $91..131 \text{ eV}$ (*Rb 3d*) and $210..270 \text{ eV}$ (substrate core levels) respectively. Larger cross sections are found especially for some substrate core levels at lower binding energy, where the photon flux of the beamline is not sufficient for absorption spectroscopy. Most of the stated core levels are found in the binding energy interval $210..270 \text{ eV}$. The region between 91 eV and 131 eV binding energy is dedicated

to the *Rb 3d* core levels, so a clear effect related to the Rb concentration is expected there.

Raw data spectra for the different levels of Rb coverage are shown in figure 12.2. The major part of the dynamics seen in the spectra is caused by the change of photon flux with photon energy during the scans. Normally, this effect could be normalized by referencing the signal to the measured mirror current, but difficulties are faced here. First, a high cumulative carbon contamination of all parts of the beamline exposed to synchrotron radiation is expected, especially for the last mirror where the mirror current is acquired. The main absorption feature of carbon is usually found near $h\nu = 280 \text{ eV}$, with some unspecific effect in a broad range, so part of the substrate absorption spectrum might be affected. As the mirror current measurement is based on absorption, a strong overestimation of the photon flux is expected for photon energies near the carbon absorption edge. Generally speaking, the determination of the photon flux is always biased by the specific absorption spectrum of the mirror. In contrast to XPS spectroscopy, where a constant photon energy is used, this effect cannot be neglected in the photon energy range applied here.

Another reason for the mirror current being an inappropriate reference here is the low photon flux. In order to minimize the beam damage on the sample, as low flux as suitable was chosen here. As a result, the measured mirror current showed up to be very noisy and biased by a systematic, alternating deviation from the true signal. Therefore, referencing the signal to the mirror current was not applied here and substrate-specific features in the spectra are always superimposed by the variation of the photon flux. In the following, local changes of the absorption spectra will be analyzed with respect to the environment, so further normalization is not necessary.

A sample-specific feature can clearly be identified in the *Rb 3d* absorption spectrum by comparing the spectra with and without Rb coverage. Two edges in the spectrum at $h\nu \approx 107 \text{ eV}$ and $h\nu \approx 115 \text{ eV}$ get more pronounced as the Rb surface density is increased. No specific changes in features of the substrate absorption spectrum were found. The unsystematic deviation between spectra at different Rb concentrations at higher photon energy are presumably an effect of beam drift, as the beam profile normalization algorithm is only capable of equalizing the brightness of one image, but cannot compensate collective brightness variation.

The spatially resolved absorption data discussed here was acquired from the same sample specimen, but at different locations, which were found to be representative for the overall state of the surface at the current stage. The best choice would be to observe the same region of the sample surface at different stages. After long-term measurements at the same region of the sample, unspecific modifications of the radiation-exposed part of the surface are usually observed and cannot be suppressed completely, even when working with low photon flux. This is commonly explained by synchrotron-assisted cracking of hydrocarbons in the residual gas of the vacuum chamber with subsequent deposition of free carbon on the nearby surface [108]. Indeed, a carbon contamination of the surface can usually be found. During data acquisition, this effect has to be tolerated

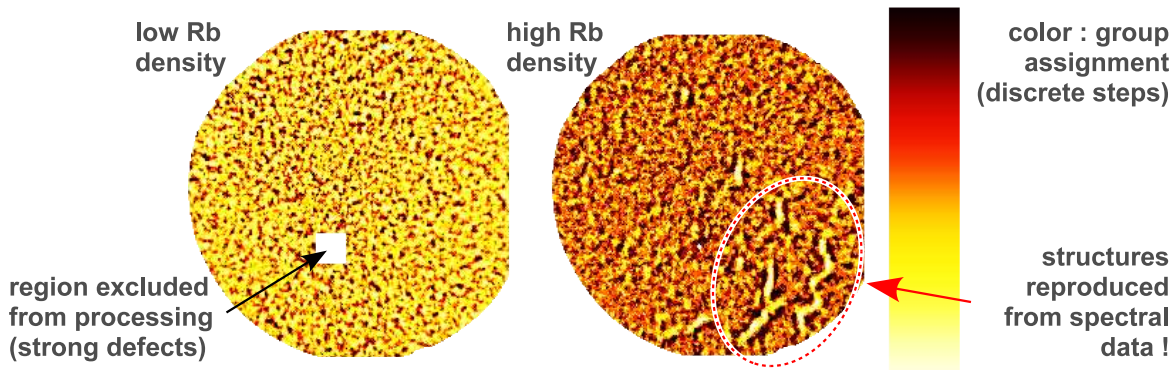


Figure 12.5.: Assignment of pixels to groups as found by the data classification algorithm. The discrete color encodes the group of a pixel. Derived from combined absorption spectra in photon energy ranges 91..131 eV and 210..270 eV at a field of view of $\approx 25 \mu\text{m}$. **Left:** No laterally structured segmentation of the data was found at low Rb coverage of the sample. **Right:** At high Rb density, part of the network seen in figure 12.4 can be reproduced from absorption data.

and the observed structures are obviously not harmed by this process. Growth processes during Rb adsorption are potentially biased in presence of a contaminant, so examining the same region twice was avoided.

For the following steps, the data from several scans was combined to obtain an enhanced signal. A reduced representation of the absorption spectra (chapter 10.2) was computed in both energy ranges and for both adsorbate concentrations. After matching the sample position in all scans, the total data per pixel is given by the first three components of the reduced representation from the absorption spectrum in each energy range, i.e., the image data is found as a set of points in a six-dimensional parameter space. As the reduced representation is computed from the energy-differentiated data, a demonstrative interpretation of the base vectors in 'spectral' space, as shown in chapter 10.2, for instance, cannot be given here.

The data clustering algorithm was configured to separate the data into 30 sets. The results for both adsorbate concentrations are depicted in figure 12.5. In the map shown there, pixels in the detector image are colored according to the group they were assigned to. The actual color of the pixels of a set was determined by the Euclidean distance of the cluster center to the center of a reference cluster in the parameter space. Here, the 'most uncommon' set was chosen as reference, i.e., the one with the largest mean distance to all other sets. It turned out that the structures are represented by this set.

Most of the sets are found to be distributed homogeneously across the detector image and to show no pronounced structure. They represent the unstructured part of the sample surface between the edges of the nanowire network. The fact that the members of these sets are scattered throughout the image indicates that no large-scale inhomogeneity

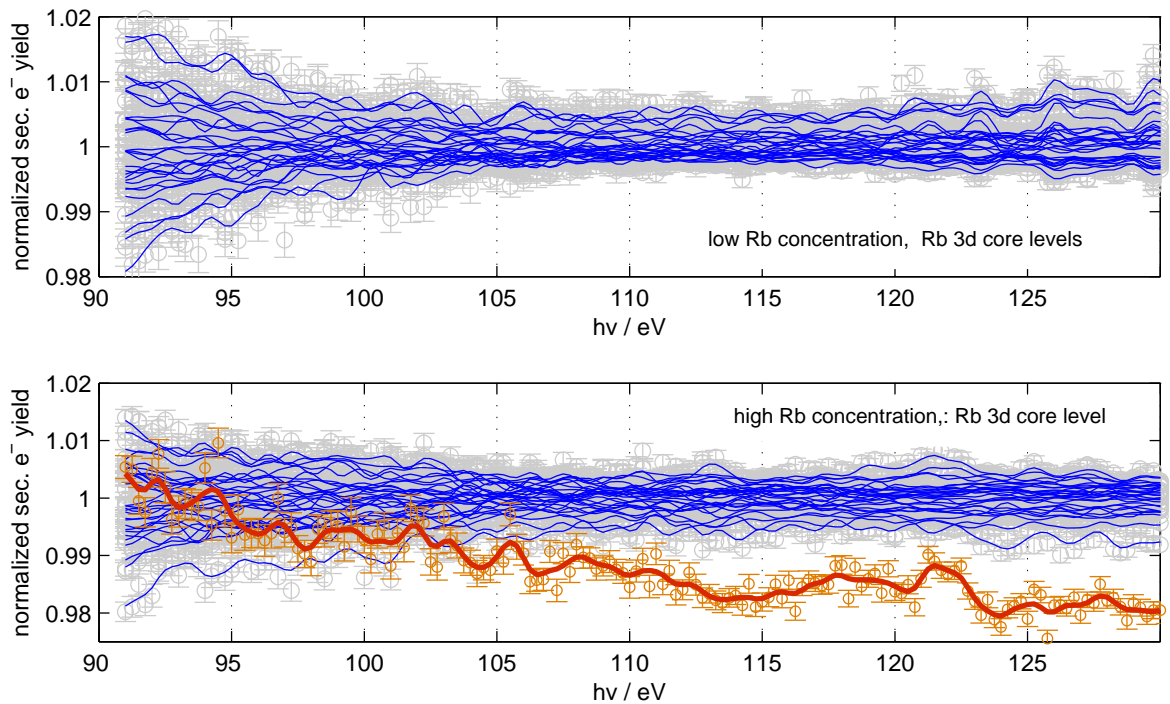


Figure 12.6.: Relative absorption spectra of the *Rb* 3*d* core level. Spectral data from regions as depicted in figure 12.5 is normalized by the signal obtained from the rest of the examined surface region. **Top:** Low Rb surface concentration. Although nanostructure networks can be identified on the surface, no significant spectral features can be identified, i.e., no group assignment representing the structures can be derived. **Bottom:** At higher Rb concentration, the network can be identified by means of the associated absorption spectra using the data classification algorithm.

is left in the image after all data processing steps. For some subsets (shown in the right image of the figure) of the data derived from absorption at high Rb adsorbate concentration, a local concentration of the associated pixels is found. The structures formed by these pixels can easily be correlated with part of the network found in the UV reference image in figure 12.4 and are highlighted there by means of the shaded areas. A large drift of the manipulator between acquisition of the UV reference and the absorption spectra must be taken into account here (see chapter 9.5).

The signal obtained from the covered region is concluded to contain spectroscopic data with a major contribution from the wire structures. Although network structures are also found in the reference image obtained from the sample with low Rb coverage, it cannot be reproduced by the classification of spectral data (see figure 12.5). Some virtual accumulation of pixels from one group is considered to be an artifact of the filtering

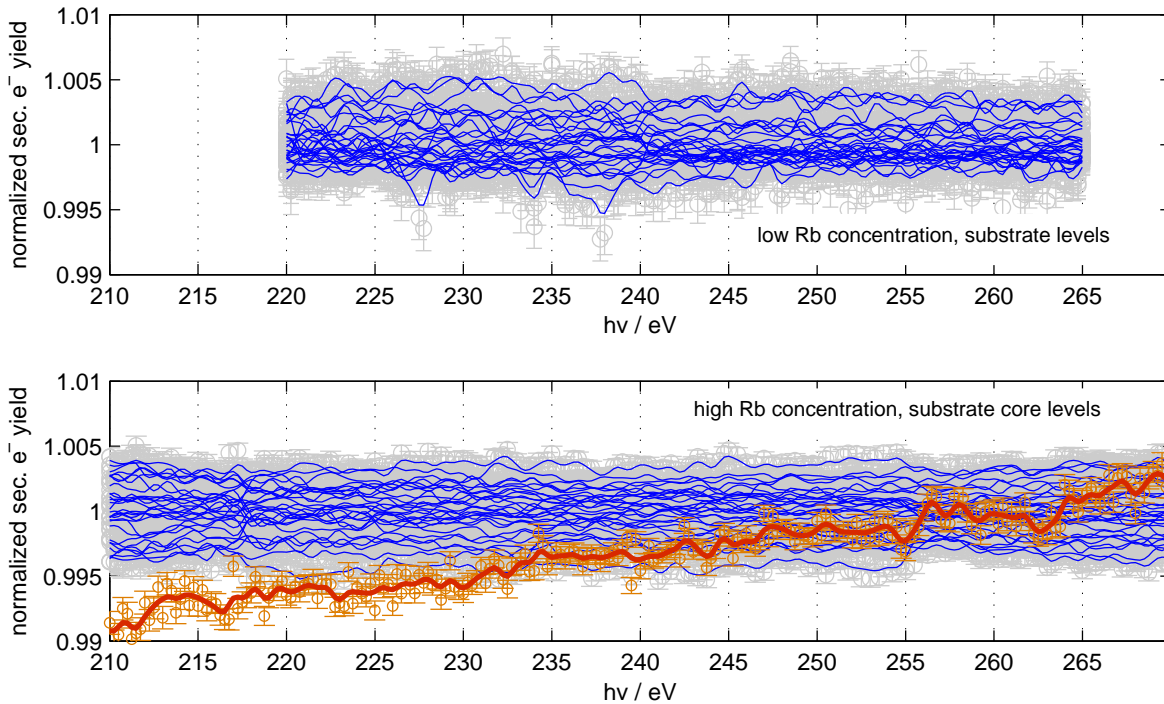


Figure 12.7.: Relative absorption spectra of selected substrate core levels (see table in fig. 12.2). **Top:** Low Rb concentration. No locally confined spectral features were found. **Bottom:** High Rb concentration. The data was separated into groups as shown in figure 12.5. One of them representing the neighborhood of the nanostructure network clearly differs from the rest.

process. No visible correlation of these groups with the observed network structure is found.

For a closer analysis, spatially resolved absorption spectra were created by means of the cluster assignment derived before, so one absorption spectrum per pixel group including the cumulative signal of all members resulted. A cluster consists of 1000–2000 data points, so the statistical noise of the cumulative absorption spectrum is drastically reduced with respect to the signal from a single pixel. The data clustering technique used here is known to group data with relatively high similarity and to separate contrasts. As a result, the maximum difference between all signals in the image is reflected by the clustered absorption spectra. All spectra found here show very low deviation from the average spectra in figure 12.2, so a representation showing the relative deviation was chosen.

The results are depicted in figures 12.6 and 12.7 for both energy ranges and adsorbate concentrations. For each cumulative signal, the data was divided by the average absorption curve of all other pixel groups, so each curve is referenced by the rest of the image.

The actual data points are represented by the open circles. As a measure of significance, the 'error bars' show the statistical uncertainty of each data point. It is derived from the standard deviation of the mean value obtained from all single-pixel signals contributing to the cumulative signal of a group. Subsequent application of Gaussian error propagation accounts for the error introduced by referencing. The solid thick line is meant to provide a guide to the eye and represents data points after binomial filtering along the photon energy axis.

No significant difference between most of the sets could be found. Basically, the spectra obtained from the regions are identical except for small, unspecific differences with a maximum between $\pm 0.4\%$ and $\pm 2\%$, depending on the examined case. According to the fact that no structure of the surface could be revealed by means of spectroscopic features, no systematic deviation of any absorption spectrum from the average was found in the data acquired at low adsorbate density.

At higher Rb concentration, one single cluster of pixels can be distinguished from the others (the red curve in figures 12.6 and 12.7). In the *Rb 3d* absorption spectrum, it can clearly be separated from the rest by its features and its reduced signal level. The nearly linear trend found for this region in the substrate absorption spectra is unique among all clusters. A small absorption edge near $h\nu = 123\text{ eV}$ might also be used for discrimination. The data originates from the core region of the wire-like structures found in the map in figure 12.5. Therefore, a fingerprint of absorption of nanowires and their closest vicinity is found in this data.

Features found in the absorption spectrum are supposed to be pronounced when examining the discrete derivative of the data, derived as shown in the data processing schematic in figure 12.3. The data can indeed potentially be interpreted by means of its derivative. However, a reliable discrimination of the groups is not possible with the given data due to the increased statistical uncertainty caused by error propagation.

The group assignment was checked intensively during many runs of the algorithm, covering a large variety of settings. Although initialized with random start positions (see chapter 10.3), the algorithm turned out to converge always to the shown cluster configuration. As artifacts of the processing routine can be excluded here, the found pixel classification is regarded as a true feature of the data. The maximum deviation found here amounts to only some percent for the single data point, but a statistical error analysis gave a strong hint for the significance of the determined effect. A detailed discussion of the observed features follows.

12.3. Discussion

The creation of network structures at the surface was observed at a relatively low Rb coverage. At this stage, the structures cannot be explained by spectroscopic features, although the applied technique showed up to be extremely sensitive to small changes in the signal. In conclusion, no evidence was found indicating that the creation of these

structures is necessarily accompanied by the accumulation of material, particularly Rb. The nanowires reported by Adelung [11] are expected to be too narrow to be imaged directly here. Instead, the observed width of the structures exceeds even the broadest wires found by STM, which is attributed to the finite resolution of the PEEM and considerable broadening by image filtering.

In cases when no spectroscopic signature of the structures could be derived, the origin of the contrast seen when using the UV source remains unexplained. Presumably, a small sensitivity of the PEEM to the topography of the surface must be taken into account here. Deviations of the electric near-field might bias the electron trajectories, so electrons emerging from structures would virtually originate from the vicinity. Assuming that, at least at an early stage, the networks are constituted by cracks, the contrast might be explained by this. An increased sensitivity to local changes of the work function due to the low photon energy of 4.9 eV was suggested [108].

Part of the network could be separated from the unmodified surface spectroscopically after increasing the density of the adsorbate. From the differences found in the absorption spectra, it can be concluded that some material was accumulated near the crack network. As basically connected parts of the network are found, earlier findings [11] that the cracks are filled up subsequently are confirmed in general. The obvious conclusion that rubidium is accumulated in the cracks can neither be confirmed nor denied from the absorption spectra as no clear modification of the absorption edge is found in the according region. The significance of a small effect found in the photon energy range from 110 eV to 115 eV can be speculated about, and associating the edge found near $h\nu = 123\text{ eV}$ with the *Rb 3d* core levels would require highly oxidized Rb. Nevertheless, the absence of a specific change of the *Rb 3d* absorption edge does not necessarily mean that no Rb is concentrated in the cracks. The spatial resolution of the PEEM is expected to be clearly above the width of the nanowires, so the contribution of the actual crack might be too low for a distinguished signal.

It could be shown that networks of extremely thin cracks can be observed using photoemission electron microscopy. Although the structures cannot be resolved directly, a sufficient influence on the photoemission signal is found to allow for the identification of the network structure. Even though an extremely small contrast was observed, the application of sophisticated data classification routines proved high reliability. Hereby, part of the network could be distinguished from the environment by spectroscopic means. Significant, but unspecific changes were found here, so a deviation of the chemical composition of the nanowires is likely, but cannot be quantified using the shown data. Because of the lack of pronounced features in the spectra, it can be suspected that the absorption is dominated by unconsidered atomic orbitals at lower binding energy. Especially for the W 4f, Se 3d and Rb 4p core levels, high absorption cross sections are known [60], so extending the experiments to photon energies between 10 and 100 eV using an appropriate radiation source is highly motivated. The high potential of the concept developed here has been proven, so a clear impact on future PEEM projects can be expected.

Part III.

Analysis of nanostructure networks

13. Introduction and experiment

The earlier parts of this work dealt with spectroscopic experiments with the aim of revealing the microscopic structure of the networks observed on the surface of WSe_2 after the deposition of Rb . A crucial result was that the accumulation of material near the edges of the network is basically independent from its formation. A deviation from the stoichiometric composition of the Rb-covered surface was not found at low adsorbate density, and possibly, the creation of the network does not imply any accumulation of adsorbates at all. It was proposed that nanowire structures are basically created as a network of cracks [11], but little is known about the suspected mechanism in this system.

In this part, a complementary approach to the characterization of the observed nanostructure networks is pursued. Using the PEEM setup (chapter 8) and the UV source, mainly topographic effects allow sharp and high-contrast imaging of the crack networks direct after creation. They are usually found covering the complete sample surface, so large-scale studies are motivated. The work presented here aims at the quantification of structures of the complete network using statistical means. From the analysis of geometrical features, a deeper insight into the microscopic structure creation process is expected, especially with respect to the hypothesis of stress-induced crack creation. In this context, a first attempt is presented to derive a theoretical explanation of the observed features. A spatially resolved analysis of the crack density and orientation might reveal the presence of intrinsic stress in the bulk material, caused by imperfections of the crystal. Due to the crystal structure, globally preferred directions of crack propagation are expected for a single crystal. Local deviations might hence be exploited for the identification of grain boundaries.

The statistical approach requires data from a sufficiently large region on the surface in order to obtain an adequate sample of the network with low statistical uncertainty. As the field of view of the microscope is limited to only a few micrometers at considerable magnification, large sets of neighbored regions were imaged separately and assembled to a single, large-scale survey image afterwards. When merging overlapping PEEM images, a careful analysis of imaging errors and image brightness has to be carried out to ensure that the consistency of the data in overlapping regions is not violated. Related effects and compensation techniques are discussed in detail in chapter 14.1.

In this part of the work, the data extracted from two surveys acquired at different settings will be analyzed. The first one has already been shown in figure 11.4. It consists of 19 images at a field of view of $\approx 25 \mu m$. As the sample is covered with the large scale texture there, nanostructure networks could only be extracted from part of the image. For the second survey, the single images were taken using the $10 \mu m$ field of

view of the microscope. The PEEM was operated in the modified setup using -10 kV sample-to-objective voltage (see chapter 8). The imaged region was shifted using the 'Object Align X/Y' settings of the imaging column, which provides well-reproducible, stable motion with no need for mechanical intervention. A grid of 7×7 images was used here. All applied processing techniques were developed during this work and are discussed in detail in chapter 14.1.

From the survey scans, features of the network could be recognized in an unbiased way by means of dedicated image processing algorithms. The required routines for conversion of the bitmapped PEEM images to a vectorized representation of the nanostructure network are inspired by well-established algorithms in image processing. Detailed documentation of the applied techniques is found in sections 14.3 and 14.4.

Part of the findings from the statistical network analysis are compared with the results of a simple theoretical model of surface crack creation. Details of the model are discussed in chapter 16. Compared to experimental findings, the results give evidence that the proposed tension-induced crack creation mechanism holds to some extent.

After introducing of some basic data processing steps in chapter 14, the results derived from the experimental data are presented (chapter 15). Throughout this part, the applicability of all steps in the data processing scheme is demonstrated by numerous examples derived from artificial and experimental data. Particular interest is directed towards the theoretical model developed here (chapter 16), as it relies on ample simplifications, which are motivated with full details. Results of a numerical simulation based on this model are compared to the experimental data in chapter 17.

14. Data processing techniques

Deriving morphological features from a network of nanostructures in PEEM data requires specialized image processing routines, which are introduced in this chapter. As the network is to be analyzed in a large region of the sample surface, a method to merge PEEM images was developed. Special attention was paid to PEEM-specific limitations of this approach. A suitable solution is presented in section 14.1. An unbiased, automatic way of extracting the network structure from the merged image is highly desirable. The essential steps are performed using well-known image processing techniques, but considerable individual modifications are necessary here. Automatic structure recognition requires a robust separation of desired and undesired information which can be achieved by image filtering. An individual implementation of a linear filter is presented in section 14.2 with a focus on the performance, especially for certain structure sizes. Sections 14.3 and 14.4 are dedicated to methods of extracting a vector representation of the network from the filtered, bitmapped data. The results discussed in chapter 15 were obtained after applying the presented techniques to the experimental data.

14.1. Composing survey images

In a photoemission electron microscope, a small region of a sample surface is imaged to the detector. The diameter of the region, called field of view (FOV), is defined by the settings of the imaging column of the microscope. For the Elmitec PEEM III, the predefined settings allow for FOV ranging between $70 \mu\text{m}$ and $1 \mu\text{m}$. As the image in the detector plane has a constant size, the FOV setting defines the total magnification. In cases when objects to be imaged are larger than the FOV at the desired magnification, the object has to be imaged part by part by shifting the surface region using the sample manipulator.

When a survey scan of a connected area is acquired in this way, it is desirable to extend the field of view virtually by assembling all acquired images to one. This requires a homogeneous illumination over the complete FOV. Thus, the methods outlined here can only be applied properly to data acquired using the UV source of the experiment. The small focus of the synchrotron radiation will give strongly inhomogeneous brightness (i.e. photoelectron yield) over the imaged part of the surface at larger FOV ($\geq 10 \mu\text{m}$), which can only be normalized under special circumstances (see chapter 9.3).

PEEM images usually include aberrations at large FOV, even at optimal alignment. A reasonable field of curvature can be found, which causes objects located far from the

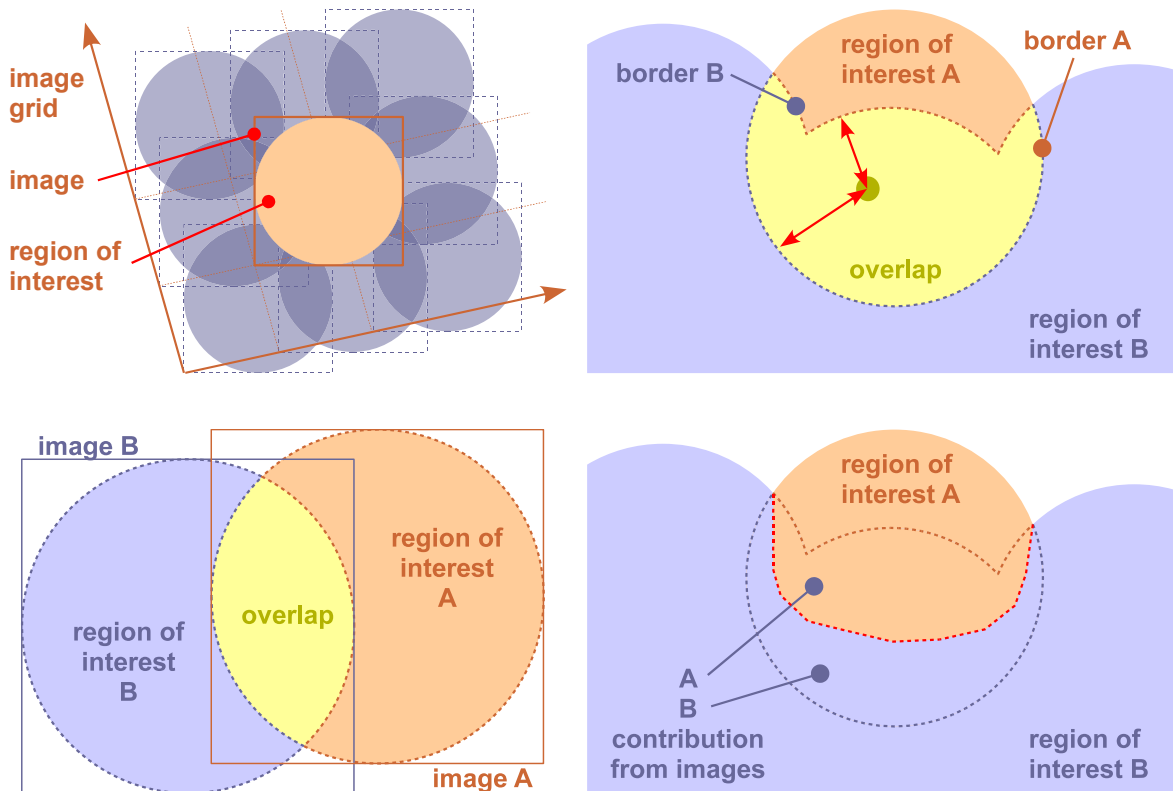


Figure 14.1.: **Upper Left:** Images are acquired such that a large connected region of the sample surface is covered. **Lower Left:** Considerable overlap between the images ensures correct determination of the relative shift. **Upper Right:** When assembling images, pixels in the overlapping region are chosen from raw data with the lowest imaging error. For this purpose, the distance of each pixel to the borders of the source image is evaluated. **Lower Right:** The overlapping region is separated into contributions from the two source images and merged.

optical axis to appear smeared out radially. Furthermore, features far from the optical axis are usually found to be imaged sharp at a different objective current than objects on the axis, i.e., in the center of the detector plane. Two images can only be aligned with certainty when they have considerable overlap. The presence of imaging errors will cause the data to be inconsistent in the overlapping region. Therefore, matching two images works best using intermediate magnification at a field of view of $25\ \mu\text{m}$ or $10\ \mu\text{m}$. For the $-10\ \text{kV}$ setup, data acquired with these settings showed no significant errors over the full magnified area. At large FOV, the outer regions have to be truncated, so, finally, not more area is covered per image. The matching of images is expected to work better the smaller the FOV is chosen.

In the following paragraphs, some prerequisites and details of a semi-automatic algo-

rithm for the assembly of images are discussed. Starting with two images, the approximate relative shift between them has to be known. A defined shift cannot be achieved with sufficient precision at the stage of data acquisition. The obvious option by shifting the manipulator against the microscope is always biased by mechanical tolerances. The second option to tune the imaging column by the 'Object Align X/Y' settings gives better results, but is applicable only for a limited range. Both methods will shift the image along axes that do not necessarily match the axes of the rasterized camera image, because the image is always rotated by the magnetic lenses of the microscope.

Usually, the shift must be determined by identifying the position of features in both images by eye. In the algorithm that was developed and implemented in the course of this work, this approximate shift is used as starting point for an automated procedure that finds the optimal shift. As the pixel information is scalar (gray scale data, no RGB channels), a numerical measure for the fit of two images is given by the least-squares sum of brightness differences of the pixels in the overlapping region. The size of the overlapping region varies with the applied shift, so an adequate normalization factor has to be introduced here. Alternatively, the optimal shift might be found subject to the correlation coefficient in the overlap. Minimizing the least-squares sum as a function of the relative shift has proven to yield an optimal result that shows up to be consistent with the values found from other image pairs in a grid of images.

Having determined the relative shift, the pixel information can be merged. If located in the overlapping region, a quantitative measure is required to decide from which image a pixel value is taken. The panels in figure 14.1 give an overview of the steps performed here. Especially when merging a new image to a set of readily-assembled ones, the overlapping regions can have extremely irregular shape. Hence, the obvious measure of taking a pixel value from the source image where it is found at the 'most central' position is not suitable in general. Instead, a complementary measure is used by equalizing 'most central' with 'least peripheral': Data originating from the precursor where the pixel has the largest distance to the border contributes to the assembly. The right panels of figure 14.1 give an impression of the strategy pursued here.

Both images to be merged always have an associated binary mask indicating the positions of valid image data, the so-called region of interest (ROI). The overlap is determined by simply applying Boolean logic to both ROIs. The overlapping part has borders with the non-overlapping regions of both precursors (called 'A' and 'B' in the figure). Inside the overlap, the minimum distance to each border is computed for every pixel. Image information is used from that source where the pixel is located most distant from the border. This measure assures that however irregular two source images are shaped, they will contribute their inner pixels to the merged image. Potential imaging errors from the outer regions of an image will be truncated automatically by this procedure, so the assembly is always made up by the best available data in a set of images.

Using this technique, the overall quality achieved for the merged image only depends on the quality of the source data. Even when using well-truncated precursors and applying the standard preprocessing techniques such as normalization by the sensitivity of

the multichannel plates (chapter 9.2), a large-scale brightness gradient is still found in the data, so an unstructured surface would appear at different brightness at opposing sides of the image. The reason for this is presumably caused by slightly inhomogeneous illumination or laterally variable transmission of the microscope. Usually, this effect is small with respect to the contrast found at features of the sample surface. When assembling large surveys, this variation results in annoying steps that become visible clearly at the distinct borders between the elements of the combined image. Assuming that all images mainly consist of unstructured, homogeneous areas with a rather small amount of features at moderate contrast, an unjustified, yet effective method of brightness equalization can be applied.

As long as there is no pronounced periodicity found in the data, the features cancel upon superposition of all raw data. This results another normalization image which can be applied to the original data before merging. This method has proven to be an effective way to remove the remainders of inhomogeneous brightness in the images.

Application examples of the routines outlined here can be found in figures 11.4, 11.10, and 15.2. This method gives the opportunity to analyzing large-scale structures such as the nanowire networks discussed later in this part. Merging PEEM data has proven to be a suitable technique to accumulate sufficient data for a statistical analysis of structural features within a connected region.

14.2. Contrast-enhancing image filter

The signal level acquired in PEEM images is very low in common cases, so raw data generally includes a significant amount of statistical noise. An improved signal-to-noise level can be achieved when the image information is accumulated over several neighbored pixels, but the excellent spatial resolution of the microscope would be degraded artificially by this measure. In order to retain the full spatial information, the signal level of each pixel can be estimated by computing the sliding average of the neighborhood of each pixel under the assumption of an equivalent signal. Near the border of structures, a systematic error introduced hereby must be tolerated. The computation of the two-dimensional sliding average can be performed by a discrete convolution with an $N \times N$ matrix (N odd) with subsequent resizing of the result to the size of the image. The elements of the matrix define the neighborhood of pixels that contribute to the estimate of a pixel's signal value.

When the result is truncated symmetrically, the neighborhood is symmetric around

the center point. For instance, convolution with the matrix

$$M = \frac{1}{6} \cdot \begin{pmatrix} & & \dots & & & \\ & 0 & 0 & 0 & 0 & 0 \\ \vdots & 0 & 0 & 1 & 0 & 0 \\ \vdots & 0 & 1 & 2 & 1 & 0 \\ \vdots & 0 & 0 & 1 & 0 & 0 \\ & 0 & 0 & 0 & 0 & 0 \\ & & \dots & & & \end{pmatrix} \quad (14.1)$$

would result the weighted mean of a pixel (weight 2) and its four next neighbors (weight 1). In analogy to a one-dimensional smoothing window, the neighborhood to include in the average is defined by non-zero, positive matrix elements in the most simple case, whereas all other elements are set to zero. In order to obtain an estimate of the mean value of all involved pixels, the matrix elements must sum up to 1.

Due to the selectivity of spatial frequencies achieved by this method, it is also referred as spatial filtering. During this work, matrices with approximate circular symmetry were applied in order to have an isotropic filter characteristic. The actual image information from the microscope is confined to a circular region inside the rectangular camera image. The useful part of the image is usually separated from the rest by means of a binary mask, the 'region of interest' (ROI). Arbitrary shapes of the ROI are possible in general. When an irregularly-shaped mask is used, special measures have to be taken in order to validate the filtered data near the borders, i.e., when part of a pixel's neighborhood is located beyond the ROI. Without special treatment near the borders, the filtered data needs to be truncated by shrinking the region of interest. Thus, part of the image information is lost when applying a spatial filter.

The methods developed in this chapter aim at the reliable identification of spatial structures. Filtering is a crucial step to enhance the image information with certain selectivity to the expected shapes. The filter applied in the following chapters is designed to pronounce contrasts. From the field of image processing, a well-known approach to edge detection is known. It is based on the implementation of the discrete Laplacian as a matrix

$$\Delta = \begin{pmatrix} 0 & -1 & 0 \\ -1 & 4 & -1 \\ 0 & -1 & 0 \end{pmatrix}, \quad (14.2)$$

which is applied to the data by convolution as well. The Laplacian is defined as the sum of the second partial derivatives $\Delta = \frac{\partial^2}{\partial x^2} + \frac{\partial^2}{\partial y^2}$ of the coordinates x and y . Applying this filter can therefore be interpreted as computing the discrete second derivative of the image information. Gaussian error propagation causes the derivative to have an even increased noise level, so the need for smoothing becomes even more crucial. Smoothing and differentiation can be performed by a special filter design in one step. Applying

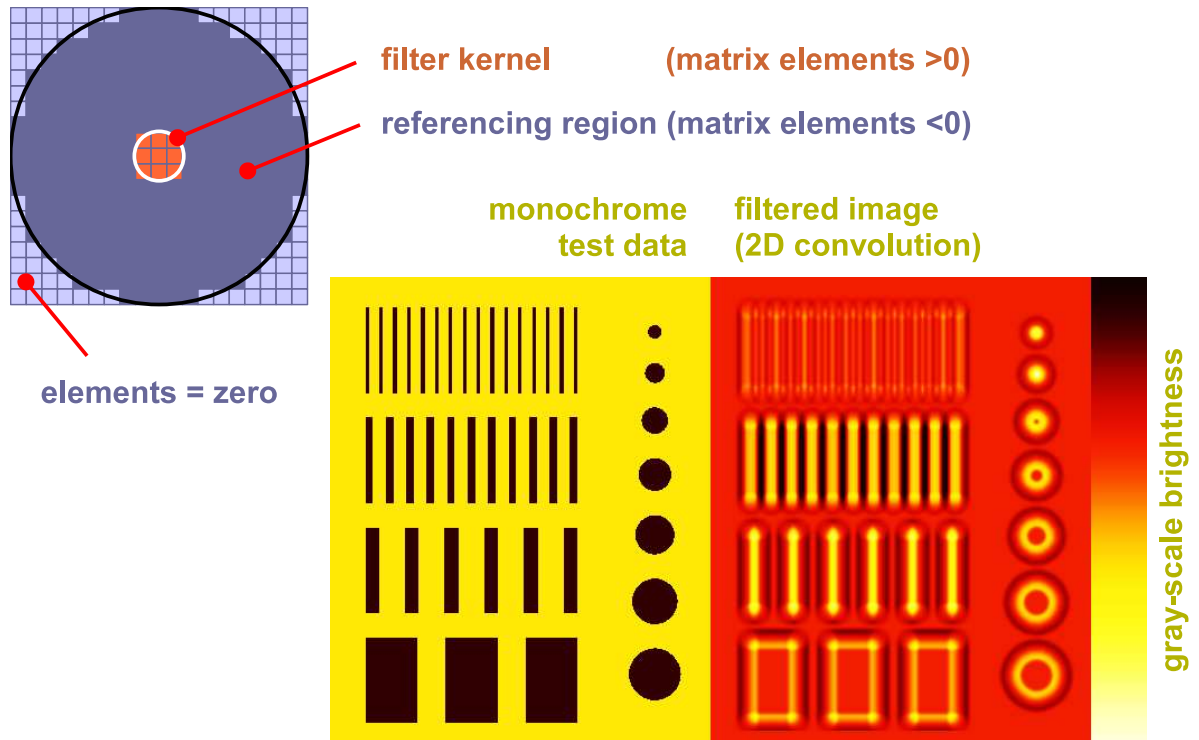


Figure 14.2.: **Upper Left:** Schematic of the matrix representing the two-dimensional convolution window that is applied throughout this work as a linear image filter. Contrast enhancement in the data is achieved by inherent numerical differentiation and smoothing. **Lower Right:** Result of applying the filter to a gray scale image with artificial structures. A pronounced size selectivity is found. Edges are pronounced by the filter (large structures). The approximate circular symmetric design results an isotropic filtering characteristic (circles).

Δ to rasterized data basically results the difference of a pixel value and the average of its next neighborhood. In order to provide an improved mean value estimation, the neighborhood of the pixel is extended strongly, as can be seen in the design of the filter matrix ('referencing region' in figure 14.2). The signal of the pixel is estimated by the pixels in the 'filter kernel'. As the kernel includes a relatively small number of pixels, the noise level of the result is dominated by the number of kernel pixels. The elements of the filter matrix have only two different non-zero values, a positive one in the kernel, and a negative one in the referencing region. Both values are scaled in such a way that the complete matrix sums up to 0, as featured by the implementation of the discrete Laplacian.

Figure 14.2 provides sample data to illustrate the effect of filtering an monochrome image. As seen from the larger structures at the bottom, high magnitude is found espe-

cially at the edges of structures. The filter shows a pronounced selectivity for structure size, so the group of intermediate sized bars is enhanced best, while the fine bars are clearly suppressed. The filter is designed to have an isotropic characteristic, which can only be achieved approximately when handling discrete, gridded data. The circular structures to the right show that sufficient isotropy is achieved by the design.

The fact that certain structure size is 'preferred' by the filter requires a customized version for the expected structure size. Thus, a generally optimal filter design cannot be stated here. Various application examples are found throughout the work. Filtering is a crucial step for the automated detection of network structures. An impressive intermediate step of this process, i.e., after the filter had been applied to the data, is shown in figure 15.2.

14.3. Skeletonization of monochrome bitmaps

The common representation of image information is a matrix containing brightness information in one (gray scale) or three (color) channels. Whenever this information is to be interpreted with the intention to identify objects, a method to extract primitive geometrical features, i.e., points and lines, from the rasterized image is required. Before proceeding with the actual vectorization of bitmaps in the following chapter, an algorithm that is capable of reducing the image to lines is introduced here. It is a crucial part of the processing chain applied for the automated recognition of the Rb-induced networks on WSe_2 and provides data to which the vectorization algorithm can be applied.

The starting point is a monochrome (not grayscale!) image resulting from raw data processing. Here, a monochrome representation of the gray scale map is derived from applying a brightness threshold to the preprocessed data as it results from the procedures discussed in chapter 9. In the following, a pixel is called 'white', when its gray scale brightness exceeds this threshold, otherwise it is called 'black'. What appears to the human eye as curvy lines, is a lengthy cluster of white pixels that are interconnected directly or indirectly via next-neighbor relations. In the input data, the lines have an irregular width of > 1 pixel, so stepping from one pixel to its next neighbor does not necessarily result in stepping along the line.

Furthermore, applying a brightness threshold may not be suitable for all areas of the filtered image. This results in gaps between the pixels of a line occurring occasionally. The first step is to close these gaps. Throughout this chapter, a 4-pixel next neighborhood is considered, i.e., the pixels above, below, to the left, and to the right. In order to close small gaps in a line, it is sufficient to simply expand clusters of white pixels until their borders coincide. This is achieved by the simple rule of converting a black pixel into white, if at least one of its next neighbors is white. Figure 14.3 shows the result obtained after 2 iterations of this procedure applied to real data. In the field of image processing, this rule is known as 'dilation' [113]. The actual number of iterations to apply depends on the individual data quality and, in this case, the size of the mesh in

pixels, because excessive use of this measure will give undesired interconnections inside the mesh.

Dilation will modify the topology of the mesh, as it potentially connects pixels that did not have at least an indirect next-neighbor relation. While this effect was taken into account intentionally in order to tolerate small defects, the next step is explicitly meant to be topology-preserving. The main task is to reduce the width of lines in the mesh to 1 pixel by successive removal of redundant white pixels at the border of a broad line. Again, the algorithm is meant to operate locally, i.e., only on next-neighbor relationships. As the pixels of the bitmap can only be black or white, only 2^4 configurations of the direct neighborhood are found. For each configuration, a pixel is considered redundant, when two of its neighbors also have an alternative connection among each other. All configurations can be enumerated and be tested individually, as is shown in figure 14.3. For instance, when the left and upper neighbor are white, the central pixel is redundant if the pixel to the upper left is white, i.e., a connection exists via this pixel. Hence, the central pixel is turned black. In case three next neighbors exist, two diagonal neighbors have to be evaluated. If all four neighbors are white, this indicates that a pixel belongs to the interior of the line and must be kept white. The global behavior of the algorithm can be tuned by the way pixels with one white neighbor are handled. The primitive steps discussed here are usually denoted as *erosion*. The algorithm is iterated until it has converged, i.e., no further redundant pixels can be removed.

The width of all lines is reduced to 1 pixel then, so a common point in a line has 2 white neighbors, except for junctions (nodes) of a network. Pixels having only one white neighbor are considered end points of a line. Removing these pixels will thus result in removal of nodes in the mesh that have only one edge attached. Otherwise, the algorithm tends to create branched, reduced lines from broad, fuzzy lines. This behavior may not give acceptable results, as it tends to overestimate the complexity of the structure and result an inappropriate reduction. Another special case is found when an all-black neighborhood is detected. Such pixels originate from isolated islands without mesh structure, so if these pixels are considered 'features' or 'redundant' depends on the user's policy. In image processing, this algorithm is known as *skeletonization* [113] of a bitmap, and its result is called the *skeleton* of the input data.

For the actual PEEM data that is meant to be processed with the methods introduced here, removal of white pixels with one or less white neighbor was selected. As the line width of the structures is rather constant here, a defined number of steps of the algorithm is applied to the data instead of iterating until convergence, so open ends are trimmed, but preserved in general.

In the following paragraphs, some implementation-specific features are discussed. It can be thus be skipped at first reading.

Simply by counting the number N of white next neighbors in the skeleton, every white pixel can easily be identified as part of a line ($N = 2$), an end section of a line ($N = 1$), or a node ($N = 3, N = 4$). As a node has only four next neighbors in this lattice, it can have a maximum of four edges attached to it. Using this simple discriminator, the

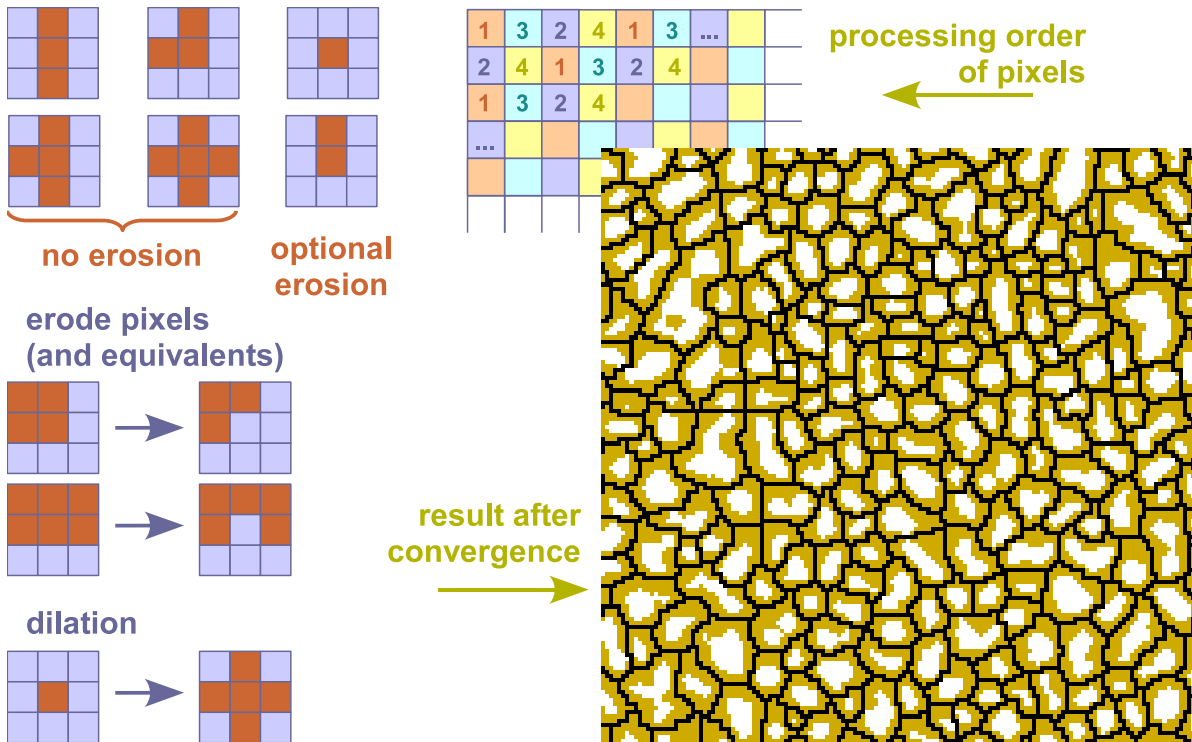


Figure 14.3.: **Left:** Next neighborhood of pixels to be processed when thinning lines. Only configurations shown below (and rotated/mirrored equivalents) contribute to the skeletonization process. After convergence, the network is made up by elements show in the upper part. **Upper Right:** Processing order of pixels during skeletonization. One iteration of the process is made up by 4 runs. This strategy avoids interference between pixels without need for double buffering the image. **Lower Right:** Light colors indicate 'white' pixels of the monochrome bitmap after two steps of dilation. The dark pixels make up the skeleton. The excerpt originates from real experimental data (figure 11.4).

network structure can be extracted and analyzed easily.

The direct neighborhood contains one bit of information per pixel, so the complete configuration can be encoded in the lower four bits of a byte to give a unique numerical code for each neighborhood, by which the required connectivity tests can be identified. To simplify the code, the encoding for all pixels can be performed at once by a discrete convolution of the bitmap with the matrix M

$$M = \begin{pmatrix} 0 & 1 & 0 \\ 2 & 0 & 4 \\ 0 & 8 & 0 \end{pmatrix} \quad (14.3)$$

and cutting the result appropriately to the former dimensions. Here, white pixels must be represented by 1, and black pixels by 0. Pixels at the border of the image must be excluded from the skeletonization algorithm, as a proper determination of the code will fail here. The actual implementation will therefore never remove pixels located at the border of a bitmap. As a workaround, the user might want to define the 'exterior' of the image to be black or white by extending the bitmap with a frame of the appropriate color.

To avoid excessive removal of pixels, the neighborhood needs to be updated after modifying a single pixel. Computing the neighborhood relationship for the complete bitmap as discussed in the preceding paragraph would be in vain. Instead, one step of skeletonization is subdivided into four substeps. In each substep, the pixels of the sublattices depicted in figure 14.3 are tested for redundancy and removed if possible. The lattices are chosen such that the direct neighborhoods of elements on the lattice do not interfere. Thus, updating the next-neighbor analysis becomes necessary only after one substep is completed. As long as the sublattices are processed in an appropriate order, so that the treatment of neighbored pixels does not take place in descending or ascending order, the algorithm will contract a thick line to its center. Although the algorithm has long been published and has become member of specialized toolboxes like the Image Processing Toolbox of the MATLAB data processing software, an individual implementation was created here to grant full access to all optional behavior as stated before.

After the skeletonization algorithm has converged, i.e., no more data points can be removed from the bitmap, the network structure can be identified easily by analysis of next-neighbor relationships. The survey image of the nanostructure-covered surface as presented in figure 11.4 was processed up to this stage in order to determine the inter-structure area (i.e. fragment size). The skeleton is used as starting point for the determination of a vectorized representation as discussed in the following section.

14.4. Vectorization of bitmapped data

Once the skeleton of the bitmap is found, a vector representation can be determined. As mentioned before, every line in the skeleton has distinct starting and ending points, which are identified by the number direct neighbors of the same color ($\neq 2$, see previous section). Lines are traced by stepping from a pixel to its next neighbor successively, starting at an end section or a node. The resulting series of points at discrete coordinates can be approximated by linear segments within given tolerance. A method performing this task will be introduced now. It must provide an approximation of the given data points by a series of linear segments that need to fit the pixel positions locally. A variable number of segments must be assumed in order to process lines of arbitrary complexity, but should be kept as low as possible for an effective reduction of the data.

A suitable solution to the problem is provided by an iterative algorithm. It is based

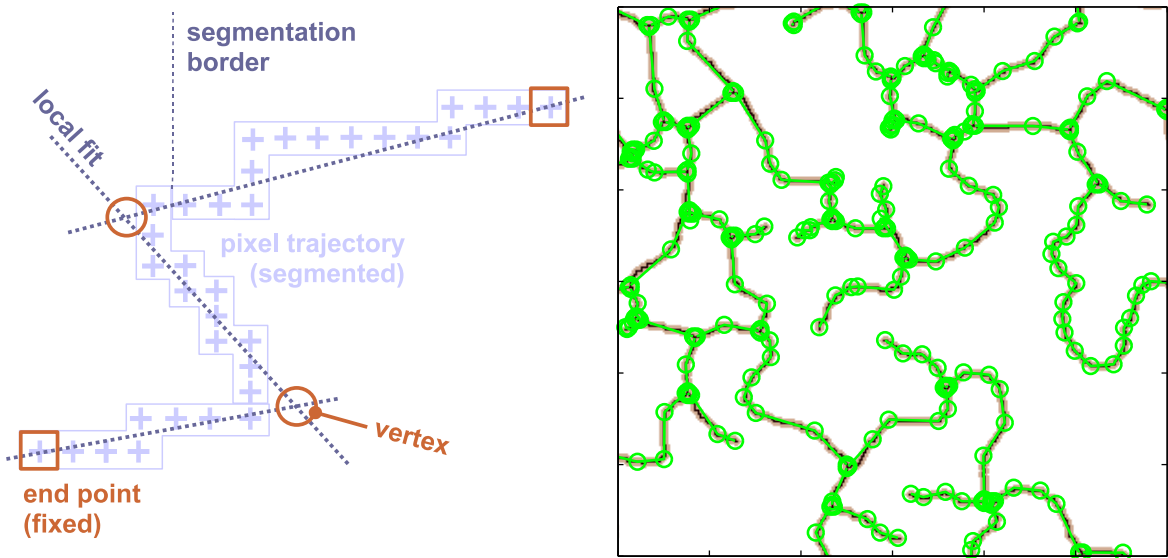


Figure 14.4.: **Left:** Vectorization of monochrome bitmapped data by approximation of pixel trajectories by linear sections. The method requires the skeleton of an image (section 14.3). **Right:** Result of vectorization applied to the nanostructure network. The skeleton is shown black, the result of vectorization is shown as green line. Vertices are highlighted by circles.

on the fit of linear functions to subsets of the data consisting of subsequent pixels (see figure 14.4). At each iteration step, one out of three rules is applied to each interval: The current interval is divided into two parts if the maximum deviation of a point from the fit exceeds a given threshold value. If the fits to two subsequent intervals have an angle below a certain threshold, they are united. If points at the end of an interval show up to be approximated better by the fit to the neighbored interval, the points are reassigned to that interval. Intervals including less than five points are united with a neighbor, because no reliable local fit can be found for such small amount of supporting points.

This procedure is iterated until a stable state is achieved, i.e., no thresholds are exceeded and no data points were reassigned throughout one run. Then, the vertices of the vectorized representation are determined by computing the intersection between neighbored intervals. Special rules apply to the ends of a pixel series. In order to upkeep junctions when vectorizing a network of structures, the coordinates of the first and the last point in a series are always included as vertices.

Figure 14.4 shows a detail view of a PEEM survey image from a sample with nanostructure network (see chapter 12). The data was filtered and skeletonized (black pixels). A light environment of the skeletonized pixels was added in order to provide better visibility. The vectorized representation is shown as green lines in the figure. Every vertex

is highlighted by an open circle.

The vectorized representation of rasterized images allows for the identification of geometrical features in the data, so an analysis of structural properties becomes possible. Similar algorithms are known in fields like computer vision [114]. Using the routines introduced in this chapter, large data sets can be processed automatically. In the following, they will be applied to the nanostructure networks presented before. Hereby, a completely new point of view with a focus on structural properties is achieved.

15. Results

The survey image obtained from raw data at relatively large field of view (fig. 11.4) was filtered using the convolution window presented in chapter 14.2 in order to enhance the contrast of the nanostructure network. The result was converted into a monochrome bitmap by applying a brightness threshold to the gray-scale data. The topology of the network is represented well by the monochrome bitmap, but its edges appear rather broad, so skeletonization (chapter 14.3) was applied. After treating the data with the mentioned methods, the network is represented by 'white' pixels separating the imaged surface into conglomerates of connected 'black' regions, the intermediate spaces of the network.

In regions where the network can be traced using these methods, it shows up to be closed, i.e., with a very low amount of open ends. Due to the crystal structure of the surface, propagation of cracks along directions of high symmetry is expected to occur preferably. Hence, a sixfold symmetric distribution of the crack direction is expected here. No such feature can be derived from the data, presumably because of the rather low resolution of the bitmapped data. Note that the fragments have dimensions of only a few pixels here, so a considerable amount of uncertainty is introduced by the discrete grid. Further errors might occur in the data processing chain.

Assuming that the network is made up by cracks, the intermediate areas represent fragments of the top crystal layer. From the treated data, the size distribution of the fragments can be extracted. To this end, an algorithm working analogous to the 'bucket fill' tool of common graphics applications is applied to all intermediate spaces, so connected areas are identified by their 'color' and the size is determined by simply counting the number of appropriate pixels.

All fragment sizes that could be registered by this procedure were histogrammed. The result is shown in figure 15.1. A total of 5048 fragments contributes to the observed distribution. As can be seen in the figure, most of the fragment sizes range between an area of 30 pix^2 and 130 pix^2 with a maximum at $\approx 60 \text{ pix}^2$. As a raw data image has 512×512 pixels and the field of view measures $\approx 25 \mu\text{m}$ in diameter, 1 pix^2 corresponds to an area of $\approx 2.5 \cdot 10^{-3} \mu\text{m}^2$. A considerable part of the smallest fragments is expected to be lost during processing, especially during the dilation step (see section 14.3), when gaps between the structures are closed. Therefore, it can be assumed that the abundance of small fragments is underestimated by the procedure.

Due to the low overall signal from part of the texture, no structures could be identified there. Later measurements suggest the existence of similar structures on that part, but statements on structural features found there cannot be derived from the survey. Hence,

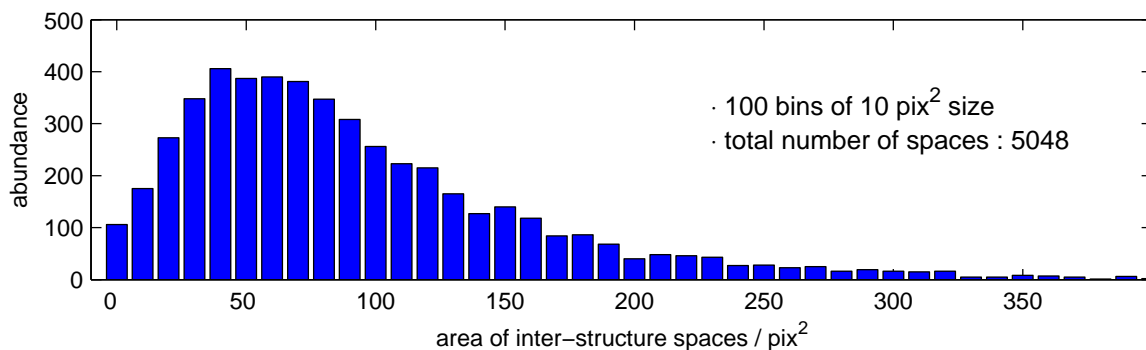


Figure 15.1.: Histogrammed distribution of inter-structure area size from experimental data, as derived from the survey image shown in figure 11.4 after contrast enhancement. Assuming the network represents cracks, the size of fragments is given hereby.

possible interactions between texture formation the nanostructure creation cannot be identified here. Except for a region with relatively large fragments at one border of the survey, no long-range effects are found. The mentioned region was mapped at rather low imaging quality, so the finding is considered to be an artifact. On the remaining part of the survey, no local deviations from the overall fragment size distribution can be identified.

A closer analysis of the aspect ratio (i.e. the ratio of length and width) of the fragments should reveal potential anisotropic stress during crack formation, as more cracks per unit length are expected in directions with high mechanical stress. From the analysis of the fragments in the survey data, no associated effect can be found, neither global nor locally constrained. A precise determination of the shape of the fragments is limited by the rather low image resolution, so data taken at higher magnification is desirable.

Figure 15.2 shows the survey scan of Rb-covered WSe_2 acquired at a field of view of $25 \mu m$. The filtered data with an artificially pronounced contrast is depicted there. It was acquired from another, identically prepared sample in a later beamtime. The network structures are reproduced in general, and some differences are found in details. The data originates from a sample that showed no tendency to form a surface texture, so a homogeneous background was found for the complete sample surface. In contrast to the first survey, no cracks were created on several regions. Especially near the boundaries of these unaffected regions, the network shows a rather large amount of open ends, so fragments of the surface are not separated completely in many cases. Therefore, the fragment size distribution cannot be derived from this data set. The total coverage of the surface with crack networks was estimated to be 50 – 70%.

The clearly improved resolution of the image with respect to the former survey allows for a more detailed evaluation of the observed structures. After filtering, a skeletonized representation of the network was derived as before and the complete network was

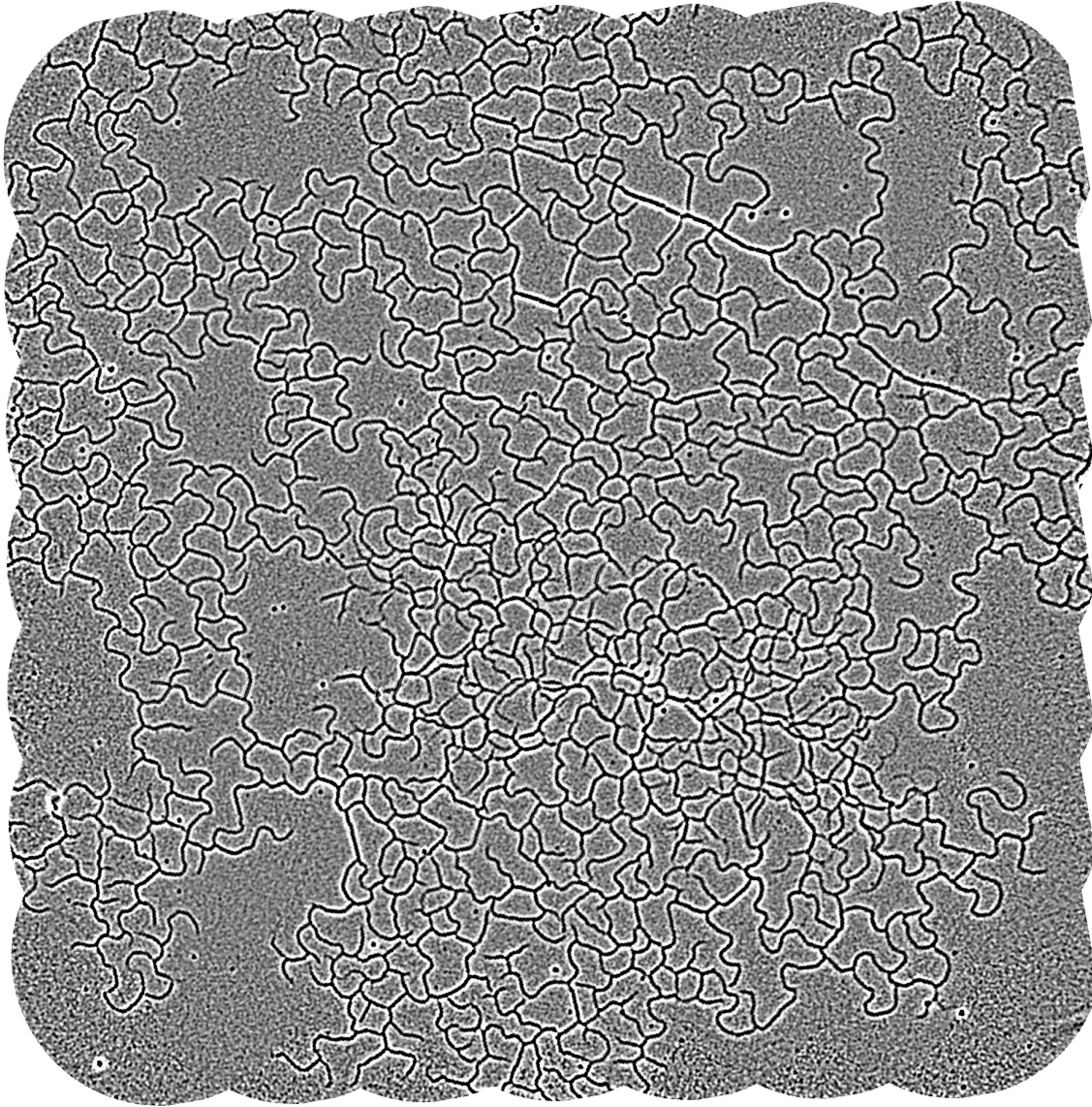


Figure 15.2.: Nanostructure network on WSe_2 after deposition of Rb . The survey was assembled from 7×7 raw data images showing a circular region on the sample surface with a diameter (field of view) of $\approx 10 \mu m$ each. The data was acquired using the UV source with $h\nu = 4.9 eV$. The contrast of the shown data was increased by the application of a two-dimensional filter (section 14.2).

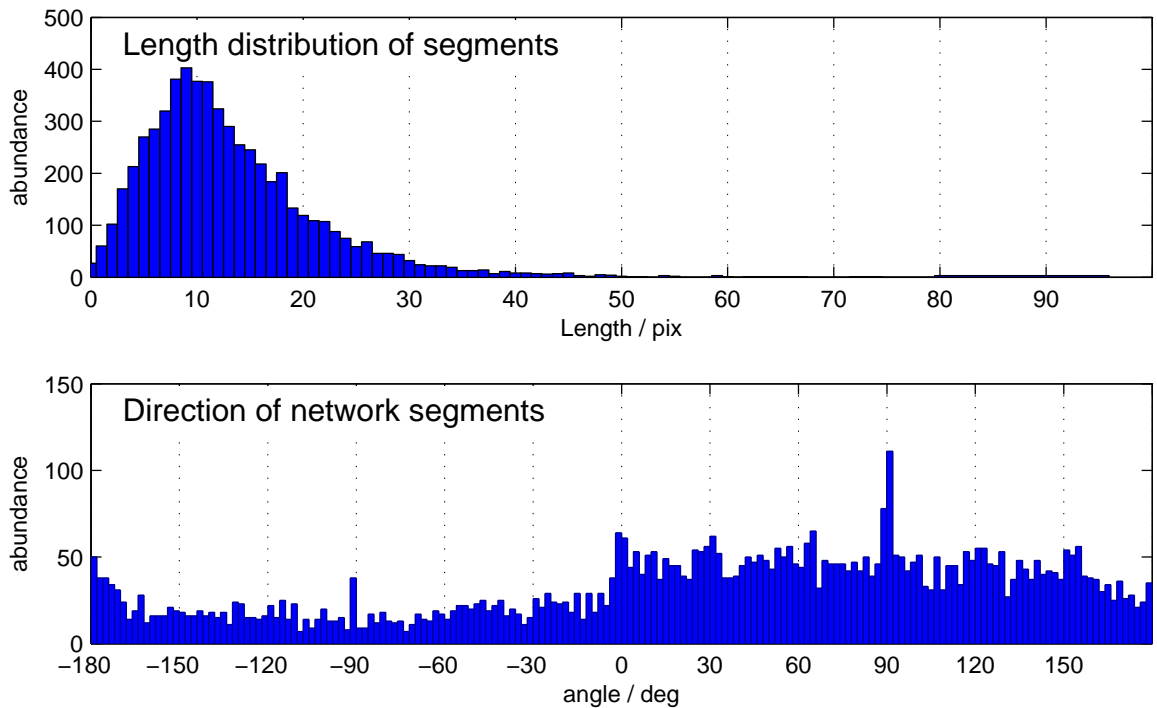


Figure 15.3.: Vectorization of the nanostructure network in figure 15.2. General geometrical features of the linear edge segments. **Top:** Length distribution of linear segments in the network. **Bottom:** Direction of linear segments.

transferred into a vectorized representation applying the methods introduced in chapter 14. After vectorization, the network is represented as a graph whose nodes are connected by the curvy edges. In the vectorized representation, the edges are approximated by a sequence of connected linear segments. Having reduced the data into points and lines allows for evaluating geometric properties of the crack network. Several representative features were determined and summarized in histograms representing the complete data shown in figure 15.2. The results are found in figures 15.3, 15.4, and 15.5.

First, the analysis is focussed on the properties of the smallest units, i.e., the linear segments that make up the edges of the network. The upper panel in figure 15.3 shows the length distribution in pixels. At the chosen magnification, a distance of one pixel is equivalent to $\approx 200 \text{ nm}$. As the diameter of the field of view was not calibrated exactly for the modified PEEM setup, some uncertainty is introduced to the physical length scales. No specific features are found in the experimental length distribution. As already found from the survey at large field of view discussed above, no evident local deviations from the overall distribution are found in the image.

The lower panel in figure 15.3 shows the distribution of the absolute direction of the linear edge segments in the network. Zero degrees is equivalent with the positive

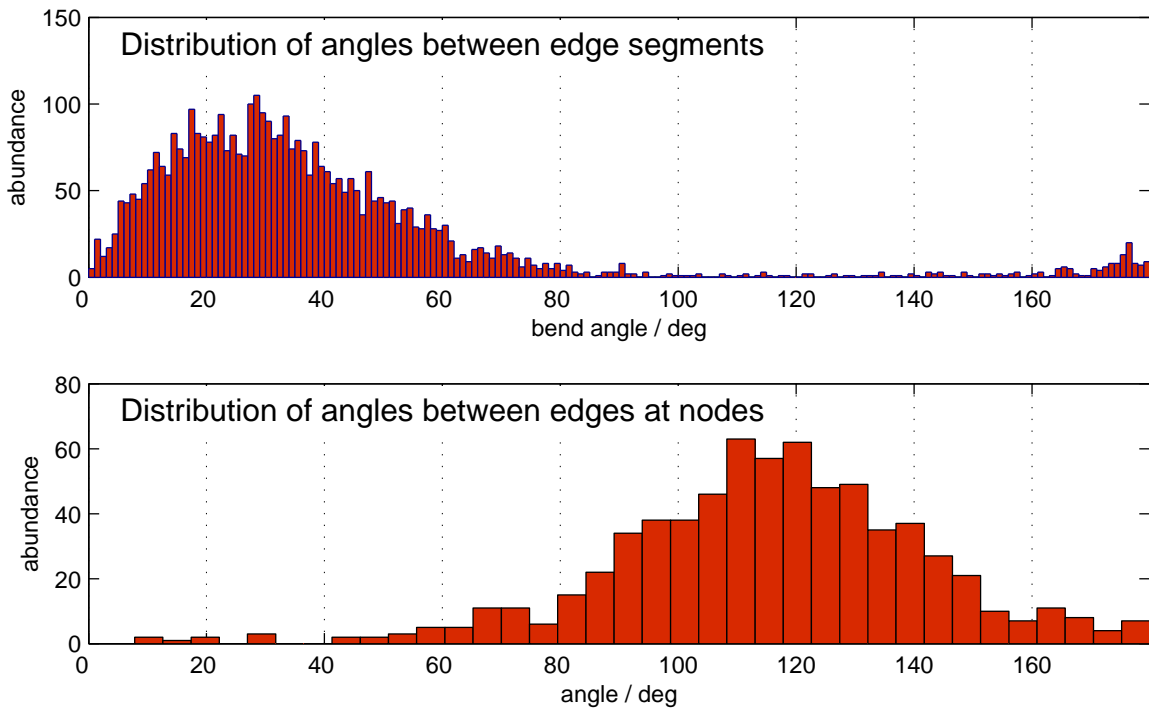


Figure 15.4.: Vectorization of the nanostructure network in figure 15.2 (continued). Local orientation of linear network components relative to neighbored features. **Top:** Angles between segments of network edges. **Bottom:** Angles between edges at nodes.

horizontal direction. The histogram shows a slightly increased concentration at multiples of 45° . This effect is not considered to be intrinsic, but has to be interpreted as an artifact of the gridded data. With respect to the interval of negative angles from -180° to 0° , an increased amount of edges in the interval of positive angles is caused by the processing order during vectorization. Both intervals basically contain identical information, as an angle α is equivalent to $\alpha + 180^\circ$ here. Besides the artifacts caused by the pixel grid, a small modulation at multiples of 30° plus a small positive offset is found in the data, which indicates only a weak tendency of the cracks to propagate along high-symmetric directions of the sample.

An impression of the relative orientation of the network elements is seen in the panels of figure 15.4. The histogram in the upper panel shows the distribution of angles found from the data between adjacent segments in all edges of the network. An angle of zero degrees between two segments means that they are parallel, i.e., the edge is not bent at all between them. As the vectorization algorithm requires a minimum bend in order to approximate a trajectory of pixels by two segments instead of one (see chapter 14.4), a small, systematic underrepresentation at small bend angles in the experimental

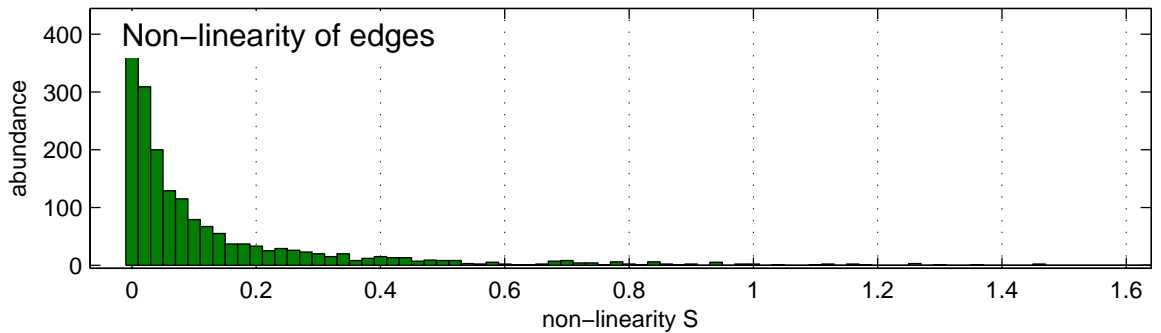


Figure 15.5.: Vectorization of the nanostructure network in figure 15.2 (continued). Overall linearity of edges consisting of more than one linear segment. For the definition of the linearity measure S , see text.

distribution is likely. A small amount of angles near 180° , i.e. nearly anti-parallel segments originate from occasional artifacts produced by the vectorization procedure and are ignored. The broad distribution of bend angles between 10° and 50° show that rather smooth directional changes along the cracks dominate.

In the lower panel of figure 15.4, the angles between the edges are analyzed at the nodes of the network. The results confirm the impression that acute angles are very unlikely to occur at crack bifurcations. Most of the nodes have three edges attached to it, so the mean angle near 120° which is found here basically indicates uniform segmentation of the full circle. Again, no clear preference of certain angles is found.

Common edges range nearly linear from one node of the network to another. Low deviation from the direct connection from node to node is found. In order to quantify this statement, a numerical measure for the non-linearity of a edge is required. Let P and Q be the end points of a curvy edge. The total length of the vectorized edge is given by the cumulative length L of its linear segments. Then, the normalized deviation from the shortest connection between P and Q is $S = (L - |\overline{PQ}|) / |\overline{PQ}|$. As can easily be seen, S becomes zero for a straight connection and has no upper limit if arbitrary complexity of edges is presumed. This measure has been computed for every edge in the network and is shown in figure 15.5. A considerable part of the edges consisting of more than one segment is found to have very low non-linearity parameters. This indicates that the total curvature of edges is usually small.

Having quantified some geometrical features of the crack network which are considered to be crucial, some statements on the creation mechanism and mechanical properties of the sample surface can be derived. These are discussed in the following.

16. Simple theoretical model of crack creation

In addition to spectroscopic properties of the network structures observed on WSe_2 : Rb presented in part II of this work, some statistical properties of the morphology were determined from the large-area overview images shown in chapter 15. The results presented in chapter 12 give some evidence that the creation of network structures is not necessarily accompanied, though followed, by the accumulation of a certain atomic species. Earlier work on this subject [11] showed that the observed nanostructures are made up by trenches, and the formation of tension cracks across the top crystal layer was proposed as a creation mechanism. Here, the adsorbed Rb is assumed to induce a slight reduction of the equilibrium lattice constant of at least the top crystal layer and therefore create lateral tension.

In this chapter, a simple mechanical model of tension-induced crack creation is developed. The analysis of the network structure in chapter 15 suggested that the crystal structure of the material can be neglected at the relevant length scale, so the model is based on continuum mechanics. An extensive discussion of further assumptions made here is given. From simplified expressions of the involved potentials, equations for the stress and strain are derived for the one-dimensional case. A heuristic generalization into two dimensions can be made as shown in section 16.6. The results of a numerical simulation based on this model will be compared to the statistical data derived from the large-scale experimental data at the end of this chapter.

16.1. Introduction

Modifying the lattice constant of a TMDC's topmost layer means modifying its equilibrium next-neighbor distance, while the in-plane potentials of the underlying layers are assumed to be unaffected by alkali adsorption. The result is a competition between the two potentials determining mechanical stress in the surface layer. These are the in-plane potential with its reduced equilibrium lattice constant and an additional potential modeling the interaction with the misfit underlying layers (called 'substrate' in the following). The general layout is depicted in figure 16.1. Note that the circles are explicitly meant to model finite, continuous elements of the crystal, not atoms!

TMDC have a strong covalent intra-layer bonding and a rather small coupling by van der Waals-forces across the crystal planes, giving the inter-layer potential a relatively

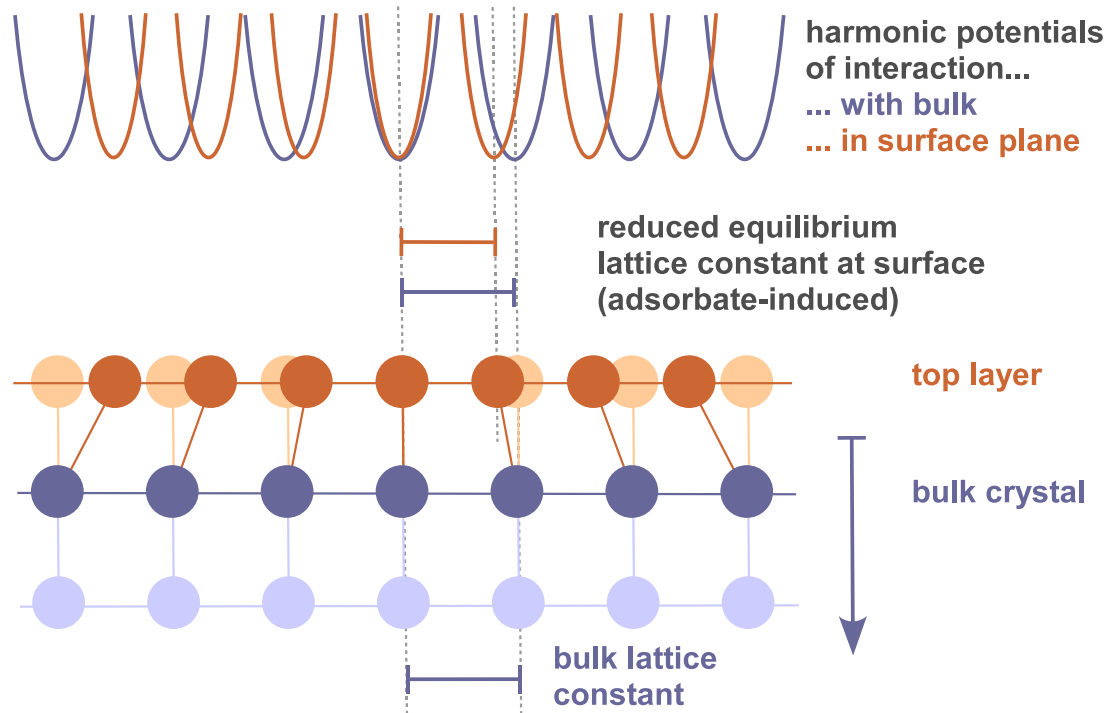


Figure 16.1.: Competing harmonic potentials introduced by adsorption of Rb on WSe_2 . The elements depicted by circles here are not meant to represent atoms, but small elements of a continuous material. Reductions of the equilibrium distances between the surface elements are a consequence of the reduced lattice constant of the crystal.

small contribution to the total elastic energy. For simplicity, the calculations will be done in only one dimension, neglecting cross-dimensional stress-strain effects, i.e., Poisson's ratio is assumed to equal zero in the top layer. An average of some ten to some hundred nanometers has been reported for the mesh size of nanowire networks and thus for the size of the resulting fragments of the top layer that are surrounded by wires. Hence, assuming a homogeneous material and hereby neglecting the atomic structure is justified here. Even small strain will cause the crystal layer to break, so there is no need to model the realistic elastic potentials given by the crystal lattice geometry and the chemical bond. Instead, harmonic potentials are used here, which can be thought of approximation to the realistic potentials around the equilibrium position.

First, the one-dimensional analytical model will be derived. Some implications of the result will be discussed, giving evidence for the plausibility of the assumptions made during development of the model. A heuristic generalization in two-dimensions is introduced afterwards. Finally, results of a simulation implementing the model will be compared to the experimental data.

16.2. Definitions

The aim is to model the distortion of a perfectly elastic one-dimensional rod with free ends and with arbitrary, but constant cross-section under substrate-induced stress. Points on the rod are addressed by a unitless parameter $\tau \in [-1; 1]$ running across the length of the rod, from the 'left' end at $\tau = -1$ to the right one at $\tau = 1$. The function $\ell(\tau)$ gives the position of the rod element τ . Therefore,

$$L(\tau) := \frac{\partial \ell}{\partial \tau}(\tau) - \dot{\ell}_0 \quad (16.1)$$

with the 'equilibrium' length $\dot{\ell}_0$ (defined below) is the local, differential strain. Note that the total length of the rod equals $\ell(1) - \ell(-1)$, i.e., the unstrained rod has a length of $2 \cdot \dot{\ell}_0$!

The interaction of the top crystal layer with the substrate is given by means of a harmonic potential. In equilibrium, a certain atom is stuck to the next local minimum of a potential that must follow the crystal periodicity on a larger scale, but displacements of individual atoms are assumed to be small all over the rod, compared to the lattice constant. As a continuous medium is assumed here, each length element of the rod is exposed to the potential

$$\Phi_s(\ell) := \alpha_s (\ell(\tau) - \ell_0^s \cdot \tau)^2 \quad (16.2)$$

which can be seen as a harmonic approximation at the minimum of the true potential. The constants introduced here are:

- α_s : Elastic constant, $[\alpha_s] = \frac{N}{m}$
- ℓ_0^s : equilibrium unit length of the rod when in-plane potential would be dominated by the substrate potential, $[\ell_0^s] = m$

The in-plane potential includes the energy that is required to stretch or compress the rod. Hence, it is a function of the strain (eq. 16.1):

$$\Phi_0(\dot{\ell}) := \alpha (\dot{\ell} - \dot{\ell}_0)^2 \quad (16.3)$$

- with α : in-plane elastic constant, $[\alpha] = \frac{N}{m}$
- $\dot{\ell}_0$: equilibrium unit length when in-plane potential dominates, $[\dot{\ell}_0] = m$

The reduced lattice constant of the top layer implicates that $\dot{\ell}_0 < \ell_0^s$. This choice constitutes the competition between both potentials, as the minima of potential energy are not commensurate then.

Using the symbols defined above, the total potential energy of the system can be written down:

$$W = \int_{\tau=-1}^1 \Phi_s(\ell) + \Phi_0(\dot{\ell}) d\tau \quad (16.4)$$

Claiming equilibrium implicates $\ell(\tau)$ to be an extremal solution of this equation, so that the potential energy is minimized globally.

16.3. General solutions of the system

Equation 16.4 gives an expression for the total energy of the system as a function of the unknown 'length function' ℓ and its first derivative. Rewriting the problem as

$$Min! \int_{\tau=-1}^1 \Phi(\ell(\tau), \dot{\ell}(\tau), \tau) d\tau, \quad (16.5)$$

it can easily be seen that it belongs to a well-known class of problems in variational calculus, which can be solved using the Euler-Lagrange equation [115]:

$$\frac{\partial}{\partial \tau} \left(\frac{\partial \Phi}{\partial \dot{\ell}} \right) = \frac{\partial \Phi}{\partial \ell} \quad (16.6)$$

Solutions of this differential equation are known to provide extremal solutions of the minimization problem in equation 16.4. First, a parameterized general solution will be derived. From this family of curves, the actual solution of the problem will be determined by boundary conditions in the following.

Inserting equations 16.2 and 16.3 for the potential $\Phi = \Phi_s + \Phi_0$ into equation 16.6 gives the inhomogeneous differential equation

$$\begin{aligned} \frac{\alpha}{\alpha_s} \ddot{\ell} - \ell &= -\ell_0^s \tau, \\ \text{and } \frac{\alpha}{\alpha_s} \ddot{\ell} - \ell &= 0 \end{aligned}$$

for the homogeneous equation. It can be solved by using the the ansatz

$$\ell_{hom} = c_1 e^{\lambda \tau} + c_2 e^{-\lambda \tau} \quad (16.7)$$

$$\text{with } \lambda = \sqrt{\frac{\alpha_s}{\alpha}} \quad (16.8)$$

The complete solution of the inhomogeneous equation is hence given by

$$\ell(\tau) = c_1 e^{\lambda \tau} + c_2 e^{-\lambda \tau} + \ell_0^s \tau \quad (16.9)$$

The parameters c_1 and c_2 can be determined from physical boundary conditions now. Due to the symmetry of the involved potentials, symmetry for the solution $\ell(\tau)$ and $\ell(0) = 0$ in particular can be claimed:

$$\begin{aligned}\ell(0) = 0 &\Rightarrow c_1 = -c_2 =: \frac{c}{2} \\ \Rightarrow \ell(\tau) &= c \cdot \sinh(\lambda\tau) + \ell_0^s \tau\end{aligned}\quad (16.10)$$

Until now, the constant c is not determined according to the fact that the solution $\ell(\tau)$ still contains all possible strains of the rod. The 'ground state' of the rod, i.e., the strain curve ℓ_0 at minimum total energy, must be found from the general solution. Thus, c can be determined by evaluating the following expression:

$$\frac{\partial}{\partial c} \int_{\tau=-1}^{+1} \Phi(\ell(\tau)) d\tau \stackrel{!}{=} 0. \quad (16.11)$$

Inserting eq. 16.10 and using

$$\begin{aligned}\alpha\lambda^2 &= \alpha_s, \\ \dot{\ell}(\tau) &= c\lambda \cdot \cosh(\lambda\tau) + \dot{\ell}_0^s, \\ \cosh 2\lambda\tau &= \sinh^2 \lambda\tau + \cosh^2 \lambda\tau\end{aligned}$$

gives an explicit expression for c via the following intermediate steps:

$$\begin{aligned}\Rightarrow \int_{\tau=-1}^{+1} c\lambda \cdot \cosh 2\lambda\tau + (\dot{\ell}_0^s - \dot{\ell}_0) \cdot \cosh \lambda\tau d\tau &= 0 \\ \frac{c}{2} \cdot \sinh(2\lambda\tau) + \frac{(\dot{\ell}_0^s - \dot{\ell}_0)}{\lambda} \cdot \sinh(\lambda\tau) \Big|_{-1}^{+1} &= 0 \\ \Rightarrow c = 2 \cdot \frac{(\dot{\ell}_0) - \dot{\ell}_0^s}{\lambda} \cdot \frac{\sinh \lambda}{\sinh 2\lambda}\end{aligned}\quad (16.12)$$

The order of differentiation and integration has been swapped here. Using this result, an explicit formulation of the function $\ell(\tau)$ can be given for the actual case.

16.4. Results

By inserting eq. 16.12 into eq. 16.10, the 'length function' $\ell_0(\tau)$ for the minimum energy can be rewritten as

$$\ell_0(\tau) = \left(\dot{\ell}_0 - \dot{\ell}_0^s\right) \cdot \frac{\cosh \lambda(\tau + 1) - \cosh \lambda(\tau - 1)}{\lambda \sinh 2\lambda} + \dot{\ell}_0^s \tau \quad (16.13)$$

using

$$\sinh(a) \cdot \sinh(b) = \frac{1}{2} \cdot (\cosh(a + b) - \cosh(a - b))$$

Equation 16.13 gives the position at minimum energy of the rod element τ . The aim is to derive a formulation of the local stress from the potentials and the length function $\ell_0(\tau)$ with minimum total energy. This will help to predict where the rod is likely to collapse. The total energy of the rod is given by

$$W(\ell) = \int_{-1}^{+1} \Phi_s(\ell(\tau)) + \Phi_0(\dot{\ell}(\tau)) d\tau \quad (16.14)$$

To compute the stress at $\tau_0 \in [-1, 1]$, a small displacement $\Delta\ell$ is defined, by which part of the rod with $\tau \in [\tau_0, 1]$ is shifted towards the rest of the system. The energy of this configuration can be computed with

$$\begin{aligned} W(\ell, \Delta\ell) &= \int_{-1}^{\tau_0} \Phi_s(\ell(\tau)) + \Phi_0(\dot{\ell}(\tau)) \\ &\quad + \int_{\tau_0}^{+1} \Phi_s(\ell(\tau) + \Delta\ell) + \Phi_0(\dot{\ell}(\tau)) d\tau \end{aligned} \quad (16.15)$$

Note that the in-plane contribution to the total energy is not affected according to the fact that the first derivative of ℓ is not modified. The stress $\sigma(\tau_0)$ at a certain rod element τ_0 can be expressed as differential energy gain ΔW per unit displacement $\Delta\ell$ of the rod segment:

$$\begin{aligned} \sigma(\tau_0) &:= \lim_{\Delta\ell \rightarrow 0} \frac{W(\ell, \Delta\ell) - W(\ell, 0)}{\Delta\ell} \\ &= \frac{\partial W}{\partial \Delta\ell} \end{aligned}$$

Inserting the expression in eqn. 16.13 for the minimum energy and eqns. 16.2, 16.3 into this, the stress is given by:

$$\begin{aligned} \sigma(\tau_0) &= \frac{\partial}{\partial \Delta\ell} \int_{\tau_0}^{+1} \Phi_s(\ell + \Delta\ell) - \Phi_s(\ell) d\tau \\ &= \dots \\ &= \frac{2c\alpha_s}{\lambda} \cdot (\cosh \lambda - \cosh \lambda\tau_0) \\ &= \underbrace{4 \cdot \alpha \cdot (\ell_0^s - \dot{\ell}_0)}_{[.] = N!} \cdot \frac{\sinh \lambda}{\sinh 2\lambda} \cdot (\cosh \lambda - \cosh \lambda\tau_0) \end{aligned} \quad (16.16)$$

The distribution of mechanical tension along the rod will be used in section 16.6 to estimate probable locations of cracks. As the derivations made here are based on strong simplifications, some basic features of the solution will be checked first in order to provide some evidence for the plausibility of the model.

16.5. Limiting cases

In this section, two important conditions the function $\ell_0(\tau)$ has to meet will be checked. Keeping in mind that equation 16.13 is the solution of the rod length function for two competing harmonic potentials with different elastic constants and different equilibrium distances. Here, two limiting cases are discussed for which the solution can easily be checked for plausibility. When one of the two potentials is absent, i.e., its elastic constant is reduced towards zero, ℓ_0 must become linear with the elevation equal to equilibrium length of the other potential. The elastic constants α and α_s contribute to ℓ_0 implicitly

$$\begin{aligned} (I) \quad \alpha \rightarrow 0 & : \lim_{\lambda \rightarrow \infty} \ell_0(\tau) \stackrel{!}{=} \ell_0^s \cdot \tau \\ (II) \quad \alpha_s \rightarrow 0 & : \lim_{\lambda \rightarrow 0, \lambda > 0} \ell_0(\tau) \stackrel{!}{=} \dot{\ell}_0 \cdot \tau \end{aligned}$$

Case (I) requires the λ -dependent part of ℓ_0 tending towards zero. With $|\tau| \leq 1$ in general and $\tau \geq 0$ in particular, (I) can be estimated as:

$$\begin{aligned} 0 & \leq \lim_{\lambda \rightarrow \infty} \frac{\sinh \lambda \cdot \sinh \lambda \tau}{\lambda \sinh 2\lambda} \\ & \leq \lim_{\lambda \rightarrow \infty} \frac{\sinh^2 \lambda}{\lambda \sinh 2\lambda} \\ & = \lim_{\lambda \rightarrow \infty} \frac{1}{2} \cdot \frac{\cosh 2\lambda - 1}{\lambda \sinh 2\lambda} \\ & \leq \lim_{\lambda \rightarrow \infty} \frac{1}{2} \cdot \frac{\cosh 2\lambda}{\lambda \sinh 2\lambda} \\ & = \lim_{\lambda \rightarrow \infty} \frac{1}{2} \cdot (\lambda \underbrace{\tanh 2\lambda}_{<1 \forall \lambda, >0 \text{ for } \lambda > 0})^{-1} \\ & = 0, \text{ qed.} \end{aligned}$$

An analogous result can be derived for $\tau \leq 0$. Case (II) requires the λ -dependent part to tend towards τ :

$$(II) \rightarrow \lim_{\lambda \rightarrow 0, \lambda > 0} \frac{\sinh \lambda \cdot \sinh \lambda \tau}{\lambda \sinh 2\lambda} \stackrel{!}{=} \tau \quad (16.17)$$

which can be shown using L'Hôspital's rule:

$$\begin{aligned} \lim_{\lambda} \lambda \frac{f(\lambda)}{g(\lambda)} & = \lim_{\lambda} \lambda \frac{\frac{\partial f}{\partial \lambda}(\lambda)}{\frac{\partial g}{\partial \lambda}(\lambda)} \\ & = \lim_{\lambda} \lambda \frac{\frac{\partial^2 f}{\partial \lambda^2}(\lambda)}{\frac{\partial^2 g}{\partial \lambda^2}(\lambda)}. \end{aligned} \quad (16.18)$$

Applying the rule once still yields the case $\frac{0}{0}$, but evaluating the second derivatives of the nominator and denominator gives the correct result.

16.6. Match with experimental data

The stress distribution along a one-dimensional rod derived in the previous sections will be used here to simulate the length distribution of fragments obtained from a strained rod. Therefore, the maximum stress σ_0 a rod element can bear before breaking has to be introduced into the system as a free parameter. Given a rod with length L , and the parameter λ (see eqn. 16.8) of the involved potentials, the mechanical stress along the rod is given by equation 16.16. In order to simulate fragment creation in one dimension, the solution is assumed to hold for a rod of arbitrary length, i.e., for arbitrarily high stress, so the stress function can be computed for the complete rod. At sufficient length, this results in a finite interval at the center where the maximum stress introduced above is exceeded. Consequently, the rod is assumed to collapse somewhere inside this interval.

Given the stress function in eqn. 16.16, the interval is defined by all values of τ_0 with $\sigma(\tau_0) > \sigma_0$, so $\sigma(\tau_{0,max}) = \sigma_0$ holds for the maximum value $\tau_{0,max}$. In order to derive an analytical expression for $\tau_{0,max}$, the hyperbolic sine and cosine are replaced by a polynomial expansion up to second order terms. This results

$$\tau_{0,max} = \sqrt{1 - \frac{\sigma_0}{2\alpha_s \cdot (\ell_0^s - \dot{\ell}_0)}} \quad (16.19)$$

for the maximum position of a crack for a rod with the length $2 \cdot \ell_0^s$. The absolute length of the interval in which a crack is likely to occur is given by $2 \cdot L$, where

$$L = \ell_0^s \cdot \tau_{0,max} = \sqrt{(\ell_0^s)^2 - \xi \cdot \ell_0^s} \quad (16.20)$$

$$\text{with } \xi = \frac{\sigma_0}{2\alpha_s \cdot \left(1 - \frac{\dot{\ell}_0}{\ell_0^s}\right)} > 0.$$

The abbreviation ξ has the unit of a length (used below: pixels) and includes all free parameters of the system. It is a constant of the modeled material, because the intrinsic and the relaxed length of the rod, ℓ_0^s and $\dot{\ell}_0$, are assumed to have a constant ratio. As a reduced lattice constant of the top crystal layer was introduced in section 16.2, $\dot{\ell}_0/\ell_0^s < 1$ and thus $\xi > 0$ for arbitrary, meaningful values of the remaining constants. Equations 16.19 and 16.20 give real results in cases when the maximum stress σ_0 is exceeded. Otherwise, no tension-induced crack will appear.

In a numerical simulation, a rod with a starting length $l_0^s \gg \xi$ is virtually exposed to tension. A break is introduced at a random, uniformly distributed position inside the interval $[-L, L]$. Then, the stress inside the two fragments is computed. This procedure is iterated until the maximum stress in any fragment is found to have relaxed below σ_0 . Hereby, a specific length distribution is found, as can be seen in the upper left panel of figure 16.2.

The maximum stable fragment size is given by $2 \cdot \xi$, as the radicand in the stated equations becomes negative for $\ell_0^s < \xi$. In larger pieces, the tension near the center would exceed σ_0 , so another iteration would be performed. The minimum length of a fragment created in a step with given rod length can be estimated by

$$L_{min} = \ell_0^s - \ell_0^s \cdot \tau_{0,max} = \ell_0^s \cdot \left(1 - \sqrt{1 - \frac{\xi}{\ell_0^s}} \right). \quad (16.21)$$

For $\ell_0^s > \xi$, the following approximation holds:

$$\frac{\xi}{2} \leq L_{min} \leq \ell_0^s \left(1 - \frac{1}{2} \left(1 - \frac{\xi}{\ell_0^s} + 1 \right) \right) = \xi$$

and (without proof) $\lim_{\ell_0^s \rightarrow \infty} L_{min} = \frac{\xi}{2}$.

In order to obtain a sufficiently high number of fragments, $\ell_0^s \gg \xi$ must be chosen for the starting parameter. Though $\lim_{(\ell_0^s \rightarrow \infty)} \tau_{0,max} = 1$, the minimum fragment size is confined to the interval stated above and no arbitrarily small pieces can be created. Hence, it can be assumed that the length distribution of the fragments is not affected by the choice of the starting length and ξ is the only free parameter in the system. The simulated length distribution shown in figure 16.2 was derived using $\xi = 0.5 \cdot \sqrt{330 \text{ pix}^2} \approx 9.08 \text{ pix}$, a value that is motivated in detail below. The starting length of the rod amounted to $1 \cdot 10^7 \text{ pix}$, and $\approx 9 \cdot 10^5$ fragments resulted from the simulation. All physical parameters introduced above are contained exclusively in ξ . It can be tuned to arbitrary values $0 < \xi < \infty$ by any of the included symbols, provided all of them are chosen to be positive, which is a preliminary arising from physical considerations. As a consequence, it is not possible to derive values of certain model parameters from ξ without further assumptions.

In order to derive a distribution of the area of two-dimensional cracks, further assumptions have to be introduced. As already stated before (section 16.1), the Poisson number of the material is assumed to be zero here, such that no transversal contraction of the material under stress appears. This allows to handle the stress in each dimension independently and the previously determined fragment length distribution is assumed to hold for each direction individually. Therefore, the fragment area distribution can be derived by creating products of randomly chosen members of each distribution. Here, the actual fragment size series was multiplied with a random permutation of itself member by member. The histogrammed fragment area can be seen in the upper right of figure 16.2.

The parameters of the simulation were chosen to give a good match with the experimental fragment area distribution in figure 15.1.

Two attempts to reproducing the experimental data by the simulation are shown in the lower panel of figure 16.2. For the given data, the required value of ξ can be

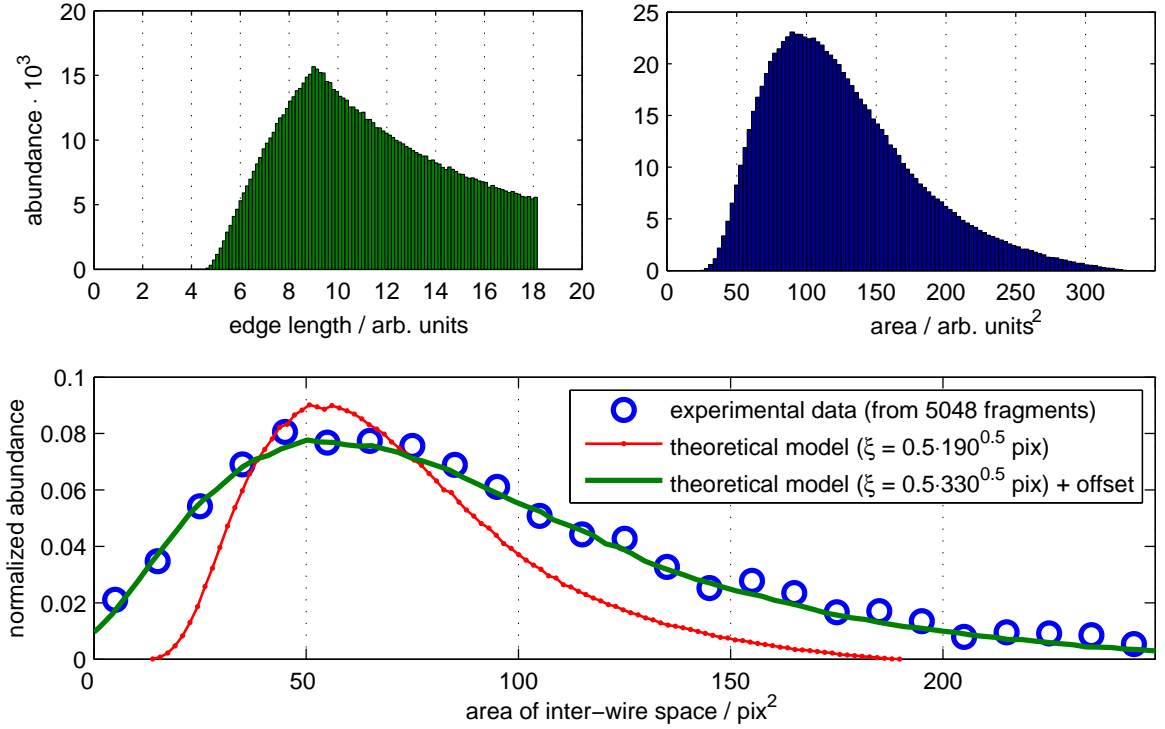


Figure 16.2.: **Upper Left:** Distribution of one-dimensional fragments as derived from the simulation for $\xi = 0.5 \cdot \sqrt{330 \text{ pix}^2}$. **Upper Right:** Simulated two-dimensional fragment distribution derived from the one-dimensional results of the model (see text). **Bottom:** Distribution of the fragment area, derived from the data shown in figure 11.4. Relative good agreement of the observed data and the theoretical model is found here.

estimated by the maximum observed size of the fragments with considerable abundance, $A_{max} = 190 \text{ pix}^2$, by using $\xi = 0.5 \cdot \sqrt{A_{max}}$. The maximum of the simulated distribution is found to be in good agreement with the experiment, but a large overall deviation results. Especially at the tail, a systematic deviation from the simulation result is likely. A considerable bias of the experimental distribution in this interval probably originates from an peripheral region of the survey image with low sharpness, where extraordinary many large fragments were detected. This is considered to be an artifact of the skeletonization algorithm (compare section 15), caused by the low data quality found there.

Special difficulties arise from the presence of very small fragments, which cannot be reproduced in principle by the model at its current stage. The suspected origin of the small features is found in the data processing chain: The crack structures are identified by their contrast, i.e., by their edges. After filtering, the borders of very broad structures might appear as two separate features with a small enclosed area. These

would misleadingly be identified as fragments, so the relatively high abundance of very small features in the experimental data results. A similar undesired effect is observed with the larger structures of the demonstration data found in figure 14.2.

The observed fragment distribution is reproduced well in the complete range by choosing $\xi = 0.5 \cdot \sqrt{330 \text{ pix}^2}$. The associated result shown in figure 16.2 has an offset of -38 pix^2 . Assuming that the correct distribution was determined from the raw data, the observed width can only be simulated by choosing a large value of ξ , which automatically leads to a larger value of the maximum position. The data can be matched only when the stated offset is introduced, indicating that the fragment sizes are overestimated by the theoretical model in general, or that the data processing routines provide underestimated sizes.

Nevertheless, the results derived from the vectorization approach presented in chapter 15 motivate a closer analysis of the nanostructure data in the context of a more sophisticated numerical model. Up to now, only part of the experimental data can be reproduced by the simulation, as only a strongly heuristic approach was made to obtain two-dimensional fragments. The fragment sizes showed up to be comparable to experimental data, so this aspect confirms the interpretation that the observed structures are a direct consequence of mechanical stress introduced to the top region of the WSe_2 crystal during *Rb* deposition. A detailed interpretation of the derived results is hindered by the remaining discrepancy between experiment and theory. An extensive review of the applied techniques and the theoretical model is indicated in order to eliminate the remaining contradictions. The model at its current state should not be taken too serious, as it includes a variety of rough assumptions. The first agreement with experimental data can only be a stepstone towards a realistic stochastic model of nanocrack creation.

17. Discussion

Large amounts of information about the nanostructure network became available to quantitative evaluation by gathering information from a set of raw data images. High reliability of the techniques developed here was demonstrated for the actual data. It was shown that data from large connected regions of the sample surface can be combined to consistent survey images. The method allows for a large-scale study of the observed structure networks, avoiding the limitations of the microscope's field of view. No considerable mismatch of the observed structures between two raw data images in the complete survey was found, so cracks could easily be traced across borders. As the structures showed high intrinsic contrast, automated evaluation of the included features became possible after enhancing the contrast by application of a dedicated filter. The high quality of the resulting data allowed for conversion of the bitmap into a vectorized representation, so geometrical features of the network could be evaluated statistically. The algorithms developed for this purpose showed great performance and low error rate.

Despite the overall suitability of the methods presented before, some attention has to be paid to limitations of these techniques. The network structure revealed in the survey images is expected to represent only part of all self-assembled structures created at the crystal surface. Earlier work showed that much smaller cracks are created which cannot be resolved by the PEEM. Furthermore, image filtering is a crucial measure for semi-automated processing, but shows up to be rather size-selective, so structures with a less pronounced brightness gradient might be suppressed by the filter. For the current studies, the filter kernel had to be tuned individually to give the desired result. In this case, a closer examination of the unfiltered data did not show additional features that failed to pass the filter. From the data presented here, no statement on the width of the observed structures can be given, as no sharp boundaries are found, and the borders were defined as an arbitrary signal threshold of the filtered data. Furthermore, the filter is known to bias the detected width of small structures considerably.

Large-scale survey scans have been acquired from two specimen. The conditions during Rb deposition on the cleaved sample surface were intended to be identical, but certain deviations between the two cases are expected. On both samples, pronounced linear nanostructures had grown. A difference between the two cases is found in topological properties of the created networks. While a basically closed structure is found in the first survey shown in figure 11.4, an increased fraction of open ends of the cracks is found on the second (fig. 15.2). Completely separated fragments are found only in the first case, so an analysis of the fragment size can only be carried out using that data. It is suspected that the second case shows the crystal surface at a stage of crack propagation

that has not been saturated yet, presumably due to a smaller amount of deposited Rb.

As the sample needs to be transferred to the preparation chamber of the experimental setup for Rb adsorption, the evolution of crack networks could not be studied in situ, so a proof that the survey in figure 15.2 shows an intermediate state of structure growth cannot be given in the scope of this work. The constitution of *CVT*-grown WSe_2 crystals is not reproduced exactly in every run. Hence, a certain variation of the substrate character must be taken into account. A potential influence of the substrate purity on the mechanical properties of the bulk crystal have still to be explored.

The statistical analysis of geometrical features of the network was carried out with the intention to reveal potential regularities that can be attributed to the crystalline structure of the substrate. A basically uniform distribution was found for the directional alignment of the cracks. Only a small concentration was found with differences at multiples of 30° with questionable significance. From the lateral crystal symmetry, a pronounced concentration of structures is expected with relative angles of 60° , provided that cracks have an increased likeliness of propagating along high-symmetric directions of the crystal. A certain amount of error is introduced to the determination of the absolute direction of a crack by the discrete grid of pixels. Most of the linear segments in the network have a length of $\geq 10 \text{ pix}$. As the circumference of a circle of this radius is $\geq 60 \text{ pix}$, angular steps of $\leq 6^\circ$ are resolved in the grid by guarantee. As a matter of fact, it can be concluded that the network does not include the expected symmetry.

This conclusion is confirmed by the observed distribution of bend angles between adjacent segments of an edge. The result shown in figure 15.4 does not include preferred angles. The major part of angles is found well below 40° , so the bend is rather smooth and distributed uniformly along the edges instead of having straight sections with discrete bucklings. In general, even short edges usually have considerable bend, as can be seen from the distribution found for the non-linearity S (see chapter 15.5). The absence of long, straight sections gives more evidence that the crystalline structure of the substrate does not contribute to the formation of the crack network at the observed, rather large length scale. Treating the substrate as a continuous, laterally isotropic material is thus suitable. This finding motivated the simple model of crack creation introduced in chapter 16.

At the nodes of the network, average angles of $\approx 120^\circ$ are found between attached edges. In the common case, three edges per node are found, indicating that the crack creation process occurs in a hierarchical manner such that initially formed large fragments are split up further by minor cracks emerging from kinks of a fragment. The preferred angle found here is considered to be a consequence of the lateral distribution of mechanical stress, because, in a homogeneous, isotropic material, peak stress is found at kinks. This conclusion is in agreement with the finding that edges opposing each other at 180° are very unlikely, as can be seen in figure 15.4. Assuming hierarchical crack creation, new cracks emerging from straight sections of an existing crack would result in contributions near 180° and around 90° .

The results obtained from a simple theoretical model of surface fragmentation pro-

vide some evidence that the observed structures are a direct consequence of adsorbate induced lateral stress. It was shown that its free parameter ξ , can be tuned so that part of the experimental data, i.e., the distribution of fragment size, is matched. Therefore, the distribution of the fragment area in two dimensions was generalized from the basically one-dimensional model. As this approach does not include the actual geometry of the observed fragments, a more sophisticated model would be required to compare theoretical predictions with network-specific features obtained from vectorization. In the context of the comparable data, it can be concluded that lateral tensile stress is the driving force of structure creation. The origin of the stress can only be speculated about. A close relationship to the large, perpendicular electric field at the adsorbate-covered surface (see chapter 3.2) is suggested.

In general, the findings from this part of this work clearly show that, at the observed length scale, crack creation is not biased by the crystal structure of the substrate and the material can thus be treated as a continuum. The methods developed here show the great potential of large survey images for the statistical interpretation of self-organized surface structures. Especially at small field of view, the imaged area in the microscope can be extended virtually by assembling raw data. High consistency was usually found in overlapping raw data images. As effects of inhomogeneous illumination can be also be neglected for the synchrotron spot when using a small field of view, the technique has the potential to be applied to spectroscopic data. With the background of these extensions, future work on large-scale conglomerates of nanostructures using PEEM is motivated. For the current system, studies of the evolution of crack networks could reveal further information on the microscopic processes involved here.

Summary and Outlook

In this work, effects of Rb deposition on the cleaved surface of WSe_2 were studied with a focus on charge carrier dynamics and morphological aspects. Modifications of the cleaved surface of WSe_2 upon controlled deposition of Rb were examined by the application of photoemission spectroscopy (PES) and photoemission electron microscopy (PEEM). The effect of the surface potential created by charge transfer between adsorbate and substrate on the dynamics of charge carriers near the surface was quantified in the context of the surface photovoltage (SPV) effect by experiments and simulations. Spatially resolved measurements revealed the self-organized growth of Rb domains and networks of nanostructures, which were probed by core level photoemission and absorption spectroscopy. The demand for highly-precise, unbiased access to the information contained in PEEM data led to the development of novel data processing methods, whose great efficiency was shown. Basically three scientific studies are reported here, structuring the work into three parts. They can be summarized as follows:

Part I was dedicated to a combined experimental and theoretical study of the SPV effect. This concept was pursued for a characterization of charge carrier dynamics in the $p-WSe_2:Rb$ system, and estimations of crucial parameters, especially of the unoccupied adsorbate state, were obtained. Numerical simulations were carried out using a customized semi-classical model based on earlier work. As it turned out that an inversion layer is created here, a special theoretical treatment was necessary and led to a new formulation of the model as given in this work. It was shown that handling the surface as three separate regions gives a correct description of the system in presence of a large surface potential as prepared during the experiments. The surface potential is predicted by the model as a function of absorbed photon flux, which was validated in a comprehensive experimental study using valence band photoelectron spectroscopy. To this end, an optical system was designed to provide versatile in situ illumination of the sample surface by an auxiliary light source. Special measures were taken in order to guarantee full electrostatic compatibility of the device with the electron spectrometer. In the course of this work, numerous minor upgrades of the experimental setup were realized, supplying enhanced efficiency during operation and a higher degree of automation. All new components were tested extensively prior to the subsequent experiments and were found to perform satisfactorily.

The SPV effect was probed at variable adsorbate density and over a wide range of light intensity. Subsequent simulations of the actual conditions gave a solid validation of the numerical model. Especially the basic assumption of a 'local' effect, i.e., neglecting

lateral charge transport showed up to be appropriate for the chosen setup. By matching the simulated SPV effect with the experimental results, the actual values of several material constants could be estimated within the stated error margins. As predicted by the simulation, a pronounced sensitivity of the magnitude to the surface potential, the 'resonance', was found for a well-defined range of photon flux. The good agreement between experiment and theory allowed for an indirect characterization of the adsorbate state. A rather broad state, essentially located above the conduction band minimum of the substrate, could be identified. The observed SPV effect requires that it plays a major role in the recombination of electron-hole-pairs near the surface.

The overall success of the combined study presented here motivates future experiments: The integrated optical setup provides a small focus, so the SPV effect can be probed with spatial resolution by scanning the surface. An even more promising future project is the integration of the secondary light source into a PEEM setup to acquire spatially resolved data in parallel. Furthermore, an appropriate device to exploring the SPV effect in the time domain has been implemented during this work, which potentially allows for a direct observation of charge carrier recombination processes. Extending the capabilities of PES by measurements of the SPV effect with spatial resolution leads to a combined characterization of the chemical composition and electronic activity of structured semiconductor surfaces. An impact on technical applications is expected hereby.

In part II, PEEM studies of self-organized structures at the Rb-covered surface of WSe_2 are reported. Spatially resolved XPS and absorption spectroscopy was applied to this system with the intention to provide evidence for the physical effects participating in the creation of Rb domains and networks of nanostructures. The measurements and data evaluation required a variety of preparatory measures, which are summarized briefly below. All presented data were acquired at beamline UE49/PGMa at the synchrotron radiation facility BESSY II during several beamtimes. As far as known, more detailed PEEM studies of layered crystals have not been reported in the literature.

Crystal surfaces were prepared using the well-known cleaving technique, which had to be adapted to the local conditions first. The high voltage applied when using PEEM demands a high quality of the cleaved surfaces, which could be achieved with the presented method. As the PEEM method provides spatial resolution, large amounts of data are obtained in parallel. A direct quantitative evaluation of the acquired spectra is hindered by technical limitations of the optical system and mechanical components. In order to exploit the full potential of PEEM data, special attention was directed to the quantification of side effects such as drift of the sample, inhomogeneous incident photon flux, and lateral variable photon energy. The design of algorithms compensating these effects was discussed in detail. High suitability of the strategies was demonstrated by means of experimental data. No further undesired influences were revealed in the processed data, so the information from the full detector image is available for quantitative analysis after the treatment. The related procedures are therefore suggested as mandatory parts of future work.

Compared to common XPS spectroscopy, the availability of a large number of data channels with rather low individual signal level requires an alternative approach to the interpretation. In this work, some basic concepts from the field of data mining were applied to PEEM data successfully. Deriving a representation of the individual spectra with a strongly reduced number of degrees of freedom showed up to be the key measure when handling large sets in the range of 10^4 members. It was demonstrated that an appropriate application can be exploited for the separation of intrinsic features in a spectrum from statistical noise without degrading the spatial resolution in the data. Complications occurring with smoothing techniques could be circumvented here. Based on the reduced representation of spectra, data sets could be classified into groups by means of spectroscopic features. Hereby, an unbiased identification of surface structures resulted. It was shown that the method is extremely sensitive to features that could hardly be identified otherwise. The capabilities of the developed processing techniques were demonstrated using data sets from all discussed topics.

After depositing Rb at the surface, the formation of a large-scale texture was observed, which was subject to a dedicated XPS study using synchrotron radiation. Some conclusions concerning the chemical composition of the texture as well as the chemical environment of the adsorbed Rb were derived: The adsorbate is found to cover the complete surface with a heterogeneous density. The surprising result is that two discrete levels of the Rb concentration are found, so the surface can basically be classified into two types. From a closer analysis of the substrate, especially of the top Se layer that is directly exposed to the adsorbate, implications on the electronic structure were revealed. The observations might be explained by the arrangement of the rubidium atoms in two distinct types of a surface lattice.

Further experiments showed that the adsorption of Rb can be confined to a discrete region on the sample, indicating that it has a low room temperature mobility on WSe_2 . In contrast to other alkali metals or transition metal dichalcogenides, no intercalation was observed for this system. The presence of fixed surface Rb at room temperature is in contradiction to the general expectation that the individual adatom is highly mobile. This finding motivates further experiments with the intention to reveal potential immobilization mechanisms of conglomerates of Rb. An interesting phase-transition behavior is expected for two-dimensional, stable collectives of mobile individuals.

PEEM measurements using the UV source revealed the presence of pronounced networks of linear surface structures. From earlier work, these were expected to represent lateral cracks induced by Rb adsorption. Using X-ray absorption spectroscopy with monochromatic synchrotron radiation, a spectral signature of the suspected accumulation of adsorbates in the cracks was to be detected. Although very low deviation from the average signal was expected for the vicinity of the features, the observed structures could clearly be identified by means of absorption spectra using a dedicated data classification algorithm. A direct identification of Rb from spectroscopic features could not be achieved here, but part of the observed network structure is undoubtedly reproduced hereby.

The microscopic creation process of the observed nanostructures has been discussed extensively in the literature, and a definite answer has not been found yet. Since cracks introduced by lateral tensioning are expected to reveal a typical statistical distribution, a dedicated analysis of morphological network features was carried out and discussed in part III. Typical $WSe_2:Rb$ samples showed an almost complete coverage with nanostructures. Data taken from large connected areas of the surface could be merged to give survey images, where the routines developed for this task proved great suitability. From the bitmap data, a vectorized representation of the structures was derived by using well-known image processing techniques for the skeletonization and subsequent vectorization. Morphological features characterizing the network would be extracted from the results, proving the feasibility of the approach. An analysis of microscopic features was carried out for the complete network. Assuming tension as the reason for structure creation, and interpreting the structures as cracks, leads to the conclusion that the material can be assumed as a continuum at the examined length scale of some micrometers. With this background, a first attempt was made to derive a theoretical model of surface fragmentation. Although based on strong simplifications, statistical features of the experimental data could be reproduced. These first results strongly encourage further development of the model in order to allow for a more detailed comparative study.

In summary, the technical upgrades introduced to the experimental station of the workgroup proved to be suitable in general. In particular, measurements of the SPV effect using a photoelectron spectrometer could be carried out using the enhanced setup. The theoretical model of the SPV effect could be validated and was applied successfully to the experimental data, so the general understanding of the participating processes could be improved significantly. It was shown that, in combination with theory, the capabilities of PES are extended by an option to determine parameters of charge carrier dynamics that would not be accessible otherwise.

The pioneering work made in the field of PEEM data analysis is considered to improve the efficiency of this experimental technique significantly and allow for many highly-ambitioned upcoming projects. The high applicability of the correction and classification methods was demonstrated when characterizing adsorbate-induced structures at different length-scales. A comprehensive analysis of the observed spectromicroscopic features gave a profound insight into physical effects at the atomic level in large areas and at high spatial resolution.

The fact that all observations discussed here are made with the same system motivates prospective work on crucial relations between all effects, based on the findings documented in this work. Since a considerable effect of the surface structures on the local SPV characteristic can be expected, spatially resolved measurements of the SPV effect near the boundaries of structures might contribute to a complete understanding of the nature of the observed processes.

Appendix

A. Optical characterization of the SPECS UVS300 He discharge lamp

The SPECS *UVS300* He discharge lamp is optionally equipped with a focussing capillary. The focus is defined by its ellipsoidal interior surface. A theoretical spot diameter of $50\ \mu\text{m}$ (FWHM) has been specified by SPECS (and was revised to $500\ \mu\text{m}$ later). Its actual focusing capabilities are to be reviewed here. The PHOIBOS setup as used during this work requires a non-standard capillary length to bridge the large exit flange-to-sample distance of $L = 594\ \text{mm}$. Precise knowledge of the focus position inside the experimental chamber as well as the true focus diameter and beam divergence are required in order to establish an optimal alignment of the radiation source, sample holder and electron analyzer geometry.

Here, an approach to find general beam properties is presented. As the *Hamamatsu G1127-02* photodiode [131] used for laser focus scanning also shows weak sensitivity to UV radiation, the scanning setup from chapter 5.6 can be reused. A wiring diagram of the setup is shown in figure A.1. Here, a larger pinhole (diameter: $150\ \mu\text{m}$) is required to obtain a sufficiently high signal level. This should be no substantial drawback for size determination as the beam diameter is still expected to be considerably larger than the pinhole.

After manual optimization of the sample holder-mounted photodiode inside the experimental chamber, using highest photocurrent as indicator, the beam cross section was scanned using the motorized sample manipulator. A two-dimensional photocurrent-over-position map with point-to-point spacing of $\approx 50\ \mu\text{m}$ vertically, and $\approx 70\ \mu\text{m}$ horizontally, was acquired in this way. In order to avoid artifacts created by temporal inertia - especially of the analog Keithley device- the sample position was kept constant for $2\ \text{s}$ before a data point was acquired. Mechanical vibrations are assumed to be decayed after this time. This procedure was repeated for a set of cross sections at variable distance and spacing of $\approx 1.4\ \text{mm}$ to the end of the capillary, centered around the specified focal distance of $10\ \text{mm}$ from its end.

An excerpt of the resulting data is shown in figure A.2. The two-dimensional cross section of the beam can clearly be identified in the center. A slightly increased intensity on top of the image probably is an artifact created by the scanning mode: The data was acquired column-by-column, crossing the beam at each return of the photodiode to the upper position.

Temporal inertia should give a virtually increased signal then, because the high measured signal when retracting the manipulator has not decayed completely upon the start

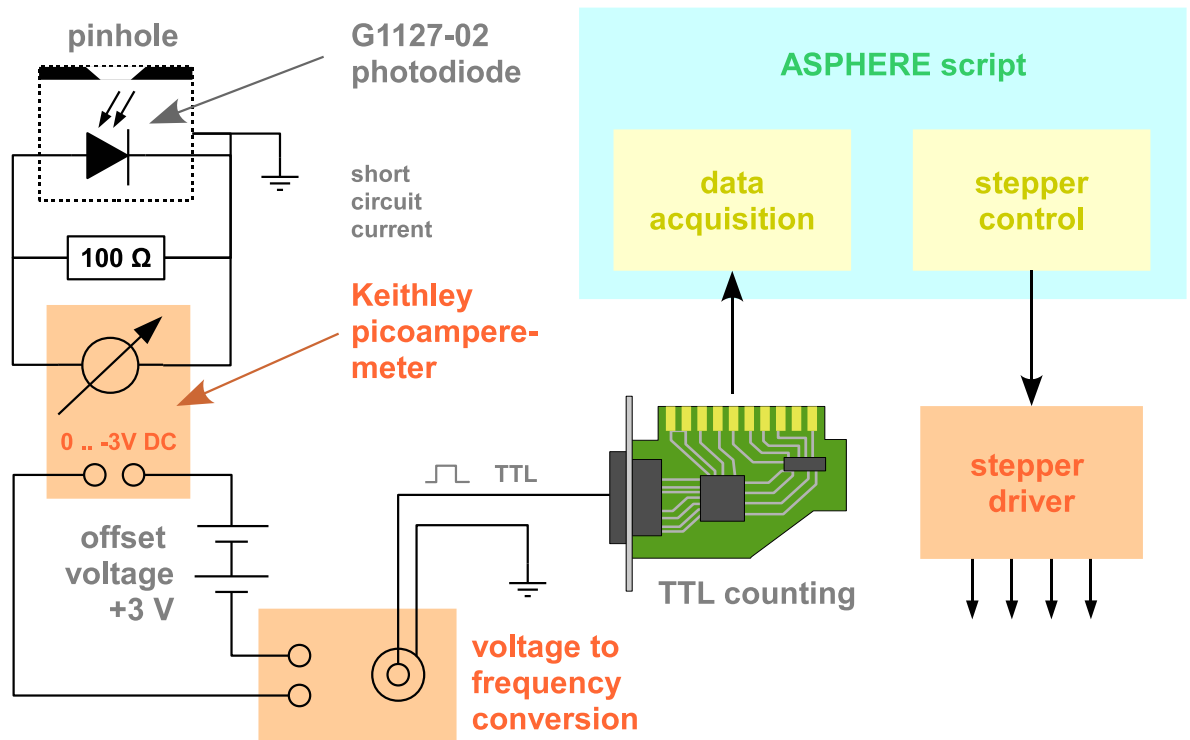


Figure A.1.: Wiring diagram of the setup used for the focus scanning measurements. The voltage acquired over the short-circuit resistor is converted in several steps into a rate of TTL pulses. The digitalized signal is recorded by a PC counting card driven by ASPHERE [53].

of the new column. The findings from the data set can be summarized as follows:

- The best focus that could be found using the scanning technique is much bigger than the (theoretical) value stated by the distributor and can be nominated to 1.5...1.8 *mm* (full width at half maximum, FWHM).
- No information on the beam divergence can be gained from the data. The FWHM value of the cross section shows no pronounced global minimum, even though the wide scanning range should include the nominal focal distance of 10 *mm*.
- The signal obtained from the out-of-focus region is not high enough to give a final statement about the actual focus profile function. As confirmed by SPECS, it appears to be clearly non-Gaussian with a slowly decaying tail such that a relatively small fraction of the total flux is concentrated inside the FWHM interval.

These findings give rise to the idea that under realistic conditions, the capillary might not focus the radiation at all. Therefore, the experimental setup needs to be reviewed critically, assuring integrity and proper alignment of the capillary. Final data should

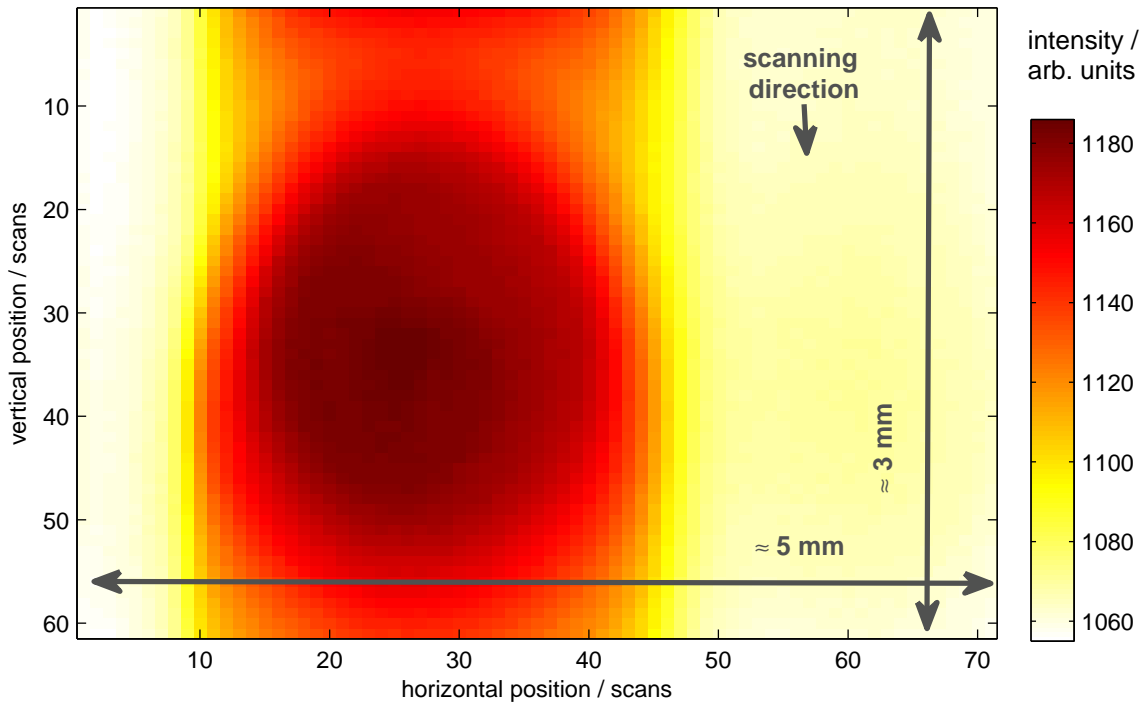


Figure A.2.: Result of scanning the beam profile with the beam probe (see figure 4.8). The data was taken at $\approx 8 \text{ mm}$ distance from the end of the capillary using $He I_\alpha$ radiation ($h\nu = 21.22 \text{ eV}$) in the second diffraction order of the monochromator. The nominal focus diameter of $500 \mu\text{m}$ cannot be achieved using the current setup including the elongated focussing capillary.

be recorded using a Faraday cup instead of the photodiode. The use of state of the art-electronics is highly recommended here, so the Keithley picoamperemeter should be replaced by a newer version. Perhaps a more sophisticated capillary mount could help finding a setup that really provides something sort of a focus. But anyway, it can be doubted that SPECS specifications can ever be reached in a real-world ARPES setup.

B. Some remarks concerning the SPV simulation code

The numerical model of the SPV effect presented in chapter 3 has been implemented in a simulation program in order to provide appropriate simulation results for a comparative study (chapter 6). It is based on previous work by Trares-Wrobel, but was modified to fit the requirements found in this work. Major changes and new features are summarized here. Comprehensive documentation is prepended to the newest version of the code (last change: Sep 15, 2009).

- **Structure**

The complete code was extended from the *C* specification to *C++*. The code was rearranged in several modules. The simulation code was tested for p-type substrates for the first time. Several bugs were identified and fixed in the course.

- **Three-region model**

Initially intended for debugging, much of the code concerning charge carrier dynamics has been ported to MATLAB. In the current version, only space charge configurations are computed using this code, though the full functionality is retained. For an implementation of the three-region model, refer to the MATLAB code.

- **Output file format**

The format of the output file was modified, so tab-delimited ASCII tables are returned now. One line per data point is included in these files, so data import to alternative applications is eased. The order of entries corresponds to that defined in [8], (appendix A). Floating point numbers are exported with seven digit-precision, not five.

- **Precision**

The complete code was updated to operate with double-precision floating point numbers internally. Working with single precision often resulted severe problems due to low precision.

- **Fermi functions**

A new implementation of approximate Fermi functions was created, including data derived by [116], [65], [66]. Clearly improved approximation resulted. Part of these

functions is approximated by spline functions. A new approach ensures continuous differentiability at the border between the spline and the analytical approximation. Furthermore, much higher computation speed could be achieved.

- **Physically correct computation of z^***

The numerical integration of equation 3.20 is required to determine the width of the space charge layer. The approximation in early versions of the simulation code is not accordable with basic mathematics and, hence, physics. An alternative strategy is introduced below.

- **Adaptive step size**

Common series of data points are simulated much faster by adaptive step sizes. Details are discussed at the end of this section.

- **Compiler switches**

Optional behavior of the program was introduced to the code by defining a set of compiler switches. These include the definition of the output file format, selecting the quantities to be computed, as well as switching to early versions of the program for compatibility reasons. A detailed discussion is given by the developer's diary prepending the actual code.

Some of the mentioned points have long-range implications, so they will be discussed in detail now.

In appendix A of [8], the length of the space charge layer z^* is determined by computing the integral of the inverse space charge density function. Precise knowledge of this quantity is crucial for the interpretation of the simulation results, because it is used to estimate the strength of the electric field at the surface using $|E| = (E_{is} - E_{ib})/z^*$ (eqn. 6.17 in [8]) and thus determines the drift part of the total charge carrier transport. Here, E_{is} is the intrinsic equilibrium Fermi level at the surface, and E_{ib} is its analogue in the bulk. Thus, the nominator in the above equation is equal to the band bending V_s . The integral to be solved numerically reads

$$z^* = L_D \cdot \int_{u_b}^{u_s} \frac{1}{\mathcal{F}(u, u_b, \delta u_n, \delta u_p)} du; u_s \leq u_b \quad (\text{B.1})$$

with the reduced quasi-Fermi-levels $\delta u_n, \delta u_p$ and the reduced equilibrium bulk and surface Fermi levels u_b and u_s respectively (see chapter 3 and [8]). \mathcal{F} gives the amount of excess charge that is concentrated in a layer beneath the semiconductor surface in an arbitrary non-equilibrium state defined by the four arguments. For further discussion in terms of the complete simulation framework, see [8]. Computational aspects of equation B.1 are discussed here..

A major problem results from the fact that \mathcal{F} approaches zero for $u_s = u_b$, i.e. the integrand in B.1 has a singularity at one of the integration limits. There are two questions

emerging from this point. First, does the integral exist at all? Second, how can a numerical quadrature algorithm deal with the singularity?

In [8], the first question is not answered by a formal discussion. The physical interpretation only requires that

$$\lim_{V_s \rightarrow 0} \frac{V_s}{z^*} = 0, \quad (\text{B.2})$$

meaning that the electric field at the surface must vanish when there is no band bending and thus no accumulation of space charge. Avoiding an answer to the second question, reference [8] states to perform the integration inside the interval $[u_s, u_b - \epsilon]$ with finite $\epsilon = 0.005 \cdot (u_b - u_s)$. There is no approximation of the error introduced here, and no proof that the error will at least be a constant fraction of the result found this way. In the following, it will be shown that the integrand can be well approximated near the singularity such that the integral exists and can be evaluated analytically, avoiding the singularity at the limit of the integration interval.

First of all, the structure of \mathcal{F} has to be explored to derive an approximate expression. Following [8], eqn. 2.32, \mathcal{F} is given by

$$\begin{aligned} \frac{\mathcal{F}(x, \dots)}{\sqrt{n_i} \cdot \text{sign}(u_b - u_s)} = & \quad (\text{B.3}) \\ & \left\{ N_A \ln \frac{1 + \alpha_1 e^{x+b_1}}{1 + \alpha_1 e^{b_1}} \right. \\ & + N_D \ln \frac{1 + \alpha_2 e^{-x+b_2}}{1 + \alpha_2 e^{b_2}} \\ & + \frac{4}{3\sqrt{\pi}} N_C \left(\mathcal{F}_{\frac{3}{2}}(x + b_3) - \mathcal{F}_{\frac{3}{2}}(b_3) \right) \\ & \left. - \frac{4}{3\sqrt{\pi}} N_V \left(\mathcal{F}_{\frac{3}{2}}(b_4) - \mathcal{F}_{\frac{3}{2}}(-x + b_4) \right) \right\}^{\frac{1}{2}}, \end{aligned} \quad (\text{B.4})$$

using the abbreviations

$$\begin{aligned} x &= u_s - u_b \\ b_1 &= u_b + \delta u_p - \omega_{A,i} \\ b_2 &= \omega_{D,i} - u_b - \delta u_n \\ b_3 &= u_b + \delta u_n - \omega_{C,i} \\ b_4 &= \omega_{V,i} - u_b - \delta u_p \\ \alpha_1 &= 1/g_A \\ \alpha_2 &= g_D \end{aligned} \quad (\text{B.5})$$

for the general case without further assumptions about doping levels and adsorbate concentration (computation method called 'exakt' there). The meaning of the constants

appearing in the equation can be found in [8]. The function $\mathcal{F}_{\frac{3}{2}}(\eta)$ is the Fermi-Dirac integral of order $\frac{3}{2}$. To find an approximate solution of the integral B.1 near $u_s = u_b$ (i.e. $x \approx 0$ in B.3), an analytical expression for this function is derived.

Many approaches, predominantly polynomial expansions, of the Fermi-Dirac-integral are known from the literature (see [65] and references herein), which usually hold for a limited argument range, except for values $\eta \leq -2$, where the function values are well reproduced by exponentials [116] over a wide range. Coefficients are tabulated in [66], for instance. The implementation of the SPV simulation used in [8] computes the function values over the full argument range by tabulated function values with spline interpolation. Inserting the definitions of the symbols used in eqn. B.3, one can easily see that the argument η to the Fermi-Dirac integral becomes much smaller than -2 , so the exponential approximation is sufficient for this purpose. Hence, the function \mathcal{F}_j , defined by

$$\mathcal{F}_j(\eta) := \int_0^\infty \frac{x^j}{1 + \exp(x - \eta)} dx \quad (\text{B.6})$$

can be written as (for $j = 3/2$)

$$\mathcal{F}_{\frac{3}{2}}(\eta) \approx \frac{3}{2} \sum_{n=1}^5 a_{n-1} e^{n\eta} ; \eta \leq -2. \quad (\text{B.7})$$

Using the coefficients a_n from [66], the error to the approximation is as good as $5 \cdot 10^{-6}$. Now, the expression under the square root in eqn. B.3 can be expanded up to linear terms in $x \approx 0$ using

$$\mathcal{F}_{\frac{3}{2}}(x+b) - \mathcal{F}_{\frac{3}{2}}(b) \approx x \cdot \underbrace{\frac{3}{2} \sum_{n=1}^4 a_{n-1} \cdot n \cdot e^{nb}}_{=: \Sigma_b} \quad (\text{B.8})$$

and

$$\ln \frac{1 + \alpha e^{x+b}}{1 + \alpha e^b} \approx x, \quad (\text{B.9})$$

eqn. B.3 can be rewritten as

$$F_{\frac{3}{2}}(x) = \frac{\text{sign}(-x)}{\sqrt{n_i}} \cdot \left\{ N_A + N_D + \frac{2N_C}{\sqrt{\pi}} \Sigma_{b_3} - \frac{2N_V}{\sqrt{\pi}} \Sigma_{b_4} \right\}^{\frac{1}{2}} \cdot \sqrt{x} \quad (\text{B.10})$$

Inserting this result into B.1, the integral can be solved analytically. The expression derived here is explicitly meant as an approximation to the charge function in the vicinity of its singularity ($u_b = u_s$). It gives appreciable precision in this region. When computing the integral in eqn. B.1 over a larger range, a combination of the numerical solution and the approximation derived here is suitable.

The following topic covers crucial issues concerning the applied strategy of computing non-equilibrium configurations. In reference [8], all basic equations modeling charge

accumulation in non-equilibrium are given. All features have been implemented as a numerical simulation program, which was applied successfully to some cases. When handling the inversion layer on $WSe_2 : Rb$, some limitations of the implicit assumptions made during the implementation of his code are revealed. In an early version of the simulation code, i.e. in the state as it had been archived in 1995, the surface potential and the quasi-Fermi levels are computed sequentially.

As the quasi-Fermi levels are parameters to the space charge function, they must be known when computing the band bending in a non-equilibrium configuration by claiming neutrality for the excess charges in the space charge region (eqn. 2.35 in [8]). Here, a specific value of one quasi-Fermi level is claimed, and the second is determined such that the equation is satisfied. Both values are referenced to the bulk Fermi level here, so no surface potential and the changed relative position to the band edges is taken into account. Note that the band bending cannot be determined prior to finding the quasi-Fermi levels!

Large surface potentials, especially at inversion, lead to great modifications of band occupancy and, of course, large changes of $\partial\mathcal{F}/\partial E_{F_{n,p}}$ (see eqn. 2.32, [8]). Therefore, these quasi-Fermi levels are invalid in presence of a surface potential. Basically, both equations stated above must be solved in parallel as a coupled system. The current implementation of the simulation code includes a workaround. In common runs, the program is initialized with a given substrate configuration and the task is to compute a sequence of data points, starting at thermal equilibrium and stepping towards larger perturbations. This is exploited to give 'nearly self-consistent' solutions by computing the quasi-Fermi levels using the band bending found in the previous step. This approach is problematic in general, as it must be guaranteed that the step size does not get too large.

Due to the demand for short computation time, redundant steps must be avoided as good as possible. With this intention, the step sizes are chosen adaptively so that a low density of data points is computed in regions with low dynamics. As the elevation of one of the computation results exceeds a threshold, the step size is reduced, so high-dynamic regions are computed with the required high precision. As a rough estimate of the elevation of the currently computed curve, only the last two data points are used.

The general design of the code requires careful operation and critical inspection of the results.

C. Calibration of the light source for the SPV experiment

The surface photovoltage effect was measured at variable generation rate of electron-hole pairs, which are created when photons with energy exceeding the direct bandgap of the semiconducting sample are absorbed. In the PHOIBOS photoemission spectroscopy setup, laser light from a green laser pointer is used as additional light source, providing an estimate power of 5 *mW* at a wavelength of $\lambda = 532 \text{ nm}$, corresponding to a photon energy of $h\nu \approx 2.32 \text{ eV}$. The partially polarized output is attenuated by a pair of polarization filters with variable rotation angle. This chapter deals with the calibration of the generation rate at the sample surface in dependence of the polarizer angle

The first polarizer was aligned such that it has maximum transmission of the laser light and is held at a constant angle throughout the experiments and the calibration procedure. The second, mounted between laser and the first polarizer, is the one to be rotated for attenuation.

An International Radiation Detectors *SXUV20HS1* photodiode [132] was used to measure the light intensity at the end of the optical bench where the beam would otherwise enter the vacuum chamber. Its short circuit current was measured by a Keithley Instruments Model 6485 picoamperemeter, giving precise and stable readings down to the low *nA* range. For the wavelength used here, the photodiode has a sensitivity of 0.23A/W [132].

Figure C.1 shows the photocurrent as a function of the rotation angle δ . The expected behavior is given by Malus' law $I = I_0 \cdot \cos^2 \delta$ for the transmission of an ideal polarization filter. For a real polarizer, the law must be modified to

$$I = I_0 \cdot (\beta + (1 - \alpha - \beta) \cos^2 \delta) \quad (\text{C.1})$$

with the absorption of the filter at maximum transmission α and the minimum transmission β . The calibration data in figure C.1 fits this law very well which confirms the correctness of the procedure described here. Especially nonlinear response of the photodiode can be excluded. For the fit of equation C.1, the parameters I_0 , α , and β have to be replaced by

$$\begin{aligned} a &= \beta \cdot \sqrt{I_0}, \\ b &= (1 - \alpha - \beta) \cdot \sqrt{I_0} \end{aligned}$$

to obtain a set of independent fit variables. Arbitrary offset angles between the polarization angle of the laser light and the maximum transmission angle of each of the single filters have to be introduced giving the function

$$\begin{aligned} I^{(1),(2)}(\omega) &= I_0^{(1),(2)} \cdot (a + b \cdot \cos^2 \omega), \\ \frac{I}{I_0} &= I^{(1)}(-\omega + \delta) \cdot I^{(2)}(\omega - \theta). \end{aligned} \quad (\text{C.2})$$

Unfortunately, this means that there is no possibility to determine an absolute value for the laser output power I_0 . Nevertheless, the fit results inserted in equation C.2 give robust information on the polarizer transmission. Additional controlled attenuation of the laser intensity can be achieved by inserting a dielectric bending mirror into the beam, transmitting only 0.5% of the light. Calibration data for this was also recorded, but cannot be fit by a simple law, probably caused by a polarization-selective transmission of the mirror. Thus, a spline function is used in this case.

To find an estimate of the total photon flux that is absorbed at the sample surface, the reflection losses on the optical path after the position of the photodiode have to be estimated. Approximately 4% of the intensity is reflected at each of the 4 glass-vacuum/air-surfaces of the vacuum feedthrough and the focusing lens, giving a total transmission to the sample surface of 85%. More intensity (roughly $50 \pm 10\%$) is lost as it is reflected by the sample itself.

In the next step, the spot size of the laser at the sample position has to be approximated. The focus was intentionally misaligned to cover most of the spot of the UV source for photoemission, which has a FWHM diameter of approximately 1.8 mm (app. A). According to the fact that the photoemission spectra include components without SPV shift, the laser spot diameter is supposed to be reasonably smaller than the diameter of the area the photoelectrons originate from.

Considering the approximate Gaussian shape of both intensity distributions with width σ , this should be satisfied by choosing $\sigma(\text{Laser}) \leq 0.5 \cdot \sigma(\text{UV})$. The lateral intensity distribution is not rotational symmetric because of the 60° angle of incidence of the laser beam towards the sample normal. Thus, the lateral intensity profile reads

$$\begin{aligned} I(x, y) &= \frac{1}{2\pi\sigma_x\sigma_y} \cdot \exp\left(-\frac{1}{2}\left(\frac{x^2}{\sigma_x^2} + \frac{y^2}{\sigma_y^2}\right)\right) \\ \text{with } \sigma_y &= \frac{\sigma_x}{\cos 60^\circ}. \\ \Rightarrow I(x, y) &= \frac{1}{4\pi\sigma_x^2} \cdot \exp(\dots), \\ \text{giving } I_{max} &= I(0, 0) = \frac{1}{4\pi\sigma_x^2}. \end{aligned}$$

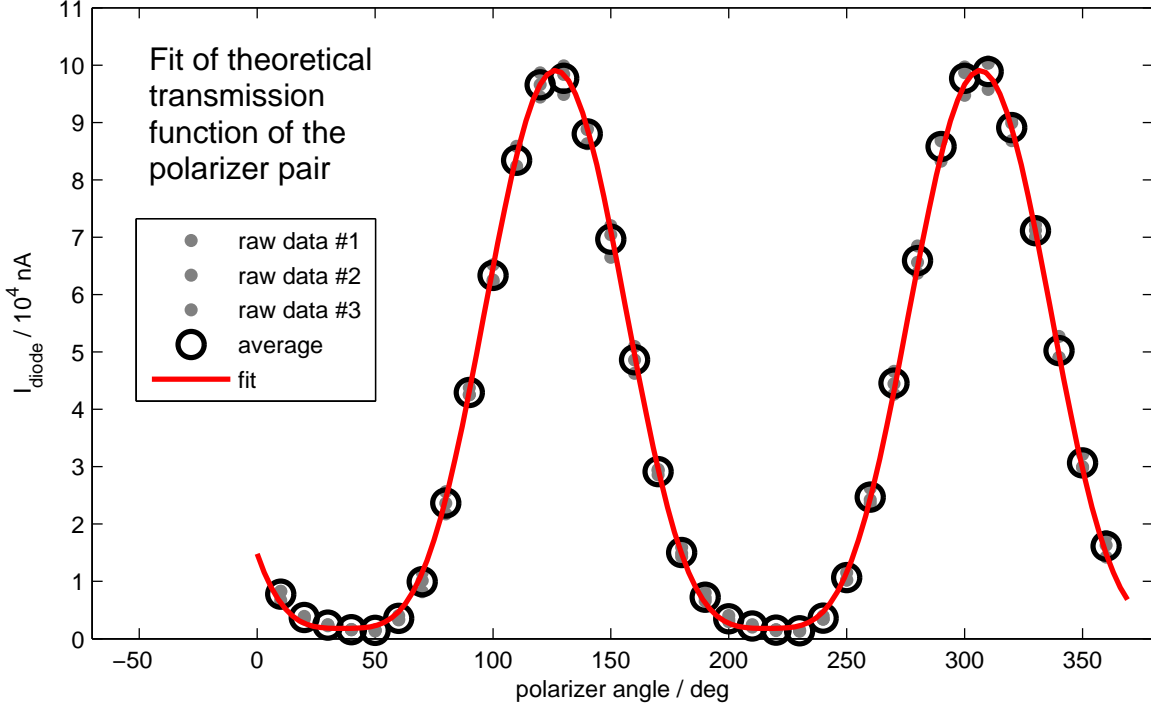


Figure C.1.: Calibration data of the polarizer pair. The photon flux was probed as a function of the polarizer rotation using a photodiode with well-known sensitivity. The theoretical curve was derived from an extension of Malus' law taking care of finite absorption at maximum transmission and non-zero minimum transmission. The parameters introduced here were determined by fitting the experimental data.

Then the maximum generation rate G_0 per volume can be computed by

$$\begin{aligned}
 G_{0,max} &= \underbrace{\frac{\alpha}{4\pi\sigma^2} \cdot T \cdot \frac{\lambda}{hc} \cdot \frac{1}{\eta}}_{5.453 \cdot 10^{31} \text{ m}^{-3} \text{ s}^{-1} \text{ A}^{-1}} \cdot I_{diode} \quad (\text{C.3}) \\
 &= 5.453 \cdot 10^{31} \text{ m}^{-3} \text{ s}^{-1} \text{ A}^{-1}
 \end{aligned}$$

where I_0 is the measured diode current, η is the conversion efficiency of the photodiode of 0.23 A/W , T is the ratio of absorbed photon rate and photon rate detected by the photodiode ($T = 0.96^4 \cdot 0.5$), and $\alpha = 3.9 \cdot 10^7 \text{ m}^{-1}$ is the absorption coefficient for WSe_2 at $\lambda = 532 \text{ nm}$ [39]. The proportionality factor given in equation C.3 results for an estimated laser spot size of $\sigma = 750 \text{ }\mu\text{m}$.

C. Calibration of the light source for the SPV experiment

This proportionality factor was used throughout the work in order to determine the actual rate of absorbed photons at the sample surface from the polarizer configuration. The absolute value of G_0 has a rather large error, as many parameters must be estimated here. Nevertheless, exploiting the good fit to the extension of Malus' law gives a robust measure of the relative photon flux, so the G_0 -scale of the SPV measurements presented in chapter 6 are expected to be free of nonlinearities. As was shown there, the absolute flux has been estimated reasonably.

D. Pulsed MCP operation for the PHOIBOS analyzer

When using pulsed sources (or when time-resolved information is required), it might be desirable that the activity of the electron detector becomes synchronized with the source. In common cases, the inter-pulse spacing is found to be much longer than the pulse duration, so the detector would be likely to collect much noise in times without signal. The easiest approach to time-resolved detection would be using a high-speed camera with very short shutter time. Unfortunately, the highly sensitive CCD cameras used for acquiring images from phosphor screens do not support frequent high-speed snapshots at an acceptable frame rate. In addition, the time-sensitivity would be restricted by the decay time of the luminescent screen, which amounts to 1 *ms* for the actual model used in the PHOIBOS experiment. Even though fast screens have clearly shorter decay times of down to 100 *ns*, the screen would still be the major limiting factor to such an approach.

The solution presented here is based on synchronous modulation of the MCP supply voltage. In the past, this approach has not been feasible due to the lack of high-speed switches capable of interrupting sufficiently high voltages. New products have opened up the opportunity to switch the detector voltage on demand. The device presented here is based on a *Behlke HTS 41-06-GSM* 'power switch' [133]. An excerpt from the data sheet can be found in the table in figure D.2. The switch is based on a fast semiconductor component and is able to switch voltages up to 2×4 *kV*. At considerable smaller voltages rise times in the range of 10 *ns* are found. These voltages are far too small for the operation of a Chevron-configured MCP stack, which is 1500 *V* in the current setup. Here, the exponential dependence of the MCP gain factor on the supply voltage is exploited: Reducing the voltage by 300 *V* for instance, will result in strongly reduced amplification, so that the MCPs can be considered 'off'.

Sönke Harm developed a device that is capable of creating a constant voltage of up to 400 *V*. The integrated fast switch is then used to create high voltage, externally triggered boxcar pulses with excellent rise time. The 'floating triggered high-voltage module' has successfully been tested under laboratory conditions and was found to match its specifications excellently. It provides flexible shaping of the boxcar pulses, including variable pulse duration between some 100 *ns* up to several *ms*. The same holds for the delay with respect to the trigger pulses. The pulse amplitude is not fixed and can be modified by tuning a potentiometer on the main board. The device is operated 'floating' on a constant base voltage of 1100 *V*, provided by the common analyzer and detector

controller *HSA 3500*.

For operational safety, the high-voltage MCP support lines are usually equipped with an upstream voltage limiter (wiring diagram found in [74]) with high-voltage diodes connected in parallel to the MCPs to avoid reverse or excessive voltage being applied to the detector plates. The device also provides low pass filtering for voltage stabilization. As could be expected, the filter characteristic results in blurred flanks of the voltage signal and, even worse, drastically reduces the amplitude of the pulses. As a consequence, this measure of safety has to be removed from the system to grant acceptable performance.

When operating the detector in pulsed mode, frequent total loss of the amplification was observed. Even after switching back to constant supply voltage, normal operation could not be restored then. A close examination of the design of the detector assembly revealed the probable reason of the failure. All components are mounted into an axial hole of the support of the detector assembly, stacked up and secured at the top and at the bottom by retaining rings. For electric insulation, the support is made of PTFE, a material used for UHV bearing applications because of its low friction coefficient even under vacuum conditions. Surprisingly, there are no notches found to fix the retaining rings axially. So what presumably happened is that mechanical vibrations were induced to the detector plates when operated at triggered high-voltage with a repetition rate of 3 kHz . The resonance frequency of the MCPs was found in this range by simulations applying the finite element method (FEM). Anyway, some component of the broad frequency spectrum of the boxcar pulses should match. Mechanical vibrations of one or more detector components are likely to cause a subsequent loosening of the stacked components. As no elasticity in the fixation is found, the components, once loose, lose electric contact and therefore amplification. Simple decomposition and re-assembly of the parts restores normal operation, indicating that none of the components was harmed.

Here, a complete re-design of the detector support is indicated to approve proper fixation of the elements. Figure D.1 shows an exploded view of the solution. All outer dimensions of the support comply to the original layout by *SPECS*, making the new part completely compatible to the PHOIBOS analyzer.

First of all, the retaining rings were replaced by solid rings with azimuthal tothing such that they can be locked in the upper and lower notch inside the axial bore by rotation. The previous axial positions of MCP stack and phosphor screen are retained using PTFE (Teflon) spacers. This design makes the setup flexible for spare parts with dimensions deviating from those of the actual parts. The MCPs are still located precisely in the exit plane of the analyzer, so no degradation of the imaging quality is expected.

The retaining rings are toleranced large as they have to be rotated when latched in the notches. Furthermore, they are not intended to constrain the components directly. MCPs have to be handled with extreme care, so small and well-adjustable fixating forces must be provided by the design. For this reason, axial forces are applied to the stack using spring plunges (H. Kipp Werk KG) placed on the bottom ring. They are made of 1.4305 stainless steel, that is known to be full UHV compatible and non-magnetic except for a small remanence from machining.

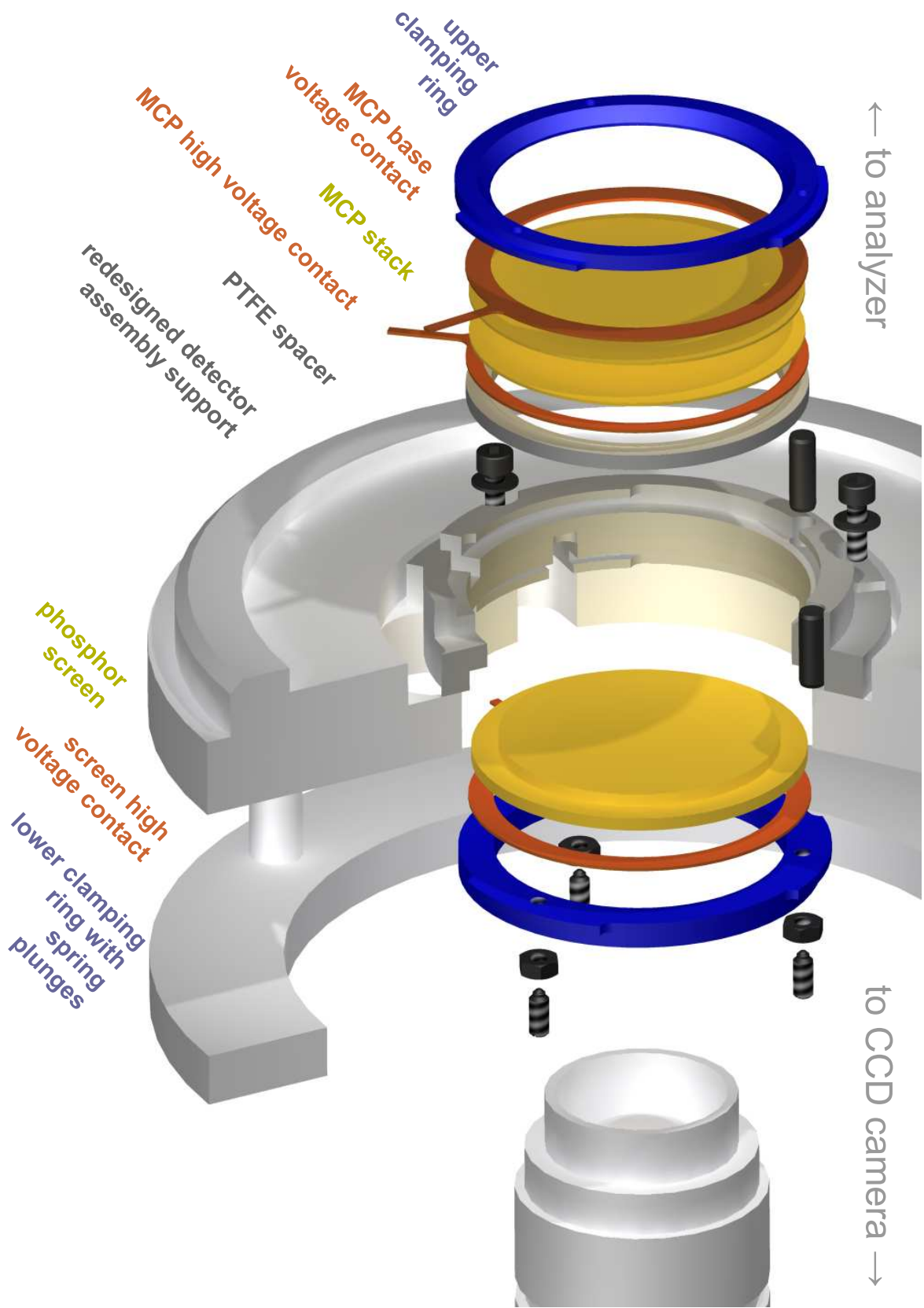


Figure D.1.: Section view of the novel MCP mounting unit

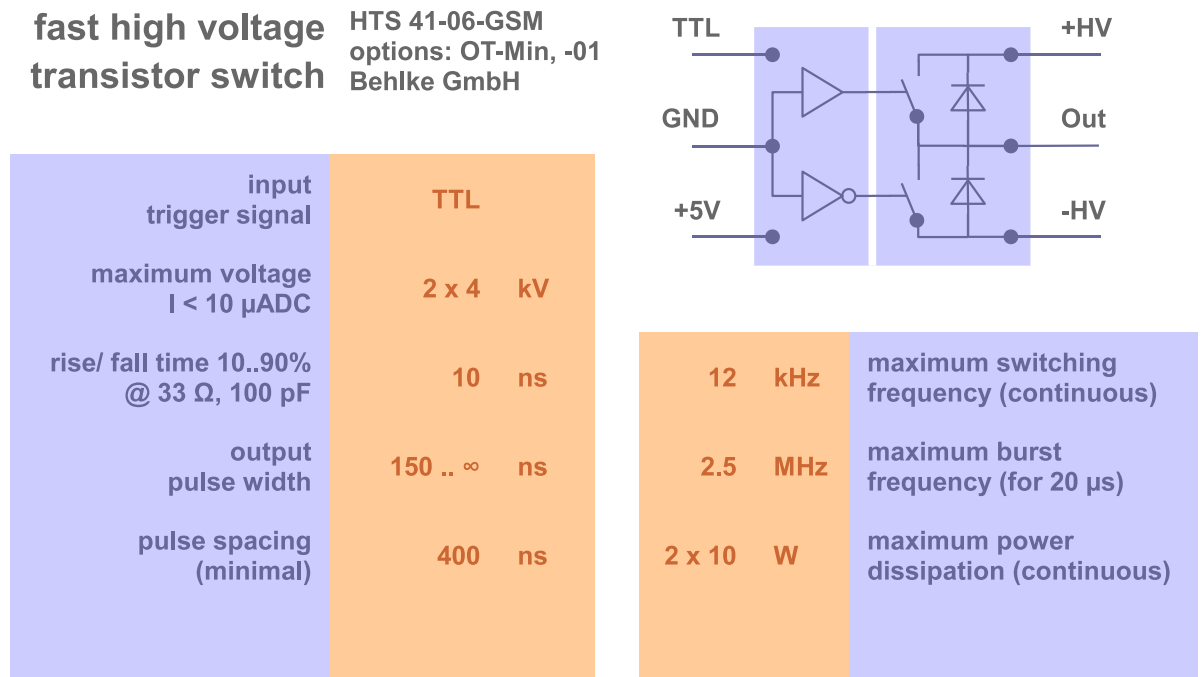


Figure D.2.: Excerpt from the data sheet of the Behlke HTS 41-06-GSM fast high-voltage switch

Once moved into the mounting position, rotation of the toothed rings is avoided by means of two axial through pins placed on the radius of the teeth. For electrical insulation, they are made of MACOR, a robust and well-machinable ceramic. No further modifications are required to use this new design with the PHOIBOS 150 electron analyzer. The existing high-voltage feedthroughs are connected as usual.

The new design has been created in the mechanical workshop of the institute and is ready to be tested in an environment where pulsed operation of the radiation source at relatively low repetition rate makes pulsed operation of the detector desirable. When probing light-induced effects such as the SPV effect, triggered MCP action should open up the possibility for time-resolved measurements, as charge carrier dynamics takes places at a quite large timescale in the μs -range, which is easy accessible with the switching speed achieved here. Direct measurement of surface carrier lifetime should thus be possible in the current ARPES setup.

E. High power laser light supply

The Empower 30 (Newport Corp.) is an integrated laboratory laser source for high-power applications. It is based on a Nd:YLF crystal that is applied to produce laser light at a basic wavelength of 1054 nm , which is internally frequency-doubled to give the output wavelength of 527 nm . By specification, the laser module emits pulses with a maximum energy of 12.6 mJ at a repetition rate of typically 3 kHz and a FWHM pulse duration between 400 ns and 800 ns (measured values at end of fiber, see figure E.3) depending on the mean output power. These characteristics lead to an average power of 38 W . The laser mainly acts as seed for a femtosecond higher-harmonic generation (HHG) source in a dedicated setup that is developed and maintained by the workgroup of Prof. Bauer (for reference, see [78]).

High-power laser radiation might also get used for sample manipulation and preparation. This motivates the plan to provide laser light to various experimental stations of the workgroup, among them the PHOIBOS experiment. Because the laser is located in a remote lab and integrated into the HHG setup permanently, a suitable solution for transporting the laser light over a distance of approximately 25 m had to be found. Here, not only efficiency issues had to be taken into account, but also safety, as the laser is classified in group *IV*. A multi-mode optical fiber was chosen for the transport of the radiation that is especially suitable for guiding high laser power. Some specifications can be found in the table in figure E.1. Special care has to be taken of the fiber ends, onto which the free beam usually gets focussed for optimal coupling. Small deviations from the ideal alignment might result in the destruction of a common fiber when its coating is not designed to stand high absorbed power. Therefore, the fiber is equipped with modified SMA connectors with a free-standing fiber core.

An adjustable coupling stage was implemented on an alternative beam path. The laser beam can be switched between fiber coupling and HHG stage using a mirror on a precision flip mount. The fiber end is fixated on an adjustable mount with three translational axes and a two-axes precision goniometer to grant optimal coupling efficiency. The laser beam is focused to the fiber end by a biconvex lens that can be aligned to match the beam center with two more translational axes. The laser beam has considerable divergence, so part of the light is lost on the distance to the coupling stage. To reduce heat load induced by absorbed light at the components of the coupling stage, the beam is partially shadowed by two iris apertures. These also define the optical axis. In a well-adjusted state, no light is absorbed at the mounts of the focussing lens or the fiber end. Great long-term stability of the transmitted laser power could be observed in this case.

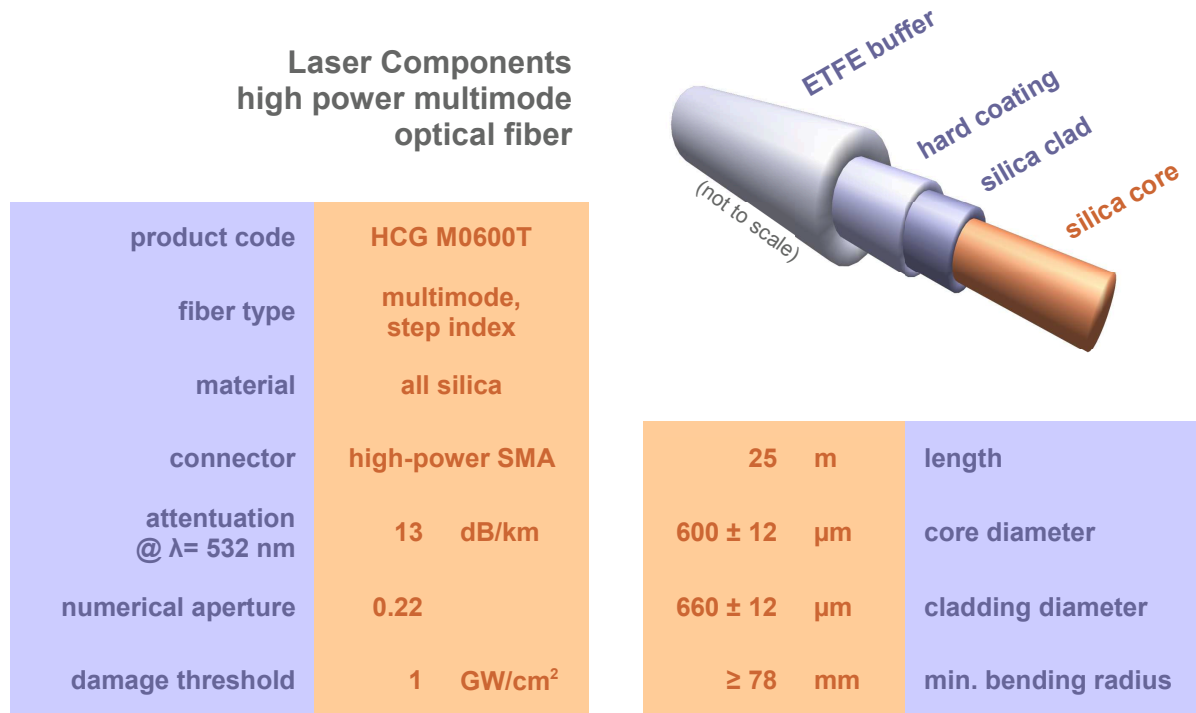


Figure E.1.: General specifications of the high-power optical fiber used for transporting laser light with a power of up to 11 W (measured at end of fiber) to several experimental stations.

The beam shows large divergence at the fiber end station, so a suitable fiber collimator is necessary to reduce divergence. Both fiber end and collimator are integrated in the optical bench assembly described in chapter 5. When using the beam guide to transport laser radiation into the main chamber of the PHOIBOS experimental station, the beam divergence has to be reduced further by the beam expander in the optical bench. All components of the optical fiber setup at both ends were enclosed in a protective housing to avoid dust contamination and assure laser safety.

Due to rather high loss caused by divergence in the system, the total transmission of the fiber coupling system is limited to a maximum of 11 W, measured at the end of the fiber with a conventional calorimetric power meter. Most of the loss faced here results from the large distance between laser source and coupling stage. A highly recommended future upgrade is the replacement of one of the planar bending mirrors near the laser source by a parabolic mirror. Such mirrors with appropriate focal length are available commercially today. For high power applications, lens surfaces cannot be covered with anti-reflective coatings because of their relatively low damage threshold, so a certain amount of reflection loss is inevitable. No significant absorption losses inside the optical fiber were found. The maximum achievable transmission of the 25 m long fiber was found

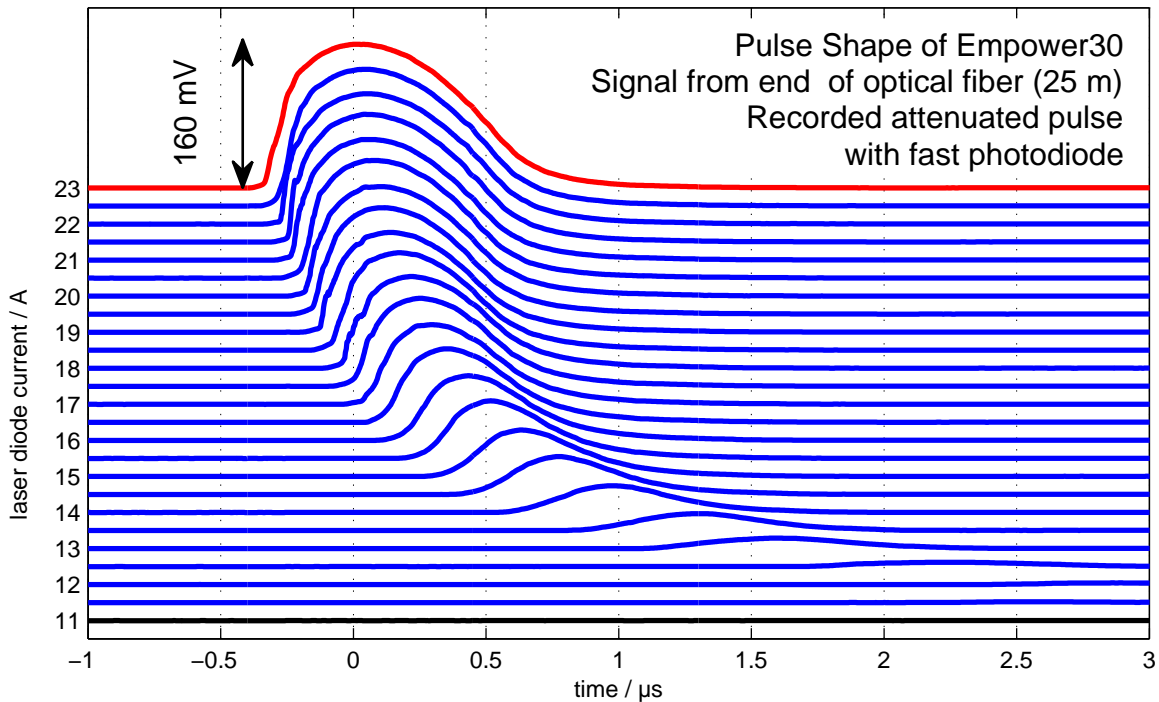


Figure E.2.: Empower pulse shape, depending on diode current. Recorded attenuated beam with fast photodiode at end of optical high-power fiber.

to be identical to that of a specimen with the length of 2 *m* and identical specification.

Remote control of the laser unit is realized by simply establishing a Windows 'Remote Desktop' connection to the laser control computer using the TCP/IP network. The optical fiber is guided through the labs in an opaque, mechanically stable cable duct. A standard BNC cable and an *RS232* compliant data line are also guided through the duct for optional data transmission. The BNC line was used to transmit the trigger output of the Empower 30 for diagnostic purpose and synchronization with the laser pulses as required for triggered operation of the photoelectron detector (appendix D, for instance). The *RS232* cable is required for remote operation of a power meter or a fast shutter device in a future upgrade. It might also serve as data line for a safety interlock system that is yet to be designed.

A fast photodiode (*Intl. Rad. Detectors SXUV20HSI*) was integrated into the optical bench in order to probe the pulse structure of the transmitted laser light during normal operation. It is mounted at the rear side of a bending mirror, so it detects the small amount of transmitted light. Nevertheless, two neutral density filters with approximately 10 % transmission each are required to attenuate the light to a non-overdriving level. The resulting signal is visualized by an oscilloscope measuring the voltage over a short-circuit resistance of 100 Ω between the diode terminals. Using the rising flank of

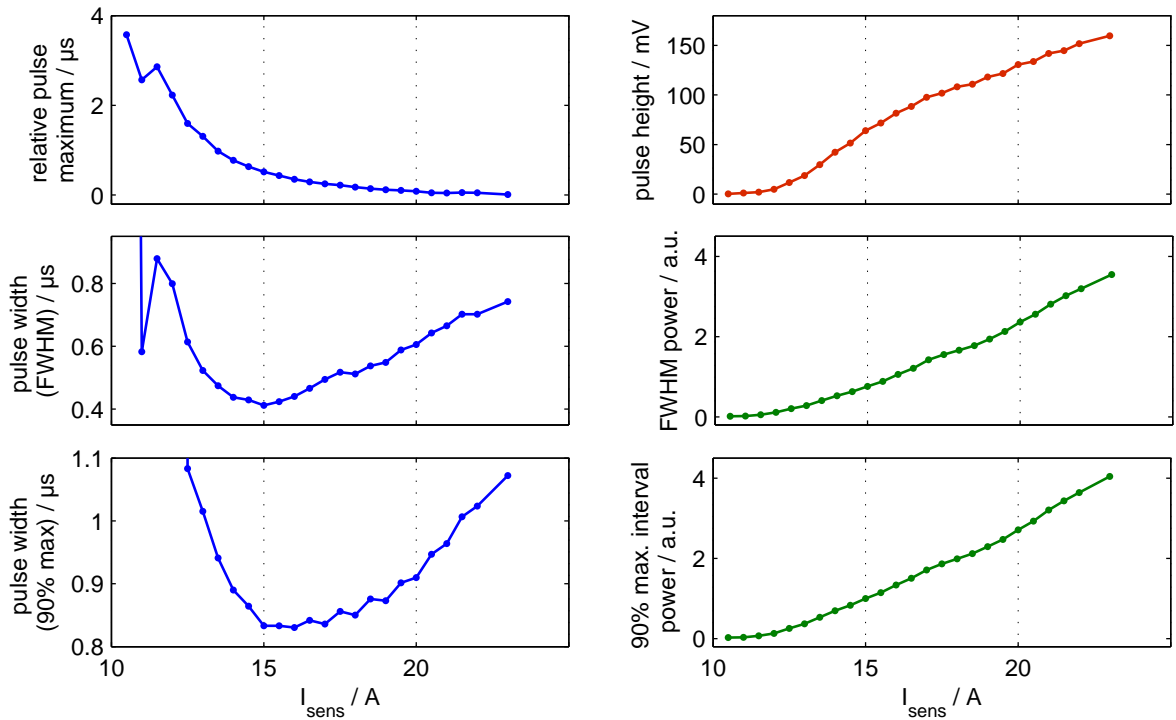


Figure E.3.: Characteristics of Empower pulses as a function of output power (tuned by laser diode current). An intensity-dependent offset with respect to the trigger pulse is found here. The obtained pulse width has a minimum at intermediate emitted flux. The expected quadratic increase of the output power cannot be observed here, presumably due to a shifted beam position at higher flux and a resulting reduced coupling efficiency.

the TTL trigger output from the Empower module as trigger signal, the laser intensity over time was measured at different laser diode current settings. The laser diode current is set by the laser control software and is used to control the output power of the laser. The pulse shape found for different laser diode settings is shown in figure E.2. Time is referenced to the trigger signal. The signal shows significant evolution of delay, duration and peak power. Some characteristics are shown in figure E.3. A noticeable result is found for the pulse duration, no matter what measure is applied. Evaluation of the pulse shape clearly shows a minimum at a diode current of ≈ 15 A, i.e. at a stage of $\approx 25\%$ of the full laser power. All data were recorded without intermittent realignment of the coupling stage. Due to a known, systematic beam shift at higher output power, the overall performance of the beam guide might still be increased remarkably.

The laser light supply established in this work opens up various options for new ex-

periments. High-power laser light might be applied for controlled sample decomposition or controlled evaporation of materials. Experiments involving charge carrier dynamics might benefit from the high available power and the pulsed structure as well. In combination with triggered operation of the photoelectron detector, even kind of direct time resolution might be introduced to the experiments. For two possible applications, Andrej Lang demonstrated feasibility in his Diploma thesis [76]. Using laser light, the thermally induced phase transition between polytypes of tantalum disulphide (TaS_2) could be observed. Furthermore, gentle cleansing of sample surfaces contaminated with rest gas atoms could be achieved using controlled heating of the surface by absorbed laser light.

F. Joypad control for ASPHERE

After all axes of the manipulator cryostat had been equipped with stepper motors, completely remote and partially automated operation of the experiment becomes possible. ASPHERE [53] implements a simple script language for automated scanning operations during long-term measurements and has been upgraded to work as an auxiliary module when the actual data acquisition is done by other programs such as SPECSLAB (appendix G). In addition, interactive control of the stepper motors during sample transfer or alignment is desirable. The integration of direct motor control using a commercially available joypad is presented in this section. Besides this new feature, an auxiliary program module is introduced for precise, interactive control of motor positions.

The novel joypad control was designed as a stand-alone module that fits well into the framework of the ASPHERE measuring software. It was implemented in Delphi, so the communication with the stepper motor drivers could basically be reused. A general interface to joypad hardware is part of the OpenGL specification [134]. In this case, a Delphi wrapper of the OpenGL libraries, namely the 'JEDI SDL' [135] was used in order to import the software interface into the Delphi environment.

Both of the new software modules are accessed from the ASPHERE main window. Screenshots of the graphical user interfaces are shown in figure F.1. The joypad control window basically consists of six segments, each representing one manipulator axis with its motor. It includes the assignment between physical motor and joypad buttons or analog axes. Each motor is assigned an individual maximum frequency. When a motor is operated via digital buttons, it will always move at the given frequency, while analog axes allow for setting the speed continuously between zero and the maximum value. The stepper motor driver supports two operating modes. When the first one is used, absolute motor positions are passed to the controller and its integrated microcontroller takes responsibility of proper motor control. This mode is used when ASPHERE works in script mode. For more dynamic applications, the second mode allows for setting the motor speed directly. Once a speed setting is accepted, the motor will drive until a new command stops it. Here, potential difficulties arise when the connection is disrupted by some reason during motor movement. As the joypad control drives the motors using this mode of operation, the user should always be aware of this danger and grant a sufficiently stable connection to the stepper driver.

The joypad control module allows for saving and restoring the settings of all motor segments in the file `JoystickMappingConfig.dat`. Several configurations can be maintained by replacing this file. Motor control settings can be defined by an interactive axis definition tool which is accessible via the 'Define Axes' button in the main window of

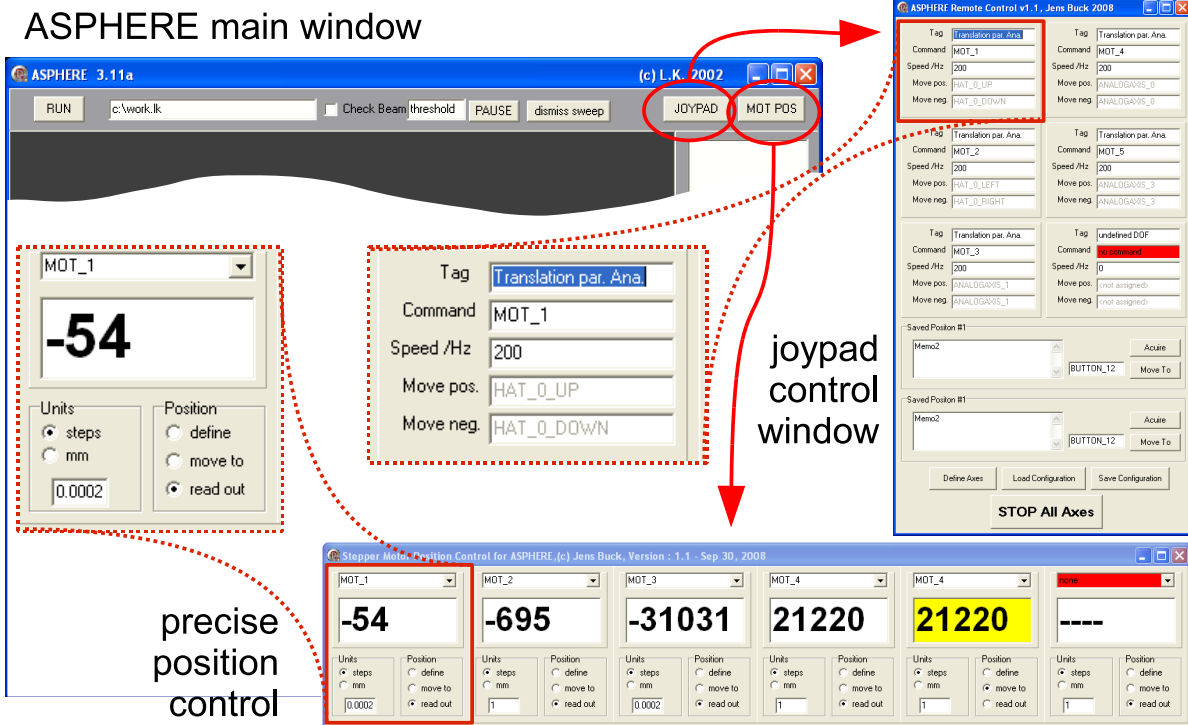


Figure F.1.: Screenshots of the graphical user interfaces to the joypad control (**upper right**) and the precise stepper position I/O control (**bottom**).

the joypad control.

The panel for precise input and output of motor position is also shown in figure F.1. In its basic configuration, it provides real-time monitoring of the internal position registers of the stepper driver for up to six motors in parallel. The position control can be driven in the background when joypad control is activated. Using the individual segments in the window, the current motor position can also be redefined. In this case, the motor will not be driven, and the current position will just be assigned a new number. By selecting the appropriate mode, motion to a user defined position can be achieved. The text boxes will also act as edit boxes here. The current frequency settings as made by ASPHERE or the joypad control, depending on the last one to be active, will be used for motion. Therefore, it's up to the user to upkeep valid settings. A motor may be chosen from more than one of the combo boxes at once, so surveillance and driving at the same time is possible.

After discussing the user interface, some details of the implementation will be outlined now. The code is organized in terms of an object-oriented approach. The different hardware components are mapped to instances of classes that implement basic I/O issues, while other encapsulated code maintains the logical assignments of joypad axes to manipulator degrees of freedom (DOF). The interface of the Jedi SDL provides a

callback mechanism. All input from the joypad is passed to the program in an event-driven manner, such that a user-side callback routine is called upon a state change of the joypad, i.e. moving the sticks, pressing or releasing a button etc. A dedicated data structure with event-specific information is passed then. Some classes that are directly involved in the event processing scheme are introduced now. For full reference, the reader should refer to the actual code and the documentation found therein.

- **TStepperMotor**

This class provides basic communication with the stepper controller including motion and position readout. An instance represents a physical motor and the associated hardware connection, so it keeps information on the COM port of the driver, the command strings to be created, the current frequency setting etc.

- **TJoystickDOF**

According to the preceding class, this class represents a physical switch of the joypad, i.e. a button, an axis of an analog stick, or a direction of the coolie hat. It keeps information on the class of events it will process. The key feature of this module is maintaining assignments between **TJoystickDOF** and **TStepperMotor** objects. Whenever a matching event occurs, an instance of this class is triggered and sends a motor command to the instance of **TManipulatorDOF** it is linked to.

- **TJoyList**

Implements a list of instances of **TJoystickDOF**. Whenever an operation is to be performed with all objects of that class, the interface of this class wraps that operation. For instance, event dispatching is done this way. All instances ever created in the program are stored in this list.

- **TManipulatorDOF**

This class is a representation of a manipulator axes at a higher level than **TStepperMotor** is. It also implements control of the associated edit boxes. When a drive command is issued from **TJoystickDOF**, it computes the stepper distance and speed from the data given in the event structure and the values stored in the edit boxes. The logical motor can be assigned a joyad button for each direction of motion, so it is referenced from two **TJoystickDOF** objects.

- **TManiList**

A list of instances for several logical manipulator axes is implemented in this class. It is conceptual equivalent with **TJoyList** and implements basically the same features, but storing **TManipulatorDOF** references instead of **TJoystickDOF** references as list members.

- **TJoystickMapping**

This class is the glue between all specialized features of the program. It maintains **TJoyList** and **TManiList** instances and contains the code to create, upkeep, and

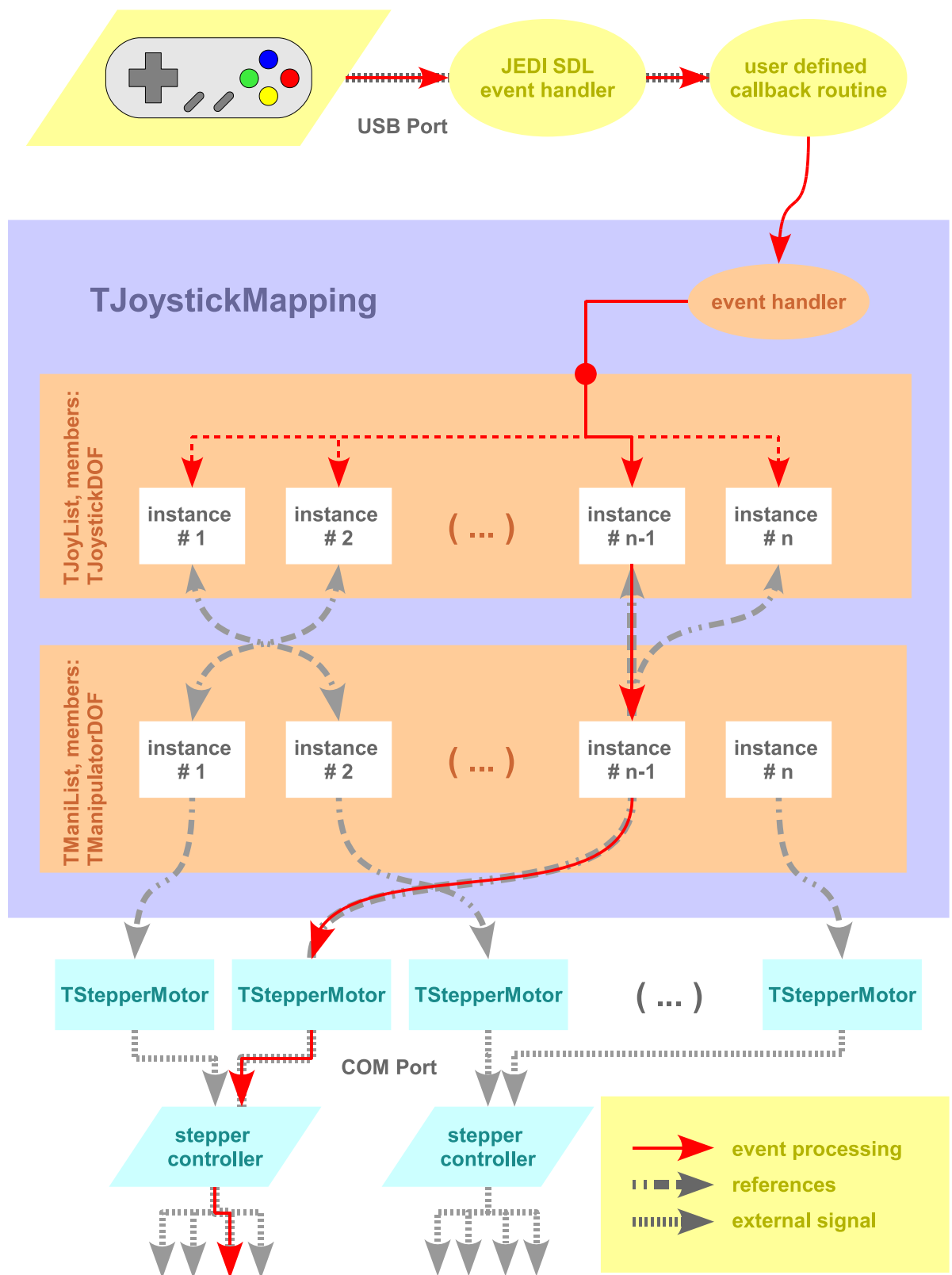
modify cross-references between logical joystick axes and the motor axes. It can be regarded as the entry point for event processing. Some service routines like loading and saving of configuration files and the interactive axes definition are implemented here. Besides the graphical user interface, this class is the only one to be instantiated explicitly when using the joystick control.

Customization of the available motors etc. is done by an outsourced procedure named `InitJoystickMapping`. For further steps when integrating the module into an application, see the documentation given in the code.

The flow chart in figure F.2 illustrates the full control flow path in the program. When called by Jedi SDL's event handler, the user-defined callback function passes the event data to the `TJoystickMapping` object. Low-level filtering of events is done at this stage. For instance, the combined motion of the coolie hat to the upper left direction needs to be excluded from further processing as unintended combined motion of the motors associated with the upper and the left direction is likely. An alternative implementation would have to separate the event into two virtual events indicating 'left' and 'up' individually. When passed to `TJoystickMapping`, the event data is compared with the patterns stored in the instances of `TJoystickDOF`. Further action is triggered exclusively for the first matching object in the list. As a consequence, the assignment of events to virtual axes does not necessarily have to be unique, but the order in this list does matter. Processing the event at the stage of `TJoystickDOF` basically means passing the data to the associated `TManipulatorDOF` with an indicator for the desired direction of movement. In case of an analog axis, events indicating a low amplitude are rejected, so unintended motion is avoided. Finally, `TManipulatorDOF` updates its associated edit boxes to indicate action and passes control to the associated instance of `TStepperMotor`, which creates and sends the actual command string to the stepper controller.

Using two layers of abstraction for the motor communication seems elaborate at a first glance. At last, this approach was realized to maintain optimal flexibility when integrating the code into a graphical user interface. None of the displayed controls need to be present in an alternative solution, or the motor configuration might change, to mention just a few potential changes in the environment. All modifications could be adapted easily by only small changes in the program structure, and even modifications of the hardware-representing program parts at runtime should be easy to implement using the object-oriented layout of the application.

The joystick control with its attached position surveillance has found great acceptance among users of the PHOIBOS experiment and showed up to be astonishingly well usable and stable during operation, so long lifetime of this extension is expected.



230 Figure F.2.: Flow chart of event processing in the joypad control module

G. ASBridge: Synchronous operation of ASPHERE and SPECSLAB

In the PHOIBOS experiment, various pure and combined photoemission techniques can be performed once the capability of moving the sample manipulator during data acquisition is established. Although the analyzer allows for a parallel detection of several angular channels covering a range of up to $\pm 13^\circ$ in 'Wide Angle Mode' [74], the full Brillouin zone can only be accessed by rotating and tilting the sample in measuring position. Using an appropriate combination of parallel detection and sample motion, electron emission can be probed along a broad 'stripe' in momentum space (see sec 4.4 for scanning modes). An exemplary result of applying this technique is presented there. It has also been applied in [76], for instance.

Photoelectron emission can be detected with respect to a small region of interest on the sample surface, either by constraining the acceptance area of the analyzer or by using an excitation source with a small focus. In this configuration, kind of imaging of the sample becomes possible by scanning the probed region, i.e., when the surface is shifted laterally. Further tasks include the characterization of the optical performance of the setup developed in chapter 5, for instance. The general approach made here was to use a modified sample holder in order to probe the beam diameter of the UV source (appendix A) and the laser beam (appendix 5.6). All mentioned measuring modes are based on scanning the sample manipulator.

In the course of this work, all degrees of freedom of the manipulator have been equipped with high-resolution stepper motors (as documented in section 4.3) that are controlled via four-channel stepper controllers developed in the workgroup and applied for many years. The data acquisition software ASPHERE [53] provides comfortable access to a set of motorized axes by implementing a script language to define scan grids for measuring applications. The joystick control for random access to motor positions has been implemented to fit in the framework of ASPHERE (appendix F). Although designed as an all-in-one solution for driving experiments (originally only for the ASPHERE photoemission experiment at the HONORMI end station of DORIS III, DESY, Hamburg), it can also be configured to perform only specialized tasks such as motor operation.

SPECS provides SPECSLAB as data acquisition tool to work with its analyzer hardware, including control of analyzer voltages, detector supply voltage, data readout from the CCD detector and basic data processing, as well as a quite comfortable data handling system. Its architecture is based on the middleware CORBA [136], an open source

TCP/IP-based communication protocol that is meant to enable inter-process communication across the boundaries of address space and operating system. Communication between processes is not limited to the exchange of data packages, but a framework to provide true 'remote procedure calls' is set up by an implementation of the CORBA specification. Therefore, program modules located on a remote machine may be called as if they were included as a library in the local program. Several projects are dedicated to the implementation of the abstract interface definitions on different platforms. SPECS applies the CORBA implementation 'OmniORB' [137] for its application architecture, which provides a Win32/C++ front end of the CORBA specification. SPECSLAB implements several independent modules, starting with low-level device operation and ending up with the user front end. All modules are designed to communicate via the CORBA protocol, potentially allowing for distributed operation of the components on different computers that are connected via TCP/IP. For easy extensibility, SPECSLAB implements the option to call third-party modules at defined stages of the data acquisition process via a given CORBA interface, enabling automated operation of arbitrary devices during measurement.

In this scope, the software module *ASBridge* was designed as a stepstone between the interfaces offered by the programs SPECSLAB and ASPHERE. Some details of the implementation will be discussed in the following.

For the desired application, the SPECSLAB-related efforts reduce to implementing a child class of the interface *IRemote*. Some sample code concerning the external interfaces of SPECS software are shipped with SPECSLAB. *ASBridge* itself is based on the 'IRemote' example that is found in the subfolders of the software. SPECSLAB's CORBA interfaces are exported for customized applications by using the 'Interface Definition Language'(IDL), so the abstract interface definitions must be converted into an actual programming language by means of an IDL compiler. This project was realized using the C++ programming language [117] and the *Microsoft Visual Studio* 6.0 IDE ('Integrated Development Environment'). As the SPECS software is based on *OmniORB* natively, this CORBA implementation was also used for *ASBridge*. Although different implementations should be completely compatible in interaction among each other, potential compatibility problems are minimized by this decision.

Objects implementing specific interfaces must be registered at CORBA's object relocation system after creation in order to publish their availability. This service is offered by a SPECSLAB module named 'ObjectServer'. When registered, the instance of the object can be located and configured in the SPECSLAB graphical user interface, so no further steps are necessary here. Detailed information on setting up *ASBridge* can be found in a dedicated manual shipped with ASPHERE, version 2.75 and above [118].

As the intended synchronization between acquisition of spectra and motor motion basically affects ASPHERE script execution, the script language had to be extended by some dedicated commands covering synchronization issues. The major command, `WAIT_FOR_SYNC`, is inserted into the script code to define changes between script execution and SPECSLAB activity.

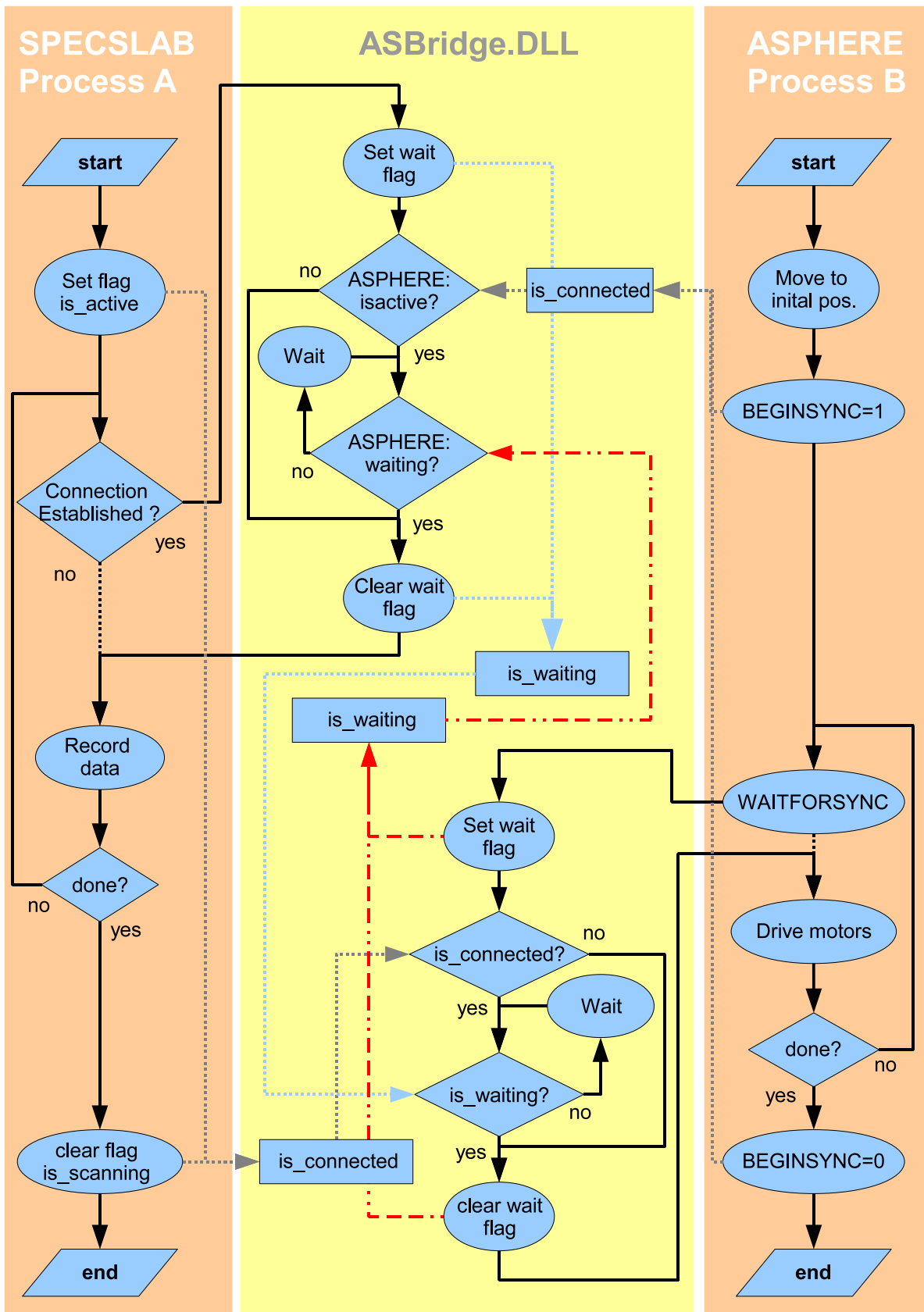


Figure G.1.: Control flux in ASBridge DLL

The implementation of the IRemote interface and the actual processing of the new ASPHERE script commands were encapsulated in a Windows DLL (Dynamic Link Library) that links with ASPHERE, version 2.74 and above. Upon startup, an instance of the IRemote implementation is created and registered, so ASBridge is available to SPECSLAB henceforward. The interface to the DLL is documented in the manual of ASBridge. Further information is found in the detailed reference of the source code.

The basic idea of combined operation of SPECSLAB and ASPHERE is to ensure strict separation of moving motors and data acquisition. Hence, the operation mode should be called 'anti-synchronous'. Inside the DLL, the code for this mode is implemented. In figure G.1, the control flow inside ASBridge.DLL during anti-synchronous operation is shown. The left column of the chart shows the common actions of SPECSLAB, while ASPHERE is found in the right column.

The library is designed to be multi-threaded, and both programs use their individual entry points in parallel. The algorithm applied here is rather trivial : It basically consists of two waiting loops. One is for a thread originating from SPECSLAB and the second one is called from script execution in ASPHERE. Once one of the waiting loops is entered, the thread will only proceed when the other side enters its waiting loop, indicating it has finished its current part of the job. Communication between the two loops is done by sharing library-internal flags. The rest of the flow chart includes code to ensure that neither of the programs can ever lock the other just because it is not doing any job at the moment.

ASBridge showed up to ease acquisition of large amounts of data, which would be extremely elaborate otherwise. It was applied for the various jobs mentioned in the introduction of this chapter and has also been adapted by co-workers to acquire multi-dimensional photoemission data. Apart from usability issues of the graphical user interface, the basic architecture of SPECSLAB shows up to be very well suited for user-extensions. The object-oriented interface design using the CORBA specification requires solid coding skills and might be daunting to the less-ambitioned user, but shows up to be a well-standardized and well-implemented approach with great versatility.

H. Compact laser alignment system for PHOIBOS

In a photoemission setup, a precise and reproducible sample alignment is desirable. Although the axes of the manipulator cryostat can be considered stable, full control of the sample position is not approved in general. Absolute position measurements cannot be made using stepper motor positions as these are stored internally in the stepper driver's volatile memory. Tolerances and modifications of the sample holder introduce an offset to position measurements by the manipulator, so it would have to be calibrated individually for each sample holder. In addition, the motorized transmission of motion suffers a non-negligible lag, especially for the *VG* manipulator that was integrated into the experimental setup during this work. Therefore, an absolute reference point inside the vacuum chamber needs to be defined, enabling the user to restore the sample position in relation to the analyzer exactly. The focus of the electron analyzer is adjusted to the center of the vacuum chamber by default. This point is traditionally marked with two laser beams aligned to intersect exactly in the chamber's center. An angle of typically 60° to 90° between the beams is established for precise definition of the intersecting point. When setting up the laser beams, the geometry of the chamber is exploited: They are aligned to enter and exit the chamber through opposing window flanges pointing radially towards the center of the experimental chamber, so only the paraxial alignment to the flanges needs to be granted.

The approach presented here is basically not a fundamentally new idea. It can rather be seen as re-design from scratch avoiding some difficulties experienced with the operation of the previous setup. The cross section view in figure H.1 gives an overview of the new design. The complete device is mounted directly to a *CF* 35 UHV window flange at the experimental chamber. By the low tolerance of the mounting unit, the laser beam is automatically centered to the window. The unit is fixated to the flange rigidly by three radial clamping screws requiring no tools for mounting and unmounting. The compact design and the good fixation make an undesired readjustment of the device unlikely.

All optical components are integrated into the *Linos* Microbench optical bench system. This makes the construction variable for extensions. All components are auto-aligned axially by the system with very low tolerance, achieved by precise the *H7/g6* fitting of the bore holes and rods. The rods are made from hardened steel, so an excellent stiffness can be achieved in small assemblies. The system allows for compact and time-saving development and was hence chosen for the implementation.

The laser beam is provided by a miniaturized, low-cost laser module with 1 *mW*

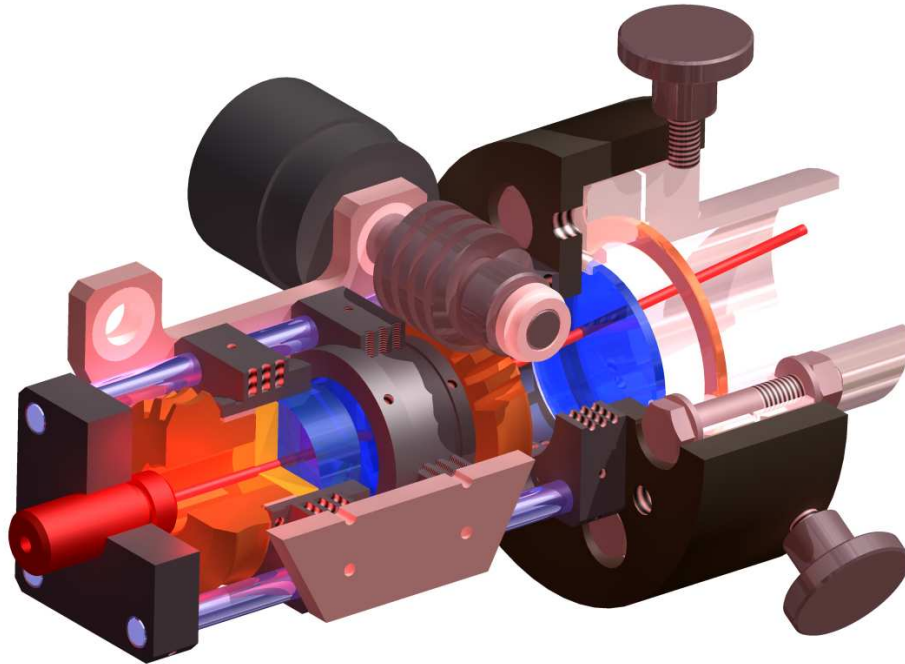


Figure H.1.: Section view of the alignment laser. The mechanical components are based on the Linos Microbench system. Beam steering is performed using two independently rotatable wedge prisms.

output power at a wavelength of 635 nm . The beam diameter at the edge of the module housing amounts to $\approx 1 \text{ mm}$. Considerably smaller spot sizes at the desired reference point are achieved by means of a tunable collimation lens that is integrated into the module.

In order to match both laser beams exactly, and to enable the user to aim at an arbitrary point, though within a limited volume, a precise and stable beam steering device is integrated into the laser alignment system. It consists of a pair of wedge prisms in a rotary mount, so that they can be rotated about the beam direction individually. The front and back surfaces of the actual prisms are titled at an angle of $\beta = 1.93^\circ$ towards each other. When passing a prism, the beam is refracted by an angle α , found by using Snell's law

$$\alpha = \arcsin(n \cdot \sin \beta). \quad (\text{H.1})$$

With the index of refraction of the glass substrate $n \approx 1.515$ (*BK7*-glass for $\lambda = 635 \text{ nm}$), a deviation of $\alpha \approx 2.9^\circ$ is found for the single prism. The envelope of the beam refracted at arbitrary rotation angle δ of the prism is a cone surface with half opening

angle α . Combining two prisms with independent rotation angles, every direction within a cone with half opening angle $2 \cdot \alpha$ can be adjusted. Due to the fact that all angles here can be considered small, the precise formula for the refraction at the second prism with non-perpendicular incident beam can be neglected. Instead, the same angle of refraction α is assumed for both prisms.

Precisely speaking, the finite distance between the prisms and the vacuum feedthrough leads to an offset of the beam position. This is found not to affect the overall positioning performance much and is ignored here. Consider a plane at the working distance L of the alignment laser, i.e., where the reference spot is located. Let the plane be perpendicular to the optical axis, i.e., to the unrefracted beam and let the origin be defined by the intersection of the plane with the optical axis. Then the Cartesian position of the laser spot is given by

$$\begin{pmatrix} x \\ y \end{pmatrix} = D \cdot \begin{pmatrix} \cos \delta_1 + \cos \delta_2 \\ \sin \delta_1 + \sin \delta_2 \end{pmatrix}, \quad (\text{H.2})$$

where $D = L \cdot \sin \alpha$ is the radius of the circle described by the beam as a single prism is rotated. The rotation angles of both prisms δ_1, δ_2 are counted towards the x -axis here. Steering the beam by moving a single prism often leads to unexpected, contra-intuitive motion of the spot in the working plane, because the center of the circular trajectory is not necessarily known a priori. Hence, the prism pair is best operated at simultaneous parallel or anti-parallel motion of both prisms. When transformed to polar coordinates, the spot position reads

$$R = 2 \cdot D \cdot \sin \left(\frac{1}{2} (\delta_1 - \delta_2) \right), \quad (\text{H.3})$$

$$\Phi = \frac{\delta_1 + \delta_2}{2}. \quad (\text{H.4})$$

As can be seen easily, anti-parallel operation will move the spot radially in the working plane. Moving the prisms in parallel results azimuthal motion. The origin of the working plane can be determined by positioning the prisms at an angular difference of 180° .

The rotary mounts cannot be accessed directly. Instead, the rotation of the turning knobs is transmitted to the prisms via worm gears, giving a gear reduction ratio of $1 : 10$.

Special interest is dedicated to the overall positioning accuracy that can be achieved with the alignment device. An expression for the spot displacement ΔR at given angular error ϵ of one of the prism angles can be formulated and reduced as below:

$$\begin{aligned} \Delta R &= \left| \begin{pmatrix} x(\delta_1 + \epsilon, \delta_2) \\ y(\delta_1 + \epsilon, \delta_2) \end{pmatrix} - \begin{pmatrix} x(\delta_1, \delta_2) \\ y(\delta_1, \delta_2) \end{pmatrix} \right| \\ &= \dots \\ &= D \cdot \sqrt{2 \cdot (1 - \cos \epsilon)} \\ &\approx \sqrt{2} \cdot D \cdot \epsilon. \end{aligned}$$

In the last step, it was assumed that the deviation ϵ is small. The surprising result is that the positioning accuracy does not depend on the actual spot position. Compiling all results derived here, an equation for the positioning accuracy can be given:

$$\frac{\Delta R}{\epsilon} = \frac{\sqrt{2}\pi}{180^\circ} \cdot n \cdot L \cdot A \cdot \sin \beta = 0.07 \frac{mm}{deg}. \quad (\text{H.5})$$

Here, the gear reduction ratio $A = 1/10$ is introduced. The result is found for the device parameters stated above and a typical working distance in the PHOIBOS setup of $L = 40 \text{ cm}$.

The design has proven its applicability at various experimental stations inside the workgroup, among them the PHOIBOS ARPES setup and the combined photoemission and inverse photoemission (CARPIP) experiment. Even when mounted to a rotating analyzer in the new PETRA III setup, excellent stability could be achieved, once more demonstrating its superior design.

I. Shape preserving smoothing window for noisy data

Experimental data in general and spectroscopic data in particular is usually superimposed by noise which arises from statistical uncertainty when registering a rate of uncorrelated events, as given by photoelectrons hitting the detector within a defined time interval. In this case, the distribution of registered events follows a Poisson distribution with variance \sqrt{N} at an expectancy value of N . Therefore, measuring uncertainty can be reduced by a large measuring interval. In cases where this is not applicable, the estimation of the expectancy value may be improved by smoothing, i.e., correlating neighbored data points that are assumed to have nearly identical expectation values. For spectroscopic data, this is usually done by computing the moving average of a spectrum. In practice, it is obtained by convolution of the discrete experimental data A_n with a so-called convolution window b_n . Depending on the application and the desired degree of smoothing, the number of points in the discrete window and its actual values can be chosen individually. The simplest case is a window with N points and values $b_n = 1/N$, the so-called boxcar window. The degree of reduction of noise in the experimental data depends on the number of points and becomes better as N increases. Unfortunately, this procedure introduces an error to the data when neighbored data points do not have the same expectancy value. For a peak in a spectrum, this error results in a systematic overestimation of the peak width, no matter which measure is applied, and a systematic underestimation of the peak height. For the individual case, an acceptable trade-off between noise reduction and smoothing error has to be found. Several modifications to the boxcar window are well-known in order to achieve optimal performance, but all suffer from general limitations of data smoothing.

A somewhat more sophisticated approach to the design of an appropriate convolution window is introduced here. Typical experimental data consists of equidistant samples of the smooth relation between two physical quantities such as photoelectron yield inside a narrow interval of kinetic energy. Hence, the function the measuring signal is based on can be assumed to vary slowly between subsequent samples. Its statistical nature implies that the noise is not correlated between neighbored data points. This is, the true spectral data is found at rather low frequency-components in frequency space, whereas the noise is found to have a 'white' spectrum. In conclusion, a well-suited smoothing window should provide an enhanced suppression of high-frequency components in the signal in order to retain the true signal.

Basic smoothing is performed by a narrow convolution window with 'triangular' shape

$$b = \frac{1}{4} \cdot [1 \ 2 \ 1]$$

Smoothing is not performed on the signal alone, but also on its derivatives. For this purpose, the data is differentiated numerically, the window is applied, and the smoothed data is integrated afterwards, retaining the constant of integration. Smoothing of higher derivatives is achieved in an iterative process:

```

smooth signal
differentiate
    smooth 1. derivative
    differentiate
        smooth 2. derivative
        ...
    integrate
integrate
    
```

Differentiation can also be expressed as convolution using the window function $\delta = [-1 \ 1]$. This operation is reversed by computing the cumulative sum for the data points A_n

$$\begin{aligned}
 a &= A \otimes [-1 \ 1] \\
 \Rightarrow A &= \sum_{j=1}^n a_j
 \end{aligned}$$

and removing the additional $a_n \neq 0$ created by the convolution. This operation is equivalent to the convolution with a step function $\Sigma = [1 \dots 1; 0 \dots 0]$, so the complete algorithm can be summarized to convolution with one window. An exemplary case including smoothing up to the second derivative is shown below. Given the signal A , the smoothed signal \tilde{A} is found by

$$\begin{aligned}
 \tilde{A} &= \Sigma \otimes \Sigma \otimes (b \otimes \delta \otimes (b \otimes \delta \otimes (b \otimes A))) \\
 &= \frac{1}{64} \cdot [1 \ 6 \ 15 \ 20 \ 15 \ 6 \ 1] \otimes A.
 \end{aligned}$$

The performance of this algorithm is now demonstrated using artificial data. It was applied to a data set of 10^6 Gaussian random numbers with variance $\sigma = 1$. Figure I.1 shows the Fourier transform of the results for different settings. After transforming the data, it was summarized into 1000 frequency bins with number proportional to frequency. The artificial data shows the expected behavior of white noise. As a reference,

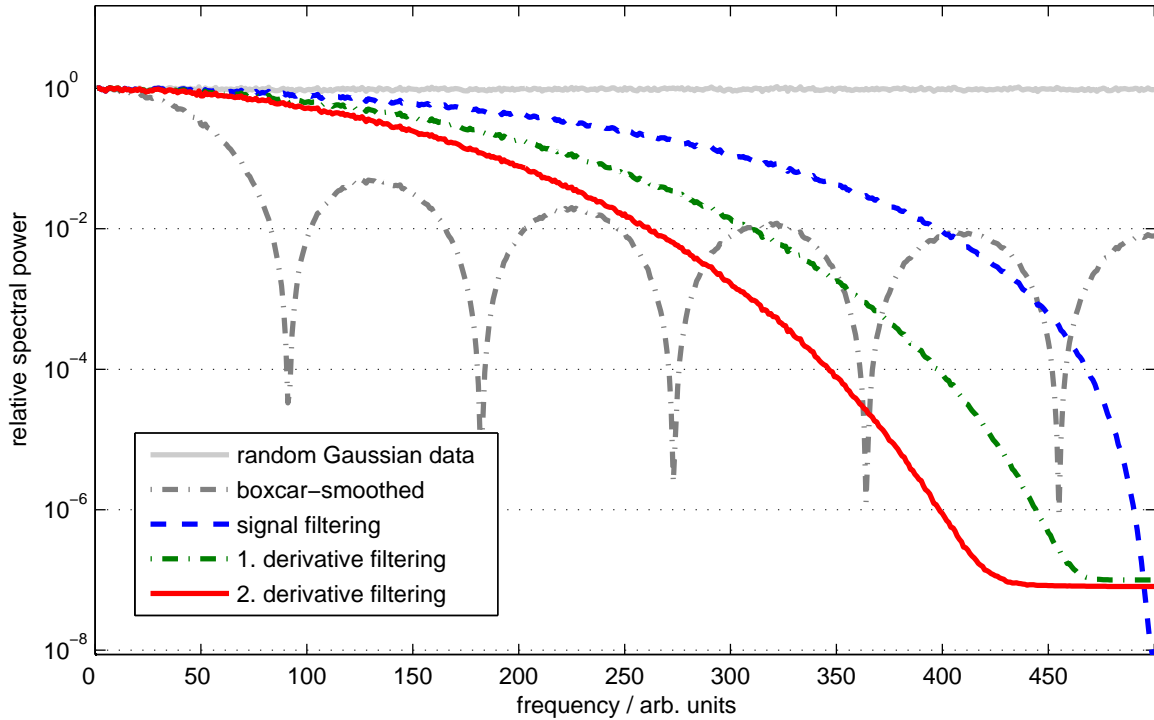


Figure I.1.: Frequency domain behavior of the filtering procedure described in the text. Random Gaussian data (white noise) was filtered using the convolution windows described in the text. 10^6 data points were used here, and the spectrum was binned into 10^3 bins. High frequency components are suppressed well, while the low frequency regime is not bothered. Compared to the conventional, boxcar-smoothed data, the actual shape of a spectrum is expected to be retained better, because low-frequency parts of the data are less affected. Here, a boxcar window consisting of 11 elements was applied.

the performance of a box-car smoothing window with $N = 11$ is shown in the figure. As is well-known, it shows up to remove spectral power of the signal over a wide range. Even worse, periodic dips indicate a pronounced frequency-selective filtering behavior at distinct frequencies. The smoothing window derived here shows up to perform worse in the low frequency regime and is thus expected to introduce only a small error to the estimation of the true spectrum. In comparison to the boxcar window, high frequency noise components are suppressed much better. The smoothed data involving the second derivative even shows a broad interval of suppressed noise.

Although it would be desirable to extend the smoothing to arbitrary high derivatives of the data, this technique is limited by floating point precision. Nested computation of the cumulative sum when re-integrating the data introduces a small summation error to the data, giving a polynomial trend of the order $N - 1$ when occurring at the integration of

the N -th derivative. Precomputing a convolution window for the complete process such as in the equation above would help to work around these difficulties, if effects caused by the finite length of the experimental data can be circumvented. This smoothing procedure was successfully applied to photoelectron spectra (chapter 6) and some other cases found throughout this work.

The coefficients in the basic smoothing window b also appear in the second row of Pascal's triangle. As the combined integration and differentiation operations form linear combinations of this window, iterated application directly leads to line number $2 \cdot N$ in Pascal's triangle at step N . Hence, the considerations made here are in accordance with the binomial filters derived by Marchand [119] earlier, though with a different background. There, the frequency behavior of such filters is analyzed in detail, generally confirming the results found here. The advantages of this filter design compared to the performance of alternative techniques like the smoothing algorithm by Savitzky and Golay [120] is discussed there in the frequency domain as well. With the arguments found there, it can be concluded that this technique has general relevance and its application is justified well.

J. Automated operation of the FUG power supply

The lab power supplies by FUG used in the workgroup are versatile devices that are capable of supplying experiments with currents up to 35 A at a maximum voltage of 20 V. Among common tasks, oven heating and the operation of evaporation sources is found. For remote operation, the devices are equipped with an analog programming line. Modern laboratory applications make remote operation via a control PC and a standard digital communication channel desirable. A solution that meets this demand was implemented by Jörg Neubauer using a microcontroller integrated into the device housing. It is capable of controlling the variable current and voltage limitation of the supply and provides readout of the operational parameters such as current, voltage, and device temperature. Communication with the microcontroller is performed using the *RS232* serial interface. Its software implements a simple communication protocol for command and data transmission, so driving the device from arbitrary software is easy to implement.

In this section, the implementation of a stand-alone driver software for the power supply is presented. Using this software, full control of the FUG power supply is provided by a graphical user interface (GUI). Its basic code is designed to be easy reusable, so the software might be extended to work with more devices in the future. The program code has completely been developed in MATLAB. It might be driven in the MATLAB environment, but is also available in a compiled stand-alone version, so no MATLAB license would be required in this case.

The program code is separated into several modules that implement basic or specialized functionality. Each module has a software interface providing its functionality to other program parts by calls to standard MATLAB functions. For configuration and basic operation, each module has an individual GUI that can be accessed using the main bar in a window that opens after the program has started. Screenshots of the GUIs are shown in figure J.1. The functionality of the modules will be outlined in the following.

The 'SerialComm' module provides basic access to arbitrary devices with *RS232* interface. For operating a device with the program, the appropriate COM interface has to be reserved system-wide using the controls found here. This allows for parallel operation of several programs occupying different serial interfaces at the same computer. A text console allows for sending basic command strings and monitoring the data traffic on the interfaces.

The actual communication with the microcontroller is done in the 'FUG module'.

**SerialComm
module**
basic serial
communication

FUG module
power supply
specific operation

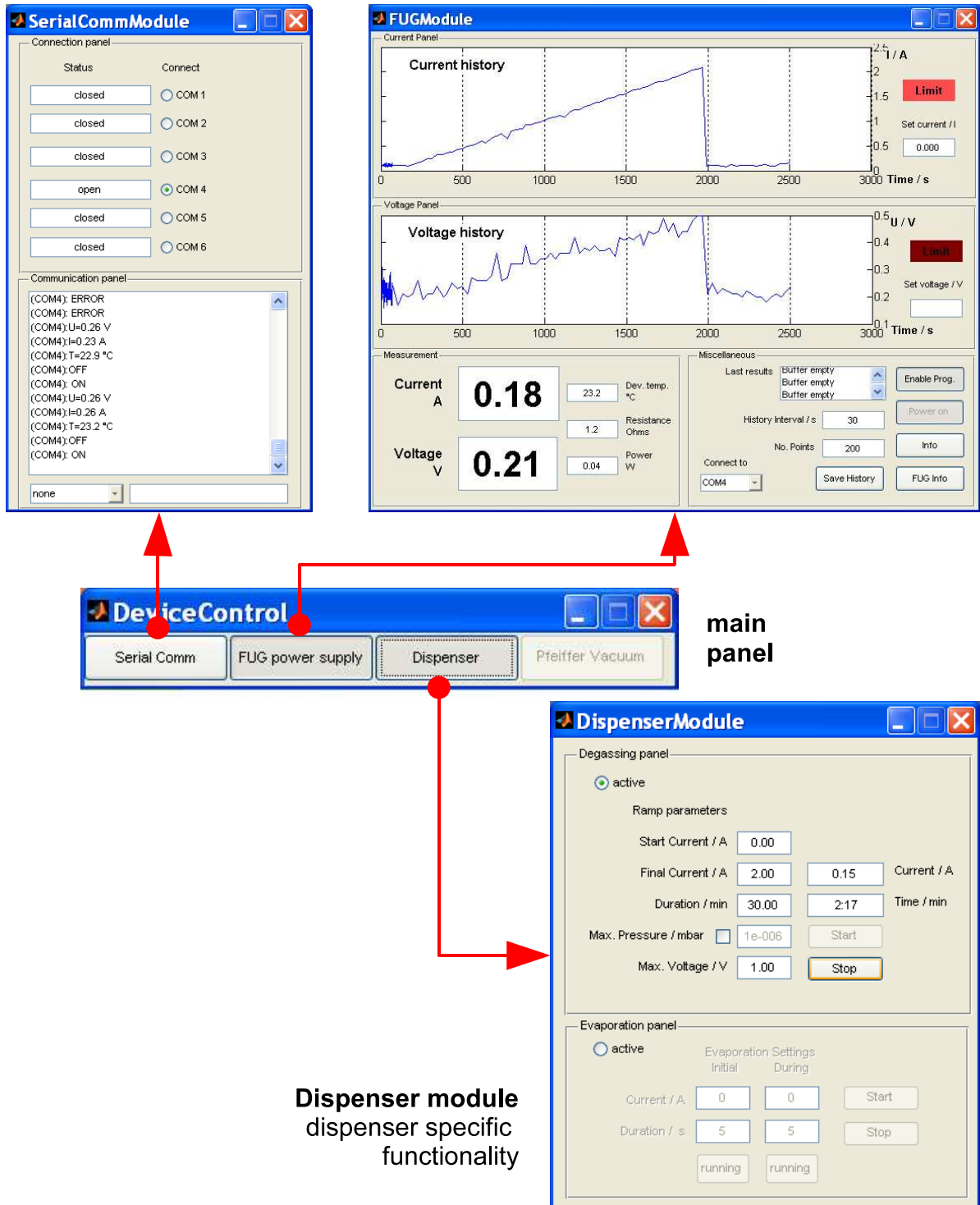


Figure J.1.: User interface of the power supply control

It requires an existing connection in the 'SerialComm' module and the correct COM port assignment to be selected in the GUI. The low-level communication protocol is summarized in table J.2. Once a connection to the power supply is established, the program will record the current and voltage settings at a user-defined rate. The module may be driven for surveillance purpose only. When current and voltage control are desired, the mode must be enabled explicitly by clicking the 'Enable prog.' button. Only in this mode, setting the power supply parameters via the GUI is possible. Note that the turning knobs at the device housing are disabled under these circumstances. The user should always be aware of the meaning of the parameters entered here. Both current and voltage settings are upper limitations. The actual values that are achieved by a certain setting are determined by the load resistance. Although the power supply is capable of providing currents up to 35 A, it is limited to a maximum of 7 A by the software. This ensures safe operation of the dispenser sources used in this work. Not all controls can be introduced in detail, but with the background given here, they should be rather self-explanatory.

The low-level access implemented in the 'FUG module' is used by the 'Dispenser module' to perform specialized operations when driving the *SAES Getters* Rubidium dispenser. The GUI mainly consists of two sections. The first one is applied for degassing the dispenser. Starting at a given base value, the current is increased linearly with time up to a given maximum value. Slowly increasing the current to its maximum value avoids keen degradation of the vacuum when atoms evaporate that contaminate the vacuum parts of the dispenser assembly. A pressure limit can be defined for the degassing period, but full access to the Pfeiffer pressure gauge controller had not been implemented in the current program version, so disabling this option is highly recommended. After some runs, the dispenser may abruptly be switched on. In order to evaporate a defined amount of Rubidium, the dispenser has to be driven with a defined current for a defined period of time. These parameters can be defined by the user in the second part of the panel and step-wise evaporation can be executed there.

The software described here was used successfully during the experiments discussed in chapter 6. Especially the option to drive current ramps showed up to save much time compared to manual operation of the power supply. An unexpected application was found at the inverse photoemission experimental setup (IPES). The Ohmic heating of an electron-emitting cathode applied there requires careful ramping of the heating current when switched on and off. This procedure usually lasts several hours to avoid destruction by thermally induced mechanical stress.

The framework developed here is designed for easy integration of communication modules for further devices such as pressure gauges, sublimation pumps, temperature probes etc. Long-term automated surveillance of vacuum conditions is desirable for a modern experimental setup, which might be implemented in the scope of the presented framework.

FUG power supply serial communication protocol

General

- Standard settings : 9600 Baud, 8 data bits, no parity bit, one stop bit (8N1)
- Every command is confirmed by returning the string ' ____OK\r' (4 spaces)
- Message string when switched on : ' FUG_System_on!_ \r'
- Use decimal point instead of comma!

Error messages

'RANGE?\r'	parameter value out of range
'PARAM?\r'	wrong number of parameters
'ERROR\r'	unknown command string

	command	return string	description	remarks
set commands	SI	%f\r	set current (in A)	
	SU	%f\r	set voltage (in V)	
	SB	%f\r	set baud rate	1200, 2400, 9600, or 19200 (restart required)
	PE	\r	programming mode	on
	PD	\r		off
	P0	\r	switch power supply	on
	P1	\r		off
read commands	RI	\r	'I=%0.2f_A\r'	read current (in A)
	RU	\r	'U=%0.2_V\r'	read voltage (in V)
	RT	\r	'T=%0.2f_°C\r'	read temperature (°C)
	CC	\r	'_ON\r', 'OFF\r'	constant current flag
	CV	\r	'_ON\r', 'OFF\r'	constant voltage flag
	V	\r	6 x '%s\r'	retrieve version string

Conventions

- C-style format strings → '\r' means ASCII character 13 (0x0D)
- Whitespace mentioned explicitly using '_'

J. Buck 11/2009
J. Neubauer 1/2007

Back matter

List of Publications

Reviewed publications

1. J. Buck, J. Iwicki, K. Rossnagel, and L. Kipp: *Surface photovoltage effect at the p-WSe₂:Rb - surface traced by photoemission spectroscopy*
in preparation
2. J. Buck, K. Rossnagel, and L. Kipp: *Methodical developments in PEEM data handling: XPS and absorption spectroscopy of adsorbate-induced, self-organized growth of structures at the p-WSe₂:Rb-surface*
in preparation
3. J. Buck, D. Rahn, K. Rossnagel, and L. Kipp: *Low room temperature mobility of Rb at the cleaved surfaces of the layered crystals WSe₂ and TaS₂*
in preparation
4. M. Kalläne, S. Harm, J. Buck, K. Rossnagel, R. Seemann, and L. Kipp: *Focusing X-rays with arrays of nano-mirror or nano-absorbers*
in preparation
5. D. Rahn, M. Kalläne, J. Buck, J. Bartussek, S. Harm, K. Rossnagel and L. Kipp: *Theoretical and experimental approaches to the characterization of reflective focusing photon sieves*
in preparation
6. D. Rahn, K. Rossnagel, E. Ludwig, J. Buck, ..., and L. Kipp: *PEEM of Rb/TaS₂: Probing a metal-to-insulator transition with nanoscale precision*
in preparation
7. J. Iwicki, E. Ludwig, M. Kalläne, J. Buck, F. Köhler, R. Herges, L. Kipp, and K. Rossnagel: *Photoswitching of azobenzene multilayers on a layered semiconductor*
submitted
8. J. Iwicki, K. Rossnagel, E. Ludwig, M. Kalläne, J. Buck, F. Köhler, R. Herges, and L. Kipp: *Electronic structure of photoisomers on layered crystals*
in preparation

Annual reports

1. M. Marczynski-Bühlow, J. Buck, K. Rossnagel, and L. Kipp N. Janke-Gilman, A. Walter, L. Broekman, and J. Riley
Matrix-Element Effects in Valence Band Photoemission on FeTiS₂ Using Circularly Polarized Light
BESSY Annual Report 2006
2. J. Buck, F. Kronast, K. Rossnagel, H. Dürr, L. Kipp
Microstructure formation at the surface of the intercalation system Rb:TaS₂
BESSY Annual report 2007
3. Jens Buck, Dirk Rahn, Erik Kröger, Florian Kronast, Hermann Dürr, Kai Rossnagel, Lutz Kipp
Probing synchrotron radiation induced local surface potential modifications on the semiconductor p-WSe₂:Rb using PEEM
BESSY Annual Report 2008
4. D. Rahn, E. Ludwig, J. Buck, K. Rossnagel, F. Kronast, H. Dürr, and L. Kipp
PEEM of Rb/TaS₂: Probing a Metal-to-Insulator Transition with Nanoscale Precision
BESSY Annual Report 2008
5. M. Källäne, J. Buck, S. Harm, K. Rossnagel, R.L. Johnson, and L. Kipp
Advances in nanofocusing with reflective photon sieves
HASYLAB Annual Report 2004
6. Murphy, B., Quitzau, M., Buck, J., Källäne, M., Rossnagel, K., Johnson, R.L., Kipp, L.
Structural changes to NbSe₂ upon iron intercalation
HASYLAB Annual Report 2005
7. Källäne, M., Rahn, D., Harm, S., Buck, J., Marczynski-Bühlow, M., Riedel, T., Rossnagel, K., Kipp, L.
First spatially resolved photoemission measurements at BW3 using reflective photon sieves
HASYLAB Annual Report 2006
8. D. Rahn, M. Marczynski-Bühlow, J. Buck, T. Riedel, K. Rossnagel, and L. Kipp
Photoelectron spectroscopy on inhomogeneously Rb adsorbed 1T-TaS₂
HASYLAB Annual Report 2007
9. D. Rahn, Hans Starnberg, M. Marczynski-Bühlow, J. Buck, T. Riedel, K. Rossnagel, and L. Kipp

Poster contributions

1. J. Buck, M. Källäne, S. Harm, M. Skibowski, R. L. Johnson, and L. Kipp
Focussing XUV photons with high contrast
DPG Spring Meeting 2004
2. Jan Bartussek, Jens Buck, Matthias Källäne, Sönke Harm, Kai Rossnagel, and Lutz Kipp
Advances in nanofocusing with reflective photon sieves
DPG Spring Meeting 2005
3. D. Rahn, J. Bartussek, C. Thede, J. Buck, M. Källäne, S. Harm, K. Rossnagel, and L. Kipp
Theoretical and experimental approaches to the characterization of reflective nanofocusing photon sieves
DPG Spring Meeting 2006
4. Dirk Rahn, Hans Starnberg, Jens Buck, Sönke Harm, Kai Rossnagel, and Lutz Kipp
Photoelectron microscopy on inhomogeneously alkali adsorbed transition metal dichalcogenides
DPG Spring Meeting 2007
5. M. Marczynski-Bühlow, S. Lang, J. Buck, K. Rossnagel, and L. Kipp N. Janke-Gilman, A. Walter, L. Broekman, and J. Riley
Matrix-Element Effects in Valence Band Photoemission of FeTiS₂ Using Circularly Polarized Light
DPG Spring Meeting 2007
6. Jens Buck, Ole Mühlfeld, Kai Rossnagel, Florian Kronast, Ruslan Ovsyannikov, Hermann Dürr, and Lutz Kipp
The metal-insulator transition of Rb:TaS₂ observed with PEEM
DPG Spring Meeting 2007
7. Matthias Källäne, Tim Riedel, Dirk Rahn, Sönke Harm, Kai Rossnagel, Jens Buck, Martin Marczynski-Bühlow, Claas Thede, and Lutz Kipp
Spatially resolved photoemission measurements using reflective photon sieves
DPG Spring Meeting 2007
8. Jens Buck, Eric Ludwig, Florian Kronast, Kai Rossnagel, Hermann Dürr, and Lutz Kipp

- Microscale structure formation at the surface of the intercalation system TaS₂ : Rb*
DPG Spring Meeting 2008
9. Dirk Rahn, Hans Starnberg, Martin Marczyński-Bühlow, Tim Riedel, Jens Buck, Kai Rossnagel, and Lutz Kipp
Photoelectron microscopy of the Mott-Hubbard transition at inhomogeneously Rb adsorbed 1T-TaS₂ surfaces
DPG Spring Meeting 2008
10. Martin Wiesenmayer, Jens Buck, Timm Rohwer, Kai Rossnagel, Lutz Kipp, and Michael Bauer *Two-photon Photoemission spectroscopy of the clean and alkali-doped 1T-TiSe₂ transition-metal dichalcogenide*
DPG Spring Meeting 2008
11. Dirk Rahn, Martin Marczyński-Bühlow, Jens Buck, Tim Riedel, Kai Rossnagel, and Lutz Kipp
Photoelectron spectroscopy on inhomogeneously Rb adsorbed 1T-TaS₂
HASYLAB User Meeting 2007
12. M. Källäne, J. Buck, S. Harm, R.L. Johnson, K. Rossnagel, and L. Kipp
Advances in nanofocussing with reflective photon sieves
HASYLAB User Meeting 2007
13. J. Buck, K. Rossnagel, F. Kronast, R. Ovsyannikov, H. Dürr, L. Kipp
The metal-insulator transition of Rb:TaS observed with PEEM
BESSY User Meeting 2006
14. M. Marczyński-Bühlow, J. Buck, K. Rossnagel, and L. Kipp N. Janke-Gilman, A. Walter, L. Broekman, and J. Riley
Matrix-Element Effects in Valence Band Photoemission of Fe_xTiTe₂ Using Circularly Polarized Light
BESSY User Meeting 2006
15. J. Buck, F. Kronast, O. Mühlfeld, K. Rossnagel, H. Dürr, L. Kipp
Microscale structure formation at the surface of the intercalation system TaS₂:Rb
BESSY User Meeting 2007
16. D. Rahn, J. Buck, E. Ludwig, K. Rossnagel, F. Kronast, C. Enderlein, H. Dürr, K. Horn, and L. Kipp
PEEM of Rb/TaS₂: Probing a Metal-to-Insulator Transition with Nanoscale Precision
BESSY User Meeting 2008

Research proposals

1. Jens Buck, Florian Kronast, Ruslan Ovsyannikov, and Kai Rossnagel
Spatial dependence of the metal-insulator transition on nanostructured TaS₂ surfaces
BESSY, 1st semester 2007
2. Jens Buck, Florian Kronast, and Kai Rossnagel
Electronic and geometric structure of Cu adsorbed TaS₂ surfaces
BESSY, 1st semester 2008
3. Jens Buck, Florian Kronast, and Kai Rossnagel
Effects of self-assembled nanowires on the charge carrier dynamics at the p-WSe₂:Rb surface
BESSY, 2nd semester 2009

Supervised diploma theses

1. Frank Baehr *Untersuchungen zur Oberflächenphotospannung an reinem und mit Rubidium bedeckten WSe₂ mittels Photoelektronenspektroskopie*
Institute of Experimental and Applied Physics (IEAP), Christian-Albrechts-Universität zu Kiel, 2006
2. Dirk Rahn *Theoretische und experimentelle Untersuchungen reflektiver Photonen-siebe als Fokussierungsoptik für ortsaufgelöste Photoelektronenspektroskopie*
Institute of Experimental and Applied Physics (IEAP), Christian-Albrechts-Universität zu Kiel, 2006
3. Jan Bartussek *Experimentelle Untersuchung der Fokussierungseigenschaften neuartiger reflektiver Beugungsoptiken*
Institute of Experimental and Applied Physics (IEAP), Christian-Albrechts-Universität zu Kiel, 2006
4. Andrej Lang *Untersuchung der laserinduzierten Phasentransformation von 1T-TaS₂ zu 2H-TaS₂ durch winkelaufgelöste Photoelektronenspektroskopie*
Institute of Experimental and Applied Physics (IEAP), Christian-Albrechts-Universität zu Kiel, 2009

List of Figures

2.1.	Crystal structure and first Brillouin zone of WSe_2	11
2.2.	ARPES data showing the occupied band structure of WSe_2	12
2.3.	Datasheet of WSe_2	15
3.1.	Energy diagram for the photoemission process	18
3.2.	Definition of emission angles in ARPES	19
3.3.	Band diagram of the space charge layer on a p-type substrate	25
3.4.	Surface charge carrier concentration as function of adsorbate concentration	26
3.5.	Schematic of the dynamic processes involved in the model.	28
4.1.	Principle sketch of a hemispherical electron analyzer.	41
4.2.	Schematic drawing of an multi-channel plate electron detector (MCP) . .	42
4.3.	Interior of the main chamber of the photoemission setup	45
4.4.	Raw data images acquired using the PHOIBOS analyzer	49
4.5.	Standard symbols in vacuum technology following DIN 28401	50
4.6.	Chart of the vacuum system of the PHOIBOS setup	51
4.7.	Logical wiring diagram of the PHOIBOS setup	53
4.8.	Calibration data of the motorized manipulator cryostat	56
4.9.	Two-dimensional angular resolving ARPES modes	57
4.10.	Experimental map of the valence band maximum of WSe_2	58
5.1.	Drawing of the optical beam guide	61
5.2.	Analysis of the vibrational modes of the beam guide	63
5.3.	Electrical screening of the focussing lens	66
5.4.	Implementation of the beam shaping system	68
5.5.	Details of the in-situ beam probe	69
5.6.	Focussing study of the auxiliary light source	71
8.1.	Magnetic structure of the APPLE II undulator	89
8.2.	Parameters of beam UE49/PGMa at BESSY II	90
8.3.	Layout of the electron optics of the Elmitec PEEM III	92
8.4.	Overview of the PEEM experimental station	95
8.5.	Modified sample holder system for the PEEM experiment	96
8.6.	Photograph of the scalpel used for sample optimization	97
8.7.	The Rb dispenser device used for laterally confined adsorption	98

9.1. Lateral dependency of mean photon energy	106
9.2. Example of drift correction using the feature tracing method	109
9.3. Drift trajectories determined from actual data by tracing features	110
9.4. Drift correction for low intensity images by correlation	112
10.1. Principle sketch of the separating hyperplane determination	115
10.2. Application of the data reduction algorithm to spectroscopic data	118
10.3. Reconstruction of photoemission spectra from reduced data	119
10.4. Principle of operation of the data classification algorithm	122
11.1. XPS spectra of the cleaved surface of WSe_2	129
11.2. Fit parameters for the core levels doublets of the substrate	131
11.3. Spatially resolved analysis of the clean surface of WSe_2	132
11.4. Panorama of the Rb covered surface of WSe_2	135
11.5. Surface texture for the current position	137
11.6. Spatial variation of XPS spectra on $WSe_2 : Rb$	138
11.7. Spatially resolved study of the adsorbate-induced texture	139
11.8. Spatially resolved study of the adsorbate-induced texture (continued)	140
11.9. Detailed analysis of the $Se\ 3d$ core level	143
11.10 Rb stripe adsorbed on WSe_2	146
12.1. Configuration of the PEEM setup for absorption spectra	149
12.2. Absorption spectra of the Rb covered surface / Table of core levels	150
12.3. Structure of the complete data processing procedure	151
12.4. Nanowire map for the current position	153
12.5. Grouped pixels after data classification	155
12.6. Relative absorption spectra of the sorted data	156
12.7. Relative absorption spectra of the sorted data (continued)	157
14.1. Schematic of the image composition algorithm	166
14.2. Application of the two-dimensional filter to a gray scale image	170
14.3. Details of the line shrinking algorithm	173
14.4. Result of vectorization applied to the nanostructure network	175
15.1. Distribution of island size	178
15.2. Nanowire network at high magnification (assembled UV images)	179
15.3. Selected nanostructure network properties	180
15.4. Selected nanostructure network properties (continued)	181
15.5. Selected nanostructure network properties (continued)	182
16.1. Competing harmonic potentials in the crack creation model	184
16.2. Distribution of the fragment area	192
A.1. Wiring diagram used for focus scanning measurements	206

A.2. Beam profile of the <i>UVS</i> 300 He lamp	207
C.1. Calibration of the polarizer pair	215
D.1. Section view of the novel MCP support	219
D.2. Datasheet of the high-voltage switch	220
E.1. Specification of the high-power optical fiber	222
E.2. Temporal profile of laser pulses from the Empower 30	223
E.3. Characteristics of the laser pulses	224
F.1. User interface of the joypad control program	227
F.2. Event processing in the joypad control program	230
G.1. Flux diagram of the ASBridge DLL	233
H.1. Section view of the alignment laser	236
I.1. Frequency domain characteristic of the linear filter	241
J.1. User interface of the power supply control	244
J.2. Communication protocol for external control of the FUG power supply	246

Experimental data used in this work

Here, a complete list of the experimental data used in this work is given. References to the lab journals do not include the volume, so the date of acquisition must be checked to find the actual journal entries. Results obtained with the PEEM experiment during night shifts might be found in folders of the following day.

Data from chapter 2

data	ARPES raw data images of WSe_2
seen in figure	2.2
lab journal,	
page (beam time)	PHOIBOS, p. 143, p. 147 (Kiel)
acquisition date	Mar 30, 2009; Apr 2, 2009
file(s)	090330PH001.sh5, 090330PH001.sh5, 090402PH001.sh5

data	2D angular resolved scan in Γ -K direction
seen in figure	4.10
lab journal,	
page (beam time)	PHOIBOS, p. 144 (Kiel)
acquisition date	Mar 30, 2009
file(s)	090330PH012.xml, ..., 090330PH024.xml

data	2D angular resolved scan in Γ -M direction
seen in figure	4.10
lab journal, page (beam time)	PHOIBOS, p. 143 (Kiel)
acquisition date	Mar 30, 2009
file(s)	090330PH002.xml, ..., 090330PH011.xml

Data from chapter 4.4

data	2D angular resolved scan in Γ -K direction
seen in figure	4.10
lab journal, page (beam time)	PHOIBOS, p. 144 (Kiel)
acquisition date	Mar 30, 2009
file(s)	090330PH012.xml, ..., 090330PH024.xml

data	2D angular resolved scan in Γ -M direction
seen in figure	4.10
lab journal, page (beam time)	PHOIBOS, p.143 (Kiel)
acquisition date	Mar 30, 2009
file(s)	090330PH002.xml, ..., 090330PH011.xml

Data from chapter 6

data	Valence band spectra showing
seen in figure	SPV effect
lab journal,	??
page (beam time)	PHOIBOS, p. 185 (Kiel)
acquisition date	May 13, 2009
file(s)	090513PH004.xml

Data from chapter 9.4

data	XPS spectrum, <i>W</i> 4 <i>f</i> core level
seen in figure	9.1
lab journal,	
page (beam time)	PEEM, p.29 (Dec 2008)
acquisition date	Dec 14, 2008
file(s)	AnalyzerScan_075.txt

Data from chapter 9.5

data	Series of PEEM images under identical conditions (UV lamp, FOV $\approx 25 \mu m$)
seen in figure	9.2
lab journal, page (beam time)	PEEM (Jul 2009)
acquisition date	Jul 28, 2009
file(s)	WSE2C_000566, ..., WSE2C_000648

data	Series of PEEM images under identical conditions (UV lamp, FOV $\approx 10 \mu m$)
seen in figure	9.4
lab journal, page (beam time)	PEEM (Jul 2009)
acquisition date	Jul 28, 2009
file(s)	WSE2C_000480, ..., WSE2C_000565

Data from chapter 11.2

data	XPS spectrum, <i>W 4f</i> core level
seen in figure	11.1
lab journal,	
page (beam time)	PEEM, p. 24 (Dec 2008)
acquisition date	Dec 13, 2008
file(s)	AnalyzerScan_071.txt

data	XPS spectrum, <i>Se 3d</i> core level
seen in figure	11.1
lab journal,	
page (beam time)	PEEM, p.24 (Dec 2008)
acquisition date	Dec 13, 2008
file(s)	AnalyzerScan_070.txt

Data from chapter 11.4

data	Grid of connected UV images showing surface texture
seen in figure	11.4
lab journal, page (beam time)	PEEM, p.73 (Dec 2008)
acquisition date	Dec 19, 2008
file(s)	WSe2D_000144.dat, ..., WSe2D_000164.dat

data	XPS spectrum, <i>W 4f</i> core level
seen in figure	11.6
lab journal, page (beam time)	PEEM, p.29 (Dec 2008)
acquisition date	Dec 14, 2008
file(s)	AnalyzerScan_075.txt

data	XPS spectrum, <i>Se 3d</i> core level
seen in figure	11.6
lab journal, page (beam time)	PEEM, p.30 (Dec 2008)
acquisition date	Dec 14, 2008
file(s)	AnalyzerScan_085.txt

data	XPS spectrum, <i>Rb 3d</i> core level
seen in figure	11.6
lab journal, page (beam time)	PEEM, p.29 (Dec 2008)
acquisition date	Dec 14, 2008
file(s)	AnalyzerScan_076.txt

Data from chapter 11.6

data	Connected series of UV images
seen in figure	11.10
lab journal,	
page (beam time)	PEEM, p. 99 (Jul 2009)
acquisition date	Jul 28, 2009
file(s)	WSe2D_000006.dat, ..., WSe2D_000022.dat

Data from chapter 12

data	Absorption spectrum, <i>Rb3d</i> core level, clean surface
seen in figure	12.4
lab journal, page (beam time)	PEEM, p. 88 (Jul 2009)
acquisition date	Jul 28, 2009
file(s)	MonochromatorScan_051.txt

data	Absorption spectrum, substrate core levels, clean surface
seen in figure	12.4
lab journal, page (beam time)	PEEM, p.87 (Jul 2009)
acquisition date	Jul 28, 2009
file(s)	MonochromatorScan_049.txt

data	Absorption spectrum, <i>Rb3d</i> core level, low Rb concentration
seen in figure	12.4
lab journal, page (beam time)	PEEM, p. 85 (Jul 2009)
acquisition date	Jul 28, 2009
file(s)	MonochromatorScan_043.txt, MonochromatorScan_044.txt, MonochromatorScan_045.txt, MonochromatorScan_046.txt

data	Absorption spectrum, substrate core levels, low Rb concentration
seen in figure	12.4
lab journal, page (beam time)	PEEM, p.85 (Jul 2009)
acquisition date	Jul 28, 2009
file(s)	MonochromatorScan_035.txt, MonochromatorScan_036.txt, MonochromatorScan_037.txt, MonochromatorScan_038.txt

data	Absorption spectrum, <i>Rb3d</i> core level, high Rb concentration
seen in figure	12.4
lab journal, page (beam time)	PEEM, p. 95 (Jul 2009)
acquisition date	Jul 28, 2009
file(s)	MonochromatorScan_077.txt, MonochromatorScan_078.txt, MonochromatorScan_079.txt

data	Absorption spectrum, substrate core levels, high Rb concentration
seen in figure	12.4
lab journal, page (beam time)	PEEM, p. 94 (Jul 2009)
acquisition date	Jul 28, 2009
file(s)	MonochromatorScan_073.txt, MonochromatorScan_074.txt, MonochromatorScan_075.txt, MonochromatorScan_076.txt

Data from chapter 15

data	Grid of connected UV images of the nanowire network
seen in figure	15.2
lab journal, page (beam time)	PEEM, p. 71 (Jul 2009)
acquisition date	Jul 25, 2009
file(s)	WSe2C_000052.dat, ..., WSe2D_000100.dat

Data used in the appendix

data	Appendix A: Scans of the beam profile of the SPECS UVS300 He discharge lamp
seen in figure	A.2
lab journal, page (beam time)	PHOIBOS (Kiel)
acquisition date	May 16, 2008
file(s)	080516PH007.dat, ..., 080516PH015.dat

Bibliography

- [1] M. Boehme, R. Adelung, M. Traving, L. Kipp, and M. Skibowski, *Appl.Surf.Sci.* **123/124**, 91(1998)
- [2] J. E. Demuth, W. J. Thomson, N. J. DiNardo, and R. Imbihl, *Phys. Rev. Lett.* **56**, 1408 (1986)
- [3] S. Chang, I. M. Vitomirov, L. J. Brillson, D. F. Rioux, P. D. Kirchner, G. D. Pettit, J. M. Woddall, and M. H. Hecht, *Phys. Rev. B* **41**, 17 (1990)
- [4] C. M. Aldao, G. D. Waddil, P. J. Benning, C. Capasso, and J. H. Weaver, *Phys. Rev. B* **41**, 9 (1990)
- [5] M. Alonso, R. Cimino, and K. Horn, *Phys. Rev. Lett* **64**,16 (1990)
- [6] M. Bujatti, *Proc. IEEE* **53**, 397 (1965)
- [7] D. R. Frankl and E.A. Ulmer, *Surf. Sci.* **6**, 115 (1966)
- [8] N. Trares-Wrobel, *Experimentelle und theoretische Untersuchungen zur Oberflächen-Photospannung bei Photoelektronenemission von der (110)-Spaltfläche von Gallium-Arsenid*, Ph.D. thesis, Inst. f. Exp. u. Ang. Phys. der CAU Kiel (1995)
- [9] R. Adelung, *Quantitative Untersuchungen zur Oberflächenphotospannung an GaAs(110) mittels Photoemission*, Diploma thesis, Inst. f. Exp. u. Ang. Phys. der CAU Kiel (1997)
- [10] L. Kipp, R. Adelung, N. Trares-Wrobel, and M. Skibowski, *Appl.Phys.Lett.* **74**,13 (1999)
- [11] R. Adelung, L. Kipp, J. Brandt, L. Tarcak, M. Traving, C. Kreis, and M. Skibowski, *App. Phys. Lett* **74**, 20 (1999)
- [12] R. Adelung, *From dopants to nanowires: rubidium adsorption on layered crystal surfaces*, Ph.D. thesis, Inst. f. Exp. u. Ang. Phys. der CAU Kiel (2000)
- [13] J. Bardeen and W. H. Brattain, *Phys. Rev.* **74**, 230-231 (1948)
- [14] J. J. Kopanski and C. E. Schuster, *Semicond. Sci. Technol.* **8**, 888-910 (1993)

- [15] J. Carstensen, G. Popkirov, J. Bahr, and H. Föll, *Solar Energy Materials & Solar Cells* **76**, 599 (2003)
- [16] A. Kaminski, O. Breitenstein, J. P. Boyeaux, P. Rakotoniaina and A. Laugier, *J. Phys.: Condens. Matter* **16** (2004)
- [17] J. Marek, *J. Appl. Phys.* **55**,2 (1984)
- [18] C. Donolato, *Solid State Electronics* **25**, 11, pp. 1077-1081 (1988)
- [19] M. Lanir, A. H. B. Vanderwyck, and C. C. Wang, *J. App. Phys.* **49**, 12, pp. 6182-6184 (1978)
- [20] D. L. Polla, S. P. Tobin, M. B. Reine, and A. K. Sood, *J. App. Phys.* **52**, 8, pp.5182-5194 (1981)
- [21] H. Carstensen, *Kombinierte winkelaufgelöste Photoemission und inverse Photoemission an reinen und metallbedeckten III-V (110)- Halbleiteroberflächen*, Ph.D. thesis, Inst. f. Exp. Physik der CAU Kiel(1991)
- [22] M. Skibowski and L. Kipp, *J. Electron Spectr. Rel. Phen.* **68**, 77 (1994)
- [23] J. A. Wilson, A.D. Yoffe, *Adv. Phys. C* **18**,193 (1969)
- [24] B. Sipos, A. F. Kusmartseva, A. Akrap, H. Berger, L. Forro, E. Tutis, *Nature Materials* **7**, 12, 960-965 (2008)
- [25] S. V. Borisenko, A. A. Kordyuk, A. N. Yaresko, V. B. Zabolotnyy, D. S. Inosov, R. Schuster, B. Büchner, R. Weber, R. Follath, L. Patthey, H. Berger, *Phys. Rev. Lett.* **100**, 19 (2008)
- [26] S. Y. Hu, M. C. Cheng, K. K. Tiong, and Y. S. Huang, *J. Phys.: Condens. Matter* **17**, 3575-3583 (2005)
- [27] K. E. Goodson, *Science* **315**, 342 (2007)
- [28] C. Chiritescu, D. G. Cahill, N. Nguyen, D. Johnson, A. Bodapati, P. Keblinski, and P. Zschack, *Science* **315**, 351 - 353 (2007)
- [29] J. J. Devadasan, C. Sanjeeviraja, M. Jayachandran, *Mater.Chem. Phys.* **77**, 397 (2002)
- [30] H. Tributsch, *Faraday Discuss. Chem. Soc.* **70**, 189 - 205 (1980)
- [31] N. D. Boscher, C. J. Carmalt and I. P. Parkin, *J. Mater. Chem.* **16**, 122-127 (2006)
- [32] K. Rossnagel and N. V. Smith, *Phys. Rev. B* **76**, 7 (2007)

-
- [33] T. Buslaps, *Elektronische Struktur und Phasentransformationen der Tantal-dichalkogenide*, Ph.D. thesis, Inst. f. Exp. u. Ang. Phys. der CAU Kiel (1991)
- [34] R. Vaidya, N. Bhatt, S. G. Patel, A. R. Jani, A. B. Garg, V. Vijayakumar, B. K. Godwal, *Pramana* **61**, 1, 183 (2003)
- [35] C. Kreis, *Heteroepitaxial Growth and Electronic Structure of Transition Metal Dichalcogenide Clusters and Ultrathin Films*, Ph.D. thesis, Inst. f. Exp. u. Ang. Phys. der CAU Kiel (2002)
- [36] M. Traving, M. Boehme, L. Kipp, M. Skibowski, F. Starrost, E. E. Krasovskii, A. Perlov, and W. Schattke, *Phys.Rev.B* **55**,16 (1997)
- [37] T. Finteis, M. Hengsberger, T. Straub, K. Fauth, R. Claessen, P. Auer, P. Steiner, S. Hüfner, P. Blaha, M. Vögt, M. Lux-Steiner, and E. Bucher, *Phys. Rev. B* **55**,16 (1997)
- [38] R. Spaeh, U. Elrod, M. Lux-Steiner, E. Bucher, and S. Wagner, *Appl.Phys.Lett* **43**,1 (1983)
- [39] R. F. Frindt, *J. Phys. Chem. Solids* **24**, 9, 1107-1108 (1963)
- [40] H. Schäfer, *Chemical Transport Reactions*, Academic Press, New York, 1963
- [41] L. C. Upadhyayula, J. J. Loferski, A. Wold, W. Giritat, and R. Kershaw, *J. Appl. Phys.* **39**, 4736 (1968)
- [42] B. Davey and B. L. Evans, *Phys. Stat. Sol. A* **13**, 483 (1972)
- [43] V. Podzorov, M. E. Gershenson, C. Kloc, R. Zeis, and E. Bucher, *Appl.Phys.Lett.* **84**,17 (2004)
- [44] F. Consadori and R.F. Frindt, *Phys. Rev. B* **2**,12 (1970)
- [45] K.-K. Kam, C.-L. Chang, and D. W. Lynch, *J. Phys. C: Solid State Phys.* **17**, 4031-4040 (1984)
- [46] D.N. Gujarathi, G.K. Solanki, M.P. Deshpande, M.K. Agarwal, *Materials Science in Semiconductor Processing* **8**, 576-586 (2005)
- [47] Y. Feldman, G.L. Frey, M. Homyonfer, and R. Tenne, *J. Am. Chem. Soc.* **118**, 5632 (1996)
- [48] L. Rapoport, V. Leshchinsky, M. Lvovsky, I. Lapsker, Yu Volovik, and R. Tenne, *Tribol. Int.* **35**, 47 (2002)

- [49] J. Yang, H. Yao, Y. Liu, and Y. Zhang, *Nanoscale Research Letters* **3**, 12, 481-485 (2008)
- [50] S.K. Srivastava and B. N. Avasthi, *J. Mat. Sci.* **20**, 3801-3815 (1985)
- [51] F.-R. F. Fan, H. S. White, B. L. Wheeler, and A. J. Bard, *J. Am. Chem. Soc.* **102**, 5142-5148 (1980)
- [52] G. Prasad and O. N. Srivastava, *J. Phys. D: Appl. Phys.* **21**, 1028-1030 (1988)
- [53] M. Kalläne, *Towards Angle and Space Resolved Photoemission: Bonding in Layered Misfit Compounds and Development of Reflective Photon Sieves*, Ph.D. thesis, Inst. f. Exp. u. Ang. Phys. der CAU Kiel (2007)
- [54] M. Boehme, *Electronic structure of the layered materials TaS₂ and Rb-covered WSe₂*, Ph.D. thesis, Inst. f. Exp. u. Ang. Phys. der CAU Kiel (1998)
- [55] M. Traving, *Photoemission, Inverse Photoemission und Raster-Tunnel-Mikroskopie and der WSe₂-Oberfläche*, Diploma thesis, Inst. f. Exp. u. Ang. Phys. der CAU Kiel (1995)
- [56] S. Hüfner, *Photoelectron Spectroscopy*, Springer, Heidelberg, 1995
- [57] H. Hertz, *Über den Einfluß des ultravioletten Lichtes auf die elektrische Entladung*, *Ann. Phys.* **267**,8, 983 (1887)
- [58] A. Einstein, *Über einen die Erzeugung und Verwandlung des Lichtes betreffenden heuristischen Gesichtspunkt*, *Ann. Phys.* **322**,6 , 132 - 148 (1905)
- [59] W. E. Spicer, *Phys. Rev.* **112**, 114 (1958)
- [60] J. J. Yeh and I. Lindau, *Atomic Data and Nuclear Data Tables* **32**, 1-155 (1985)
- [61] M. P. Seah and W. A. Dench, *Surface and Interface Analysis* **1**,1 (1979)
- [62] K. Seeger, *Semiconductor physics: An introduction*, Springer, Berlin, 2004
- [63] S. M. Sze, *Semiconductor Devices: Physics and Technology*, Wiley, (1985, 2002)
- [64] W. Mönch, *Electronic properties of semiconductor interfaces*, Springer, 2004
- [65] J. S. Blakemore, *Solid State Electronics* **25**, 11, 1067-1076 (1982)
- [66] C. Arpigny, *Astrophysical Journal* **138**, 607-609 (1963)
- [67] R. Seiwatz and M. Green, *J. Appl. Phys.* **29**, 7 (1958)
- [68] W. Shockley and W. T. Read jr., *Phys.Rev.* **87**,5 (1952)

-
- [69] R.N. Hall, Phys. Rev. **87**, 387 (1952)
- [70] D. T. Stevenson and R. J. Keyes, Physica **20**, 11 (1954)
- [71] R. H. Kingston, Ann. Phys. **27**, 101 (1956)
- [72] J. Iwicki, *Photoelektronenspektroskopie von Photoisomeren auf Schichtkristalloberflächen sowie Herstellung und Untersuchung des organischen MOP₄-Kristalls*, Ph.D. thesis, Inst. f. Exp. u. Ang. Phys. der CAU Kiel (2009)
- [73] PCO AG, *Manual of the Sensicam QE*
- [74] SPECS GmbH, *Manual of the PHOIBOS 150 electron analyzer and detector unit*
- [75] M. Wutz, H. Adam, and W. Walcher, *Theorie und Praxis der Vakuumtechnik*, Vieweg, Braunschweig (1986)
- [76] A. Lang, *Untersuchung der laserinduzierten Phasentransformation von 1T-TaS₂ zu 2H-TaS₂ durch winkelaufgelöste Photoelektronenspektroskopie*, Diploma thesis, Inst. f. Exp. u. Ang. Phys. der CAU Kiel (2009)
- [77] B. Slomksi, *Pulscharakterisierung mittels SHG-FROG und Erzeugung hoher Harmonischer*, Diploma thesis, Inst. f. Exp. u. Ang. Phys. der CAU Kiel (2008)
- [78] C. Sohr, *Zeitaufgelöste Photoelektronenspektroskopie eines laserinduzierten Phasenübergangs in 1T-TaS₂ am Freie-Elektronen-Laser und der Hohe-Harmonische-Quelle*, Diploma thesis, Inst. f. Exp. u. Ang. Phys. der CAU Kiel (2009)
- [79] P.C. Chou and N. J. Pagano, *Elasticity: Tensor, Dyadic, and Engineering Approaches*, Dover Publications, 1992
- [80] L.D. Landau and E.M. Lifshitz, *Course of Theoretical Physics: Theory of Elasticity*, Pergamon Press, Oxford, 1970
- [81] T. Peter, *Weiterentwicklung eines Experiments zur kombinierten direkten und inversen Photoelektronenspektroskopie*, Diploma thesis, Inst. f. Exp. u. Ang. Phys. der CAU Kiel (2008)
- [82] S. Kobelt, *Optimierung des Elektronenstrahlverlaufs durch die Elektronenoptik im Experiment zur inversen Photoemission mit dem Simulationsprogramm SIMION*, Diploma thesis, Inst. f. Exp. u. Ang. Phys. der CAU Kiel (2008)
- [83] S. E. Stoltz, H. I. Starnberg, and L. J. Holleboom, PRB **71**,12 (2005)
- [84] S. E. Stoltz and H. I. Starnberg, J. Phys.:Cond. Matt. **15**,30, 5231-5242 (2003)

- [85] U. Johansson, R. Nyholm, C. Törnevik, and A. Flodström, *Rev. Sci. Instrum.* **66**, 1398 (1995)
- [86] P. Hoffmann, *Solid State Electronics* **44**, pp. 837-843 (2000)
- [87] J. D. Jackson, *Classical Electrodynamics*, John Wiley and Sons, New York, London, Sidney, Toronto (1975)
- [88] D. Attwood, *Soft X-rays and Extreme Ultraviolet Radiation: Principles and Applications*, Cambridge University Press, 1999
- [89] S. Sasaki, K. Miyata and T. Takada, *Jpn. J. Appl. Phys.* **31**, 1794 (1992)
- [90] S. Sasaki, K. Miyata, T. Takada, T. Shimada, K. Yanagida and Y. Miyahara, *Nucl. Instr. and Meth. A* **331**, 763-767 (1993)
- [91] S. Sasaki, *Nucl. Instr. and Meth. A* **347**, 83-86 (1994)
- [92] J. Bahrtdt, W. Frentrup, A. Gaupp, M. Scheer, and U. Englisch, *Nuclear Instruments and Methods in Physics Research A* **516**,575-585 (2004)
- [93] T. Schmidt, S. Heun, J. Slezak, J. Diaz, K. Prince, G. Lilienkamp, and E. Bauer, *Sur. Rev. Lett.* **5**, 1287 (1998)
- [94] N. M. Buckanie, J. Göhre, P. Zhou, D. von der Linde, M. Horn-von Hoegen, and F.-J. Meyer zu Heringdorf, *J. Phys.: Condens. Matter* **21**,314003 (2009)
- [95] F. Guo, T. Wakita, H. Shimizu, T. Matsushita, T. Yasue, T. Koshikawa, E. Bauer and K. Kobayashi, *J. Phys.: Condens. Matter* **17**, 1363-1370 (2005)
- [96] G. Rempfer, *Ultramicroscopy* **36**, 196-221 (1991)
- [97] J. Falta and T. Möller, *Forschung mit Synchrotronstrahlung*, Vieweg+Teubner Verlag, Chapter 4, Wiesbaden (2010)
- [98] D. Rahn, E. Ludwig, J. Buck, K. Rossnagel, F. Kronast, H. Dürr, and L. Kipp, *PEEM of Rb/TaS₂: Probing a Metal-to-Insulator Transition with Nanoscale Precision*, BESSY Annual Report 2008
- [99] T. M. Roach and D. Henclewood, *J.Vac.Sci.Tech. A* **22**,6 (2004)
- [100] J. Buck, *Charakterisierung und Parametrisierung der Fokussierungseigenschaften von Photonensieben*, Diploma thesis, Inst. f. Exp. u. Ang. Phys. der CAU Kiel (2004)
- [101] J. Buck, F. Kronast, K. Rossnagel, H. Dürr, and L. Kipp, *Microstructure formation at the surface of the intercalation system Rb:TaS₂*, BESSY Annual report 2007

-
- [102] Jens Buck, Dirk Rahn, Erik Kröger, Florian Kronast, Hermann Dürr, Kai Rossnagel, and Lutz Kipp, *Probing synchrotron radiation induced local surface potential modifications on the semiconductor p-WSe₂:Rb using PEEM*, BESSY Annual Report 2008
- [103] I. Witten and E. Frank, *Data mining: practical machine learning tools and techniques*, Morgan Kaufmann, San Francisco (2005)
- [104] V. Vapnik, *Statistical learning theory*, Wiley, New York (1998)
- [105] J. O'Rourke, *Computational Geometry in C*, Cambridge University Press, 1994
- [106] F. Aurenhammer, *Voronoi diagrams – A survey of a fundamental geometric data structure*, ACM Computing Surveys, **23**,345-405 (1991)
- [107] C. B. Barber, D.P. Dobkin, and H.T. Huhdanpaa, ACM Transactions on Mathematical Software **22**, 4, (1996), (Available online at <http://www.acm.org/pubs/citations/journals/toms/1996-22-4/p469-barber/>)
- [108] F. Kronast, *personal communication*
- [109] A.Thompson, I. Lindau, D. Attwood, P. Pianetta, E. Gullikson, A. Robinson, M. Howells, J. Scofield, K.-J. Kim, J. Underwood, K. Kirz, D. Vaughan, J. Kortright, G. Williams, and H. Winnick, *X-Ray Data Booklet*, Center for X-ray Optics and Advanced Light Source, Lawrence Berkeley National Laboratory (available online at <http://xdb.lbl.gov/xdb.pdf>)
- [110] D. A. Shirley, Phys.Rev. B **5**,12 (1972)
- [111] S. E. Stoltz, H. I. Starnberg, and L. J. Holleboom, PRB **67**,12 (2003)
- [112] D. Rahn, K. Rossnagel, E. Ludwig, J. Buck, ..., and L. Kipp, *PEEM of Rb/TaS₂: Probing a metal-to-insulator transition with nanoscale precision*, in preparation
- [113] B. Jähne, *Digital image processing*, Springer, Berlin, 2005
- [114] *Graphics Recognition Algorithms and Systems. Second International Workshop, GREC' 97 Nancy, France, August 22-23, 1997 Selected Papers*, Springer, Berlin, Heidelberg, 1998 (ISBN 978-3-540-64381-4)
- [115] P. Kosmol, *Optimierung und Approximation*, De Gruyter, Berlin, 2010
- [116] S. Chandrasekhar, *Stellar Structure*, p. 401, University of Chicago Press, Chicago, 1939
- [117] B. Stroustrup, *The C++ Programming Language*, Addison-Wesley, 2009

- [118] J. Buck, *ASBridge manual*, in ASPHERE, version 2.75 and above, 2008
- [119] P. Marchand and L. Marmet, Rev. Sci. Instrum. **54**,8 (1983)
- [120] A. Savitzky and M. J. E. Golay, Anal. Chem. **36**,8 , 1627-1639 (1964)
- [121] I. N. Bronstein and K. A. Semendjajew, *Taschenbuch der Mathematik*, Teubner, Frankfurt a. M., 2005

Online Resources

- [122] Deutsche Vakuumgesellschaft e.V., <http://www.physik.uni-kl.de/dvg/>
- [123] H. Kobayashi, S. Sasaki, T. Shimada, M. Takao, A. Yokoya and Y. Miyahara, *Design of variable polarizing undulator (APPLE-type) for SX beamline in the SPring-8*, <http://accelconf.web.cern.ch/AccelConf/e96/PAPERS/THPG/THP113G.PDF>
- [124] Performance of the beam line UE49 at BESSY, http://www.bessy.de/bit/bit_show_object.html.php?i_bit_id_object=152
- [125] Features of the experimental end station UE49/PGMa:(S)PEEM, http://www.bessy.de/bit/bit_show_object.html.php?i_bit_id_object=194
- [126] *Beamline 31 at MAXlab: Short information*, <http://www.maxlab.lu.se/beamline/max-i/bl31/bl31.html>
- [127] S. Urquhart, A. Hitchcock, U. Lanke, B. Haines, and J. Stewart-Ornstein, *Users' Manual for CaPeRS*, <http://exshare.lightsource.ca/sm/Documents/CaPeRS-user-manual-v-3.8.pdf>
- [128] Elmitec Homepage, <http://elmitec.de/>
- [129] Homepage of the QHull project, <http://www.qhull.org/>
- [130] N. Nilsson, *Introduction to Machine Learning*, 'An early draft of a proposed textbook', <http://robotics.stanford.edu/~nilsson/mlbook.html>
- [131] Hamamatsu Photonics K. K., *Datasheet of the G1127-02 photodiode*, http://sales.hamamatsu.com/assets/pdf/parts_G/G1126-02_etc.pdf

- [132] International Radiation Detectors, Inc., *Datasheet of the SXUVHS1 photodiode*,
<http://www.datasheetarchive.com/pdf/Datasheet-026/DSA00450737.pdf>
- [133] Behlke Power Electronics GmbH, *Datasheet of the fast high-voltage transistor switch No. HTS 41-06-GSM*
<http://www.behlke.de/pdf/61-03-gsm.pdf>
- [134] *OpenGL - The Industry's Foundation for High Performance Graphics*,
www.opengl.org
- [135] Homepage of the Jedi SDL project, jedi-sdl.pascalgamedevelopment.com
- [136] Specification of the CORBA middleware, <http://www.corba.org/>
- [137] OmniORB: Free High Performance ORB ,<http://omniorb.sourceforge.net/>

Acknowledgment

A large project such as this thesis would not be feasible without the support from my supervisors and colleagues. Therefore, I would like to acknowledge the following persons for contributing to this thesis:

- First of all, Prof. Dr. L. Kipp for defining and assigning an amazing project in semiconductor physics with various technical, experimental, and theoretical aspects. The balanced mixture of tasks always guaranteed high, long-term motivation. Without his assistance during the application phase to the scholarship grant, this work could not have started in this context.
- K. Roßnagel for his engagement when reviewing and discussing lots of reports, applications and publications as well as for being the driving force of the PEEM projects.
- All former and current Diploma and PhD students of the workgroup for an excellent working atmosphere, company during the beamtimes, reviewing documents and an endless list of supporting jobs during the past years of struggling. Among them are: M. Kalläne, M. Garbrecht, M. Marczynski-Bühlow, J. Iwicki, D. Rahn, M. Helle, M. Quitzau, F. Baehr, J. Bartussek, C. Hamann, C. Thede, O. Mühlfeld, S. Kobelt, S. Lang, T. Peter, E. Ludwig, S. Hellmann, C. Sohr, A. Lang, and E. Kröger.
- J. Iwicki for the good cooperation concerning all aspects of setting up and operating the photoelectron spectrometer.
- M. Kalläne for careful test reading, especially of this thesis, and numerous fruitful discussions on all aspects of this work.
- T. Riedel for his good advice and excellent expertise in mechanical engineering.
- J. Neubauer for his assistance in electronics, especially for designing and implementing the upgrade of the FUG power supply.
- S. Harm for initiating and aid with the implementation of the project to create the triggered detector unit.
- W. Krüger for finding solutions in every field of technical issues with inspiring creativity.
- M. Stiller for doing a great job in any kind of electrical engineering in the laboratory and around.
- M. Brix and the complete staff of the mechanical workshop for their high professionalism in manufacturing uncounted parts of experimental setups.
- Florian Kronast (BESSY, Berlin), responsible of the PEEM station at beamline UE49/PGMa at BESSY, for valuable advice during the PEEM experiments.
- The 'Studienstiftung des deutschen Volks' for a PhD scholarship grant.

Lebenslauf

Jens Buck
geb. 5.2.1979 in Stade

Familienstand ledig, keine Kinder
Staatsangehörigkeit deutsch

Schulische Ausbildung

1985 - 1989 Grundschule Stadtmitte, Bremervörde
1989 - 1991 Orientierungsstufe Bremervörde
1991 - 1998 Gymnasium Bremervörde,
Juni 1998 allgemeine Hochschulreife

Ersatzdienst

1998 - 1999 Deutsches Rotes Kreuz, Ortsverband Bremervörde,
in der Abteilung Rettungsdienst
1998 Ausbildung zum Rettungshelfer

Universitäre Ausbildung

WS 1999 - WS 2004 Studium der Physik an der
Christian-Albrechts-Universität(CAU) zu Kiel
2001 Vordiplom
2003 - 2004 Diplomarbeit am Institut für Experimentelle und Ange-
wandte Physik (IEAP) der CAU in der Arbeitsgruppe
'Electronic Structure / Synchrotron Radiation' von
Prof. Dr. L. Kipp mit dem Titel *Charakterisierung und
Parametrisierung der Fokussierungseigenschaften von
Photonensieben*
2005 - 2010 Arbeiten zur Promotion in der o.g. Arbeitsgruppe
unter Betreuung von Prof. Dr. L. Kipp
Jul. 2005 - Dez. 2005 Promotionsstipendiat des Landes Schleswig-Holstein
Jan. 2006 - Mär. 2008 Promotionsstipendiat der
'Studienstiftung des deutschen Volkes'

Eidesstattliche Erklärung

Hiermit versichere ich an Eides Statt, dass ich diese Arbeit selbständig unter der Betreuung meiner wissenschaftlichen Lehrer und nur mit den angegebenen Hilfsmitteln erstellt habe. Sie wurde unter Einhaltung der Regeln guter wissenschaftlicher Praxis der Deutschen Forschungsgemeinschaft verfasst. Diese Arbeit wurde weder ganz noch in Teilen an anderer Stelle im Rahmen eines Prüfungsverfahrens vorgelegt. Frühere Promotionsversuche wurden von mir nicht unternommen.

Kiel, den

(Jens Buck)